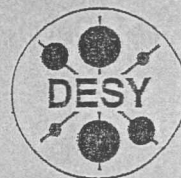


DEUTSCHES ELEKTRONEN-SYNCHROTRON



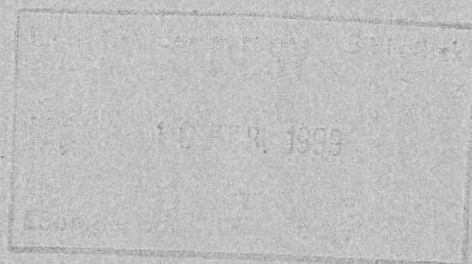
DESY-THESIS-1999-002

January 1999

Measurement of the Heavy Flavour and
Trilinear Gauge Boson Couplings at LEP

by

S. Petzold



ISSN 1435-8085

NOTKESTRASSE 85 - 22607 HAMBURG

DESY behält sich alle Rechte für den Fall der Schutzrechtserteilung und für die wirtschaftliche Verwertung der in diesem Bericht enthaltenen Informationen vor.

DESY reserves all rights for commercial use of information included in this report, especially in case of filing application for or grant of patents.

To be sure that your reports and preprints are promptly included in the HEP literature database send them to (if possible by air mail):

DESY
Zentralbibliothek
Notkestraße 85
22603 Hamburg
Germany

DESY
Bibliothek
Platanenallee 6
15738 Zeuthen
Germany

Measurement of the Heavy Flavour and Trilinear Gauge Boson Couplings at LEP

Dissertation
zur Erlangung des Doktorgrades
des Fachbereiches Physik der
Universität Hamburg

Silke Petzold
aus Günzburg

Hamburg 1998

Gutachter der Dissertation:

Prof. Dr. A. Wagner
Prof. Dr. F.-W. Büßer
Prof. Dr. D. Schaile

Gutachter der Disputation:

Prof. Dr. A. Wagner
Prof. Dr. B. Naroska

Datum der Disputation:

18.12.1998

Dekan des Fachbereichs Physik und

Vorsitzender des Promotionsausschusses : Prof. Dr. G. Kramer

Inhalt

Abstract

An analysis of the charm and bottom forward-backward asymmetries in e^+e^- collisions at LEP is presented, based on the full LEP1 statistics of approximately 4.5 million multihadronic Z^0 decays. In order to tag heavy flavour events, D mesons are reconstructed in seven different channels. Lifetime information and jet-shape variables are used to disentangle the contributions from charm and bottom events to this sample. The asymmetries are determined by a likelihood fit to the charge weighted thrust distribution. The resulting charm and bottom asymmetries, for three different energy ranges on and near the Z^0 pole, are

$$\begin{array}{lll} A_{\text{FB}}^c = 0.039 \pm 0.051 & A_{\text{FB}}^b = -0.086 \pm 0.108 & \langle E_{\text{cm}} \rangle = 89.45 \text{ GeV} \\ A_{\text{FB}}^c = 0.063 \pm 0.012 & A_{\text{FB}}^b = 0.094 \pm 0.027 & \langle E_{\text{cm}} \rangle = 91.22 \text{ GeV} \\ A_{\text{FB}}^c = 0.158 \pm 0.041 & A_{\text{FB}}^b = -0.021 \pm 0.090 & \langle E_{\text{cm}} \rangle = 93.00 \text{ GeV} \end{array}$$

in good agreement with the Standard Model expectations. In order to interpret the results in terms of the Standard Model the effects of the strong interaction in the final state have to be determined. These QCD effects are estimated for three OPAL measurements of the heavy flavour asymmetries. Subsequently, these OPAL measurements are combined, taking into account their statistical and systematic correlations. The OPAL combined results for the bottom and charm forward-backward asymmetries, after correcting for QCD and higher order electroweak effects, yield $A_{\text{FB}}^{b,0} = 0.0968 \pm 0.0037$ and $A_{\text{FB}}^{c,0} = 0.0673 \pm 0.0064$. From these results the value of the weak mixing angle has been determined to be $\sin^2 \theta_{\text{W}}^{\text{lept,eff}} = 0.23270 \pm 0.00060$.

In a second analysis the W-pair production is studied and a measurement of the trilinear gauge couplings with the spin density matrix method in e^+e^- collisions at LEP2 is described. The analysis is based on an integrated luminosity of 57pb^{-1} taken at a centre-of-mass energy of 183 GeV. W-pairs are reconstructed in the decay channel $W^+W^- \rightarrow q\bar{q}l\bar{l}$. The polarisation properties of the W bosons are investigated by extracting the spin density matrix elements from the distributions of the W production and decay angles. From the diagonal elements of the single W spin density matrix the fraction of W bosons with longitudinal polarisation has been determined to be $0.242 \pm 0.091(\text{stat.}) \pm 0.023(\text{syst.})$. A fit is performed to derive the parameters for anomalous trilinear gauge boson couplings in various models. For the three parameters $\Delta\kappa_\gamma$, Δg_1^Z and λ_γ the fits for a single parameter yield

$$\begin{array}{l} \Delta\kappa_\gamma = -0.67 \pm_{-0.36}^{+0.45} \\ \Delta g_1^Z = +0.14 \pm_{-0.21}^{+0.22} \\ \lambda_\gamma = -0.17 \pm_{-0.18}^{+0.19} \end{array}$$

A simple and model-independent test of CP invariance of the WWZ/WW γ vertex is performed by comparing the imaginary parts of the density matrices of the W^- and W^+ bosons and fits for the CP-violating trilinear gauge boson coupling parameters $\tilde{\alpha}_{\text{BW}}$ and $\tilde{\alpha}_{\text{W}}$ yield $\tilde{\alpha}_{\text{W}} = +0.09 \pm_{-0.14}^{+0.18}$ and $\tilde{\alpha}_{\text{BW}} = +0.33 \pm_{-0.57}^{+0.78}$.

Es wird eine Analyse der Charm- und Bottom-Vorwärts-Rückwärts-Asymmetrie präsentiert, die auf der gesamten LEP1-Statistik von ungefähr 4.5 Millionen multihadronischen Z^0 -Zerfällen basiert. Um Ereignisse mit schweren Quarks im Anfangszustand zu selektieren, werden D-Mesonen in sieben verschiedenen Kanälen rekonstruiert. Lebensdauerinformation und typische Jet-Eigenschaften werden verwendet um die Beiträge von Charm und Bottom Ereignissen zu trennen. In einem Likelihood-Fit an die Verteilung der ladungsgewichteten Thrust-Achse werden die Asymmetrien bestimmt. Die resultierenden Charm- und Bottom-Asymmetrien für drei verschiedene Energiebereiche auf und nahe der Z-Resonanz sind

$$\begin{array}{lll} A_{\text{FB}}^c = 0.039 \pm 0.051 & A_{\text{FB}}^b = -0.086 \pm 0.108 & \langle E_{\text{cm}} \rangle = 89.45 \text{ GeV} \\ A_{\text{FB}}^c = 0.063 \pm 0.012 & A_{\text{FB}}^b = 0.094 \pm 0.027 & \langle E_{\text{cm}} \rangle = 91.22 \text{ GeV} \\ A_{\text{FB}}^c = 0.158 \pm 0.041 & A_{\text{FB}}^b = -0.021 \pm 0.090 & \langle E_{\text{cm}} \rangle = 93.00 \text{ GeV} \end{array}$$

Die Ergebnisse sind in guter Übereinstimmung mit dem Standardmodell. Um diese Resultate im Rahmen des Standardmodells zu interpretieren, müssen die Effekte der starken Wechselwirkung in den Endzuständen abgeschätzt werden. Diese sogenannten QCD-Effekte werden für die verschiedenen OPAL-Messungen der Asymmetrien schwerer Quarks bestimmt. Diese Messungen werden unter Berücksichtigung der statistischen und systematischen Korrelationen kombiniert. Die Resultate der Bottom- und Charm- Vorwärts-Rückwärts-Asymmetrien, die sich nach der Korrektur der QCD-Effekte und Berücksichtigung der elektroschwachen Korrekturen höherer Ordnung auf der Z^0 -Resonanz ergeben, sind $A_{\text{FB}}^{b,0} = 0.0968 \pm 0.0037$ und $A_{\text{FB}}^{c,0} = 0.0673 \pm 0.0064$. Von diesen beiden Werten läßt sich der schwache Mischungswinkel, $\sin^2 \theta_{\text{W}}^{\text{lept,eff}} = 0.23270 \pm 0.00060$, ableiten.

In einer zweiten Analyse wird die W-Paar-Produktion in e^+e^- -Kollisionen bei LEP2 untersucht und die Trilinearen Kopplungen der Eichbosonen gemessen. Diese Analyse basiert auf einer integrierten Luminosität von 57pb^{-1} , die bei einer Schwerpunktsenergie von 183 GeV aufgezeichnet wurden. W-Paare werden im Zerfallskanal $W^+W^- \rightarrow q\bar{q}l\bar{l}$ rekonstruiert. Die Polarisations-eigenschaften der W-Bosonen werden mit Hilfe der Spindichte-Matrix-Elemente untersucht. Diese können aus den Verteilungen der W-Produktions- und Zerfallswinkel bestimmt werden. Aus den Diagonalelementen der Spindichte-Matrix wird der Anteil der longitudinal polarisierten W-Boson abgeleitet. Hierbei wird der folgende Wert gemessen: $0.242 \pm 0.091(\text{stat.}) \pm 0.023(\text{syst.})$. Die Parameter, die anomale Trilineare Eichkopplungen in verschiedenen Modellen beschreiben, werden in einem Fit bestimmt. Für die drei Parameter $\Delta\kappa_\gamma$, Δg_1^Z und λ_γ werden folgende Werte gemessen:

$$\begin{array}{l} \Delta\kappa_\gamma = -0.67 \pm_{-0.36}^{+0.45} \\ \Delta g_1^Z = +0.14 \pm_{-0.21}^{+0.22} \\ \lambda_\gamma = -0.17 \pm_{-0.18}^{+0.19} \end{array}$$

Durch den Vergleich der Imaginärteile der Spindichte-Matrizen der W^- - und W^+ -Bosonen kann der WWZ/WW γ -Vertex auf einfache und modellunabhängige Weise auf CP-Invarianz überprüft werden. Die CP-verletzenden Parameter $\tilde{\alpha}_{\text{BW}}$ und $\tilde{\alpha}_{\text{W}}$ werden in einem Fit mit folgenden Ergebnissen bestimmt: $\tilde{\alpha}_{\text{W}} = +0.09 \pm_{-0.14}^{+0.18}$ und $\tilde{\alpha}_{\text{BW}} = +0.33 \pm_{-0.57}^{+0.78}$.

Contents

1	Physics Processes at LEP	1
1.1	Introduction	1
1.2	Physics at Energies around the Z Resonance	2
1.3	Physics at Energies above the Z resonance	6
2	The OPAL Detector	11
2.1	The Central Detectors	11
2.2	The Calorimeter System and the Muon Chambers	14
2.3	The Forward Detectors	15
2.4	The Time-of-Flight Counter in the Endcap Region	15
2.4.1	Motivation	17
2.4.2	Design	17
2.4.3	Performance	20
3	Analyses of the Heavy Flavour Asymmetries	21
3.1	Phenomenology of Heavy Flavour Asymmetries	21
3.2	Measuring Heavy Flavour Asymmetries	22
3.2.1	Lifetime/Jet-charge Analysis	24
3.2.2	The Lepton Analysis	25
3.3	Analysis of the Heavy Flavour Asymmetries using D Mesons	28
3.3.1	Selection of D Candidates	28
3.3.2	Charmed Mesons in $c\bar{c}$ and $b\bar{b}$ Events	36
3.3.3	Determination of the Asymmetries	41
3.3.4	Cross Checks and Systematic Errors	50
3.3.5	Results and Summary	56
3.4	QCD Corrections	56
3.4.1	Introduction	56

3.4.2	Generator Studies and Hadronisation Effects	59
3.4.3	Experimental Bias	62
3.4.4	Results and Conclusions	66
3.5	Combination of the Analyses	66
3.5.1	Interpretation of the Results	68
3.5.2	World Averages and Discussion	75
4	Measurement of the Triple Gauge Boson Couplings	81
4.1	Introduction	81
4.2	Phenomenology of the Triple Gauge Couplings	82
4.2.1	The Trilinear Gauge Boson Vertex	82
4.2.2	Parametrisations of the Triple Gauge Boson Couplings	83
4.2.3	W-Pair Production and Polarisation of the W Bosons	85
4.2.4	Spin Density Matrices	91
4.2.5	Test of CP-Invariance	92
4.3	The Spin Density Matrix Analysis	93
4.3.1	Data Sample and Angular Reconstruction	94
4.3.2	Monte Carlo Samples	95
4.3.3	Event Selection	97
4.3.4	Extraction of the Spin Density Matrix Elements	102
4.3.5	What can be gained from Folded Angular Distributions	106
4.3.6	Extraction of the Anomalous TGC	107
4.3.7	Comparison of the Sensitivity to Anomalous TGC	108
4.4	Extracting TGC including Experimental Effects	109
4.4.1	The 'naive' Method: Correction of the Data	110
4.4.2	The Reweighting Method	117
4.5	Results from the OPAL Data	121
4.5.1	The Correction Method	121
4.5.2	Results from the Reweighting Fit	128
4.5.3	CP Tests	128
4.5.4	Systematic Error Studies	132
4.5.5	Determination of the Longitudinally Polarised Cross-Section	134
4.5.6	Summary	136
4.6	Comparison of Different Methods to Measure TGC	136

4.6.1	The Maximum Likelihood Method	136
4.6.2	The Method of Optimal Observables	138
4.6.3	Comparison of the Methods	139
4.7	Combination with other OPAL Measurements	140
4.7.1	The Analysis of the $q\bar{q}q\bar{q}$ and $l\bar{\nu}l\nu$ Channels	140
4.7.2	The Analysis of the Total Cross-section	142
4.7.3	Combined Results	142
4.8	Present Constraints on TGC Parameters	144
4.9	Future Prospects	150
5	Summary	154

List of Tables

1.1	Values for the correction factors κ_f and ρ_f for electrons, bottom and charm quarks	5
3.1	Summary of the of systematic errors for the lepton analysis.	28
3.2	List of cuts used in the D^* reconstruction.	30
3.3	List of cuts used in the D^0 and D^+ reconstruction.	32
3.4	Percentage of candidates lost in the multiple candidate rejection.	34
3.5	Number of D mesons reconstructed in the different decay modes	36
3.6	Summary of the different background estimators used in the seven D meson channels.	38
3.7	List of charm fractions in the different channels with their statistical and systematic errors.	39
3.8	Summary of the background asymmetries as determined in the fit.	53
3.9	List of the systematic errors contributing to the measured asymmetries of charm and bottom events	54
3.10	Overview of the polarised cross-sections in terms of the quark current products for the pure electroweak process and the case where QCD corrections are included.	57
3.11	Different values of δ_{QCD}	61
3.12	Different values of δ_{QCD}	61
3.13	Estimated value of $\delta_{\text{QCD}}^{\text{had,T}}$	62
3.14	Table of experimental biases and final QCD corrections for the three OPAL asymmetry analyses.	66
3.15	Table of the final QCD corrected asymmetries	67
3.16	The total number of events used in the different analyses and the number of events which are tagged by more than one analysis.	67
3.17	Statistical error correlation matrix of the charm and bottom asymmetry measurements of the three analyses.	68
3.18	Overview over the correlated and uncorrelated errors for the on peak measurements of the bottom and charm asymmetries.	69
3.19	The summary of the systematic and statistical errors of the bottom and charm asymmetries measured at the different centre-of-mass energies.	70

3.20	Error correlation matrix of the combined fit to all three measurements for the three energy ranges.	72
3.21	Summary of the measurements of the effective weak mixing angle performed at LEP and SLD.	77
3.22	Summary of the values for the bottom and charm asymmetry parameters as extracted from LEP and SLD measurements.	79
4.1	Subamplitudes A, B and C for the reduced helicity amplitudes \bar{F} for processes with a transfer of the total angular momentum of $J_0 = 1$	87
4.2	Overview of the helicity amplitudes.	90
4.3	The Monte Carlo samples without anomalous couplings used in this analysis.	97
4.4	The Monte Carlo samples with anomalous couplings, produced with the EXCALIBUR generator in the WW (CC03) mode.	98
4.5	The Monte Carlo samples with anomalous couplings, produced with the EXCALIBUR generator in the 4-fermion mode.	99
4.6	Background cross-sections for the 183 GeV W^+W^- selections	102
4.7	Correlations between the different spin density matrix elements	106
4.8	The symmetric and anti-symmetric parts of the projection operators	106
4.9	The results of the χ^2 -fit to Monte Carlo samples with anomalous couplings, where the 'true' correlations or the Standard Model correlations are used.	108
4.10	Comparison of the sensitivity of the individual angular distributions to anomalous couplings	109
4.11	The fit results of generator level fits to fully simulated data, where the centre-of-mass energy in the χ^2 -fit is stepwise reduced	111
4.12	Comparison of the χ^2 fit results for the full Monte Carlo information (generator level) with the sample of selected events only, where the reconstructed angles have been used and the selection efficiency and resolution correction have been applied.	113
4.13	Test of the reweighting method with large Standard Model Monte Carlo samples.	121
4.14	Results and statistical errors of the χ^2 -fits to the corrected distributions.	124
4.15	Results of the reweighting fit for the various models of anomalous couplings.	128
4.16	Contributions to the total systematic errors of the different TGC parameters	134
4.17	Results of the reweighting fit including bias correction for 4-fermion effects and systematic errors.	136
4.18	The errors for three different TGC parameters as expected from a sample of 57 pb^{-1}	140
4.19	Summary of the results of the event shape analysis of the three different channels.	141
4.20	Combined results from the event rate and spin density matrix analysis for the $q\bar{q}\nu$ channel	144
4.21	Combined results of all three channels for the three TGC parameters.	144
4.22	Results of the four LEP experiments and the D0 experiment together with the combined results for the three TGC parameters.	150

List of Figures

1.1	The different Feynman diagrams contributing to the weak corrections.	4
1.2	Cross sections for some typical Standard Model processes.	6
1.3	4-fermion production classes of diagrams	7
1.4	The cross-section for the W -pair production near the threshold	8
2.1	The OPAL-detector.	12
2.2	Position of the Tile Endcap and MIP-plug detectors with respect to the neighbouring sub-detectors.	16
2.3	Design of the tile endcap sectors	18
2.4	Design of the MIP-plug sectors	19
2.5	Time resolution of the MIP-plug and the TE detector.	20
3.1	Distributions of the difference $M_{D^*} - M_D$ reconstructed in the different D^* channels.	31
3.2	Invariant mass spectra for the D^0 and the D^+ channels.	33
3.3	Distribution of the decay length significance and the neural network output in data and Monte Carlo.	40
3.4	Sketch of the method of determining the charge correlation factor.	44
3.5	The jet-charge identification probability η_q for bottom and charm quarks as a function of the weight factor κ as determined from the Monte Carlo.	45
3.6	The ratio of unlike sign to all events, after background subtraction, as a function of the decay length significance.	48
3.7	Differential asymmetry as a function of $y = q \cos \theta_{thrust}$	50
3.8	Results for the b and c asymmetries at energies on and around the pole of the Z resonance.	51
3.9	Comparison of the measured b and c asymmetries on the peak of the Z resonance with the Standard Model prediction	52
3.10	The results for the charm and bottom asymmetries for the individual channels	53
3.11	Feynman graphs of the process $e^+e^- \rightarrow q\bar{q}(g)$	57
3.12	Pictorial representations of the different topologies which can influence the asymmetry.	58

3.13	Dependence of the QCD correction of the charm forward-backward asymmetry in charm events	63
3.14	QCD correction including all experimental biases for the lepton sample in bottom events as a function of the output of the neural network.	65
3.15	QCD correction including all experimental biases for the D meson sample in $e^+e^- \rightarrow b\bar{b}$ events as a function of the scaled energy of the D meson	65
3.16	The results of the individual bottom and charm asymmetry measurements together with the OPAL combined value.	71
3.17	Summary of the results for the b and c asymmetries at energies on and around the pole of the Z resonance from different OPAL analyses and their combination.	73
3.18	Summary of the LEP results for the bottom and charm asymmetries.	76
3.19	The LEP combined result for the bottom and charm forward-backward asymmetries as a two dimensional contour plot.	77
3.20	Summary of the measurements of the weak mixing angle performed at LEP and SLD.	78
4.1	Feynman diagrams of W pair production in e^+e^- collision.	81
4.2	The various helicity cross-sections (τ_-, τ_+) as a function of $\cos\theta$ at a centre-of-mass energy of 183 GeV.	89
4.3	An illustration of the definitions of the W production and decay angles.	91
4.4	The angular resolution for the W production and decay angles	94
4.5	The projection functions	103
4.6	The spin density matrix elements extracted from the leptonically decaying W of a generator level Monte Carlo	105
4.7	Fit results in the $W\Phi$ model for 120 fits to small Monte Carlo samples, where the $\cos\theta$ only or all angular information is used.	109
4.8	The angular distributions of the three angles $\cos\theta$, $\cos\theta^*$ and ϕ^*	112
4.9	The acceptance and resolution corrections for four bins in $\cos\theta$	114
4.10	The density elements extracted from the KORALW Monte Carlo on generator level compared to those, where selected events only and the reconstructed angles are used and the correction has been applied.	115
4.11	Summary of the bias checks for the methods which corrects the data to tree level	116
4.12	Summary of the bias checks for the reweighting method with Monte Carlo samples of 183 GeV.	119
4.13	Summary of the bias checks for the reweighting method with Monte Carlo samples of 183 and 184 GeV.	120
4.14	Fit results of 118 subsamples of the EXCALIBUR Monte Carlo with luminosities corresponding to 57pb^{-1}	122
4.15	The fraction f of the fit results, where the χ^2 -difference between the fitted value and the Monte Carlo input value is below the value of the abscissa.	123

4.16	The differential cross-section reconstructed from data.	124
4.17	The spin density matrix elements of the leptonically decaying W as a function of $\cos\theta$ determined from data.	125
4.18	The spin density matrix elements of the hadronically decaying W as a function of $\cos\theta$ determined from data.	126
4.19	The χ^2 -curves for the fit to various triple gauge boson coupling parameters	127
4.20	The χ^2 -curves for the reweighting fit to the OPAL data.	129
4.21	The imaginary parts of the density matrices determined from data.	130
4.22	The differences and sums of the imaginary parts of the density matrices determined from data.	131
4.23	The χ^2 -curves for the fit to CP violating TGC parameters, where $\Delta\chi^2 = \chi^2 - \chi_{min}^2$	132
4.24	Differential cross-section to produce a transversely polarised W and a longitudinally polarised W in a W-pair event, where the second W can have any polarisation.	135
4.25	The χ^2 -curves for the fit results including the systematic errors	137
4.26	The log likelihood curves of the event rate and spin density matrix method of the $qq\bar{l}$ channel together with that of the combined results	143
4.27	The likelihood curves of the event shape and event rate analyses, both combined for all channels and the overall combined results	145
4.28	The likelihood curves of the three channels individually and the combined results for the three trilinear gauge coupling parameters.	146
4.29	The likelihood curves of the combined results of the four LEP experiments	148
4.30	The LEP combined results for two-dimensional fits to the three coupling parameters.	149
4.31	The helicity amplitudes as a function of the W production angle for a centre-of-mass energy of 500 and 183 GeV.	152
4.32	The contribution of the longitudinally and transversely polarised cross-section $e^+e^- \rightarrow W_{L,T}W$	153

Chapter 1

Physics Processes at LEP

1.1 Introduction

The e^+e^- collider LEP has been in operation since 1989, delivering data with centre-of-mass energies between 90 and 190 GeV to the four LEP experiments ALEPH, DELPHI, L3 and OPAL. In the years 1990 till 1995 LEP was running on top of the Z^0 resonance with a centre-of-mass energy around 91 GeV. In this period LEP delivered around 175 pb^{-1} of data to each of the four experiments, corresponding to about 4.5 million multihadronic Z^0 decays. This huge amount of data allows very precise investigations of the physics of the neutral current. In addition to measurements of the mass and the width of the Z^0 boson, measurements of the weak coupling constants are a major goal of the physics program of LEP1.

The measurement of quantities like the partial hadronic decay width of the Z^0 boson or the forward-backward asymmetries allows to determine the couplings of the neutral current and to compare the results with the expectation of the Standard Model. Due to the precision achievable with the LEP data radiative corrections to the observables have to be taken into account. Even particles which are too heavy to be produced at LEP play an important role for the radiative corrections. In the context of the Standard Model it is possible to derive information on the mass of these heavy particles from precision measurements at LEP1. This was done very successfully with the determination of the mass of the top quark, which was subsequently confirmed by the direct measurements at the Tevatron. Today it is even possible to restrict the range of the Higgs boson mass by extracting the information from the combined precision data of electroweak physics.

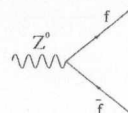
From the year 1995 onwards, the centre-of-mass energy at LEP was raised stepwise. With this increase in energy a large variety of additional physics investigations is possible: the Standard Model reaction $e^+e^- \rightarrow (Z^0/\gamma) \rightarrow q\bar{q}$ at energies above the Z^0 resonance allows a test of the interplay between the Z^0 and γ boson. In addition the higher energy extends the search range for the last missing particle in the Standard Model, the Higgs boson, or for extensions of the Standard Model like Supersymmetry or other phenomena of 'New Physics'. The W-pair production at energies above its threshold of 161 GeV allows to examine the charged current, complementary to the measurement of the neutral current of the weak interaction. A precise measurement of the mass of the W boson is one of the major goals of the LEP2 program. The production mechanism of W-pairs via a neutral gauge boson as an intermediate state allows to test directly the couplings among the three gauge bosons $WW\gamma$ and WWZ , which is an

important test of the $SU(2)_L \times U(1)_Y$ gauge invariance of the Standard Model. Whereas the couplings of the gauge bosons to fermions have been measured precisely, the self coupling of the vector bosons is experimentally not yet very well explored. The W pair production in the clean environment of an e^+e^- collider is the ideal laboratory for a measurement of these trilinear gauge boson vertices. Moreover various Standard Model processes and QCD phenomena like the running of α_s can be investigated at higher energies.

In 1995 an intermediate energy range between the Z^0 resonance and the W-pair production was covered and around 6 pb^{-1} data were taken with a centre-of-mass energy between 134 and 136 GeV (LEP 1.5). In 1996 LEP was running with an energy just above the threshold for W-pair production of 161 GeV, followed by a period with a centre-of-mass energy of 172 GeV. Around 10 pb^{-1} were collected at each of these energies per experiment. In 1997 LEP delivered around 60 pb^{-1} of data with an energy of 183 GeV, and this year (1998) data are taken with a centre-of-mass energy of 189 GeV.

1.2 Physics at Energies around the Z Resonance

At energies on top of the Z^0 resonance, physics processes of e^+e^- -colliders are dominated by the Z^0 production and its decay into a $f\bar{f}$ pair. Thus the physics program at LEP allows an investigation of the neutral weak current in a pure environment and with high statistics. The Feynman rule for the coupling of the neutral gauge boson to a pair of fermions is given by



$$-i \frac{g}{\cos \theta_W} \gamma^\mu \frac{1}{2} (c_V^f - c_A^f \gamma^5). \quad (1.1)$$

Here θ_W denotes the weak mixing angle and g is the coupling constant of the $SU(2)$ gauge group. The axial- and vector coupling constants for a fermion f can be written in terms of the third component of the weak isospin I_3 , the charge q_f of the fermion f and the weak mixing angle according to

$$\begin{aligned} c_V^f &= I_3 - 2q_f \sin^2 \theta_W \\ c_A^f &= I_3. \end{aligned} \quad (1.2)$$

The origin of equation 1.2 is, that the physical Z^0 boson contains aspects both of the non-abelian $SU(2)$ and the abelian $U(1)$ interaction. The vector-fields A_μ and Z_μ of the mass eigenstates of the γ and Z^0 boson are built through mixing of the two neutral fields B_μ and W_μ^3 . The rotation is given by the mixing matrix

$$\begin{pmatrix} \gamma \\ Z^0 \end{pmatrix} \leftarrow \begin{pmatrix} A_\mu \\ Z_\mu \end{pmatrix} = \begin{pmatrix} \cos \theta_W & \sin \theta_W \\ -\sin \theta_W & \cos \theta_W \end{pmatrix} \begin{pmatrix} B_\mu \\ W_\mu^3 \end{pmatrix}. \quad (1.3)$$

Combining equations 1.1 and 1.2 shows that e^+e^- -collisions on top of the Z^0 resonance are an ideal environment to determine the weak mixing angle $\sin^2 \theta_W$. In today's Standard Model of elementary particles this angle is one of the fundamental parameters, which cannot be predicted from first principles, but has to be determined by experiments.

Experimentally the neutral current coupling can be probed by measuring the partial width Γ_{ff} of the Z^0 boson decays into pairs of fermions and the angular distribution of these decays. The measurements of the partial decay widths of the Z^0 boson are sensitive to the sum of the axial and vector coupling

$$\Gamma_{ff} \propto (c_V^f)^2 + (c_A^f)^2. \quad (1.4)$$

The different strength of the right- and lefthanded coupling of the neutral gauge boson to the fermions results in an asymmetric angular distribution with respect to the angle θ between the incoming electron beam and the direction of the outgoing fermion. The experimental quantity used to investigate this characteristic behaviour is the forward-backward asymmetry, A_{FB} , which is defined as the normalised difference between the cross-section in the forward¹ and the backward hemisphere, σ_F and σ_B , respectively:

$$A_{FB} = \frac{\sigma_F - \sigma_B}{\sigma_F + \sigma_B}. \quad (1.5)$$

The forward-backward asymmetry is proportional to the product of the weak coupling constants according to the tree level formula

$$A_{FB}^f \propto \mathcal{A}_e \cdot \mathcal{A}_f = \frac{2(c_V^e)(c_A^e)}{(c_V^e)^2 + (c_A^e)^2} \frac{2(c_V^f)(c_A^f)}{(c_V^f)^2 + (c_A^f)^2}. \quad (1.6)$$

The investigation of the angular distribution of the Z^0 decay allows to test the spin structure of the neutral current coupling.

In order to compare the measurements of various experimental observables to the theoretical predictions of the Standard Model, hadronic uncertainties as well as radiative corrections have to be taken into account in addition to the lowest order electroweak processes. Radiative corrections can be divided into two classes:

- QED corrections come into play by either the emission of a real *bremsstrahlung* photon or via virtual photonic loops. Calculations of these corrections are well-understood and can be performed within QED, with all parameters being well-known.
- weak corrections are relevant for either vector boson propagators, vertex corrections or box diagrams, c.f. figure 1.1. The theoretical estimates in the context of the Standard Model for this class of radiative corrections are given as functions of various parameters of the electroweak theory, depending on the renormalisation scheme adopted. The most important contributions are those quadratic in the mass of the top quark m_t and those arising from large logarithms of the form $(\frac{\alpha}{\pi} \ln \frac{m_Z}{m_f})$ involving light fermions (c.f. for example [1]). Although particles like the top quark and the predicted Higgs boson are too heavy to be produced at LEP, they play a crucial role in the radiative corrections through their contributions via virtual loops. While on the one hand side this complicates the comparison of the

¹forward with respect to the direction of the incoming electron beam, i.e.

$$\sigma_F = \int_0^1 (d\sigma/d\cos\theta) d\cos\theta \quad \text{and} \quad \sigma_B = \int_{-1}^0 (d\sigma/d\cos\theta) d\cos\theta$$

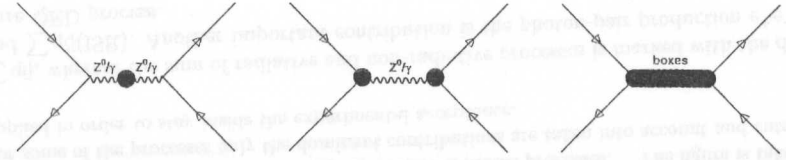


Figure 1.1: The different feynman diagrams contributing to the weak corrections, i.e. corrections to the vector boson propagators, vertex corrections or box diagrams.

measurements with analytical estimates, it allows on the other hand to predict unknown parameters like the Higgs mass within the Standard Model. Expressing the measured quantities with Standard Model relations as a function of these unknown parameters, they can then be determined in a fit to the experimental data. This method is adopted for example by the LEP Electroweak Working Group [2]. It was applied very successfully to the determination of the mass of the top quark prior to its confirmation by the direct measurements at the Tevatron. The sensitivity of the experimental data to the Higgs mass is lower than that to the mass of the top quark, because the leading m_t dependence is quadratic, whereas it is logarithmic ($\propto \ln \frac{m_Z}{m_t}$) in the mass of the Higgs boson. By combining the world's precision electroweak data it is today nonetheless possible to restrict the range of the Higgs boson mass. Especially the measurements of the forward-backward asymmetries play a crucial role in constraining the Higgs mass due to their large sensitivity to the weak mixing angle and subsequently the mass of the Higgs boson.

For a centre-of-mass energy corresponding to the mass of the Z^0 boson, it is convenient to express the experimental observables in terms of the effective axial- and vector-coupling parameters $\tilde{c}_{V,A}^f$. These effective coupling parameters directly replace the original parameters and include all electroweak corrections. For the forward-backward asymmetries in the Z^0 -pole approximations for example, equation 1.6 then reads

$$A_{FB}^f \propto \frac{2(\tilde{c}_V^f)(\tilde{c}_A^f)}{(\tilde{c}_V^f)^2 + (\tilde{c}_A^f)^2} \frac{2(\tilde{c}_V^e)(\tilde{c}_A^e)}{(\tilde{c}_V^e)^2 + (\tilde{c}_A^e)^2}. \quad (1.7)$$

Theoretically, $\tilde{c}_{V,A}^f$ can be derived from the electroweak form factors. They are constant in the Z^0 -pole approximation $\sqrt{s} = m_Z$. The effective couplings can be parametrised (e.g. in ZFITTER [3]) according to

$$\begin{aligned} \tilde{c}_V^f &= \sqrt{\rho_f}(I_3 - 2\kappa_f q_f \sin^2 \theta_W) \\ \tilde{c}_A^f &= \sqrt{\rho_f} I_3. \end{aligned} \quad (1.8)$$

and can be derived from equation 1.2 by introducing the correction factors ρ_f and κ_f . Each of these correction factors contain leading terms, which are usually flavour independent, as well as the so-called remainder terms, i.e. all non-leading terms, including the corrections involving the Higgs boson. The latter are normally small and in general depend on the flavour of the fermion. Moreover, the correction factors ρ_f and κ_f depend on the renormalisation scheme adopted.

Using the effective coupling constants $\tilde{c}_{V,A}^f$ an effective weak mixing angles $\sin^2 \theta_W^{f,\text{eff}}$ can be defined according to equation 1.8 as

$$\sin^2 \theta_W^{f,\text{eff}} = \kappa_f \sin^2 \theta_W. \quad (1.9)$$

With this definition $\sin^2 \theta_W^{f,\text{eff}}$ is almost independent of m_t . This makes it possible to calculate a value for $\sin^2 \theta_W^{f,\text{eff}}$ without too large theoretical uncertainties from quantities with sizeable experimental errors. In order to compare the values for the weak mixing angle determined from different measurements, like for example the leptonic and the hadronic forward-backward asymmetries, it is convenient to express the experimental results in terms of $\sin^2 \theta_W^{f,\text{eff}}$ of one fermion species. Usually the results of various measurements are transformed into a value for the effective leptonic angle $\sin^2 \theta_W^{\text{lept},\text{eff}}$, where $\sin^2 \theta_W^{\text{lept},\text{eff}}$ is defined as

$$\sin^2 \theta_W^{\text{lept},\text{eff}} = \frac{1}{4} \left(1 - \frac{\bar{c}_V^l}{\bar{c}_A^l} \right). \quad (1.10)$$

From equation 1.10 the reason for the low m_t -dependence becomes evident: the leading radiative correction where m_t is involved is the flavour independent part of ρ_f . This correction factor ρ_f cancels in the ratio \bar{c}_V^l/\bar{c}_A^l (c.f. equation 1.8) and thus in the definition of $\sin^2 \theta_W^{f,\text{eff}}$. This cancellation of the leading radiative corrections allows to constrain the mass of the Higgs boson by measurements of the forward-backward asymmetries, although m_H enters solely in the remainder terms of κ_f and its dependence is logarithmic. Typical values of the correction factors for electrons, bottom and charm quarks, estimated using the ZFITTER program, are given in table 1.1.

	bottom	charm	electron
κ_f	1.04447	1.03823	1.03868
ρ_f	0.99400	1.00608	1.00541

Table 1.1: Values for the correction factors κ_f and ρ_f for bottom and charm quarks as well as for electrons, estimated with the program ZFITTER. A top and a Higgs mass of $m_t = 175$ and $m_H = 100$, respectively, and $\alpha_s = 0.120$ have been assumed.

While the investigation of the leptonic couplings $Z^0 \rightarrow \bar{l}l$, for $l = e, \mu, \tau$ is reasonably straight forward, the examination of the couplings to the quarks requires the identification of the individual quark species and in addition demands the consideration of QCD effects like the radiation of gluons from quarks or vertex corrections involving gluons and the fragmentation process. For heavy quark flavours these difficulties can be handled reasonably well. The identification of bottom and charm quarks is comparably easy because of the relatively large masses and long lifetimes of the corresponding hadrons. In addition, the possible production of these heavy flavours in the fragmentation and gluon splitting $g \rightarrow q\bar{q}$ processes is significantly suppressed. In order to keep the corrections due to QCD and hadronisation effects small, only the ratio $R_q = \Gamma_{q\bar{q}}/\Gamma_{\text{had}}$ is usually determined from the data. For this ratio the QCD corrections cancel in first order. For a measurement of the heavy flavour asymmetries it turns out that the QCD effects are important despite their smallness of the order of a few percent. Because of the high precision reached in the measurements especially of the bottom quark, the effect of the QCD correction is of the same order as one standard deviation of the LEP combined value for A_{FB}^b .

In this thesis a measurement of the heavy flavour forward-backward asymmetries A_{FB}^c and A_{FB}^b will be presented, where D mesons serve as a tag for charm and bottom quarks. Subsequently this measurement is combined with other analyses of the heavy flavour asymmetries performed with the OPAL detector, where both the statistical as well as the systematic correlations are taken into account. A study of QCD corrections is presented for the OPAL analyses

of the bottom and charm asymmetries. From the combined result of the OPAL heavy flavour asymmetries a value for the weak mixing angle is extracted. Finally a comparison of the bottom and charm asymmetry measurements performed at LEP and SLD is presented and the results are discussed.

1.3 Physics at Energies above the Z resonance

At energies above the Z^0 resonance the following two 2-fermion reactions are important: the reaction where an off-shell gauge boson decays into a fermion pair ($Z^0/\gamma^* \rightarrow f\bar{f}$), corresponding to the 2-fermion process at LEP1, and ‘radiative returns to the Z^0 ’, where a hard photon is radiated off the e^+e^- system such, that with the remaining energy an on-shell Z^0 boson is produced, which subsequently decays into a fermion-pair. The cross-sections for a selection of Standard Model physics processes at LEP2 are shown in figure 1.2 as a function of the centre-of-mass energy. For the non-radiative 2-fermion processes, the cross-section is marked with

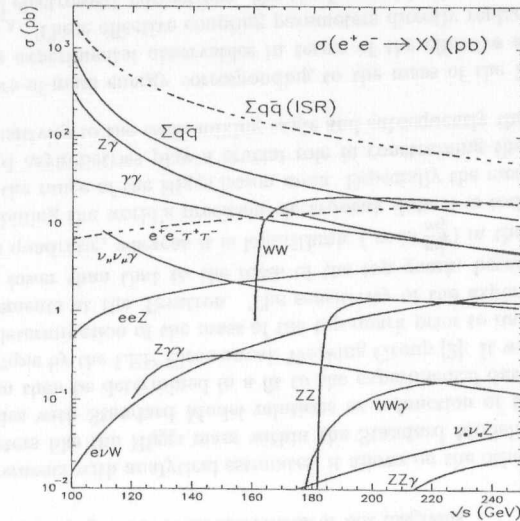
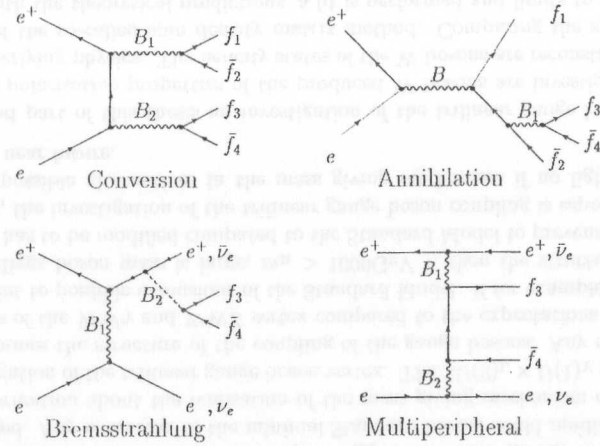


Figure 1.2: Cross sections for some typical Standard Model processes. The figure is taken from [4]. For some of the processes only the dominant contributions are taken into account and cuts have been applied in order to stay inside the experimental acceptance.

$\sum q\bar{q}$, whereas the sum of radiative and non-radiative processes is marked with the dashed line and $\sum q\bar{q}(\text{ISR})$. Another important contribution is the photon-pair production $e^+e^- \rightarrow \gamma\gamma$, a pure QED process.

In addition various 4-fermion processes start to come into play. The different production mechanisms are summarised in figure 1.3. The dominant process at LEP2 is the so-called

Abelian Classes



Nonabelian Classes

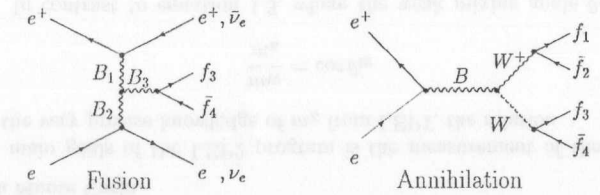


Figure 1.3: 4-fermion production classes of diagrams [4]. Here B denotes a neutral gauge boson, while B_1, B_2, B_3 stands for either a Z^0, γ or W^\pm boson. The 4-fermion production graphs where Higgs bosons are involved are not included.

two-photon production $e^+e^- \rightarrow e^+e^-X$, where X is produced in the scattering of two quasi-real photons $\gamma\gamma \rightarrow X$. It proceeds via *multiperipheral* diagrams. In contrast to most of the physics processes, the cross-section of two-photon production grows with rising energy, i.e. like $(\ln s/m_e^2)^2$. At energies above twice the mass of the heavy gauge boson, doubly resonant gauge boson production becomes possible. In contrast to the resonant single Z production at LEP1, the dominant W production mechanism in an e^+e^- collider is by pair-production due to charge conservation. The W-pair production is one of the main goals of the LEP2 program. In the Standard Model it proceeds via abelian 4-fermion reactions (*conversion* diagrams) and non-abelian *annihilation* diagrams. The latter allows the investigation of the non-abelian structure of the Standard Model and the test of the $SU(2)_L \times U(1)_Y$ gauge invariance by an investigation of the W-pair production. The contributions from the different mechanisms as a function of the centre-of-mass energy are shown in figure 1.4, together with the combined measurements of the four LEP experiments at energies of 161, 172 and 183 GeV. The predictions for the production via *conversion* (ν_e exchange) only, *conversion* plus γWW vertex (i.e. without the ZWW vertex)

and the full set of the Standard Model diagrams are shown. As can be seen from figure 1.4, the cross-section where all possible production mechanisms are included is smaller than that of the t -channel ν_e exchange only. This behaviour is due to negative interference effects between the three graphs and will be discussed in more detail in section 4.2.

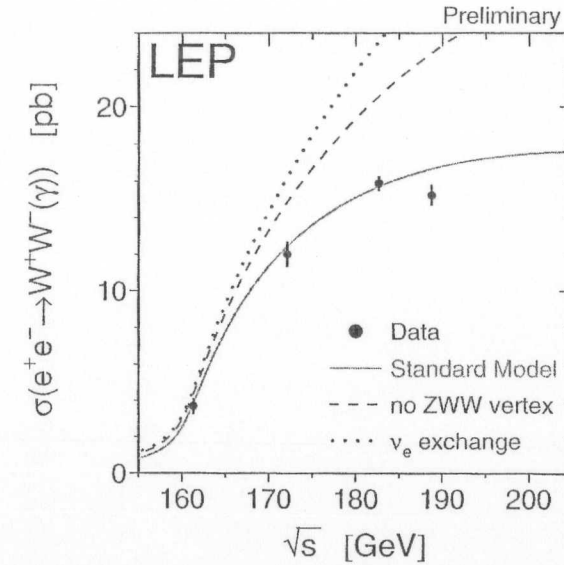


Figure 1.4: The cross-section for the W-pair production near the threshold including the LEP combined measurements at various energies. Overlaid is the cross-section for the WW-production via the t -channel ν -exchange only.

In the Standard Model Z-pair production, in contrast to the W-pair production is possible solely via *conversion* diagrams. The threshold for Z-pair production is a bit higher than that for W-pair production due to the higher mass of the Z-boson. But even after overcoming threshold effects the cross section for Z-pair production is significantly smaller than for the W-pair production due to the differences in the coupling constants. This can be read off the Feynman rules for the neutral and charged gauge boson coupling to fermions, given in equations 1.1 and 1.11.

$$\begin{array}{c}
 W^- \\
 \diagup \\
 \text{---} \\
 \diagdown \\
 \bar{\nu}_e
 \end{array}
 \begin{array}{c}
 e^- \\
 \diagdown \\
 \text{---} \\
 \diagup \\
 \bar{\nu}_e
 \end{array}
 = -i \frac{g}{\sqrt{2}} \gamma^\mu \frac{1}{2} (1 - \gamma^5). \quad (1.11)$$

Another class of processes is the single-resonant gauge boson production. For the W boson the cross-section for this process is, however, much lower than the cross-sections for the W-pair

production. Both W^- ($e^+e^- \rightarrow We\nu_e$) as well as Z -production ($e^+e^- \rightarrow Zee$) are possible. These reactions proceed mainly via *fusion* and *bremsstrahlung* diagrams, but also in *abelian-annihilation* and single-resonant *conversions*.

As can be seen from figure 1.3, a given 4-fermion final state can be produced via different processes. Thus interference processes have to be taken into account. As mentioned earlier W -pair production, for example, can proceed via the *conversion* and *annihilation* diagrams. Because of the interference effects, these processes (called CC03 diagrams) cannot be analysed separately from all other ('background') processes, yielding the same 4-fermion final states. In principle a full 4-fermion analyses has to be performed. It turns out, however, that the resulting effects due to interferences between W -pair production and other 4-fermion processes are relatively small, because most of the background processes populate a different phase-space-region than the W -pair production. The former is characterised by the mass of the W boson for the two pairs of fermions. In addition, the interference effects are small, because the W -pair production cross-section dominates most of the other 4-fermion processes, as can be read off from figure 1.2. Thus the full 4-fermion analyses can be simplified by investigating the CC03-signal processes and the various background sources individually. The remaining systematic effects are subsequently estimated by comparing this simplified analysis with the results from a full 4-fermion Monte Carlo.

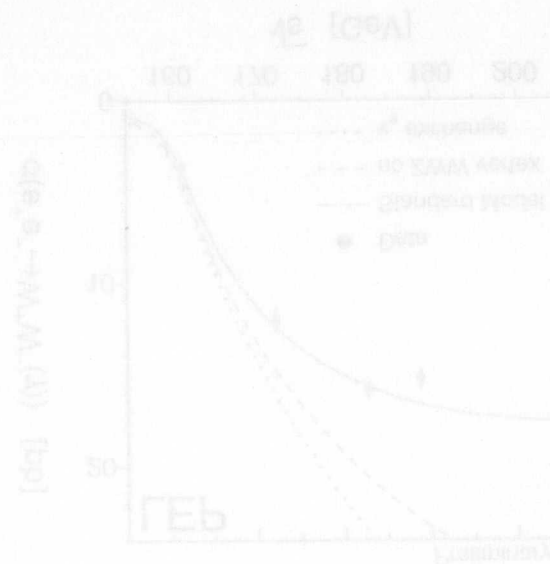
One of the main goals of the LEP2 program is the measurement of the W boson mass. Together with the very precise knowledge of m_Z from LEP1, the relation

$$\frac{m_W}{m_Z} = \cos \theta_W \quad (1.12)$$

can be tested. In contrast to equation 1.3, where the weak mixing angle θ_W denotes solely the $\gamma - Z^0$ mixing in the electroweak theory, with the relation 1.12 the mass mechanism in the Standard Model can be tested. Equation 1.12 is, in lowest order, fulfilled if the minimal version of the Standard Model with the simple Higgs mechanism giving mass to the vector bosons is realised. Any extension of the minimal Standard Model could modify equation 1.12. Additional information about the realisation of the mass giving mechanism can be extracted from an investigation of the trilinear gauge boson vertex. The $SU(2)_L \times U(1)_Y$ gauge invariance uniquely determines the structure of the coupling of the gauge bosons. Any deviations of the gauge couplings of the $WW\gamma$ and WWZ vertex compared to the expectations of the Standard Model would hint to possible extensions of the Standard Model. If for example no Higgs boson exists (or the Higgs boson mass is large, $m_H > 1000\text{GeV}$), then the structure of the gauge boson coupling has to be modified compared to the Standard Model to prevent the violation of unitarity. Thus, the investigation of the trilinear gauge boson coupling is especially important in pointing to possible alternatives in the mass giving mechanism if no light Higgs will be detected in the near future.

In the second part of this thesis an investigation of the trilinear gauge boson coupling is described. The polarisation properties of the produced W bosons are investigated, giving insight in the underlying physics. The helicity states of the W bosons are reconstructed explicitly with the help of the so-called spin density matrix method. Comparing the spin density matrix elements with the theoretical predictions, a fit is performed and limits to the triple gauge coupling parameters in various scenarios are extracted. Moreover, this method allows a simple and model-independent test of CP invariance of the $WWZ/WW\gamma$ vertex. For these analyses W -pairs are reconstructed in the decay channel $W^+W^- \rightarrow q\bar{q}l\bar{l}$. Subsequently the measure-

ments are combined with the information extracted from the total cross-section and with other channels and the actual limits on anomalous trilinear gauge coupling are presented.



Chapter 2

The OPAL Detector

The OPAL (Omni Purpose Apparatus for LEP) detector is one of the four detectors at the LEP e^+e^- collider. The conceptual idea for this detector was to build a detector at relatively low cost with a well-known and tested detector technology. This should ensure a reliable running of the OPAL detector from the beginning of the LEP physics program.

Track reconstruction is achieved by the central tracking system, consisting of different wire- and jet chambers, complemented by a silicon micro-vertex detector. Embedded in a magnetic field of an aluminium coil, this system ensures the measurement of the direction, momentum and charge of the particles and in addition the reconstruction of the primary and secondary decay vertices. The identification of the particle type is possible through a measurement of the specific energy loss in the jet chamber. The direction and energy of electrons and photons are measured in the electromagnetic calorimeter, consisting of segmented lead glass. The return yoke of the magnetic coil serves as the absorber for hadrons. The measurement of the energy of the hadronic systems is ensured by layers of thin wire chambers, which are deposited in a sandwich technique within the iron yoke. The outermost layer of the detector are the muon chambers. The particles, which are not absorbed in the hadronic calorimeter but leave traces in the connecting drift chambers can almost certain be identified as muons. The detector is complemented by a system of forward detectors, consisting of calorimetry and drift chambers at positions more than 2.4 meters from the interaction point. Through the measurement of Bhabha-scattering, it ensures a precise measurement of the luminosity. In addition a time of flight counter is used to deliver trigger signals. An overview of the OPAL detector is shown in figure 2.1. A detailed description of the OPAL detector can be found in [5]. The z-direction of the OPAL coordinate system is fixed in the direction of the e^+e^- -beam.

2.1 The Central Detectors

The central part of the OPAL detector consists of a silicon micro-vertex detector and a system of drift chambers. The sub-detectors lie within a magnetic field of 0.436 Tesla, provided by an aluminium solenoid. This assures the measurement of the charge and momentum of charged particles. The central detectors are embedded in a pressure vessel, filled with a mixture of 88.2% argon, 9.8% methan and 2.0% isobuthan. The pressure in the vessel is 4bar.

The silicon micro-vertex detector was installed during the LEP running period in 1991, in order to improve the track resolution in the immediate neighbourhood of the interaction

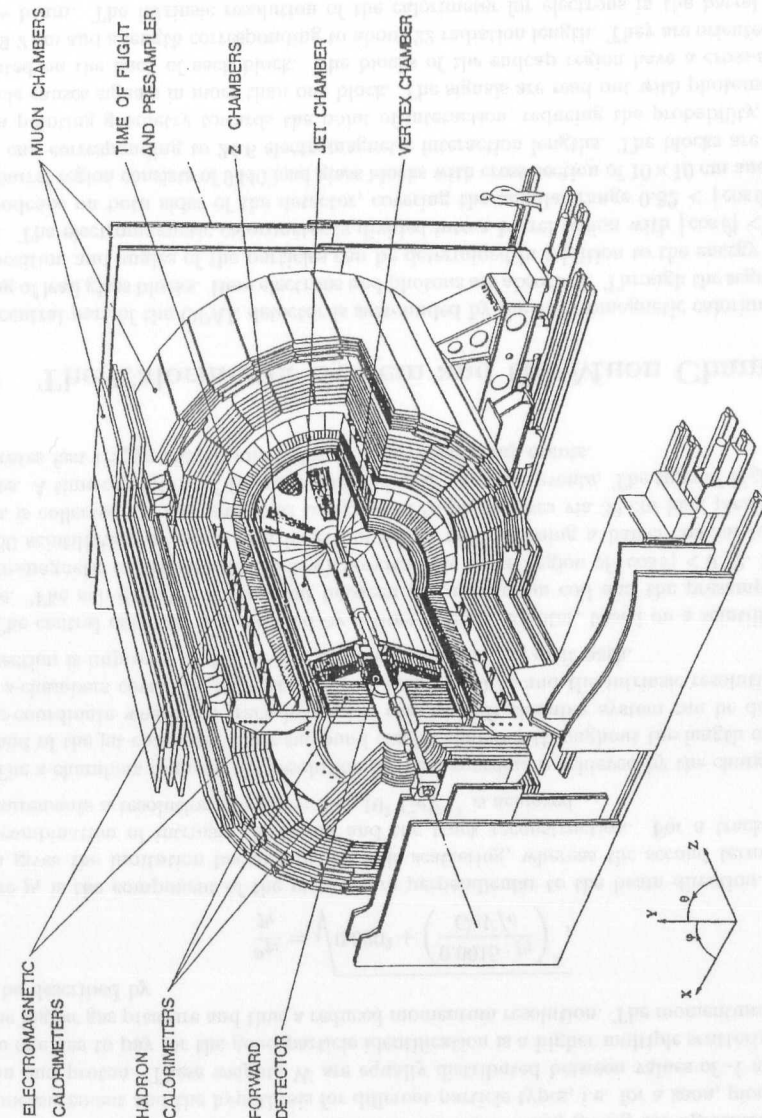


Figure 2.1: The OPAL-detector.

point and thus to reconstruct secondary vertices of heavy flavour hadrons or other long-living particles. Lifetime measurements of around 10^{-13} s are achievable. The sub-detector surrounds directly the beam pipe. After an extension of the micro-vertex detector in 1993 and 1995, it consists of two layers of 12 (inner) and 15 (outer) ladders equipped with single sided silicon strip detectors at radii of 6.1 cm and 7.4 cm, respectively. Five detectors are mounted together in the z -direction to form a ladder with a length of 30 cm. The angular acceptance for the inner layer is given by $|\cos\theta| < 0.93$, of the outer layer by $|\cos\theta| < 0.89$. The impact parameter resolution is determined from lepton pairs originating from Z^0 decays. In the plane perpendicular to the beam axis a resolution of $\sigma(d_0) = 18 \mu\text{m}$ and in the direction of the beam axis a resolution of $\sigma(d_0) = 24 \mu\text{m}$ is achieved [6].

The central drift chamber system consists of vertex detectors, a jet chamber and is complemented by so-called z -chambers to improve the resolution in the z -direction. The vertex drift chambers are directly connected to the silicon detector. The vertex detector consists of two chambers, segmented azimuthally into 36 sectors. The inner chamber covers the region between 8.8 and 15.5 cm radially from the interaction point, the radius of the outer chamber is 23.5 cm. With a length of 1m, the vertex chamber covers the angular range of $|\cos\theta| < 0.98$. The wires of the inner chamber lie parallel to the z -axis of the OPAL coordinate system, whereas the so-called stereo-wires of the outer chamber are tilted by 4° to allow for a more precise determination of the z -coordinate. By this arrangement a hit resolution of $55 \mu\text{m}$ is achieved in the r - ϕ plane and the z -resolution of the stereo-wires is $700 \mu\text{m}$.

The vertex chambers are surrounded by a large volume jet chamber, ensuring a good space and double track resolution and good particle identification. It consists of 24 azimuthal sectors, each equipped with 159 axial anode wires parallel to the beam axis. The outer radius of the jet chamber reaches 185 cm and the chamber is 4m long. The maximal drift length in the innermost region of the jet chamber is 3 cm and 25 cm in the outer radius. A track within an angular range of $|\cos\theta| < 0.73$ passes all 159 wires. This environment is called the barrel region. For a particle to pass a minimum of eight wires it has to be within $|\cos\theta| < 0.98$. The coordinates of the charged tracks in the r - ϕ plane are determined by the position of the wires and a measurement of the drift time, achieving a spatial resolution of $135 \mu\text{m}$. Both ends of the anode wires are read out, the information of the z -coordinate is extracted by comparing the integrated charge of the two ends, reaching an accuracy of 6 cm. The sum of the charges of both ends is used to measure the specific energy loss per path length (dE/dx) of the charged particle. The differential energy loss is a characteristic function of the momentum and the mass of the particle and can be described by the Bethe-Bloch formula [7]. Thus measuring the energy loss and the momentum of the particle allows a determination of the mass and therefore an identification of the particle type. An relative error on the differential energy loss of $(\sigma_{dE/dx}/dE/dx) = 3.8\%$ is achieved with the jet chamber for minimum ionising particles. Here the relatively high pressure of 4bar in the jet chamber is advantageous, because the energy loss is proportional to the gas density. By comparing the measured value for the specific energy loss, $(dE/dx)^{(m)}$, with the theoretically predicted value by the Bethe-Bloch formula, $(dE/dx)^{(0)}$, and taking into account the error of the measurement $\sigma_{(dE/dx)^{(m)}}$, the hypothesis for a specific particle type can be tested by estimating the chi-square for the track to agree with the theoretical prediction according to

$$\chi^2 = \left(\frac{(dE/dx)^{(0)} - (dE/dx)^{(m)}}{\sigma_{(dE/dx)^{(m)}}} \right)^2.$$

These χ^2 values can be transformed into a probability W by integrating a gaussian distribution.

Then W describes the agreement between the measurement and the hypothesis. Subsequently the probabilities W are signed. A negative or positive weight W describes values, where the measurement lies below or above the expectation, respectively. With the method described above, a set of probabilities can be calculated for each track, giving the agreement between the measurement and the hypothesis for different particle types, i.e. for a kaon, pion, electron, muon and proton. These weights W are equally distributed between values of -1 and 1. The price one has to pay for the good particle identification is a higher multiple scattering because of the higher gas pressure and thus a reduced momentum resolution. The momentum resolution can be described by

$$\frac{\sigma_{p_t}}{p_t} = \sqrt{0.020^2 + \left(\frac{0.0015 \cdot p_t}{\text{GeV}/c} \right)^2},$$

where p_t is the component of the momentum perpendicular to the beam direction. The first term gives the limitation because of multiple scattering, whereas the second term describes the combination of intrinsic resolution and the track reconstruction. For a track with 130 measurements a resolution of $\sigma_p/p = 2.2 \cdot 10^3 \text{ GeV}^{-1}$ is achieved.

The z -chambers improve the resolution in the z -coordinate achieved by the charge deviation method of the jet chamber. They surround the jet chamber throughout the length of 4m, thus the z -coordinate where the track leaves the central drift chamber system can be determined. The z -chambers cover the angular region of $|\cos\theta| < 0.72$ and the intrinsic resolution for the z -direction is improved to 100 to 300 μm , depending on the drift path.

The central detector is completed by a time-of-flight counter, based on a scintillator technique. The sub-detector is mounted between the aluminium coil and the presampler of the electromagnetic calorimeter (see below), covering the barrel region of $|\cos\theta| < 0.82$. It consists of 160 scintillation counters of a length of 6.8 m each, forming a barrel coaxial to the coil. Light is collected at both ends and transported to phototubes via 30 cm long plexiglass light guides. A time resolution of 460 ps is achieved in $Z^0 \rightarrow \mu^+ \mu^-$ events. The time-of-flight counter generates fast trigger signals and helps to reject cosmic ray events.

2.2 The Calorimeter System and the Muon Chambers

The central part of the OPAL detector is surrounded by the electromagnetic calorimeter, consisting of lead glass blocks. Here electrons and photons are absorbed. Through the segmentation the position and angles of the particles can be determined in addition to the energy measurement. The electromagnetic calorimeter is divided into a barrel region with $|\cos\theta| < 0.82$ and the endcaps on both sides of the detector, covering the angular range $0.82 < |\cos\theta| < 0.98$. The barrel region consists of 9440 lead glass blocks with cross-section of 10×10 cm and a length of 37 cm, corresponding to 24.6 electromagnetic interaction lengths. The blocks are arranged into a pointing geometry towards the point of interaction, reducing the probability, that one particle causes signals in more than one block. The signals are read out with photomultipliers, mounted on the back of each block. The blocks of the endcap region have a cross-section of 9.2×9.2 cm and a length corresponding to about 22 radiation length. They are oriented parallel to the beam. The intrinsic resolution of the calorimeter for electrons in the barrel region is $\sigma_E/E = 0.2 + 6.3\%/\sqrt{E/\text{GeV}}$, and about $\sigma_E/E = 5\%/\sqrt{E/\text{GeV}}$ for the endcaps. The spatial resolution is given by the cross-section of the lead glass blocks. Particles reaching the electromagnetic calorimeter have transversed the beam pipe, the central tracking system including

the pressure vessel and the magnetic coil, and thus material of about 2 electromagnetic radiation length. This causes showers to start usually before the particles enter the electromagnetic calorimeter. Thus a thin layer of streamer chambers, the so-called presampler, are mounted directly in front of the lead glass calorimeter in order to measure the multiplicity of the shower before it enters the calorimeter. With this information the degradation of the energy resolution because of the massive detector parts in front of the calorimeter can be minimised. As the calorimeter the presampler consists of a barrel and an endcap region.

With help of the hadronic calorimeter the energy of particles passing the electromagnetic calorimeter can be measured. The iron return yoke of the magnetic coil serves as the absorbing material of the calorimeter. It is segmented into 10 layers of 10 cm thick iron. The space inbetween is filled in a sandwich technique with thin streamer chambers. The iron yoke covers a polar angle of 97% with a hadronic radiation length of more than four. The energy resolution is limited by the material of the electromagnetic calorimeter, which corresponds to two hadronic radiation length. Thus the showers are formed before the hadronic calorimeter is reached. By combining the signals of the electromagnetic and hadronic calorimeter an energy resolution of $\sigma_E/E = 120\%/\sqrt{E/\text{GeV}}$ can be achieved.

The particles, reaching the outermost part of the OPAL detector, have passed about seven radiation length for pions over an angular range of 93%. Therefore most of the hadrons are absorbed within the calorimeter system and the particles travelling up to the outermost part are muons with a high probability. The probability for a pion not to interact in the calorimeter is lower than 0.1%. The muon detector covers the region of $|\cos\theta| < 0.98$. The barrel region consists of four layers, the endcap sub-detectors of two layers of thin wire chambers. The spatial resolution in the central part is 1.5mm and 2mm for the r - ϕ plane and in the z -direction respectively. In the endcap region a spatial resolution of 1mm in the x - and 3mm in the y -direction can be achieved.

2.3 The Forward Detectors

In the forward region a system of drift chambers and calorimeters is installed to measure small angle Bhabha scattering events ($e^+e^- \rightarrow e^+e^-$). The cross-section of this process is dominated by the t -channel γ -exchange, a pure QED process, which can be calculated theoretically with a very high precision. Therefore this process is ideal to determine the luminosity very accurately. Experimentally the measurement of the number of selected Bhabha-events and the efficiency are determined. The forward detectors are mounted at a minimal distance of 2.4m away from the interaction point. They systems consists of drift chambers in the front plane, the gamma catcher, a ring of lead-scintillator sandwich modules and the far forward luminosity monitor, a lead-scintillator calorimeter positioned 7.9m from the intersection point. The system was complemented 1993 by a silicon-tungsten calorimeter, improving the precision for the luminosity measurement from 1 to 0.1%.

2.4 The Time-of-Flight Counter in the Endcap Region

With the beginning of the LEP2 program the OPAL detector was complemented with an additional detector component in the endcap region, a time-of-flight counter consisting of scin-

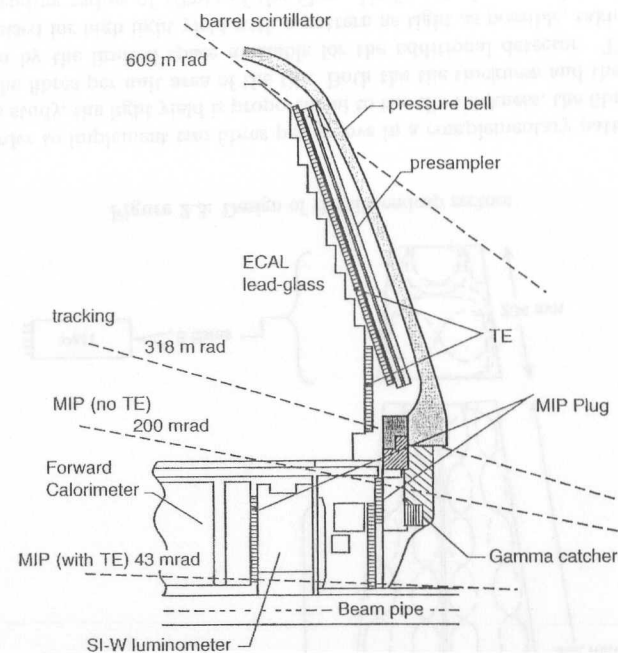


Figure 2.2: Position of the Tile Endcap and MIP-plug detectors with respect to the neighbouring sub-detectors.

tillating tiles with fibre readout. The extension of the OPAL detector was demanded in order to determine the exact interaction time and to improve the trigger conditions in the forward region in the more dense environment of LEP2. The scintillator counter consists of two parts: the first is the Tile Endcap (TE), a single segmented layer of altogether 120 tiles in the form of a truncated cone, installed in each endcap between the existing presampler and the electromagnetic calorimeter. The second part is a complementation of the forward detectors, the so-called MIP-plug, which serves as a detector for minimum ionising particles in the forward-region. It consists of 2 layers of tiles, each divided into 8 sectors. The innermost layers are situated behind the gamma-catcher, around 2.5 m from the interaction point. The position of the outermost layers are between the silicon-tungsten luminometer and the forward calorimeter. They are separated by 4mm of lead in order to reduce the background from synchrotron radiation, contrarily to the innermost layers, which lie within the angular range of the luminosity calorimeter, where material must be minimised. Here the support structure of the luminometer serves as a substitute. The MIP-plug covers the angular range between 200 and 43 mrad, thus complementing the small angle calorimetry system. The position of both sub-detector parts with respect to the neighbouring detectors is shown in figure 2.2. More details can be found in [8].

2.4.1 Motivation

With higher energy the backgrounds because of synchrotron radiation and beam-gas interactions rises. The higher backgrounds could be reduced by including information provided by the new scintillator detector for the trigger in the endcap region. Till the end of 1995, time information for the trigger was only available in the barrel region up to $|\cos\theta| < 0.82$ (609 mrad). The trigger was given, if the signal was within 50 ns from the beam crossing. With the new time-of-flight counter the angular coverage could be extended to $|\cos\theta| < 0.95$ (318 mrad), and thus down to the limit of particle tracking of the central drift chambers. Therefore a more robust trigger could be provided also in the endcap region by the usage of the time information in coincidence with the track trigger and the muon chambers.

In order to achieve the integrated design luminosity of LEP2, the machine was converted from a 8-bunch running into the bunch-train mode with in the beginning four trains with two bunchlets each. Thus the separation of the bunches is reduces to 335 ns (and for the foreseen 4×4 mode even to 247 ns), compared to the 22 μs for which the OPAL detector was originally designed. In case of events of solely neutral particles in the forward direction, no determination of the exact time t_0 of collision was possible, i.e. the bunchlet of interaction was not known. The new scintillator is able to detect neutral particles, because of the high probability of photon conversion in the aluminium pressure bell of two radiation length in front of TE and thus provide a time reference signal for the other sub-detectors. This is especially important, because the lead-glass calorimeter in the forward region has limited time measurement capability optimised for the design bunch separation of 22 μs , resulting in an up to 20% error in the energy measurement if the exact time of collision is not known. With the additional time information of TE a correction is possible. This allows a more precise investigation of physics processes with single- or multi-photon events in the Standard Model, like $e^+e^- \rightarrow \nu\bar{\nu}\gamma$, in the Higgs sector ($e^+e^- \rightarrow H\gamma$, with $H \rightarrow \gamma\gamma$), or in SUSY searches. Further background reduction could be achieved through the identification of cluster from pre-collisions of cosmic rays via coincidences between the electromagnetic calorimeter and TE time information. Again this is especially important for the single- or multi-photon events of LEP2.

The second extension, the MIP-plug, covers the region between 200 and 43 mrad, where no other sub-detector is sensitive to minimum ionising particles. This complements the existing system of forward detectors, which is hermetic for electrons and photons down to 26 mrad. With the MIP-plug the OPAL detector is also hermetic for muons down to 43 mrad, allowing a low-angle muon veto, which is especially useful for background reduction in searches with missing energy signatures. In addition, with the segmented MIP-plug a stand-alone trigger could be implemented for certain two-photon processes, if the signal of two sectors are used in coincidence.

2.4.2 Design

The extension of the time-of-flight counter is build to provide good time resolution and efficiency for minimum ionising particles. The design is constrained by the very limited space available, both for the far-forward region and in the endcap region between the pressure vessel of the central detectors with the presampler mounted on top and the lead-glass calorimeter of the endcaps. Both the limited space as well as the operation within the magnetic field prohibit a local phototube placing, leading to the solution of fibre optic technology. The position of the

TE detector is shown in figure 2.2. TE consists of two outer rings of 48 tiles each and 24 sectors for the innermost part of the detector. The layout is shown in figure 2.3. The MIP-plug is built out of for circles, segmented into eight tiles first. The shape of the MIP-plug tiles including the fibre design is shown in figure 2.4. The tiles consist of 10 mm thick scintillator material BC408, which emits blue light. On both sides of the tiles diamond-milled grooves were

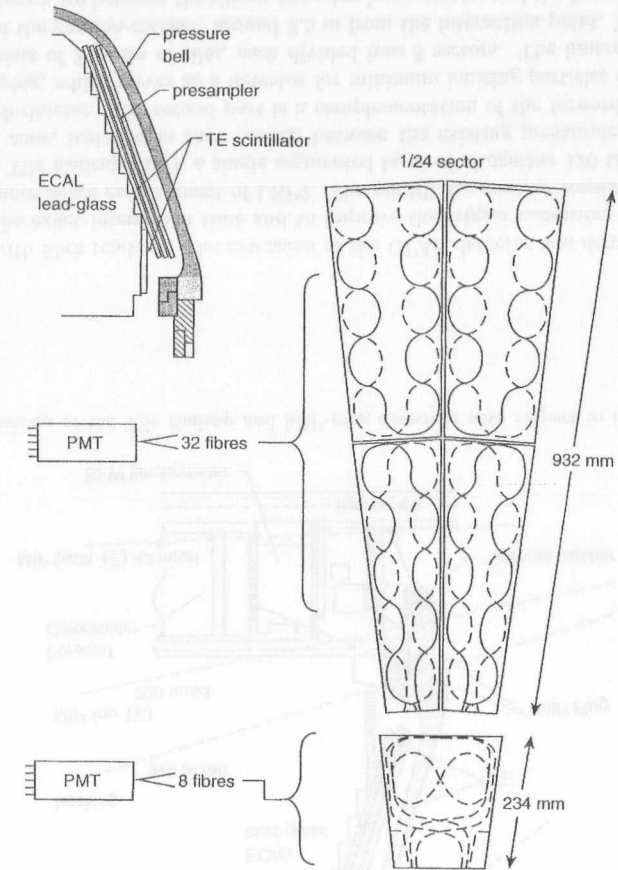


Figure 2.3: Design of the tile endcap sectors

provided, in order to implement two fibres per groove in a complementary pattern. According to a simulation study, the light yield is proportional to the tile thickness, the fibre diameter and the length of the fibres per unit area of the tile. Both the tile thickness and the fibre diameter are constrained by the limited space available for the additional detector. Thus the groove design is optimised for high light yield with a pattern as tight as possible, taking into account the minimal bending radius of 40mm of the fibre. Uniformity is ensured by distributing the grooves evenly over the tile surface. The fibres are embedded into the tiles with a optical glue

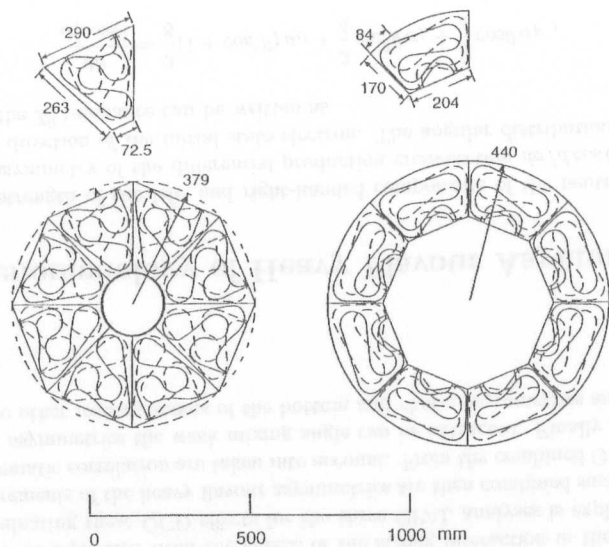
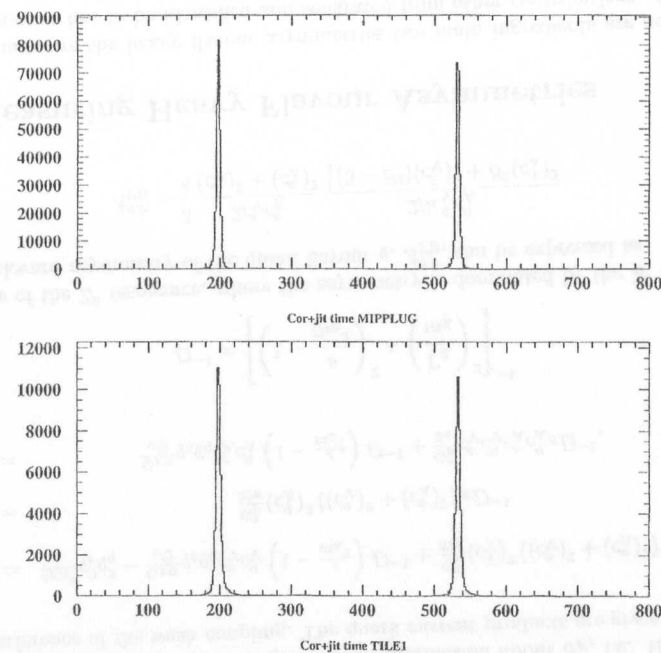


Figure 2.4: Design of the MIP-plug sectors

with the same refractive index as the scintillator, improving the light collection and holding the fibres in place. Wavelength shifting (WLS) fibres are used to transport the light of the scintillator and to match the optimal light yield of the scintillator material of $\lambda \approx 420\text{nm}$ to the peak sensitivity of the photomultipliers of $\lambda \approx 500\text{nm}$. The photomultipliers are of a type with green-extended cathodes. The light has to be transported outside the magnetic field and, because of the limited space, outside the detector, over a length of about 15 m. Therefore the WLS fibres are connected to clear fibres via optical precision connectors. The clear fibres are selected because of their low attenuation of 120dB/km at a wavelength of 500nm. Most of the light is carried in the outer 20% of the fibre diameter, and thus a connector with imperfect match would result in high light losses. Although most light is lost in the matching between the different fibre types, the loss of the additional connector is more than compensated by the much lower attenuation in the clear fibres compared to the WLS fibres. The tiles are wrapped in 150 μm Tyvek paper in order to provide high reflectivity and subsequently into 50 μm Tedlar to ensure light tightness. A blue LED in the middle of the tile serves for calibration and monitoring. Finally the tiles are mounted between two aluminium plates and sealed light tightly. Commercial photomultipliers are used because of their low costs. They are selected by their quantum efficiency of 15% for a wavelength of 500nm, their gain of $2 \cdot 10^7$ and the uniform response over most of the cathode. Especially important was the selection of phototubes with low dark counting rates, because TE is used for trigger signals.

Figure 2.5: Time resolution of the MIP-plug (upper histogram) and the TE detector (lower histogram) as determined from a Z^0 run in the bunchlet mode. The horizontal scale is in ns.

2.4.3 Performance

The new scintillator technique sub-detector for the endcaps has been running smoothly since the installation and requiring low maintenance. Studies using the correlation between track signals and TE hits show a running at low noise and an efficiency of larger than 99% for TE to detect minimum ionising particles extending the angular coverage down to $\cos\theta = 0.95$ [8]. The time measurement performance can be tested by looking at the event time distributions for $e^+e^- \rightarrow Z^0$ events. The results of the the MIP-plug and the TE detector are shown in figure 2.5 in the upper and lower histogram, respectively. The data are taken during bunch train operation with two bunchlets per train, thus expecting a spacing between the bunchlets of 334ns. The spacing observed with the two scintillator sub-detectors is 335.2ns with a standard deviation of 1ns. The peaks themselves have a standard deviation of 3ns, exceeding the design requirement of 5ns. The light yield can be determined by an investigation of low multiplicity states again in $e^+e^- \rightarrow Z^0$ events. The response to single tracks is estimated to be 14 ± 2 photoelectrons per minimal ionising particle. The uniformity of the detector is observed by the following confirmation of the measurement, but using a single channel, yielding a consistent result of 15 ± 3 photoelectrons per mip. In summary, the design performance for both the time resolution and the efficient sensitivity to minimum ionising particles has been fulfilled.

Chapter 3

Analyses of the Heavy Flavour Asymmetries

In this chapter the measurements of the heavy flavour forward-backward asymmetries performed with the OPAL detector at LEP are described. After an introduction to the phenomenology of the forward-backward asymmetries an overview of the techniques used by the OPAL collaboration to measure the bottom and charm asymmetries are given. Then an analysis based on the full LEP1 data set of about 4.5 million multihadronic Z^0 decays of the heavy flavour asymmetries, where D mesons are used to tag heavy flavour events is described in more detail. With the huge amount of data collected at LEP1 and the correspondingly high statistical precision achieved in the measurements of the heavy flavour asymmetries it becomes mandatory to combine the different analyses with care. Also, higher order corrections to the electroweak observables are becoming increasingly important. In order to interpret the measurements of the forward-backward asymmetries in terms of the Standard Model, the elementary electroweak process has to be separated from the effects of the strong interaction in the final state. The method of evaluating these QCD effects for the three OPAL analyses is explained. The three OPAL measurements of the heavy flavour asymmetries are then combined such, that the statistical and systematic correlation are taken into account. From the combined OPAL result of the heavy flavour asymmetries the weak mixing angle can be extracted. Finally this OPAL value is compared to other measurements of the bottom and charm asymmetries and the results are discussed.

3.1 Phenomenology of Heavy Flavour Asymmetries

The different strength of the left- and right-handed components of the neutral weak current results in an asymmetry of the differential production cross-section $d\sigma/d\cos\theta$ of the fermion relative to the direction of the initial state electron. The angular distribution of the reaction $e^+e^- \rightarrow f\bar{f}$ on the Z^0 resonance can be written as

$$\frac{d\sigma}{d(\cos\theta)} = \frac{3}{8}(1 + \cos^2\theta)\sigma_U + \frac{3}{4}\sin^2\theta\sigma_L + \frac{3}{4}\cos\theta\sigma_F, \quad (3.1)$$

where $\sigma_{U,L}$ are the unpolarised or longitudinally polarised cross-sections and σ_F is the difference between the right- and left-handed polarised cross-section. Equation 3.1 can be rewritten as

$$\frac{1}{\sigma} \frac{d\sigma}{d\cos\theta} = \frac{3}{8} \frac{4}{3+a} (1 + a\cos^2\theta) + A_{\text{FB}} \cos\theta \quad (3.2)$$

where the total cross-section σ and the shape parameter a are given by

$$\sigma = \sigma_U + \sigma_L \quad a = \frac{\sigma_U - 2\sigma_L}{\sigma_U + \sigma_L} \quad (3.3)$$

and the forward-backward asymmetry is defined by

$$A_{\text{FB}} = \frac{3}{4} \frac{\sigma_F}{\sigma_U + \sigma_L}. \quad (3.4)$$

In Born approximation the cross-sections can be expressed in terms of the products of the vector- and axial-vector quark current :

$$\begin{aligned} \sigma_U &= \beta\sigma_{VV} + \beta^3\sigma_{AA} \\ \sigma_L &= \frac{1}{2}\mu^2\beta\sigma_{VV} \\ \sigma_F &= \beta^2\sigma_{VA} \end{aligned} \quad (3.5)$$

where μ is the quark mass in units of the beam energy and β is the velocity of the quark $\beta = \sqrt{1 - \mu^2}$. As can be seen from equation 3.5, measurements of the difference between forward and backward cross-sections give direct information about σ_F , i.e. the vector-axial-vector interference of the weak coupling. The quark current products are given by

$$\begin{aligned} \sigma_{VV} &= \frac{4\pi\alpha^2}{s} q_e^2 q_q^2 - \frac{G_{\text{F}}\alpha}{\sqrt{2}} q_e q_q c_V^e c_V^q \left(1 - \frac{s}{m_Z^2}\right) D^{-1} + \frac{G_{\text{F}}^2}{32\pi} (c_V^q)^2 ((c_V^e)^2 + (c_A^e)^2) s D^{-1} \\ \sigma_{AA} &= \frac{G_{\text{F}}^2}{32\pi} (c_A^q)^2 ((c_V^e)^2 + (c_A^e)^2) s D^{-1} \\ \sigma_{VA} &= \frac{G_{\text{F}}\alpha}{\sqrt{2}} q_e q_q c_A^e c_A^q \left(1 - \frac{s}{m_Z^2}\right) D^{-1} + \frac{G_{\text{F}}^2}{8\pi} c_V^e c_V^q c_A^e c_A^q s D^{-1}, \end{aligned} \quad (3.6)$$

where

$$D^{-1} = \left[\left(1 - \frac{s}{m_Z^2}\right)^2 + \left(\frac{\Gamma_Z}{m_Z}\right)^2 \right]^{-1}$$

On the pole of the Z^0 resonance, where the asymmetry is dominated by the Z^0 exchange, the forward-backward asymmetry of the quark flavour q , $A_{\text{FB}}^{q,0}$, can be expressed as

$$A_{\text{FB}}^{q,0} = \frac{3}{4} \frac{2c_V^e c_A^q}{(c_V^e)^2 + (c_A^e)^2} \frac{2\beta c_V^q c_A^e}{\frac{1}{2}(3 - \beta^2)(c_V^q)^2 + \beta^2(c_A^q)^2}. \quad (3.7)$$

3.2 Measuring Heavy Flavour Asymmetries

In order to measure the heavy flavour asymmetries two main ingredients are needed: firstly the flavour species has to be identified and separated from other contributions. And secondly

the direction of the outgoing quark has to be measured. This direction is, however, experimentally not accessible because of the hadronisation and fragmentation processes. Therefore it is approximated by the thrust axis. In order to determine the orientation of the thrust axis it is necessary to distinguish the quark from the anti-quark direction.

A number of different techniques are commonly used to tag heavy flavour events. For measurements of the heavy flavour asymmetries at LEP three different analyses exist. A very successful method to tag bottom quarks is looking for displaced vertices. Bottom mesons with average energies of tens of GeV and lifetimes of about 1.3 to 1.5 ps decay typically after a flight distance of a few millimetres in the detector. With the help of today's silicon micro-vertex detectors the decay length significance of these b meson decays can be reconstructed. Such a lifetime tag does not provide any information about the charge of the primary quark for the tagged hemisphere. A distinction of quark and anti-quark is achieved in the OPAL analysis by applying either a jet-charge or a vertex charge technique in addition to the heavy flavour tag.

Another analysis tags bottom and charm events by looking for semileptonic decays. Identifying leptons with high momentum and high transverse momentum with respect to the jet axis selects primarily leptons originating either from direct decays of the bottom or charm quark¹ or so-called cascade decays, where the bottom quark decays into a charm quark and subsequently leptons from a charm decay is tagged. Here a direct charge correlations between the lepton and the primary quark allows to distinguish the quark and the antiquark, when the origin of the lepton, i.e. the contributions from $b \rightarrow l^-$, $b \rightarrow c \rightarrow l^+$ and $c \rightarrow l^+$ is known. The bottom and charm asymmetries are then determined in a two dimensional maximum likelihood fit. These two analyses are summarised in this section.

The third possibility used by the OPAL collaboration is the tag of primary charm quarks by the exclusive reconstruction of D mesons in different decay channels. Here as well either $e^+e^- \rightarrow b\bar{b}$ and $e^+e^- \rightarrow c\bar{c}$ events are tagged and the events separated according to their primary flavour with help of a lifetime and jet-shape analysis. The charge of the D meson decay products allows a direct determination of the charge of the primary quark. The heavy flavour asymmetries of bottom and charm events are subsequently determined in a two dimensional maximum likelihood fit.

In the OPAL heavy flavour asymmetry analyses hadronic Z^0 decays are selected by placing requirements on the number of reconstructed charged tracks and the energy deposited in the calorimeter. A detailed description of the criteria is given in [9]. The analysis is based on about 4 million hadronic decays of the Z^0 collected with the OPAL detector in the vicinity of the Z^0 resonance between 1990 and 1995. Of these data roughly 13.4% have been collected either below or above the maximum of the resonance.

To verify the analysis procedures and investigate possible biases, 4 million hadronic decays of the Z^0 have been simulated using the JETSET Monte Carlo model [10] with parameters tuned to represent LEP data well [11]. Several special samples have been used to study specific decays, corresponding to an additional 5 million hadronic Z^0 decays. In all samples heavy quark fragmentation has been implemented using the model of Peterson *et al.* [12]. All samples have been passed through a detailed simulation of the OPAL detector [13] before being analysed using the same programs as for data.

¹In the fragmentation process the quarks are transformed into hadrons. 'Direct decays of the bottom or charm quark' means, more correctly, that a bottom or charm flavoured hadron, containing the primary b or c quark, decays.

3.2.1 Lifetime/Jet-charge Analysis

A measurement of the bottom forward-backward asymmetry is done by tagging $e^+e^- \rightarrow b\bar{b}$ events with lifetime information. Details can be found in [14]. Long lived B hadrons are tagged with a high b purity by requiring a displaced secondary vertex in at least one hemisphere. Secondary vertices are reconstructed in an inclusive iterative procedure, and the decay length L , the distance between the primary and the secondary vertex in the xy -plane, and its error is calculated. In this analysis a decay length significance of $L/\sigma_L > 4$ is required. After that the number of tagged hemispheres is 402485, of which 20631 are in events with energies above, and 31471 below the Z^0 pole. The composition of the resulting sample is about 83% bottom events with a background of 11% charm and 6% light flavour events. The charge of the primary quark is determined by measuring the charge of the particles which form the secondary vertex (vertex charge) or a jet-charge technique.

A measurement of the vertex charge allows a better determination of the charge of the primary quark than a measurement of the jet-charge. The analysis of the two different charge measuring techniques are therefore performed separately. For the vertex charge each track in the hemisphere is weighted by a probability ω_i based on momentum, multiplicity and impact parameter information, that it comes from the secondary vertex. In order to remove vertices of neutral B mesons and poorly determined vertex charges $|q_{vtx}| > 1.4\sigma_q + 0.2$ is required. The charm background is eliminated by a tight cut on the output of an artificial neural network, which was trained to discriminate between $e^+e^- \rightarrow b\bar{b}$ and other events [15]. A sample of 12889 vertex charge tagged hemispheres remains. The bottom forward-backward asymmetry is then determined in an unbinned likelihood fit.

The jet-charge technique is used to measure the asymmetry in events without a vertex charge measurement. The jet-charge is the momentum weighted average charge of all charged tracks of a jet. The asymmetry is determined by a counting method: for a sample containing of a mixture of quark species and a varying tagging efficiency as a function of the thrust direction $|\cos\theta_T|$ and the flavour f , the charge flow $\langle Q_F - Q_B \rangle$ is given by

$$\langle Q_F - Q_B \rangle = \sum_{\text{flavours } f} s_f F_f C^f \delta_f A_{FB}^f, \quad (3.8)$$

where Q_F and Q_B are the jet-charges in the forward and backward hemisphere respectively², s_f is $+1(-1)$ for down-like (up-like) quarks, and F_f is the fraction of quark species f in the lifetime-tagged sample, as determined using an unfolding technique. The quantity δ_f is the charge separation for events with flavour f . The b quark charge separation, δ_b , was measured from the data by comparing the measured jet-charges in events where both hemispheres are tagged. The charm and light quark charge separations were taken from the Monte Carlo. The C^f factors account for the effects of the variation of tagging efficiency with $|\cos\theta_T|$ and are given by

$$C^f = \frac{8}{3} \frac{\int \bar{\eta}_f(y) y dy}{\int \bar{\eta}_f(y) (1 + y^2) dy}, \quad (3.9)$$

where $y = |\cos\theta_T|$ and $\bar{\eta}_f(y)$ is the efficiency of lifetime tagging a flavour f event. The event tagging efficiency for b and c events is determined from data in bins of $|\cos\theta_T|$, using an

²Forward is defined with respect to the direction of the incoming electron.

unfolding method. The C factors for the u, d, and s quarks are assumed all to have the same value which is taken from the Monte Carlo.

The results for the bottom forward-backward asymmetry are

$$\begin{aligned} A_{FB}^b &= 0.041 \pm 0.021 \pm 0.002 & \langle E_{cm} \rangle &= 89.44 \text{ GeV} \\ A_{FB}^b &= 0.0994 \pm 0.0052 \pm 0.0044 & \langle E_{cm} \rangle &= 91.21 \text{ GeV} \\ A_{FB}^b &= 0.145 \pm 0.017 \pm 0.007 & \langle E_{cm} \rangle &= 92.91 \text{ GeV} \end{aligned}$$

where the first error is statistical and the second systematic.

3.2.2 The Lepton Analysis

A detailed description of this analysis can be found in [16]. The analysis is restricted to $|\cos\theta_{thrust}| < 0.9$ in order to have optimal lepton identification.

Electron identification is based on a set of twelve different quantities which are measured in the central tracking chambers and the electromagnetic calorimeter. These variables are fed into an artificial neural net, which is trained on simulated data. A detailed description of the input variables, the training and systematic checks can be found in [16]. Electron candidates are required to fulfil $p > 2$ GeV and $NET_{el} > 0.9$, where p is the momentum of the electron candidate and NET_{el} denotes the output of the neural net electron selection. The remaining dominant background of electrons from photon conversions is rejected with the help of a second neural net, where different kinematic variables are used for the separation as is described in [16]. The muon selection relies on the quality of the match between a track reconstructed in the muon chambers and in the central tracker. In addition, a loose cut on dE/dx and a minimum momentum of $p > 3$ GeV is required.

Candidate leptons are classified into four distinct types: $b \rightarrow l^-$, $c \rightarrow l^+$, $b \rightarrow c \rightarrow l^+$ and non-prompt leptons and misidentified hadrons. For the measurement of the b and c quark asymmetries it is especially important to separate direct b and c decays from each other and from all other contributions. In order to optimise the separation a multi-variable analysis has been performed, where two different artificial neural nets are used to distinguish the source of the lepton candidate. One of them, NET_b separates direct $b \rightarrow l^-$ decays from the remaining contributions. The separation power is mostly due to the ‘classical’ variables, the momentum of the lepton p and the transverse momentum p_t with respect to the nearest jet axis. Another neural net helps to distinguish between $c \rightarrow l^+$ decays and the other classes. Here the main information comes from lifetime information. For both neural nets as much as possible of the additional information available is used, including jet and vertex properties. An optimal separation is reached by using the net-outputs NET_b and NET_c in a two dimensional way. A list of the different variables, the details of training and the performance reached by this technique can be found in [16]. Similar to the event probabilities in the D analysis (as will be described in section 3.3), probabilities are calculated from the outputs of the neural networks used for flavour separation (NET_b and NET_c). These are used in the asymmetry fit to separate the different contributions.

The asymmetries A_{FB}^b and A_{FB}^c are extracted from single lepton events using a binned maximum likelihood fit [16]. The differential forward-backward asymmetry³, ΔA_{FB} , measured

³ $\Delta A_{FB} = (n(\cos\theta_{thrust}) - n(-\cos\theta_{thrust})) / (n(\cos\theta_{thrust}) + n(-\cos\theta_{thrust}))$

in the data is compared to the expected asymmetry as a function of $|y| = |\cos\theta_{thrust}|$, in bins of the flavour discriminating variables NET_b and NET_c . For events containing more than one candidate lepton, the candidate with the highest NET_b value is considered in the single-lepton sample.

The measured asymmetry of bottom events depends on the mixing parameter of B^0 mesons. The corresponding average mixing parameter $\bar{\chi}$ which depends on the composition of the tagged sample, is obtained simultaneously with the asymmetries by counting the number of like-sign leptons in events with at least two ‘opposite leptons’⁴ with $NET_b > 0.8$. For events containing more than two candidate leptons that satisfy these criteria, the two leptons with the highest NET_b values are used.

Using all data collected by OPAL between 1990 and 1995 of LEP1, the b and c quark forward-backward asymmetries at three centre-of-mass energy points on and around the Z^0 peak are measured, with the following results:

$$\begin{aligned} A_{FB}^b &= (0.034 \pm 0.017 \pm 0.002) & A_{FB}^c &= (-0.068 \pm 0.024 \pm 0.005) & \text{at } \langle\sqrt{s}\rangle &= 89.49 \text{ GeV,} \\ A_{FB}^b &= (0.0892 \pm 0.0044 \pm 0.0020) & A_{FB}^c &= (0.0588 \pm 0.0059 \pm 0.0056) & \text{at } \langle\sqrt{s}\rangle &= 91.24 \text{ GeV,} \\ A_{FB}^b &= (0.105 \pm 0.014 \pm 0.004) & A_{FB}^c &= (0.154 \pm 0.020 \pm 0.010) & \text{at } \langle\sqrt{s}\rangle &= 92.95 \text{ GeV,} \end{aligned}$$

where the first error is statistical and the second is systematic. The average B^0 - \bar{B}^0 mixing parameter was found to be:

$$\bar{\chi} = 0.1142 \pm 0.0054 \pm 0.0048.$$

The lepton analysis gives for both the measurements of the bottom as well as the charm asymmetry the most precise results. Especially for the charm asymmetry the systematic error is of the same size than the statistical error, therefore the most important systematic uncertainties will be discussed briefly in the following. More details can be found in references [16, 17].

- Heavy flavour fragmentation

The parameters for the charm and bottom fragmentation function of Peterson *et al.* are varied within $\epsilon_b = 0.0055_{-0.0030}^{+0.0040}$ and $\epsilon_c = 0.07_{-0.02}^{+0.03}$. The variation is significantly larger than the experimental error on present measurements and thus accounts also for uncertainties in the choice of the model itself.

- Semileptonic decay models

The semileptonic decays of heavy hadrons are described by the free-quark model of Altarelli *et al.* (ACMM) [18], which has two free parameters: the Fermi momentum p_f and the mass of the quark produced in the decay of the heavy hadron, m_c or m_s . For b decays, values of $p_f=298$ MeV/c and $m_c=1673$ MeV/c² have been obtained from a fit to CLEO data [19], while for c decays, the combined measurements of DELCO [20] and MARK III [21] have been used to derive values of $p_f=0.467$ GeV/c and $m_s=0.001$ GeV/c². Systematic uncertainties arising from the choice of the semileptonic decay model are treated differently for b and c hadron decays by varying either the model or its parameters. For $b \rightarrow l^-$ decays, alternatively the model of Isgur *et al.* [22] and a modified version, ISGW**, is used to describe the semileptonic decays. The ISGW** description gives the largest deviation from the ACCMM model and the resulting differences obtained for the

⁴‘Opposite leptons’ are leptons associated to jets that do not belong to the same thrust hemisphere.

bottom and charm asymmetries are taken as a systematic error. Uncertainties affecting the modelling of $c \rightarrow l^+$ decay can be estimated by using various versions of the ACCMM model based on different sets of values for the fitted parameters m_s and p_l . The results with the parameters $m_s=0.001 \text{ GeV}/c^2$ and $p_l=0.353 \text{ GeV}/c$ called ACCMM1, give the largest deviation compared to the central values of $m_s=0.001 \text{ GeV}/c^2$ and $p_l=0.467 \text{ GeV}/c$ and are thus taken to derive the systematic error.

- Branching ratios

The values of $BR(b \rightarrow l^-)$ and $BR(b \rightarrow c \rightarrow l^+)$ used for this analysis are combinations [23] of measurements performed by the LEP experiments. In the measurements of $BR(b \rightarrow l^-)$ and $BR(b \rightarrow c \rightarrow l^+)$, an important part of the error is due to the choice of semileptonic decay model. This is taken into account by using the branching ratios which correspond to each choice of semileptonic decay model as the model is varied. Thus the error on the branching ratios is divided into two parts, one due to the semileptonic decay model and the other one because of other uncertainties. The branching ratios used for this analysis are $BR(b \rightarrow l^-) = 10.90 \pm 0.32(\pm 0.21)$ and $BR(b \rightarrow c \rightarrow l^+) = 8.30 \pm 0.47(\pm 0.19)$. The second part of the errors (i.e. not due to the models) is then used to estimate the additional systematic error due to the uncertainties in $BR(b \rightarrow l^-)$ and $BR(b \rightarrow c \rightarrow l^+)$, excluding the model uncertainties. $BR(c \rightarrow l^+)$ is taken from lower energy measurements performed at ARGUS, PEP and PETRA [24], giving a combined value of $BR(c \rightarrow l^+) = (9.8 \pm 0.5)\%$.

- Background asymmetry The hadronic and non-prompt background have been assumed to have no asymmetry. This assumption has been checked and confirmed using the simulation as well as data samples of tracks which did not pass the lepton selection, or using all tracks in the momentum range $p > 2 \text{ GeV}/c$ or $p > 4 \text{ GeV}/c$ weighted by the fake probability predicted by the simulation. All these tests indicated that the upper limit for any possible residual asymmetry of the background is 0.5%. This value was then used to estimate the systematic error due to a possible residual background asymmetry.

- Composition dependence on $\cos \theta_{thrust}$

Another important uncertainty is due to the modelling of the dependence of the (NET_b , NET_c) distributions on $\cos \theta_{thrust}$ in the simulation. The tracking resolution quickly degrades with increasing $\cos \theta_{thrust}$, thus affecting the NET_b and NET_c distributions. The effect is more pronounced for the NET_c output since the net is based on variables such as the decay length or impact parameter significance. Two different parametrisations of the (NET_b , NET_c) distributions are used in the analysis, one for the barrel region with $|\cos \theta_{thrust}| < 0.7$, the other one for the endcap region with $0.7 < |\cos \theta_{thrust}| < 0.9$. The effect is estimated by using only one parametrisation for the entire region instead of two.

The values of the systematic errors as determined for the measurement on top of the Z^0 resonance are summarised in table 3.1.

	A_{FB}^b (%)	A_{FB}^c (%)	\bar{X}
Fitted Value	8.92	5.88	0.1142
Statistical error	± 0.44	± 0.59	± 0.0054
Systematic error	± 0.20	± 0.56	± 0.0048
Sources of systematic errors			
$b \rightarrow l^-$ (ACCMM to ISGW**)	-0.01	+0.20	-0.0007
$c \rightarrow l^+$ (ACCMM to ACCMM1)	+0.07	-0.08	-0.0026
$\langle x_E \rangle_b - 0.02$	-0.01	+0.02	-0.0016
$\langle x_E \rangle_c + 0.02$	-0.12	+0.05	+0.0001
Total models	± 0.14	± 0.22	± 0.0031
$BR(b \rightarrow l^-) + 0.32\%$	-0.01	+0.15	+0.0005
$BR(b \rightarrow c \rightarrow l^+) + 0.47\%$	-0.02	-0.10	-0.0018
$BR(b \rightarrow \bar{c} \rightarrow l^-) + 0.50\%$	-0.02	+0.23	+0.0008
$BR(b \rightarrow \tau \rightarrow l^-) + 0.20\%$	-0.01	+0.09	+0.0003
$BR(c \rightarrow l^+) + 0.50\%$	+0.03	-0.20	+0.0002
Total branching ratios	± 0.04	± 0.37	± 0.0021
Conversion fraction increase	+0.00	+0.03	-0.0003
Decay fraction increase	+0.00	+0.00	-0.0002
Source dependence	+0.02	+0.13	+0.0010
Tracking Resolution	-0.06	+0.00	+0.0002
Input corrections	+0.02	-0.01	-0.0012
Total detector effects	± 0.07	± 0.14	± 0.0016
$\cos \theta_{thrust}$ dependence (fractions)	+0.02	-0.01	+0.0000
$\cos \theta_{thrust}$ dependence (distributions)	+0.08	-0.19	-0.0001
Monte Carlo statistics	+0.08	+0.10	+0.0026
Time dependent mixing	+0.04	+0.04	+0.0000
Background asymmetry +0.5%	+0.00	+0.26	+0.0000
Total other systematics	± 0.12	± 0.33	± 0.0026

Table 3.1: Summary of the of systematic errors for the lepton analysis.

3.3 Analysis of the Heavy Flavour Asymmetries using D Mesons

In the following section the measurement of the $c\bar{c}$ and $b\bar{b}$ forward-backward asymmetries using D mesons as a heavy flavour tag is described in more detail.

3.3.1 Selection of D Candidates

Three different D meson states are used in this paper as tags for charm and bottom: the ground state pseudo-scalar D mesons⁵ D^0 and D^+ , and the vector meson D^{*+} . After describing

⁵Throughout this paper charge conjugate modes are always implicitly included.

the requirements placed on tracks to be included in the analysis, the reconstruction and the procedures used in the identification of charged D^* mesons are discussed, followed by the analogous discussion for D^0 and D^+ mesons. Additional details on D reconstruction with the OPAL detector can be found in [25–27].

Tracks are accepted for the reconstruction if they satisfy loose track quality requirements: $|d_0| < 5$ mm; $|z_0| < 20$ cm; $p_{\perp} > 250$ MeV; $n_{CJ} > 40$. Here d_0 is the distance of closest approach in the plane perpendicular to the beam axis, between the primary vertex and the track, z_0 is the distance along the beam at this point, p_{\perp} is the momentum component perpendicular to the beam, and n_{CJ} is the number of hits on the track recorded in the jet chamber. Tracks are also required to be well reconstructed, by demanding that their polar angle θ be measured in at least two components of the tracking system, one of which must be the jet chamber.

D^{*+} Reconstruction

For this analysis D^{*+} mesons are reconstructed in five different decay channels:

$$\begin{aligned}
 D^{*+} &\rightarrow D^0 \pi^+ \\
 &\hookrightarrow K^- \pi^+ \quad \text{“3 prong”}, \\
 &\hookrightarrow K^- \pi^+ \pi^0 \quad \text{“satellite”}, \\
 &\hookrightarrow K^- \pi^+ \pi^- \pi^+ \quad \text{“5 prong”}, \\
 &\hookrightarrow K^- e^+ \nu_e \quad \text{“electron”}, \\
 &\hookrightarrow K^- \mu^+ \nu_{\mu} \quad \text{“muon”}.
 \end{aligned}$$

No attempt is made to reconstruct the π^0 in the satellite channel, nor the neutrino direction or energy in the electron and muon channels. The last two channels are referred to as “semileptonic” channels in the following text. Electrons are identified based on the energy loss in the central drift chamber and the energy deposition in the electromagnetic calorimeter. An artificial neural network trained on simulated events is used to perform the electron selection [28]. Electrons from photon conversions are rejected as in [29]. Muon candidates are identified by associating tracks found in the central tracking system with tracks in the muon chambers [29]. No momentum cut on the lepton track is applied. Such a cut is used in analyses, which require a precise knowledge of the lepton purity, which is not important for this analysis.

A number of tracks appropriate for the selected channel are combined to form a D^0 candidate and its invariant mass is calculated. The cuts applied are given in table 3.2 and explained below. Only candidates with the correct charge combinations are retained. Candidates are selected if the reconstructed mass lies within the expected range for that channel. After adding a further track as a possible pion from the D^{*+} decay, the combined mass is calculated and the candidate is selected if the mass difference $\Delta M = M_{D^{*+}} - M_{D^0}$ is within certain limits. Note that ΔM is always to be understood as the effective mass difference, calculated only from the visible tracks of the candidate. This latter requirement is particularly efficient in suppressing background, because the small mass difference between the D^{*+} and the D^0 places true D^{*+} decays very close to the kinematic threshold in ΔM at 0.139 GeV. Very little phase space remains for background events, resulting in a good signal to background ratio.

At low values of the D^{*+} scaled energy⁶, $x_{D^{*+}} = E_{D^{*+}}^{calc}/E_{beam}$, the background contribution is very high, especially from pions produced in the fragmentation. Many of the background kaon candidates are in reality fragmentation pions. Their contribution is reduced by using the particle identification power of the OPAL detector to enrich the sample in true kaons. A probability, $W_{dE/dx}^{KK}$, is calculated for a kaon candidate, that the measured specific energy loss, dE/dx , for a track is compatible with having been produced by a kaon. The probability $W_{dE/dx}^{KK}$ is signed, i.e. the probabilities have positive and negative values for above and below the expected value, respectively.

The background of the sample is further reduced by cutting on the helicity angle θ^* , measured between the direction of the D^0 candidate in the laboratory frame and the direction of the kaon in the rest frame of the D^0 candidate. True D^0 decays are expected to be uniformly distributed in $\cos \theta^*$, while background displays pronounced peaks at $\cos \theta^* = -1$ and, particularly at low $x_{D^{*+}}$, $\cos \theta^* = +1$.

cut	x range	3 prong	semileptonic	satellite	5 prong
$x_{D^{*+}}$		0.2-1.0	0.2-1.0	0.2-1.0	0.5-1.0
M_{D^0} [GeV]	full	1.79-1.94	1.20-1.80	1.41-1.77	1.79-1.94
ΔM [GeV]	full	0.142-0.149	0.140-0.162	0.141-0.151	0.142-0.149
$\cos \theta^*$	< 0.5		-0.8-0.8		-
	> 0.5		-0.9-1.0		-0.9-1.0
$ W_{dE/dx}^{KK} $	< 0.5		> 0.1		-

Table 3.2: List of cuts used in the D^* reconstruction. Note that both the scaled energy x_D and the mass difference ΔM are effective quantities, calculated from the reconstructed tracks only. The exact meaning of the different quantities is explained in the text.

The invariant mass spectra for the five reconstructed D^{*+} channels are presented in figure 3.1. Shown is the mass difference ΔM between the D^{*+} and the D^0 candidate. In all channels clear signals are visible.

D^0 and D^+ Reconstruction

The D^0 and D^+ mesons are identified in the following decay modes:

$$\begin{aligned}
 D^0 &\rightarrow K^- \pi^+ , \\
 D^+ &\rightarrow K^- \pi^+ \pi^+ .
 \end{aligned}$$

The reconstruction of these D meson states is similar to that for the D^{*+} mesons. It follows very closely the method described in [27]. The invariant mass is calculated from the appropriate number of tracks which pass the quality requirements. A D^+ candidate is rejected if the mass difference ΔM , calculated under the assumption that the three tracks form a D^{*+} candidate, is below 0.16 GeV. To suppress combinatorial background, and to allow a good measurement

⁶In this paper any reference to the scaled energy x of a D candidate is to be understood as being to the calculated energy of the D, E_D , obtained from the reconstructed tracks, without correcting for missing or wrongly associated tracks, divided by the beam energy E_{beam} .

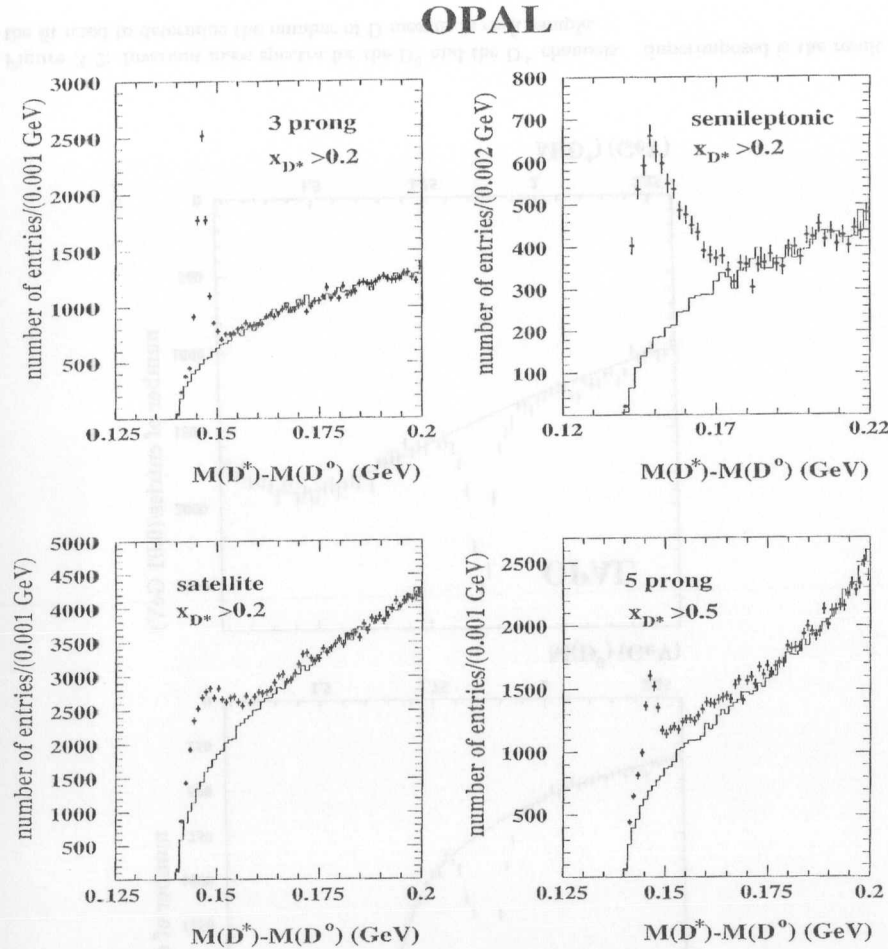


Figure 3.1: Distributions of the difference $M_{D^*} - M_D$ reconstructed in the different D^* channels. Both semileptonic decays have been combined into one plot. Superimposed are the background estimator distributions, normalised to the upper sidebands in ΔM .

of the specific energy loss dE/dx , candidates are required to have at least 30% of the beam energy, and the individual track momenta are required to be above 1.5 GeV for a kaon, and 0.5 GeV for a pion. The long lifetime of the weakly decaying D mesons is used to enrich the signal purity. A vertex is calculated in the r - ϕ plane from the tracks forming the D candidate. The distance d between this vertex and the primary event vertex is calculated. A candidate is accepted if this distance exceeds 500 μm for a D^0 candidate, or 800 μm for a D^+ candidate. Good vertex reconstruction quality is ensured by requiring that at least one (for the D^0) or two (for the D^+) tracks have at least one hit in the silicon micro-vertex detector. To stay within the acceptance of the micro-vertex detector, all tracks have to be within $|\cos\theta| < 0.85$. For the D^+ , where the three tracks in the decay allow a meaningful calculation of a vertex χ^2 , events with badly reconstructed vertices are rejected by a loose cut on this quantity.

The number of multiple candidates and wrong particle type associations is reduced by placing requirements on the dE/dx measurement. Kaon candidate tracks are required to be consistent with being a kaon with a probability $W_{dE/dx}^{KK}$ exceeding 3% if their measured dE/dx is above the value expected for a kaon, or exceeding 1% if the measured dE/dx is below the expected value. Pion background in the kaon candidate sample is rejected by accepting only tracks whose probability $W_{dE/dx}^{K\pi}$ that the kaon candidate track is consistent with a pion is less than 10%. The purity of the pion candidates is increased by requiring that these tracks are consistent with a pion with a probability exceeding 1%. The details of the cuts are listed in table 3.3. In figure 3.2 the invariant mass spectra for the D^0 and D^+ channel are plotted.

cut	D^0	D^+
x_D	0.3 – 1.0	0.3 – 1.0
$M_{D^0, D^+} [\text{GeV}]$	1.81 – 1.93	1.81 – 1.93
$\Delta M [\text{GeV}]$	-	> 0.16
$p_K [\text{GeV}]$	> 1.5	> 1.5
$p_\pi [\text{GeV}]$	> 0.5	> 0.5
$ \cos\theta_{\text{cand}} $	< 0.85	< 0.85
$d [\mu\text{m}]$	> 500	> 800
$W_{dE/dx}^{KK}$	> 0.03	> 0.03
	< -0.01	< -0.01
$ W_{dE/dx}^{\pi\pi} $	> 0.01	> 0.01
$ W_{dE/dx}^{K\pi} $	< 0.1	< 0.1

Table 3.3: List of cuts used in the D^0 and D^+ reconstruction. The exact meaning of the different quantities is explained in the text.

Multiple Candidate Rejection

Since the goal of the analysis is the determination of the angular distribution of the primary quark, not that of reconstructed mesons, only one measurement of this quantity per event is needed. If more than one candidate meson is found per event, a hierarchy is used to select the best one: low background is preferred and low multiplicity final states are favoured over higher multiplicity ones. The hierarchy used, from best to worst, is: 3 prong, semileptonic, satellite,

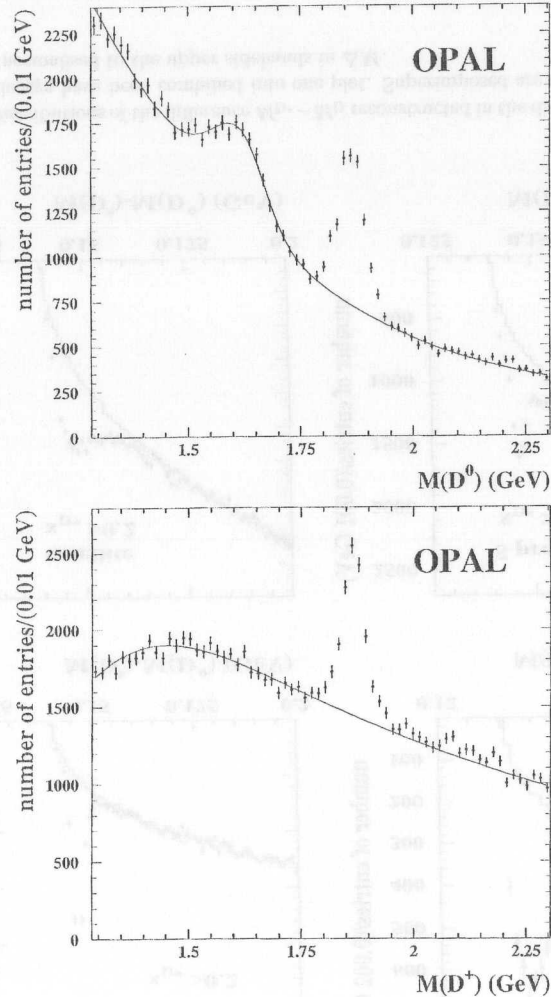


Figure 3.2: Invariant mass spectra for the D^0 and the D^+ channels. Superimposed is the result of the fit used to determine the number of D mesons in each sample.

	lost in total [%]	within channel [%]
3-prong semileptonic	9.2	9.2
satellite	17.9	12.5
5-prong	29.6	21.0
D^0	58.6	55.2
D^+	39.8	33.3
	55.6	52.6

Table 3.4: Percentage of candidates lost in the multiple candidate rejection. Given are for each channel the total percentage of candidates rejected and the percentage of candidates rejected only due to multiple candidates found within this channel.

5 prong, D^0 , D^+ . If more than one candidate is found within one D^{*+} channel, the one with the D^0 mass closest to the nominal mass is taken (the mass used is 1.865 GeV for the 3 prong, semileptonic and 5-prong decay, and 1.60 GeV for the satellite [30]). In the D^0 and D^+ decays, where a selection on the mass would result in a distortion of the invariant mass spectrum and consequently the signal over background determination, the candidate with the highest x_D is selected. Overall the number of candidates is reduced by 34.6% by the multiple candidate rejection. In table 3.4 the percentage of events rejected due to this procedure in each channel is shown. To avoid rejecting good candidates an event from an lower priority D^{*+} or D^+ decay is rejected only if another candidate has been found in a higher priority channel within the tight ΔM windows given in table 3.3. This method would severely bias the D^0 reconstruction if applied to this channel. Therefore a D^0 candidate is rejected if another candidate is found in any of the D^{*+} decays within a loose M_{D^0} mass window of $1 \text{ GeV} < M_{D^0} < 2.5 \text{ GeV}$. After all cuts a total of 73870 candidates is found.

Determination of the Signal Fraction

For the purpose of the asymmetry analysis, a signal event is defined as any event that contains enough information to reconstruct correctly the charge and flavour of the primary quark. For the D^{*+} decays two classes of events contribute to the signal sample: events where a D meson has been completely reconstructed in one of the channels described, and events where a D^{*+} decay has only partially been found, but where the slow pion is correctly tagged. The latter have broader distributions in ΔM , as is shown in figure 3.1, especially in the 5 prong channel. In either case, because of the very distinct kinematics of the D^{*+} decay, the events exhibit an enhancement in the ΔM spectra around 145 MeV. The fraction of events which is considered as signal for this analysis is determined with a background estimator, which uses a hemisphere mixing technique first described in [25]. In this estimator, the candidate for the slow pion is taken from the opposite hemisphere to the rest of the candidate tracks, and reflected through the origin before being used in the calculation of the invariant mass of the candidate. This method ensures that no correctly identified slow pions enter the background sample, and that the background shape does not exhibit any peaks in the interesting ΔM region. For this background estimator no requirements are placed on the charge of the D^0 candidate tracks, except that the sum of the charges of all tracks including the slow pion candidate should be ± 1 . Monte Carlo studies have shown that this background estimator reliably models the shape of the background in all five channels.

The background is determined by normalising the estimator distribution for $0.18 \text{ GeV} < \Delta M < 0.20 \text{ GeV}$ ($0.19 \text{ GeV} < \Delta M < 0.22 \text{ GeV}$ for the semileptonic channels) to the sideband of the signal distribution and subtracting the normalised background from the signal. Candidates are counted within the ΔM ranges given in table 3.2. Monte Carlo studies have shown that this method leads to an unbiased determination of the number of D^{*+} candidates in all channels.

The background levels in the D^0 and D^+ channels are determined from a fit to the observed mass spectra with an empirically determined functional form for the background. The background to the D^0 is described by a third degree polynomial, while for the D^+ an exponential convoluted with a Gaussian function is used. Contributions from satellite decays visible in the D^0 mass spectrum at masses around 1.6 GeV are accounted for by an additional Gaussian function. A slight asymmetry in the signal is allowed for by fitting different widths below and above the mean value. The normalisation, mean and both widths are determined in the fit. The total background is determined by integrating the fit function over the mass windows listed in table 3.3.

Background exists in both channels which distorts the expected signal shape. In the D^0 channel the decays $D^0 \rightarrow K^+K^-$ and $D^0 \rightarrow \pi^+\pi^-$ contribute to the signal, if one of the final state particles is misidentified as either a pion or a kaon, thus faking a $K\pi$ final state. Since the charge correlation between the primary quark and the reconstructed charge is broken, their estimated contribution is subtracted from the sample. Simulated events are used to estimate the contamination from these two sources. They are found to contribute less than 1% to the final sample. Backgrounds in the D^+ reconstruction are the decays of the D_s meson into $\phi\pi^+$ and $K^{*0}K^+$, both decaying into a final state $K^+K^-\pi^+$. Misidentifying a kaon as a pion will shift the mass peak to around the mass of the D^+ meson. Monte Carlo studies have shown that this background contributes approximately 10% to the D^+ signal.

The final number of D^{*+} , D^0 or D^+ events is determined by correcting the number of background subtracted events calculated above for these additional background contributions. This method has been tested using simulated events and has been found to reproduce the true number of D mesons within the statistical precision of the test.

A potentially serious problem in all channels is the presence of background where the correlation between the primary quark charge and the charge q tagged by the D candidate is preserved. These events will not be considered as signal, but they will be asymmetric in $q \cos \theta$, thereby introducing an asymmetry into the background. Such correlations are expected since the sample of candidate tracks is enriched in true kaons using the dE/dx cuts described. Many kaons are originating from the primary quark in the event, thereby preserving the charge correlation. Similar effects are expected for leptons. These events are present at levels of a few percent in all modes considered and are taken into account by fitting for a background asymmetry, as described in section 3.3.3. The background asymmetries as fitted in the data are quoted in section 3.3.4.

In table 3.5 the number of D^{*+} , D^0 and D^+ meson candidates, and the background, is shown for each channel, with statistical errors. Altogether 24195 ± 150 D^{*+} mesons and 8439 ± 132 D^0 and D^+ mesons have been reconstructed after background subtraction, over backgrounds of 24664 ± 150 events and 16558 ± 132 events, respectively.

x_D	$D^{*+} \rightarrow D^0\pi^+$ $\hookrightarrow K^-\pi^+$		$D^{*+} \rightarrow D^0\pi^+$ $\hookrightarrow K^-\pi^+\pi^0$		$D^{*+} \rightarrow D^0\pi^+$ $\hookrightarrow K^-\pi^+\pi^-\pi^+$		
	$N_{\text{cand}}^{\text{obs}}$	$N_{\text{bgd}}^{\text{rest}}$	$N_{\text{cand}}^{\text{obs}}$	$N_{\text{bgd}}^{\text{rest}}$	$N_{\text{cand}}^{\text{obs}}$	$N_{\text{bgd}}^{\text{rest}}$	$N_{\text{bgd}}^{\text{rest}}$
0.2-0.3	3036	1716 ± 39	10372	7547 ± 87			
0.3-0.4	1825	704 ± 25	5131	2999 ± 54			
0.4-0.5	1251	264 ± 15	3016	1273 ± 36			
0.5-0.6	1556	411 ± 18	3636	1753 ± 40	5417	3312 ± 52	
0.6-0.7	927	169 ± 11	1687	725 ± 25	2156	1002 ± 28	
0.7-0.8	520	76 ± 7	670	263 ± 14	908	298 ± 14	
0.8-1.0	277	34 ± 4	208	97 ± 7	357	78 ± 6	

x_D	$D^{*+} \rightarrow D^0\pi^+$ $\hookrightarrow K^-\ell^+\nu$		$D^0 \rightarrow K^-\pi^+$		$D^+ \rightarrow K^-\pi^+\pi^+$		
	$N_{\text{cand}}^{\text{obs}}$	$N_{\text{bgd}}^{\text{rest}}$	$N_{\text{cand}}^{\text{obs}}$	$N_{\text{bgd}}^{\text{rest}}$	$N_{\text{cand}}^{\text{obs}}$	$N_{\text{bgd}}^{\text{rest}}$	$N_{\text{bgd}}^{\text{rest}}$
0.2-0.3	2217	1058 ± 33					
0.3-0.4	1405	475 ± 22	4102	2655 ± 52	6314	5300 ± 72	
0.4-0.5	861	212 ± 15	2513	1636 ± 51	4089	2982 ± 55	
0.5-0.6	829	99 ± 14	1711	770 ± 28	2318	1465 ± 38	
0.6-0.7	} 597	99 ± 9	985	455 ± 21	1289	669 ± 26	
0.7-0.8			514	224 ± 15	672	242 ± 16	
0.8-1.0			224	92 ± 10	266	68 ± 8	

Table 3.5: Number of D mesons reconstructed in the different decay modes, in bins of the effective scaled energy of the candidates calculated from the reconstructed track momenta. Given are the number of D meson candidates, $N_{\text{cand}}^{\text{obs}}$, before background subtraction and the number of background events, $N_{\text{bgd}}^{\text{rest}}$. The error quoted on the estimated background is the statistical error only.

3.3.2 Charmed Mesons in $c\bar{c}$ and $b\bar{b}$ Events

In this analysis the D^{*+} , D^0 and D^+ mesons are used as tags for primary charm and bottom decays of the Z^0 . Both processes are expected to contribute roughly equally to the tagged sample, in addition to sizeable contributions from combinatorial background. Lifetime information and jet shape variables are used to separate the different sources of D mesons. First the level of background in the sample is determined, based on the D meson signal, as described in section 3.3.1, and subtracted. The remaining signal is composed essentially only of $c\bar{c}$ and $b\bar{b}$ events. Since $b\bar{b}$ events are significantly different in lifetime and jet shape properties from other events, the fraction of $b\bar{b}$ events in the sample can be determined, and therefore the $c\bar{c}$ content inferred. A small contribution to the sample of tagged events is also expected from gluon splitting processes. In this analysis these events are not subtracted from the sample, but will be considered later as a source for a systematic error. Finally for each event a probability is calculated whether this event is a $b\bar{b}$ or a $c\bar{c}$ event. These probabilities are used in the asymmetry fit to separate primary charm and bottom events.

In this section the details and the techniques used to derive the event probabilities are presented. The description starts with a general introduction into the formalism used. Next the treatment of background is discussed, and the charm and bottom fractions in the sample are determined. Finally all information is combined in the calculation of the event probabilities.

Definition of the Event Probabilities

The dominant contributions to the sample of events with tagged D mesons come from decays of primary b or c quarks. Only a small fraction of the events is expected to originate from the splitting of a gluon into a pair of charm quarks. For the sake of simplicity this contribution is neglected in the following discussion.

The event probabilities introduced above are calculated individually for each event from lifetime information. They are obtained for two jets in the event, firstly the jet containing the reconstructed D meson, referred to as the D jet in the following, and secondly the jet with the highest energy not containing the D meson candidate, called the secondary jet. They are calculated, as functions of the D meson scaled energy, $x = x_D$, and the decay length significance, δ , of the secondary vertex in each jet, by

$$w_j(x, \delta^D, \delta^{\text{sec}}) = \frac{p_j(x) \cdot L_j^D(x, \delta^D) \cdot L_j^{\text{sec}}(x, \delta^{\text{sec}})}{\sum_{l=\text{bgd}, \text{c}, \text{b}} p_l(x) L_l^D(x, \delta^D) L_l^{\text{sec}}(x, \delta^{\text{sec}})}, \quad j = \text{bgd}, \text{b}, \text{c}. \quad (3.10)$$

The functions $L_j^D(x, \delta^D)$ and $L_j^{\text{sec}}(x, \delta^{\text{sec}})$ are the probability density functions for the D jet and the secondary jet for the different samples, $j = \text{bgd}, \text{b}, \text{c}$, calculated from the decay length significance distributions. The functions L_{bgd} are derived from data, as discussed above, while the bottom and charm distributions are taken from Monte Carlo simulation. The functions $p_j(x) = N_j(x)/N_{\text{cand}}(x)$ are the total fractions of the events from the different sources in the candidate sample. These charm and bottom fractions are calculated separately for each channel from lifetime information and jet shape properties in bins of x_D , as described below, and from the probability density functions $L_j^D(x, \delta^D)$ and $L_j^{\text{sec}}(x, \delta^{\text{sec}})$ and also using the output from an artificial neural network analysis based on jet shape information [26].

Treatment of Background

The method used to determine the level of combinatorial background in the sample has been described in section 3.3.1. The background has contributions from events of all five flavours and thus contains also lifetime information as well as typical jet shapes of heavy flavour events. Thus for the purpose of flavour separation not only has the absolute level of background to be known, but also the dependence of the background on the separation variable, that is, on decay length significance or jet shape variables.

Data are used as far as possible to determine the background shapes. In the lifetime analysis an estimator is used which is constructed from a D^{*+} background event tagged by the reflected pion technique discussed in section 3.3.1. To increase the number of candidates an extended window in the mass difference ΔM is used. Secondary vertices are searched for in these events and the resulting decay length significance distributions are used to describe the expected background shape as a function of the decay length significance. In the D^0 and D^+ channels the decay length significance background distributions are calculated in sidebands of M_D , above (for the D^0 and the D^+) and below (for the D^+) the mass of the expected signal. The region below the D^0 mass cannot be used since the decay $D^0 \rightarrow K^- \pi^+ \pi^0$ contributes there. Details of the selection of the samples are given in table 3.6.

The background sample used in the jet shape analysis is based upon a wrong charge technique, where a D^0 candidate is reconstructed with an unphysical charge of ± 2 (e.g. a $K^+ \pi^+$ for

channel	variable	decay length significance		jet shape	
		range	estimator	range	estimator
3 prong satellite	$\Delta M/\text{GeV}$	0.140-0.200	R	0.180-0.200	Q
5 prong semileptonic					
D^0	$\Delta M/\text{GeV}$	0.140-0.220	R	0.190-0.220	Q
	M_{D^0}/GeV	1.95-2.50	S	-	-
D^+	M_{D^+}/GeV	1.75-1.81, 1.93-1.99	S	-	-

Table 3.6: Summary of the different background estimators used in the seven D meson channels. Shown is the variable in which the background is selected, the range over which events are accepted, and the type of estimator used. For the latter, S corresponds to the correct charge selection, in the mass range indicated, Q to the wrong charge one, and R to the reflected pion sample. Estimators are listed for the decay length significance and the jet shape analysis.

the 3 prong channel) by combining tracks appropriately. This is done in sidebands of the ΔM distribution. The reflected pion estimator has been shown in [26] to bias the jet shapes in the secondary jet significantly and therefore is not used. The ranges for the sidebands are given in table 3.6.

Using data estimators for the backgrounds has the advantage that small contributions from partially reconstructed D decays, which are present in all sidebands used, are also present in the background estimator. They therefore do not bias the flavour separation procedure. A Monte Carlo study of the fraction of partially reconstructed D mesons in the signal region compared to the sidebands can be found in [31] for the D^{*+} meson analysis and in [32] for the reconstruction of the D^0 and D^+ mesons.

The distributions obtained for the decay length significance and the jet shape analysis are used to calculate the probability functions for the background, $L_{\text{bgd}}^{D, \text{sec}}$. Monte Carlo studies show that the decay length significance and jet shape analysis output distributions expected for true background events are well reproduced by the distributions obtained in the background tagged samples.

Determination of the Charm and Bottom Fractions

The determination of the fraction of the bottom and charm signal events in the total sample, p_b and p_c , is presented in this section. These fractions are calculated for each channel, separately for each bin of x_D .

In the technique adopted, the bottom fraction in the sample of background subtracted events is determined by counting the number of bottom tags present. If f_b is the fraction of $b\bar{b}$ events in the sample, and if $N_{b\text{-tag}}$ events are tagged by the bottom tagging technique, f_b can be derived from

$$\frac{N_{b\text{-tag}}}{N_{\text{cand}}} = f_b \mathcal{P}_b + (1 - f_b) \mathcal{P}_c \quad (3.11)$$

if the tagging probabilities \mathcal{P}_b and \mathcal{P}_c are known.

The two bottom tagging techniques used are the measurement of the decay length significance and the inclusive jet shape variables mentioned above. In the first method hadronic decays

of the Z^0 into bottom quarks are tagged by taking advantage of the relatively long lifetimes of bottom-flavoured hadrons compared to light-flavoured ones. The decay length significance is measured for the D candidate and for the background sample. The tagging probabilities $\mathcal{P}_{b,c}$ are derived from the decay length significance distributions for $c\bar{c}$ and $b\bar{b}$ events, as found in the Monte Carlo simulation. An event is tagged as a $b\bar{b}$ event if the decay length significance is larger than 8. The procedure is repeated for a value of $\delta = 2, 4$ and 6, and the results are combined taking into account the statistical correlations of the samples. This measurement is performed in both the D jet and the secondary jet and the results are then combined

The second method uses the shapes of jets, which are expected to be significantly different for bottom and charm jets. The shapes are measured by a set of seven jet shape variables, containing combinations of the momenta of the particles in the jets, where both transverse and longitudinal components are used. The shape variables are only calculated for the secondary jet in the event, which does not contain the D meson candidate, since the D meson candidate does introduce a significant bias into the shape of the jet which it belongs to. These variables are used as input to an artificial neural network which has been trained using data and Monte Carlo for b/c separation. A detailed description of the variables and the method may be found in [26, 33]. The tagging probabilities \mathcal{P}_b have been calculated in [26] from data, using samples enriched in bottom decays by the presence of a high momentum lepton. The tagging probabilities for $c\bar{c}$ events, \mathcal{P}_c , have been determined using Monte Carlo simulation. They are calculated for four ranges of the output of the neural network. The number of events found in each range is determined, and the total $b\bar{b}$ fraction calculated. The network was developed for the analysis of D^{*+} decays and is applied to the D^{*+} sample only.

The results of this part of the analysis are the charm fractions in the background subtracted event sample, $f_c(x_D)_{channel}$, determined as a function of the scaled energy for each channel separately. In table 3.7 the charm fractions are given for each channel, combined into two bins of x_D . The systematic errors shown in the table are discussed in detail later. From these numbers of f_c the fraction of charm events in the signal to the total number of events including the background can be derived through the relation $p_{b,c} = f_{b,c} (1 - N_{bgd}/N_{cand})$. The decay length significance and the neural net output distributions are shown in figure 3.3 for the background subtracted candidate sample. The expected distributions for $c\bar{c}$ events are superimposed.

channel	$0.2 < x_D < 0.4$	$x_D > 0.4$
3 prong	$0.258 \pm 0.020 \pm 0.027$	$0.720 \pm 0.017 \pm 0.025$
satellite	$0.358 \pm 0.019 \pm 0.035$	$0.797 \pm 0.015 \pm 0.025$
5 prong	-	$0.841 \pm 0.017 \pm 0.032$
electron	$0.433 \pm 0.038 \pm 0.030$	$0.876 \pm 0.029 \pm 0.024$
muon	$0.306 \pm 0.036 \pm 0.028$	$0.867 \pm 0.029 \pm 0.026$
	$0.3 < x_D < 0.5$	$x_D > 0.5$
D^0	$0.369 \pm 0.034 \pm 0.099$	$0.787 \pm 0.026 \pm 0.108$
D^{*+}	$0.317 \pm 0.060 \pm 0.130$	$0.810 \pm 0.035 \pm 0.077$

Table 3.7: List of charm fractions, f_c , in the different channels with their statistical and systematic errors. The results are shown for two ranges of $x_{D^{*+}}$ to illustrate the increasing charm purity with increasing x_D . Note that the x_D used is the one calculated from the observed tracks, and the same x_D could correspond to a different true scaled energy of the D meson in different channels.

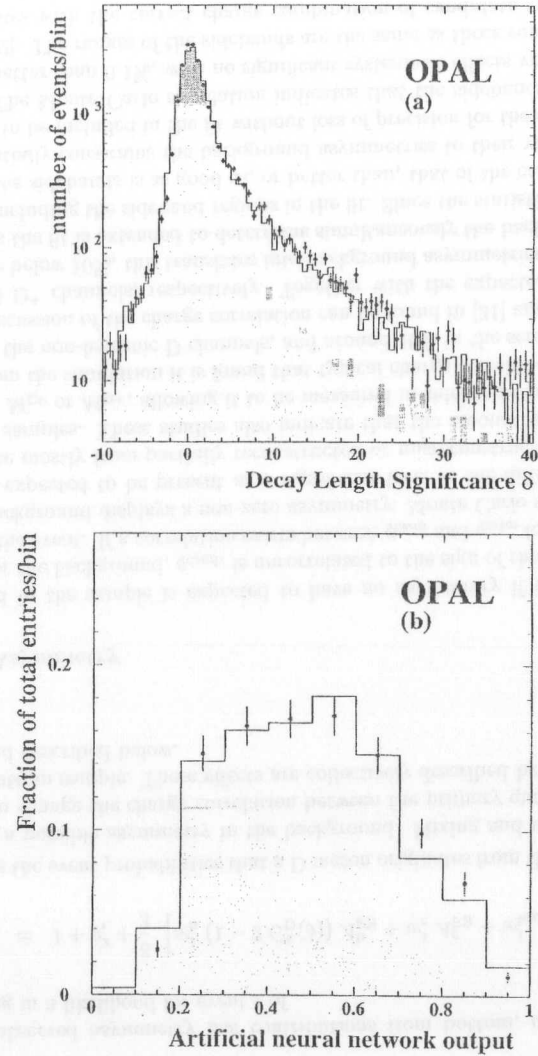


Figure 3.3: (a) Distribution of the decay length significance in data (points with error bars) and Monte Carlo (solid histogram), as reconstructed in the opposite hemisphere from the D^{*+} candidate. The shaded histogram represents the distribution for $c\bar{c}$ events, as calculated in the simulation, and normalised to the measured charm fraction in the sample. (b) Normalised distribution of the neural network output for D^{*+} candidates (points with error bars) and the Monte Carlo distribution for all and $c\bar{c}$ events as in (a).

Calculation of the Event Probabilities

The measurement of the decay length significance for each event is used to determine the probabilities defined in equation 3.10. In addition, the charm and bottom fractions p_c and p_b , derived with b tagging methods as described above are needed to calculate the event probabilities. In nearly all events at least one vertex is reconstructed, either in the D jet or in the secondary jet, from which a valid event probability can be calculated. If no vertex is reconstructed in one of the two jets considered, an event probability is still calculated if the reconstruction was successful in the other jet. If the vertex reconstruction failed in both jets considered, the event based probabilities are replaced by the mean flavour fraction, determined from the $p_j(x)$ only. The fraction of such events is less than 1% of the total sample.

3.3.3 Determination of the Asymmetries

In this section the method used to determine the asymmetries is presented. While the main thrust of the analysis is the measurement of the charm forward-backward asymmetry, a simultaneous fit is done for both bottom and charm. At the same time the method presented allows the measurement of the effective mixing of B mesons applicable to the mixture of B mesons present in this sample of events. The results of the fit are discussed in section 3.3.3.

The Likelihood Function

The forward-backward asymmetry is defined as

$$A_{\text{FB}} = \frac{\int_0^1 \frac{d\sigma}{dy} dy - \int_{-1}^0 \frac{d\sigma}{dy} dy}{\int_0^1 \frac{d\sigma}{dy} dy + \int_{-1}^0 \frac{d\sigma}{dy} dy} \quad (3.12)$$

where y is the cosine of the polar angle of the outgoing fermion direction with respect to that of the incoming fermion. In events containing a D meson, the direction y is approximately described by $y = q \cos(\theta_{\text{thrust}})$, where q is the sign of the charge of the D meson⁷, and θ_{thrust} is the angle of the thrust axis with respect to the electron beam. The orientation of the thrust axis is chosen such that the scalar product of the thrust axis with the D direction is positive.

The asymmetries are determined in an unbinned log-likelihood fit to the y distribution. The likelihood function has the form⁸

$$\log \mathcal{L} = \sum_i \log \mathcal{L}_i = \sum_i \log(1 + y_i^2 + \frac{8}{3} A_{\text{FB}}^{\text{obs}} y_i) - \sum_i \log N_{\text{norm}}^i, \quad (3.13)$$

where the sum runs over all candidates i . The normalisation is given by

$$N_{\text{norm}}^i = \int_{-1}^1 dy \alpha(y) \cdot (1 + y^2 + \frac{8}{3} A_{\text{FB}}^{\text{obs}} y), \quad (3.14)$$

⁷The charge of the D meson is defined as the sign of the charge of the charm quark in the quark model for the meson.

⁸Here the longitudinal component of the differential cross-section has been neglected. The correct expression for the differential cross-section is given in equation 3.1. The effects caused by this approximation are discussed in section 3.4.

where $\alpha(y)$ is the acceptance as a function of y . From this normalisation factor N_{norm} solely the term

$$\int_{-1}^1 dy \frac{8}{3} A_{\text{FB}}^{\text{obs}} y$$

depends on the fit parameter. This term vanishes for an acceptance which is symmetric in y and the normalisation does not contribute to the maximisation of the likelihood. Therefore the acceptance is dropped from the further discussion.

The total observed asymmetry has contributions from bottom, charm and background events, resulting in a likelihood for event i of

$$\mathcal{L}_i = 1 + y_i^2 + \frac{8}{3} \left[w_b^i (1 - 2 C_D^i(\delta)) A_{\text{FB}}^b + w_c^i A_{\text{FB}}^c + w_{\text{bgd}}^i A_{\text{FB}}^{\text{bgd}} \right] y_i. \quad (3.15)$$

Here $w_{\text{bgd},b,c}^i$ are the event probabilities that a D meson originates from the source indicated and $A_{\text{FB}}^{\text{bgd}}$ allows for a possible asymmetry in the background. Mixing and non-prompt production of D mesons can change the charge correlation between the primary quark and the detected D meson in the bottom sample. These effects are collectively described by the charge correlation factor $C_D^i(\delta)$ and described below.

Background Asymmetry

The background in the sample is expected to have no asymmetry if the sign of the charge reconstructed for the background, q_{cand} , is uncorrelated to the sign of the charge of the primary quark, q_{prim} , in the event. If a correlation exists between q_{cand} and q_{prim} for a significant fraction of events, the background displays a non-zero asymmetry. Monte Carlo studies show that such correlations are expected to be present at a significant level in the different channels. These correlations come mostly from partially reconstructed or misreconstructed D meson decays in the background samples. These studies also indicate that the amount of correlation does not depend on ΔM , M_{D^0} or M_{D^+} , allowing it to be measured in sidebands in ΔM , M_{D^0} and M_{D^+} , respectively. From the simulation it is found that typical charge correlations are of the order of a few percent in the non-leptonic D channels, and around 10% in the semileptonic channels. A more detailed discussion of the charge correlation can be found in [31] and [32] for the D^{*+} and inclusive D^0 and D^+ channels, respectively. Together with the expected asymmetries for $q\bar{q}$ events, which are below 10%, this translates into background asymmetries of typically less than 1%. Nevertheless the fit is extended to determine simultaneously the background asymmetries. This is done by including the sideband regions in the fit. Since the statistical significance of the events found in the sidebands is as good as, or better than, that of the candidates in the signal region, this essentially constrains the background asymmetries to their values in the sideband, and allows them to be included in the fit without loss of precision for the $c\bar{c}$ and $b\bar{b}$ asymmetry determination. The Monte Carlo simulation indicates that the sidebands describe the charge asymmetries to better than 0.1%, with no significant systematic effects visible. The details can be found in [31,32]. The ranges of the sidebands are the same as those summarised in table 3.6, but only candidates with the correct charge combination of candidate tracks are used in the estimation.

Determination of C_D in $b\bar{b}$ Events

The correlation between the charge of the detected D meson and the charge of the produced quark in $b\bar{b}$ events can be changed by two basic processes: mixing in the neutral B sector and the production of a D meson in $b \rightarrow (c\bar{s})c$, where the reconstructed D meson contains the charm quark produced from the virtual W. The amount of charge correlation from $B^0-\bar{B}^0$ mixing depends on the proper decay time of the B meson, whereas the correlation introduced from the second process does not. Small effects are also expected from $B_s^0-\bar{B}_s^0$ mixing. In the following paragraphs the method of measuring the amount of events with reversed charge correlation as a function of the decay length significance is described.

The probability $P(t)$ to find a \bar{B}_d^0 meson at proper time t after a B_d^0 meson is produced and thereby the contribution to C_D from $B^0-\bar{B}^0$ mixing is expected to follow [34]

$$P(t) = \sin^2\left(\frac{\Delta m_d \cdot t}{2}\right), \quad (3.16)$$

where Δm_d is the mass difference of the mass eigenstates of the \bar{B}_d^0 system. Because of the very fast oscillations of the B_s^0 system the effects from the $B_s^0-\bar{B}_s^0$ system are expected to show no time dependence, within the time resolution measurable with the detector.

Since in this analysis the lifetime information in the D hemisphere is used to help separating $b\bar{b}$ and $c\bar{c}$ events, C_D has to be known as a function of the decay length significance. Events with a large measured decay length significance are likely to be b events, and therefore will enter in the fit with a large probability to be a bottom event. Such events are also more likely to have undergone mixing, and have consequently a different charge correlation between the primary b and the tagged D meson. Therefore the appropriate charge correlation factor C_D for a certain measured decay length significance has to be used in the likelihood fit.

The charge correlation in $b\bar{b}$ events is directly measured in the sample of D^{*+} mesons used for the asymmetry fit. For this part of the analysis only D^{*+} mesons are used because of their lower background level compared to the D^0 and D^+ channels. The charge correlation is measured by comparing charges in both hemispheres of the event, where the charge information from the reconstructed D^{*+} meson is used in one hemisphere, and a jet-charge technique in the other hemisphere. For events, where for example the \bar{B}^0 meson decays directly after production into a D meson, the charge of the jet-charge measurements in one hemisphere corresponds to the same charge of the D meson in the opposite hemisphere, as determined from the decay products of the D decay. This is illustrated in figure 3.4 a). On the other hand, if the \bar{B}^0 meson is transformed into a B^0 meson by mixing, then the charge of the D meson is opposite to the measured jet-charge, as is depicted in figure 3.4b). Thus the charge correlation can be calculated from the ratio of events with opposite charges in both hemispheres to the total number of events. It is determined as a function of the decay length significance of the D candidate and, following equation 3.16, parametrised by a function of the form

$$C_D'(\delta) = a' + b' \sin^2(\nu\delta), \quad (3.17)$$

where a' , b' and ν are determined in a fit. The corresponding charge correlation function

$$C_D(\delta) = a + b \sin^2(\nu\delta) \quad (3.18)$$

with parameters a and b is diluted by the imperfect measurement of the jet-charge. $C_D(\delta)$ can be interpreted as the fraction of D^{*+} mesons with opposite charge correlation. This fraction will

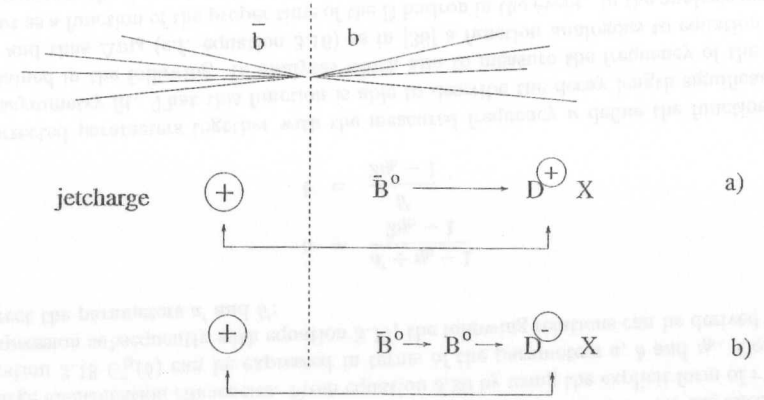


Figure 3.4: Sketch of the method of determining $C_D(\delta)$. The charges of the D decay products are compared to the jet-charge measurement in the second hemisphere.

be denoted by r^{+-} in the following. $C_D(\delta)$ is calculated from C_D' in equation 3.17 by correcting for the probability for a correct jet charge identification.

Equation 3.17 also has contributions from the background and from $c\bar{c}$ events. The charm background is suppressed by considering only events with $x_{D^{*+}} < 0.4$ for this part of the analysis, resulting in a bottom fraction of about 66.5% of the D^{*+} signal. In the following the details of this charge correlation analysis and the treatment of the different backgrounds are discussed in more detail.

Measurement of Jet-Charge Identification Probabilities The jet-charge used is defined as a momentum weighted sum over the charges of the tracks in the hemisphere⁹ considered [35]:

$$Q_{jet} = \frac{\sum_i^N |p_{||i}|^\kappa q_i}{\sum_i^N |p_{||i}|^\kappa}, \quad (3.19)$$

where the sum runs over the N charged tracks of the hemisphere, $p_{||i}$ is the momentum component of the track i along the thrust axis, q_i is the charge of track i and κ is a parameter which defines a momentum weighting for each particle. The weight factor optimal for the identification of the primary quark charge in the event has been determined to be $\kappa = 0.3$ [14, 32]. In figure 3.5 the probability to identify the flavour of the primary quark correctly is shown as a function of the weight factor κ for bottom and charm quarks as determined from the Monte Carlo. The value chosen is a compromise between an efficient charge identification for bottom and charm events. The sign of the jet-charge Q_{jet} is used to reconstruct the charge of the hemisphere.

⁹a more proper name would thus be 'hemisphere charge'.

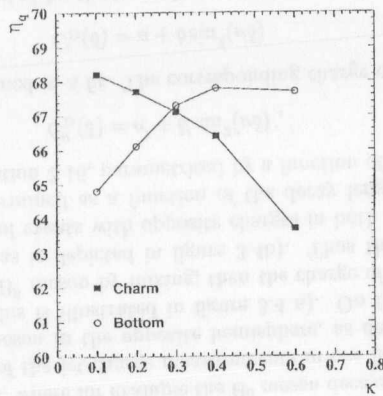


Figure 3.5: The jet-charge identification probability η_q for bottom and charm quarks as a function of the weight factor κ as determined from the Monte Carlo.

The jet-charge identification probability η_j for the different flavours j is defined as the fraction of events where the charge of the primary quark is correctly identified. The jet-charge identification probabilities for charm and bottom events are measured in data with event samples enriched in the different flavours.

A highly enriched sample of bottom decays is selected by identifying leptons with high momentum, p , and high momentum transverse to the jet direction, p_t , opposite to the hemisphere where the jet-charge is determined. The b purity of the lepton sample is $(91.2 \pm 2.0)\%$ [29] for the selection cuts of $p > 2$ GeV and $p_t > 1.3$ GeV for electron candidates, and $p > 3$ GeV and $p_t > 1.5$ GeV for muon candidates. From this the jet-charge identification probability in $b\bar{b}$ events is determined to be $\eta_b = 0.642 \pm 0.003 \pm 0.013$ where the first error is statistical and the second systematic. The systematic error is dominated by the errors on the bottom purity of the sample and the charm background.

Decays of the Z^0 into $c\bar{c}$ pairs are selected by requiring a reconstructed D^{*+} meson in one of the five channels in the opposite hemisphere with a large scaled energy $x_{D^{*+}} > 0.7$. About 3500 candidate events are selected. This sample is found to have a signal purity of $(72.4 \pm 1.1)\%$ and a charm purity of the D^{*+} signal events of $(96.9 \pm 0.4 \pm 2.0)\%$ (c.f. section 3.3.2). From this the jet-charge identification probability in $c\bar{c}$ events is determined to be $\eta_c = 0.699 \pm 0.010 \pm 0.012$, where the first error is statistical and the second systematic. Possible charge correlations in the background are corrected for by repeating the analysis in the sidebands of the ΔM distributions, analogous to the method described in the paragraph about the background asymmetry in this section. The main systematic error is due to the charm purity of the sample, and possible differences between the charge correlation of the background and the sidebands.

Determination of $C_D(\delta)$ The data sample of identified D^{*+} mesons with $x_{D^{*+}} < 0.4$ is divided into two samples, a like sign sample, where the sign of the reconstructed D meson is

equal to that of the jet-charge, and an unlike sign sample. If the charge of the primary quark is correctly tagged by the jet-charge, mesons produced in $b \rightarrow (\bar{c}s)c$ decays, and those produced in B decays where the B meson had mixed before decaying, would contribute to the unlike sign sample. Unmixed events would contribute to the like sign sample.

In the sample contributions are present from a variety of background processes. The combinatorial background has been measured as described in section 3.3.1 and is given in table 3.5. The remaining charm contribution in the signal of the sample considered here ($x_{D^{*+}} < 0.4$) has been measured as described in section 3.3.2 and found to be $(34.5 \pm 0.8 \pm 2.5)\%$. These two background sources are subtracted on a statistical basis from the sample. Firstly the combinatorial background is subtracted as a function of the decay length significance. The shape of this background is estimated using the same sideband tagged events as estimator as discussed in section 3.3.3. Secondly, the charm background is subtracted with the decay length significance distributions taken from Monte Carlo simulation, after taking the jet-charge identification probability for charm into account. The resulting decay length significance distributions contain only $b\bar{b}$ events. They are derived for both unlike sign events and for all candidates. The total fraction of unlike sign events in the b sample at decay length significance δ can be written as :

$$\frac{N_b^{\text{unlike}}(\delta)}{N_b^{\text{all}}(\delta)} = \eta_b r^{+-}(\delta) + (1 - \eta_b)(1 - r^{+-}(\delta)) = C'_D(\delta). \quad (3.20)$$

Here η_b denotes the jet-charge identification probability, and r^{+-} is the fraction of D^{*+} mesons with opposite charge correlation, i.e. where the B meson had undergone mixing or the D^{*+} meson has been produced with the wrong sign in a bottom decay $b \rightarrow (\bar{c}s)c$.

The ratio of unlike sign to all events as a function of the decay length significance is fitted with the function $C'_D(\delta)$ in equation 3.17. Free parameters in the fit are the offset a' , the amplitude b' and the frequency ν .

The variables a' and b' depend on the fraction of D^{*+} mesons originating from $b \rightarrow (\bar{c}s)c$ decays, B^0 , B_s^0 and charged B mesons. In addition experimental resolution effects both from the jet-charge reconstruction and from the decay length significance reconstruction influence these parameters. The measured parameters a' and b' have to be corrected for the effects of the jet-charge identification efficiencies. From equation 3.20 by using the explicit form of r^{+-} given in equation 3.18 $C'_D(\delta)$ can be expressed in terms of the parameters a , b and η_b . Comparing this expression subsequently with equation 3.17, the following relations can be derived in order to correct the parameters a' and b' :

$$\begin{aligned} a &= \frac{a' + \eta_b - 1}{2\eta_b - 1} \\ b &= \frac{b'}{2\eta_b - 1}. \end{aligned} \quad (3.21)$$

The corrected parameters together with the measured frequency ν define the function $C_D(\delta)$ in the asymmetry fit. That this function is able to describe the decay length significance will be explained in the following. In analyses which aim to measure the frequency of the $B^0 - \bar{B}^0$ mixing and thus Δm_d (c.f. equation 3.16) as in [36] a function analogous to equation 3.17 is used, but as a function of the proper time of the B hadron in the event. In the analysis presented here in contrast the decay length significance is used since this is the variable which enters the asymmetry fit. Although here the interpretation of the results are different than in the analyses

of the $B^0-\bar{B}^0$ mixing frequency, Monte Carlo studies show that equation 3.17 still provides a good description of the decay length significance dependence of the charge correlation. Using the bare decay length would modify the functional form of equation 3.17 due to the neglect of the boost of the meson compared to the use of the proper time. In the decay length significance, however, the boost enters implicitly in the decay length error. For an event with a large boost the measurement of the decay length is usually relatively poor due to the small opening angle of the vertex tracks. The physical interpretation of the parameters a and b is as follows. The time independent components of the charge correlation factor $C_D(\delta)$ are absorbed in the parameter a . b denotes the ‘amplitude’ of the oscillation and therefore reflects the relative contribution of time-dependent components in the sample, i.e. the B_d^0 amount in the mixture of B_d^0 , B^+ , B_s^0 and $b \rightarrow (\bar{c}s)c$ decays. The total fraction of unlike sign events can be expressed in terms of wrong sign events in a $b \rightarrow (\bar{c}s)c$ decay $N^{\bar{c}}$, contributions from $B_s^0-\bar{B}_s^0$ mixing $N^{B_s^0}$, and events which have undergone $B^0-\bar{B}^0$ mixing N^{B^0} , according to

$$C'_D = \frac{N_b^{\text{unlike}}}{N_b^{\text{all}}} = 1 - \eta_b + (2\eta_b - 1) \left(\frac{0.5N^{B_s^0} + N^{\bar{c}}}{N_b^{\text{all}}} \right) + (2\eta_b - 1) \frac{N^{B_d^0}}{N_b^{\text{all}}} \sin^2(\nu\delta). \quad (3.22)$$

The contribution from $B_s^0-\bar{B}_s^0$ mixing enters with a factor 1/2, because of the very fast oscillation of the B_s system. The lifetime of the B_s mesons is much smaller than the oscillation frequency and therefore half of the events have undergone mixing.

The distribution of the ratio of unlike sign to all events as a function of the decay length significance is shown in figure 3.6 after subtraction of the combinatorial background and the charm fraction of the signal. The dependence of this ratio on the decay length significance is clearly visible. The fit yields

$$\begin{aligned} a' &= 0.401 \pm 0.016 \\ b' &= 0.177 \pm 0.070 \\ \nu &= 0.023 \pm 0.007 \end{aligned} \quad (3.23)$$

and the result is superimposed on the plot. From that the parameters a and b can be derived according to equation 3.21 to be

$$\begin{aligned} a &= 0.151 \pm 0.064 \\ b &= 0.623 \pm 0.253. \end{aligned} \quad (3.24)$$

The errors given in equations 3.23 and 3.24 combine the statistical and the systematic component.

To compare the result of the fit with other related measurements of the mixing in the neutral B system, the effective mixing parameter χ_{eff} is derived from the fitted parameters a , b and ν . This effective mixing parameter takes into account the fact that D^{*+} samples are produced in a mixture of B^0 , B^+ , B_s^0 and $b \rightarrow (\bar{c}s)c$ decays. It is found to be $\chi_{\text{eff}} = (19.1 \pm 8.3)\%$. Moreover, the effective mixing can be determined from the individual mixing in each component and the relative importance of the different contributions. In [31, 37] the same quantity is estimated from other measurements quoted in [30] to be $\chi_{\text{eff}} = (17.8 \pm 4.3)\%$. Both results are in good agreement. Note, however, that in this asymmetry analysis no knowledge of the actual physical mixing parameter χ_{eff} is needed.

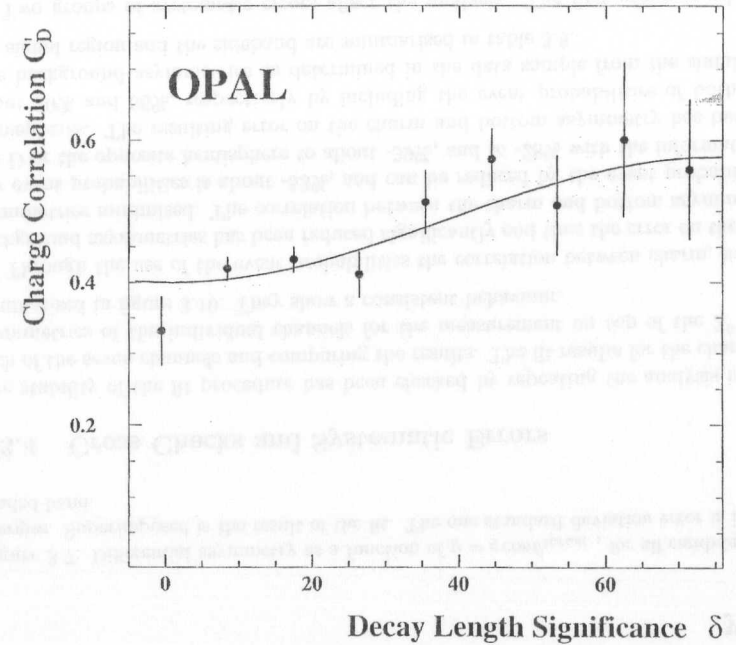


Figure 3.6: The ratio of unlike sign to all events, after background subtraction, as a function of the decay length significance. Superimposed is the fitted function C'_d with its error band.

The relative fractions of D^0 or D^+ mesons produced in B^0 and B_s^0 meson decays are different from that of D^{*+} mesons. This is mostly due to the different dominant spectator diagrams and, in addition, due to the decay chains of D^{*+} and D^{*0} mesons into D^0 and D^+ mesons¹⁰. These differences have been estimated in [32]. Comparing equation 3.22 with equation 3.17 and replacing the D^{*+} fractions by the corresponding D^0 or D^+ values, the factors a and b can be calculated for D^0 or D^+ mesons to be

$$\begin{aligned} a_{D^0} &= 0.151 \pm 0.064, & a_{D^+} &= 0.163 \pm 0.069 \\ b_{D^0} &= 0.235 \pm 0.095, & b_{D^+} &= 0.584 \pm 0.237. \end{aligned} \quad (3.25)$$

The decay length significance dependence of the charge correlation $C_D(\delta)$ is assumed to be the same as that for D^{*+} mesons. Because of the lifetime cut applied for the reconstruction of D^0 and D^+ mesons (c.f. section 3.3.1) in order to reduce the background, the probability for a selected event for having undergone mixing before decaying is enhanced. The numbers given in equation 3.25 are corrected for this effect and the errors include the systematic uncertainties.

¹⁰ $Br(D^{*+} \rightarrow D^0 X) = (68.1 \pm 1.3)\%$ and $Br(D^{*0} \rightarrow D^0 X) = 100\%$ (c.f. [38])

For a comparison with the numbers of the D^{*+} sample, the effective mixing for the D^0 tagged sample is estimated to be $\chi_{eff} = (8.0 \pm 4.4)\%$ and for the D^+ sample $\chi_{eff} = (19.4 \pm 8.4)\%$.

Results of the Asymmetry Fit

The samples collected on, below and above the peak of the Z^0 resonance have been fitted to determine A_{FB}^c and A_{FB}^b . The final probability density function used to construct the likelihood is given by equation 3.15. The bottom asymmetry, the charm asymmetry and the background asymmetries are free parameters in the fit. The latter are allowed to vary independently in each of the seven channels considered. It should be noted that the background asymmetries are nearly completely determined from the sidebands, and are very much decoupled from the charm and bottom asymmetries. Typical correlations between the background asymmetries and the charm or bottom asymmetries are below 10%.

The results of the fits are

$$\begin{array}{lll} A_{FB}^c = 0.039 \pm 0.051 & A_{FB}^b = -0.086 \pm 0.108 & \langle E_{cm} \rangle = 89.45 \text{ GeV} \\ A_{FB}^c = 0.063 \pm 0.012 & A_{FB}^b = 0.094 \pm 0.027 & \langle E_{cm} \rangle = 91.22 \text{ GeV} \\ A_{FB}^c = 0.158 \pm 0.041 & A_{FB}^b = -0.021 \pm 0.090 & \langle E_{cm} \rangle = 93.00 \text{ GeV}, \end{array}$$

with a statistical correlation coefficient between the bottom and charm asymmetry of -0.281 on-peak (-0.272 and -0.273 for the low and high energy off-peak points, respectively). The centre-of-mass energies indicated are event weighted averages of the appropriate off-peak and on-peak points [39].

The result of the fit for the on-peak data is illustrated in figure 3.7, where the differential asymmetry, $\Delta A_{FB} = (n(y) - n(-y))/(n(y) + n(-y))$ is shown as a function of y , and $n(\pm y)$ are the number of candidates in the forward (backward) y hemisphere. The results are plotted as a function of the centre of mass energy in figure 3.8. Also shown is the standard model prediction evaluated using the ZFITTER program model [3] for a top mass of 174 GeV [30] and a Higgs mass of 100 GeV. The correlation between A_{FB}^c and A_{FB}^b is illustrated in figure 3.9, together with the predictions of the standard model shown for the asymmetries on the peak of the Z^0 resonance.

The fit has been repeated with the bottom asymmetry set to its standard model expectation obtained for a Higgs mass of 300 GeV and a top mass of 180 GeV. The results of the fits for the charm asymmetry are then

$$\begin{array}{ll} A_{FB}^c = 0.020 \pm 0.049 & \langle E_{cm} \rangle = 89.45 \text{ GeV} \\ A_{FB}^c = 0.064 \pm 0.012 & \langle E_{cm} \rangle = 91.22 \text{ GeV} \\ A_{FB}^c = 0.139 \pm 0.039 & \langle E_{cm} \rangle = 93.00 \text{ GeV} \end{array}$$

in good agreement with the two parameter fit.

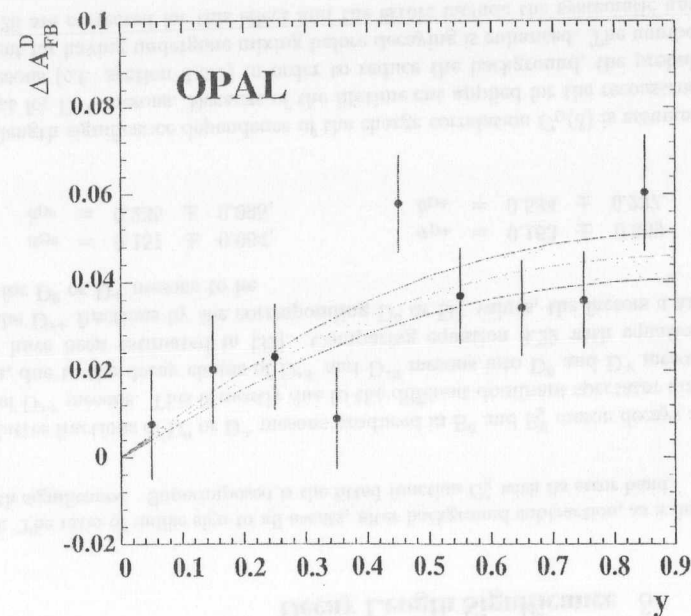


Figure 3.7: Differential asymmetry as a function of $y = q \cos \theta_{thrust}$, for all candidates, for on peak energies. Superimposed is the result of the fit. The one standard deviation error is indicated by the shaded band.

3.3.4 Cross Checks and Systematic Errors

The stability of the fit procedure has been checked by repeating the analysis individually for each of the seven channels and comparing the results. The fit results for the charm and bottom asymmetries of the individual channels for the measurement on top of the Z^0 -resonance are summarised in figure 3.10. They show a consistent behaviour.

Through the use of the event probabilities the correlation between charm, bottom and the background asymmetries has been reduced significantly and thus the error on the heavy flavour asymmetries minimised. The correlation between the charm and bottom asymmetries without any event probabilities is about -53% , and can be reduced by the event probabilities of either the D or the opposite hemisphere to about -39% , and to -28% with the information from both hemispheres. The resulting error on the charm and bottom asymmetry has been reduced by about 20% and 36%, respectively by including the event probabilities of both hemispheres. The background asymmetries as determined in the data sample from the simultaneous fit to the signal region and the sideband are summarised in table 3.8.

Two groups of systematic errors affect the analysis. The first group is related to errors specific to this analysis and the determination of the asymmetry. The second group concerns errors related to the separation of the sample into its bottom and charm components. A more detailed description of the errors relating to the determination of the charm fraction can be

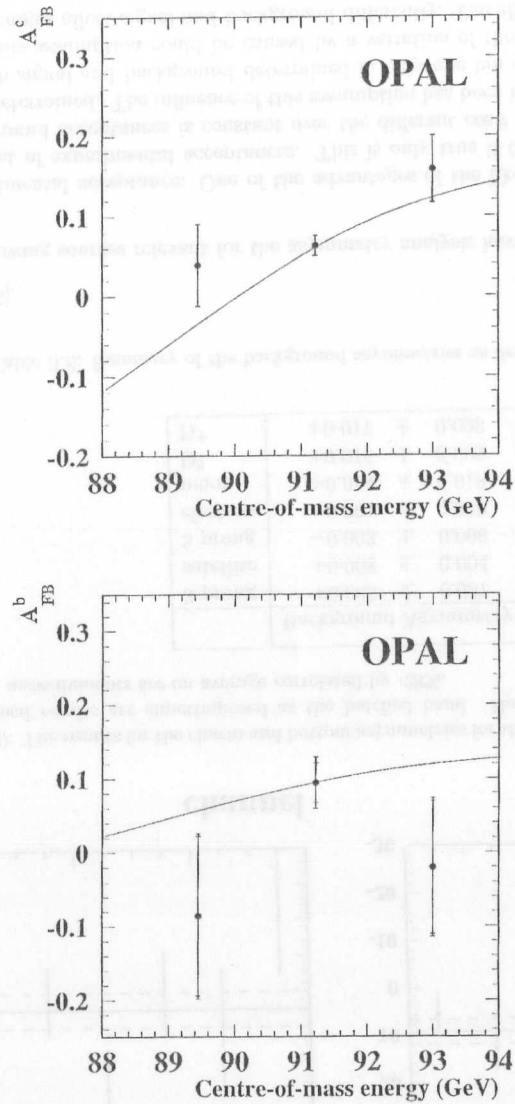


Figure 3.8: Results for the b and c asymmetries at energies on and around the pole of the Z resonance. The curve shown is the prediction of the standard model for a Higgs mass of 100 GeV and a top mass of 174 GeV. The inner error bars are the statistical errors, the outer ones the total error.

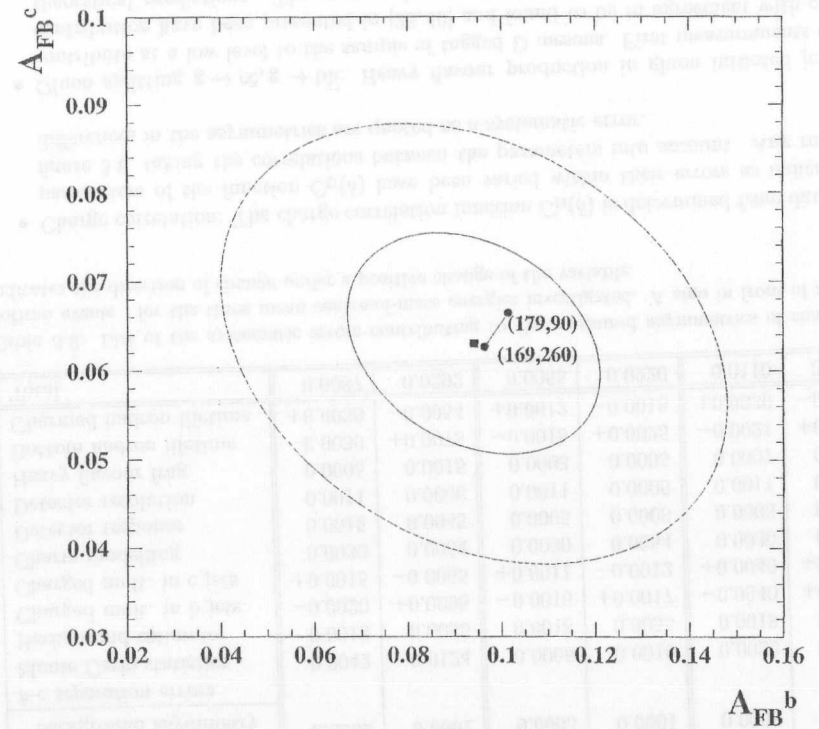


Figure 3.9: Comparison of the measured b and c asymmetries on the peak of the Z resonance with the Standard Model prediction for a range of top and Higgs masses. The top mass is measured [2] to be (174.1 ± 4.1) GeV and is varied within its errors. The central value is indicated by the square, the inner and outer contours correspond to 39% and 86% probability, respectively. The line shown illustrates the standard model predictions for the values (m_{top}, m_{higgs}) shown.

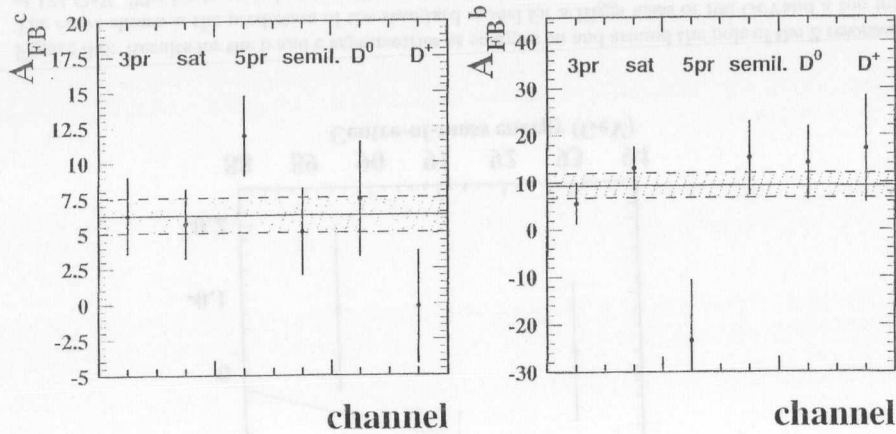


Figure 3.10: The results for the charm and bottom asymmetries for the individual channels in percent. The combined results are superimposed as the hatched band. Note that the charm and bottom asymmetry measurements are on average correlated by -28% .

	Background Asymmetry
3 prong	$+0.008 \pm 0.007$
satellite	$+0.008 \pm 0.004$
5 prong	-0.003 ± 0.006
electron	-0.001 ± 0.019
muon	$+0.014 \pm 0.018$
D^0	$+0.015 \pm 0.009$
D^+	$+0.017 \pm 0.008$

Table 3.8: Summary of the background asymmetries as determined in the fit.

found in [26].

The following sources relevant for the asymmetry analysis have been considered:

- **Experimental acceptance:** One of the advantages of the likelihood fit is that it is independent of experimental acceptances. This is only true if the ratio between signal and background acceptances is constant over the different $\cos\theta$ regions for which they have been determined. The influence of this assumption has been investigated by repeating the fit with signal and background determined in only one bin of $\cos\theta$. Possible deviations from this assumption could be caused by a variation of the mass resolution with $\cos\theta$, which might affect signal and background differently. The effect is found to be small.
- **Background level:** Uncertainties in the background fraction can introduce a bias in the asymmetry. This has been investigated by varying the background fractions within their systematic errors or $\pm 3\%$, as given in [26].

$\langle E_{cm} \rangle$	89.45 GeV		91.22 GeV		93.00 GeV	
	$\Delta(A_{FB}^c)$	$\Delta(A_{FB}^b)$	$\Delta(A_{FB}^c)$	$\Delta(A_{FB}^b)$	$\Delta(A_{FB}^c)$	$\Delta(A_{FB}^b)$
<i>General errors</i>						
same acceptance for background and signal	0.0009	0.0028	0.0009	0.0028	0.0009	0.0028
Background level	0.0038	0.0101	0.0014	0.0062	0.0038	0.0113
Charge correlation	0.0010	0.0164	0.0010	0.0186	0.0028	0.0037
$g \rightarrow c\bar{c}, b\bar{b}$	+0.0002	-0.0034	+0.0020	+0.0034	+0.0050	-0.0001
Background asymmetry	0.0010	0.0023	0.0010	0.0023	0.0010	0.0023
x_D dependence of background asymmetry	0.0002	0.0001	0.0003	0.0001	0.0008	0.0001
<i>b-c separation errors</i>						
Monte Carlo statistics	0.0042	0.0124	0.0005	0.0010	0.0022	0.0130
Background estimator	0.0018	0.0055	0.0018	0.0055	0.0018	0.0055
Charged mult. in b jets	-0.0020	+0.0095	-0.0016	+0.0017	-0.0040	+0.0100
Charged mult. in c jets	+0.0015	-0.0065	+0.0011	-0.0012	+0.0040	+0.0100
Charm modelling	0.0030	0.0054	0.0030	0.0054	0.0030	0.0054
Detector response	0.0015	0.0045	0.0005	0.0006	0.0008	0.0022
Detector resolution	0.0011	0.0006	0.0011	0.0006	0.0011	0.0006
Heavy flavour frag.	0.0005	0.0015	0.0003	0.0005	0.0007	0.0015
Bottom hadron lifetime	-0.0030	+0.0075	-0.0015	+0.0025	-0.0021	+0.0072
Charmed hadron lifetime	+0.0030	-0.0054	+0.0012	-0.0018	+0.0030	-0.0054
Total	0.0087	0.0292	0.0055	0.0220	0.0110	0.0259

Table 3.9: List of the systematic errors contributing to the measured asymmetries of charm and bottom events, for the three mean centre-of-mass energies investigated. A sign in front of an error indicates the direction of change under a positive change of the variable.

- **Charge correlation:** The charge correlation function $C_D(\delta)$ is determined from data. The parameters of the function $C_D(\delta)$ have been varied within their errors as indicated in figure 3.6, taking the correlations between the parameters into account. Any resulting differences in the asymmetries are quoted as a systematic error.
- **Gluon splitting $g \rightarrow c\bar{c}, g \rightarrow b\bar{b}$:** Heavy flavour production in gluon initiated jets will contribute at a low level to the sample of tagged D mesons. First measurements of this contribution have been presented in [26, 40] and found to be in agreement with current theoretical predictions. The measured rate of $c\bar{c}$ production from gluon splitting per hadronic event is $n_{g \rightarrow c\bar{c}} = (2.38 \pm 0.48)\%$. Systematic errors on the charm and bottom asymmetries have been calculated by assuming that all events originating from gluon splitting were assigned by the b/c separation to be $c\bar{c}$ events or $b\bar{b}$ events, respectively. The measured asymmetries have not been corrected explicitly for the effects of gluon splitting, because the event probabilities do not provide a clear assignment of these events to a specific flavour. By applying the lifetime method to the D jet, these events will most probably be counted as charm events, whereas the lifetime information in the secondary jet will preferentially assign them to the primary event flavour.
- **Background asymmetries:** The determination of the background asymmetries depends

on the assumption that the sidebands correctly reproduce the charge correlation present in the true background. This assumption has been checked in the simulation. Typical charge correlations are found to be of the order of a few percent, and differences between sideband and true background below 0.1%. The observed differences are used to estimate the systematic errors from this source.

- x_D dependence of the background asymmetries: A possible bias in the background asymmetries as a function of x_D has been investigated by splitting the background samples into two bins of x_D and repeating the fit. The difference has been assigned as the systematic error. Its size is also consistent with Monte Carlo studies.

The errors considered in connection with the flavour separation are:

- Monte Carlo statistics: The determination of the tagging probabilities relies partially on Monte Carlo simulation. An error arises owing to the limited statistics of the Monte Carlo available.
- Background estimators: Some differences may exist between the true background and the background estimators used. This has been estimated in Monte Carlo by repeating the fit with the true background.
- Heavy flavour multiplicity: The multiplicity for heavy flavour decays in the Monte Carlo has been varied by reweighting simulated events, corresponding to the current experimental uncertainties of ± 0.5 tracks in $b\bar{b}$ events and ± 0.2 tracks in $c\bar{c}$ events [41]. The systematic errors of the off-peak measurements are greater because they contain a statistical component.
- Charm modelling: The modelling of the shape of charm jets, their multiplicities and momentum flow, is another important source of systematic error in the jet shape analysis. This error also includes effects due to possible differences between data and simulation in the decay length distribution of jets originating from charm quark decays, not already covered by the other charm modelling error. This latter part of the error has been calculated by repeating the analysis after determining the charm decay length distribution nearly entirely from data. This is possible, since the decay length significance distribution of the candidates, of the background and of the bottom jets are known. The observed differences in the asymmetries are used as systematic errors.
- Detector response: Non-uniformity of the detector response as a function of $\cos\theta$ gives rise to this error. This error is present only in the jet shape analysis.
- Detector resolution: The resolution of the track parameters in the Monte Carlo is varied by $\pm 5\%$.
- Heavy flavour fragmentation: The parameters for the charm and bottom fragmentation function are varied within their experimental limits [41] of $\epsilon_c = 0.035 \pm 0.009$ and $\epsilon_b = 0.0024^{+0.0023}_{-0.0006}$.
- Bottom hadron lifetime: The B-hadron lifetime used in the Monte Carlo samples has been varied within its current experimental error. For the flavour separation performed in the hemisphere opposite to the D mesons, the mean lifetime of bottom hadrons as measured

at LEP has been varied by ± 0.021 ps. In the D hemisphere, the individual B hadron lifetimes have been varied independently by ± 0.07 ps for the B^+ , ± 0.08 ps for the B^0 , and ± 0.12 ps for the B_s^0 [30].

- Charm lifetime: The lifetime of the weakly decaying charm hadrons D^0 and D^+ has been varied independently by ± 0.004 ps for the D^0 , and ± 0.015 ps for the D^+ [30].

A list of all systematic errors considered is given in table 3.9.

3.3.5 Results and Summary

The forward-backward asymmetries of the processes $e^+e^- \rightarrow c\bar{c}$ and $e^+e^- \rightarrow b\bar{b}$ have been measured using 32634 ± 200 D^{*+} , D^0 and D^+ candidate events containing 28261 signal events on the peak of the Z^0 resonance, 1762 events below and 2611 above the peak of the resonance. The results of the fits with both the b and the c asymmetries as free parameters are

$$\begin{aligned} A_{FB}^c &= 0.039 \pm 0.051 \pm 0.009 & A_{FB}^b &= -0.086 \pm 0.108 \pm 0.029 & \langle E_{cm} \rangle &= 89.45 \text{ GeV} \\ A_{FB}^c &= 0.063 \pm 0.012 \pm 0.006 & A_{FB}^b &= 0.094 \pm 0.027 \pm 0.022 & \langle E_{cm} \rangle &= 91.22 \text{ GeV} \\ A_{FB}^c &= 0.158 \pm 0.041 \pm 0.011 & A_{FB}^b &= -0.021 \pm 0.090 \pm 0.026 & \langle E_{cm} \rangle &= 93.00 \text{ GeV} \end{aligned}$$

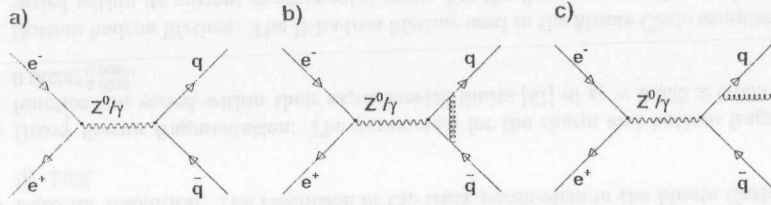
with a statistical correlation coefficient between the bottom and charm asymmetry of -0.281 on-peak (-0.272 and -0.273 for the low and high energy off-peak points, respectively). These results are in good agreement with the OPAL measurements using high momentum leptons [29] and other measurements at LEP [42].

3.4 QCD Corrections

In order to interpret the measurements of the forward-backward asymmetries in terms of the Standard Model, the elementary electroweak process has to be separated from the effects of the strong interaction in the final state, as already mentioned in the beginning of this chapter. Analytical calculations for the QCD effects of the asymmetries are available in first order and as a second order estimate. The results of these calculations, however, cannot directly be applied to the measurements, because the amount of QCD corrections actually seen in the analysis depends significantly on the details of the analysis. The experimental bias introduced by the tagging of heavy flavour events and other analysis techniques can be evaluated with Monte Carlo simulations. This procedure and a comparison of the analytical calculation with the corresponding values for the QCD corrections from different Monte Carlo generators is described, and the estimate for the QCD corrections for the three OPAL analyses are summarised.

3.4.1 Introduction

QCD effects modify the individual cross-sections in the production of $q\bar{q}$ pairs in $e^+e^- \rightarrow q\bar{q}$ and therefore the measurements of the forward-backward asymmetries. In addition to the diagrams depicted in figure 3.11a), graphs including vertex correction and gluon bremsstrahlung (fig.3.11b and c) contributes to the process. This results in a change of the direction of the final fermion

Figure 3.11: Feynman graphs of the process $e^+e^- \rightarrow q\bar{q}(g)$

and thereby affects the forward-backward asymmetry. The angular distribution of the decay of a spin one boson into two spin 1/2 fermions was given in equation 3.1. As can be directly read off from equation 3.5 there is no contribution from the axial-vector current to the longitudinal cross-section, and the vector current contribution vanishes for massless quarks. Therefore the longitudinal component of the cross-section is expected to be very small. However, in the presence of gluon radiation in the final state the relative contributions of the different cross-sections are modified. According to equation 3.4 this implies a change in the forward backward asymmetry. In particular the longitudinal cross-section increases and is no longer negligible. This can be understood intuitively for example for the case of the longitudinal cross-section. For massless quarks the quark has to be lefthanded and the antiquark righthanded, thus a longitudinally polarised Z^0 boson cannot couple to massless quarks and the contribution of the longitudinally polarised cross-section vanishes. In the presence of an additional gluon in the final state the spin states of the quarks and the gluon can be adjusted such, that a longitudinal polarisation of the final state is allowed even for massless quarks. A summary of the contributions of the various quark current products for the pure electroweak process and the quark production including gluon radiation is given in table 3.10. The $r_{U,L,F}$ parameters in table

	$e^+e^- \rightarrow q\bar{q}$	$e^+e^- \rightarrow q\bar{q}(g)$ (incl. vertex corrections)
σ_U	$v\sigma_{VV} + v^3\sigma_{AA}$	$(v + \frac{\alpha_s}{\pi}r_U^V)\sigma_{VV} + (v^3 + \frac{\alpha_s}{\pi}r_U^A)\sigma_{AA}$
σ_L	$\frac{1}{2}v\mu^2\sigma_{VV}$	$(\frac{1}{2}v\mu^2 + (\frac{\alpha_s}{\pi}r_L^V)\sigma_{VV} + \frac{\alpha_s}{\pi}r_L^A)\sigma_{AA}$
σ_F	$v^2\sigma_{VA}$	$(v^2 + \frac{\alpha_s}{\pi}r_F^V)\sigma_{VA} + (\frac{\alpha_s}{\pi}r_F^A)\sigma'_{VA}$

Table 3.10: Overview of the polarised cross-sections in terms of the quark current products for the pure electroweak process and the case where QCD corrections are included. Here $\mu = 2m_q/\sqrt{s}$ denotes the quark mass in units of the beam energy, v is the velocity of the quark and the coefficients $r_{U,L,F}$ parametrise the QCD corrections for the various polarised cross-sections. The quark current products are given in equation 3.6 and the explicit form of the additional term of the cross-section σ_F is $\sigma'_{VA} = \frac{G_F}{\sqrt{2}} q_e q_q c_A^q c_A^q \frac{1}{m_Z} D^{-1}$.

3.10 are independent of the quark flavour, but they are functions of the quark mass μ . In the high energy limit or for massless quarks the r -parameters for the total cross-section, r_U and r_L , both the vector and the axial-vector parts, are unity, whereas the parameters r_F vanish. This can be interpreted such, that the main effect of the QCD correction for the forward-backward

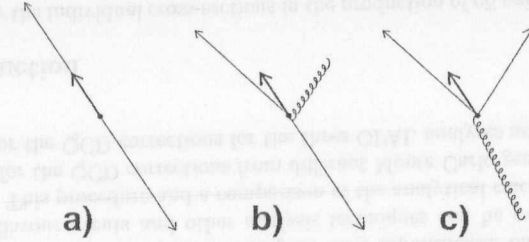


Figure 3.12: Pictorial representations of the different topologies which can influence the asymmetry. For each figure the direction of the tagged particles is indicated by the thin arrows, the gluon direction by the curled line, and the thrust direction by the thick arrow. (a) No gluon radiation: thrust direction and quark direction are equal; (b) 'Soft' gluon radiation: The thrust direction is a good estimator of the primary $q\bar{q}$ direction, and the charge of the primary quark is unambiguously related to the charge of the tagged particle in the hemisphere; (c) 'Hard' gluon radiation: The thrust direction is no longer a good estimator of the primary quark direction, and no charge information is contained in the hemisphere.

asymmetries (c.f. equation 3.4,3.5) results from a change in the normalisation, whereas the cross-section σ_F itself is nearly unaffected.

Experimentally the direction of the outgoing fermion is not measurable. It is approximated in the measurements presented in this thesis by the thrust direction. The orientation of the thrust axis is chosen such that the scalar product of the thrust axis with the momentum of the direction of the quark is positive. This direction is modified by QCD effects. In figure 3.12 some of the topologies in lowest order which might influence the asymmetry are shown. For soft gluon radiation, as depicted in figure 3.12b) the direction of thrust axis is essentially unaffected, whereas the direction of the primary quark after gluon radiation is changed. The main contribution to the QCD correction results from hard gluon radiation, where the two quarks are recoiling against the gluon into the same hemisphere. For those events any information about the asymmetry is lost and the measured asymmetry in these events is zero. Therefore the QCD correction determined for the thrust axis as the reference direction is expected to be smaller than the QCD correction based on the direction of the quark after gluon emission. In addition to these perturbative QCD processes, effects like hadronisation may also influence the direction of the hadrons compared to the direction of the partons and thus contribute to the QCD correction.

The measured asymmetry is therefore an effective asymmetry, which has to be corrected for the effects described above to get the bare asymmetry, resulting from the direction of the primary quark, A_{FB}^0 , according to

$$A_{FB}^{eff} = (1 - \delta^{QCD})A_{FB}^0. \quad (3.26)$$

Equation 3.26 is true quite generally as long as no experimental effects are taken into account. Experimental effects are, for example, the event selection, finite acceptances or the method

itself used to determine the value of the asymmetry. Such biases might change the size of the QCD corrections and thus the observed asymmetry significantly relatively to $A_{\text{FB}}^{\text{eff}}$. This is parametrised by an experimental bias factor B defined by

$$A_{\text{FB}}^{\text{obs}} = (1 - B\delta^{\text{QCD}}) A_{\text{FB}}^0. \quad (3.27)$$

It is this QCD suppression or bias factor B which is different for the individual analyses.

In the following sections the theoretical estimates of the QCD corrections will be summarised. For comparisons generator studies are performed. The analytical calculations will be used as a basis for the QCD corrections quoted in this section. With the help of the Monte Carlo generators the effects of hadronisation are estimated. Subsequently a method to evaluate the experimental effects on the QCD corrections is explained and the corresponding bias is determined for the three OPAL forward-backward asymmetry analyses described in section 3.2 and 3.3. Finally the results are summarised.

3.4.2 Generator Studies and Hadronisation Effects

A number of analytical calculations exist which predict the QCD effects for the heavy quark forward-backward asymmetries [43,44]. In most cases the correction quoted is that between the asymmetry determined from the primary quark direction and the asymmetry using the quark direction at the end of the perturbative phase ('after gluon radiation'). In [43] a correction is also quoted relative to the thrust direction, calculated using all partons before hadronisation. The calculations in [43] are to first order in α_s , while in [44] some results are given to order α_s^2 . In this note the results from the first order calculations are used, while the results from [44] are used to estimate the error made by neglecting higher order effects.

These analytical calculations for the QCD corrections, based on perturbative QCD, are performed for the partons after the perturbative phase. In order to apply these results to measurements, the changes due to non-perturbative effects like hadronisation have to be taken into account. The difference between the asymmetry calculated from, on one hand the thrust axis build from partons and, on the other hand, from all stable particles, is accessible only through Monte Carlo models. In the following section a comparison between the results from analytical calculations and Monte Carlo generators is performed and the effects of the hadronisation is estimated by comparing different Monte Carlo models.

QCD correction factors δ_{MC} are evaluated from Monte Carlo models for the following levels:

- $\delta_{\text{MC}}^{\text{quark}}$, calculated using the direction of the quark after the perturbative phase,
- $\delta_{\text{MC}}^{\text{part,T}}$, calculated using the direction of the parton-level thrust axis oriented according to the direction of the quark,
- $\delta_{\text{MC}}^{\text{had,T}}$, calculated using the direction of the thrust axis from all stable particles (including neutrinos), oriented according to the direction of the weakly decaying hadron containing the quark.

The QCD correction factors δ_{MC} are calculated by comparing the values for the forward-backward asymmetry using one of these directions with the direction of the primary quark

before gluon radiation. The definition used for the asymmetry in this context is

$$A_{\text{FB}} = \frac{n_f - n_b}{n_f + n_b} \quad (3.28)$$

where n_f, n_b are the number of events counted in the forward and backward hemisphere, respectively. The hemispheres are defined by the direction of the quark or the thrust axis at the appropriate stage in the fragmentation, relative to the direction of the incoming electron. This definition has the advantage that it is independent of the exact shape of the underlying differential cross-section. The number of events in the forward or backward hemisphere before and after QCD effects are highly correlated. These correlations are taken into account when calculating the error on the correction. Events where a gluon splits into a pair of heavy quarks will also influence the observed asymmetry. Such events have a high probability to be tagged as a heavy flavour event, however they do not contribute to the asymmetry. These types of events are explicitly considered in the individual analyses and are excluded from the calculation of the theoretical QCD corrections and from the Monte Carlo studies.

The analytical calculations for the QCD correction are summarised in [45]. The estimates of $\delta_{\text{QCD}}^{\text{quark}}$ and $\delta_{\text{QCD}}^{\text{part,T}}$ can be directly compared to the results obtained with Monte Carlo simulations. In tables 3.11 and 3.12 the results of the analytical calculations for $b\bar{b}$ and $c\bar{c}$ events, respectively, are compared with the results obtained using standard JETSET 7.4 Monte Carlo [10] or different versions of JETSET and HERWIG [11] tuned by ALEPH, DELPHI, L3 and OPAL. The tuned generators include an up-to-date description of the production and decay of b and c hadrons together with an improved description of global observables. Also shown are results for the shape parameter a introduced in equation 3.3.

In general, for the corrections to the asymmetries the agreement between analytical calculations and generators is poor when the quark direction is used (more than 30% difference in one case) while there is a much better agreement when the thrust axis is used (below 10% discrepancy). Qualitatively this pattern is expected since in a parton shower simulation many more gluons are radiated than in a fixed $O(\alpha_s^2)$ calculation. For $b\bar{b}$ -events the shape parameter a is well reproduced by the simulation. This is not the case for $c\bar{c}$ -events at the quark level. The relatively good agreement between Monte Carlo models and analytical calculations for the thrust direction encourages the use of the simulation to estimate the suppression factor of the QCD corrections induced by experimental techniques.

Tables 3.11 and 3.12 show that the predictions of the various versions of generators have some spread. Even the same generator with different tunings yields different results for $\delta_{\text{MC}}^{\text{quark}}$ and $\delta_{\text{MC}}^{\text{part,T}}$ (up to 13% discrepancy). One of the possible sources of difference between different tunings is the cut-off chosen for the energy of gluons emitted in the parton shower. The spread is slightly smaller at the hadron level, $\delta_{\text{MC}}^{\text{had,T}}$, where the simulation programs are tuned to the experimental data.

It is especially interesting to compare the results from the two Monte Carlo generators, HERWIG and JETSET, because two different approaches are used to incorporate the fragmentation process. Therefore the effects of the hadronisation process in both models are not necessarily expected to be the same. In HERWIG a cluster hadronisation model [49] is realised. After the perturbative phase all gluons are split non-perturbatively into light $q\bar{q}$ pairs. Then the quarks are combined through colour lines into 'clusters', i.e. such that they form a colour-singlet. The mass distribution and the spatial size of these clusters peak at low values and fall rapidly for larger cluster masses and sizes. Subsequently the clusters either decay into two

$b\bar{b}$ events	δ_{MC}^{quark} [%]	$\delta_{MC}^{part,T}$ [%]	$\delta_{MC}^{had,T}$ [%]	a_{MC}^{quark}	$a_{MC}^{part,T}$	$a_{MC}^{had,T}$
JETSET 7.408	3.95 ± 0.02	3.17 ± 0.02	2.94 ± 0.02	0.89	0.95	0.96
ALEPH JETSET [46] †	3.84 ± 0.09	3.07 ± 0.04	2.79 ± 0.08	0.90	0.96	0.98
DELPHI JETSET [47] †	4.38 ± 0.03	3.43 ± 0.03	3.06 ± 0.03	0.88	0.95	0.95
L3 JETSET [48] †	3.98 ± 0.06	3.15 ± 0.06	2.89 ± 0.06	0.89	0.95	0.98
OPAL JETSET [11] †	4.02 ± 0.18	3.04 ± 0.19	3.02 ± 0.20	0.89	0.95	0.95
OPAL HERWIG [11]	4.11 ± 0.14	2.86 ± 0.13	2.75 ± 0.14	0.90	0.95	0.99
Theory	δ_{QCD}^{quark} [%]	$\delta_{QCD}^{part,T}$ [%]		a_{QCD}^{quark}	$a_{QCD}^{part,T}$	
	3.30 ± 0.37	3.19 ± 0.33		0.91 ± 0.02	0.95 ± 0.01	

Table 3.11: Different values of δ_{QCD} in % (see equation 3.26) and a (see equation 3.2) for $b\bar{b}$ events. The line quoted as JETSET 7.408 is obtained using the JETSET generator with default tuning. All the other lines correspond to results obtained with generators tuned by the LEP experiments. The lines quoted with a † are used in table 3.13 to estimate the reference values of the QCD corrections at the level of the hadrons [45]. The statistical errors on a obtained with the generators are negligible compared to the theoretical errors and therefore are not quoted. While the values of the shape parameter a are not used for the final correction, they provide an additional test of the agreement between the Monte Carlo and the analytical calculations.

$c\bar{c}$ events	δ_{MC}^{quark} [%]	$\delta_{MC}^{part,T}$ [%]	$\delta_{MC}^{had,T}$ [%]	a_{MC}^{quark}	$a_{MC}^{part,T}$	$a_{MC}^{had,T}$
JETSET 7.408	5.49 ± 0.04	3.95 ± 0.04	3.51 ± 0.04	0.85	0.95	0.95
DELPHI JETSET [47] †	5.74 ± 0.03	4.12 ± 0.03	3.65 ± 0.03	0.85	0.95	0.95
OPAL JETSET [11] †	4.95 ± 0.18	4.03 ± 0.18	3.80 ± 0.19	0.86	0.96	0.96
OPAL HERWIG [11]	4.75 ± 0.17	3.18 ± 0.16	3.26 ± 0.17	0.87	0.97	0.97
Theory	δ_{QCD}^{quark} [%]	$\delta_{QCD}^{part,T}$ [%]		a_{QCD}^{quark}	$a_{QCD}^{part,T}$	
	4.18 ± 0.69	3.92 ± 0.68		0.91 ± 0.02	0.95 ± 0.01	

Table 3.12: Different values of δ_{QCD} in % (see equation 3.26) and a (see equation 3.2) for $c\bar{c}$ events. The line quoted as JETSET 7.408 is obtained using the JETSET generator with default tuning. All the other lines are calculated using generators tuned by the LEP experiments. The lines quoted with a † are used in table 3.13 to estimate the reference values $\delta_{QCD}^{had,T}$.

hadrons, where an additional quark/antiquark-pair $q\bar{q}$ and the spin states of the decay products are chosen randomly, or, if the cluster is too light for further decays, the mass of the cluster is shifted to the appropriate value by an exchange of momentum with the neighbouring cluster in the jet. The JETSET Monte Carlo adopts the Lund string fragmentation scheme. The idea of this generator is, that a ‘string’ is spanned from the quark to the antiquark, as they move apart, storing the potential energy of the colour-field. For highly virtual quarks the string may break into two parts by creating a $q\bar{q}$ -pair. The production of $q\bar{q}$ -pairs after string break-ups is an iterative process, which continues until only on-shell hadrons remain. For generating the quark/antiquark-pair after breaking the string, the process of quantum mechanical tunnelling is adopted. This leads to a suppression of heavy quarks in the fragmentation process, proportional to $\exp(-\mu^2)$, where μ is the quark mass. Within the string model no implicit predictions are made for the spin states of the mesons produced. They have to be put in by hand, usually assuming a ratio of 1:3 for the production of pseudo-scalar and vector mesons, as suggested by

the naive counting method.

Comparing the estimates of $\delta_{MC}^{part,T}$ with $\delta_{MC}^{had,T}$ indicates that the change from the parton level thrust to the hadron thrust decreases the QCD corrections significantly. The source of the decrease is the hadronisation as well as the decays of b and c hadrons, although the latter have a smaller effect. Both processes result in a poorer estimate of the thrust compared to the quark direction. It is interesting to compare the effects of the hadronisation predicted by the two different Monte Carlo generators with the spread of the results within the JETSET model, but with the various tunes of the LEP experiments. It turns out, that the differences because of the Monte Carlo tunes exceeds those due to the two generators, which have a principally different implementation of the fragmentation process. A possible explanation could again be the cut-off parameter chosen by the experiments in their tune. On the other hand the similar results for the hadronisation effects in the JETSET and HERWIG model confirm that the estimates of the hadronisation effects, although based on phenomenological models, are reliable.

The final QCD corrections, $\delta_{QCD}^{had,T}$, are obtained from the analytical calculations on the parton level thrust [45] and the Monte Carlo prediction for the hadronisation effects as

$$\delta_{QCD}^{had,T} = \delta_{QCD}^{part,T} + \left\langle \delta_{MC}^{had,T} - \delta_{MC}^{part,T} \right\rangle,$$

where $\left\langle \delta_{MC}^{had,T} - \delta_{MC}^{part,T} \right\rangle$ is the average of the differences between the QCD corrections at hadron and parton level based on the JETSET estimates quoted in Tables 3.11 and 3.12.

The uncertainties for the parton level corrections are those given in tables 3.11 and 3.12. In addition the full difference between the parton level and the hadron level correction as predicted by the Monte Carlo is taken as the systematic error. The values for the final correction, including its error, are listed in Table 3.13.

	$b\bar{b}$ events	$c\bar{c}$ events
$\left\langle \delta_{MC}^{had,T} - \delta_{MC}^{part,T} \right\rangle$ [%]	-0.23	-0.35
$\delta_{QCD}^{had,T}$ [%]	2.96 ± 0.40	3.57 ± 0.76

Table 3.13: Estimated value of $\delta_{QCD}^{had,T}$. The average value of $\left\langle \delta_{MC}^{had,T} - \delta_{MC}^{part,T} \right\rangle$ is obtained using the results quoted with a † in tables 3.11 and 3.12.

3.4.3 Experimental Bias

Experimental biases in the asymmetry measurement can be introduced by the detector and by the selection procedure used in the analysis. Detector effects are already considered in the OPAL analyses, and systematic errors are given for this. The most important detector effect is a possible charge asymmetry of the detector, an effect which is most significant for the jet-charge analysis [14]. Experimental selection biases can also change the size of the QCD corrections, in most cases decreasing the actual size of the correction. This depends entirely on the details of the analysis and the cuts used, and therefore has to be evaluated individually for each analysis.

The dominant part of the QCD corrections comes from the type of events shown in figure 3.12(c), where a hard gluon is emitted, recoiling against the $q\bar{q}$ system. As stated earlier,

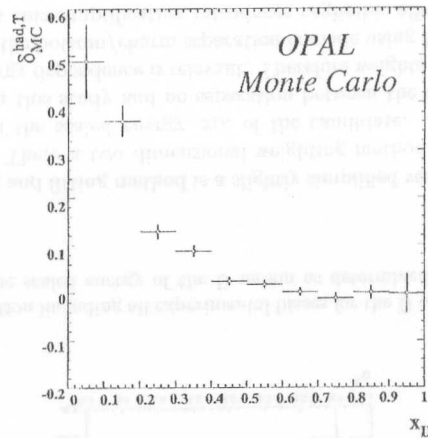


Figure 3.13: Dependence of the QCD correction of the charm forward-backward asymmetry in charm events tagged by a D mesons, as a function of the scaled energy of the D. This study is the result of a generator level Monte Carlo.

such events have no measurable asymmetry if the thrust axis is used as a direction estimate. On the other hand the selection of such events is suppressed if, for example, high momentum leptons or D mesons are selected. The fraction of events of type (c) therefore will be reduced in the sample used to measure the asymmetry, and the QCD correction in this sample will be smaller than naively expected. This is illustrated in figure 3.13, where the QCD correction is shown as a function of the scaled energy $x_D = E_D/E_{beam}$ of the selected D meson in $e^+e^- \rightarrow c\bar{c}$ events. For high energy D mesons the QCD corrections essentially disappear.

Other important effects are introduced by the fitting method itself. In the OPAL analyses the asymmetry has been fitted using equation 3.2 with $a = 1$. However, Monte Carlo studies and the theoretical estimates (c.f. tables 3.11 and 3.12) show that a differs from one by around -5% . Fitting with $a = 1$ biases the measured asymmetry, decreasing the QCD corrections by around 14% . It is therefore very important that the final bias is evaluated using as far as possible the same methods as were used in the actual analysis. The bias due to the fitting method is absorbed into the experimental suppression factor \mathcal{B} .

In the following two sections the evaluation of the experimental bias \mathcal{B} is described for each heavy flavour asymmetry analysis done at OPAL. In all cases a fit is done to the angular distribution of the thrust axis, closely following the original analyses. From this the observed asymmetry is extracted. A similar fit is performed to the angular distribution of the primary quark/anti-quark pair, and the bare asymmetry is determined. Exactly the same sample of events is used for this second fit. From this the ratio A_{FB}^{obs}/A_{FB}^0 is calculated. Similarly, using Monte Carlo events, but this time without taking detector effects into account, the ratio $A_{FB}^{had,T}/A_{FB}^0$ is calculated. Again the same events are used in calculating the ratio, thus minimising the statistical error. Note however that the events used to calculate the first and the second ratio are not identical. The experimental bias is defined in terms of these double ratio

of asymmetries:

$$\mathcal{B} = \left(1 - \frac{A_{FB}^{obs}}{A_{FB}^0}\right)_{MC}^{det} / \left(1 - \frac{A_{FB}^{had,T}}{A_{FB}^0}\right)_{MC} \quad (3.29)$$

The superscript 'det' indicates that these variables have been evaluated including experimental effects. The full QCD correction is determined by multiplying the analytical prediction for the QCD correction given in the previous section with the bias, $\delta_{QCD} = \mathcal{B}\delta_{QCD}^{had,T}$, according to equations 3.26 and 3.27.

The Lepton Analysis

In the asymmetry analysis using lepton tags the lepton selection and separation into a prompt $b \rightarrow l^-$ component, a prompt $c \rightarrow l^+$ component, and background is made using several neural nets. Instead of cutting on several quantities the analysis uses the output of two neural networks as discriminators. Individual events are weighted by these net outputs, and the asymmetry is extracted from a binned likelihood fit to the differential asymmetry distribution. The details of this weighting method can be found in [16].

The experimental bias from this method is calculated by repeating these steps for Monte Carlo events. However the method has been slightly simplified:

- Since the analysis is only done on Monte Carlo, it is possible to restrict this study to the flavours under consideration, i.e. to $b\bar{b}$ events to extract the bottom asymmetry and to $c\bar{c}$ events for the charm asymmetry. The neural nets therefore are not needed for the flavour and the signal to background separation. They are only needed insofar as they bias the event selection. Therefore a coarser binning in the net output distributions has been used.
- Similarly the fit in $q \cos\theta$, where q is the charge of the lepton, has been simplified. The complete likelihood expression given in [16] is replaced by a simpler one without background contributions. The fit itself is done as a χ^2 fit instead of the likelihood fit.

It has been verified that these approximations do not significantly influence the results for the experimental bias within the quoted statistical errors.

In figure 3.14 the QCD correction including all experimental biases is shown for the lepton sample, as a function of the output of the neural net. The final QCD correction is calculated by the weighted average of the QCD corrections as a function of the neural net outputs. The results are summarised in table 3.14. Typically the lepton analysis is sensitive to less than 70% of the underlying QCD corrections. The error on this bias factor is dominated by the statistical precision of this determination. Systematic errors of the hadronisation model etc. are already included in the original analyses.

The D Meson Analysis

Similarly to the previous method, the analysis of the charm and bottom asymmetries using D mesons relies on an event weighting method to separate background, $e^+e^- \rightarrow b\bar{b}$ and $e^+e^- \rightarrow c\bar{c}$ events.

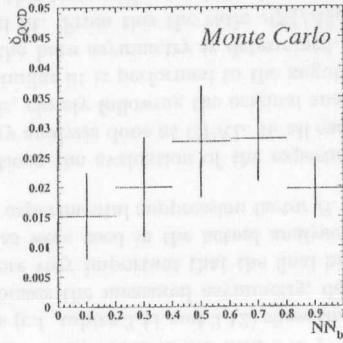


Figure 3.14: QCD correction including all experimental biases for the lepton sample in bottom events as a function of the output of the neural network.

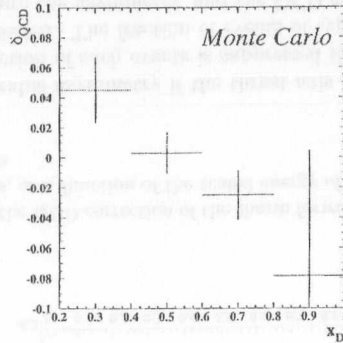


Figure 3.15: QCD correction including all experimental biases for the D meson sample in $e^+e^- \rightarrow b\bar{b}$ events as a function of the scaled energy of the D meson as determined from the JETSET Monte Carlo.

The actual weighting and fitting method is a slightly simplified version of the one described in section 3.3 and [50]. There a two dimensional weighting method has been used based on lifetime information and the scaled energy, x_D , of the candidate. Again, since here Monte Carlo events are used for this study and no separation between the different signal sources is needed, and only the energy dependence is relevant. Therefore weights have been calculated as a function of x_D only, and the bottom/charm separation is made using Monte Carlo information. It has been checked that this simplification introduces negligible effects in the determination of the QCD correction. In figure 3.15 the QCD corrections, including all detector biases, are shown as a function of x_D .

The final QCD correction is calculated as the weighted average of the QCD corrections shown in figure 3.15. The experimental bias is calculated in the same way as described before. The results are summarised in table 3.14. The error on the experimental bias is again dominated by the available number of Monte Carlo events.

The Jet-Charge Analysis

In the OPAL measurement of the bottom asymmetry using jet-charge, corrections are given to derive the quark level asymmetries from the measured ones. They include experimental biases as discussed in this note. The error quoted includes the theoretical uncertainty from the underlying QCD correction and a 50% error on the difference between the quoted bias and the fully observed QCD correction ($B = 1$) has been assigned. The error on the experimental bias factor is again dominated by Monte Carlo statistics. The results are summarised in table 3.14.

	jet-charge	lepton	D
$e^+e^- \rightarrow b\bar{b}$			
bias B	$+0.36 \pm 0.32$	$+0.692 \pm 0.133$	$+0.295 \pm 0.126$
δ_{QCD}	$+0.0103 \pm 0.0012 \pm 0.0050$	$+0.0197 \pm 0.0025 \pm 0.0038$	$+0.0084 \pm 0.0011 \pm 0.0036$
$e^+e^- \rightarrow c\bar{c}$			
bias B		$+0.366 \pm 0.081$	-0.061 ± 0.087
δ_{QCD}		$+0.0117 \pm 0.0021 \pm 0.0026$	$-0.0019 \pm 0.0004 \pm 0.0028$

Table 3.14: Table of experimental biases and final QCD corrections δ_{QCD} for $e^+e^- \rightarrow b\bar{b}$ and $e^+e^- \rightarrow c\bar{c}$ events for the three OPAL asymmetry analyses. The first error quoted is the theoretical error of the underlying QCD correction, the second one is dominated by the statistical precision with which the bias has been determined.

3.4.4 Results and Conclusions

The final results for the bias and the QCD corrections are summarised in table 3.14. The QCD corrected asymmetries are given in table 3.15 for each of the three analyses and the three energy ranges considered.

3.5 Combination of the Analyses

The three analyses are combined with the method of Best Linear Unbiased Estimate (BLUE) [51]. The averaging procedure is similar to that used by the LEP electroweak working group, which is explained in detail in [52]. Statistical as well as systematic correlations are taken into account.

The covariance matrix can be written as:

$$C = C^{\text{stat}} + C^{\text{syst}} \quad (3.30)$$

	89.44 GeV	91.21 GeV	92.91 GeV
$e^+e^- \rightarrow b\bar{b}$			
jet-charge	$0.041 \pm 0.021 \pm 0.0024$	$0.1004 \pm 0.0052 \pm 0.0045$	$0.146 \pm 0.002 \pm 0.007$
lepton	$0.035 \pm 0.017 \pm 0.020$	$0.0910 \pm 0.0044 \pm 0.0020$	$0.107 \pm 0.014 \pm 0.004$
D	$0.087 \pm 0.108 \pm 0.029$	$0.095 \pm 0.027 \pm 0.022$	$-0.021 \pm 0.090 \pm 0.026$
$e^+e^- \rightarrow c\bar{c}$			
lepton	$-0.069 \pm 0.024 \pm 0.005$	$0.0595 \pm 0.0059 \pm 0.0056$	$0.156 \pm 0.020 \pm 0.010$
D	$0.039 \pm 0.051 \pm 0.009$	$0.063 \pm 0.012 \pm 0.006$	$0.158 \pm 0.041 \pm 0.011$

Table 3.15: Table of the final QCD corrected asymmetries for $e^+e^- \rightarrow b\bar{b}$ and $e^+e^- \rightarrow c\bar{c}$. The errors shown are the statistical error and the total systematic error.

In the following sections the determination of the statistical correlation between the measurements is described and the correlation of systematic errors are discussed.

Statistical Correlations

In order to extract the statistical correlations between the different measurements of the heavy flavour asymmetries first the statistical overlap of the three samples is determined. The total number of events used in the different analyses and the number of events which are tagged by more than one analysis are summarised in table 3.16.

sample	lepton	D meson	jet-charge
lepton	512125	16235	98806
D meson		73856	19301
jet-charge			353085

Table 3.16: In the diagonal the number of events used for the individual asymmetry measurements are given, whereas in the off-diagonal the number of events which were used in two of the analyses are quoted.

Each of the samples has a specific signal to background ratio and flavour composition due to the different flavour tagging techniques. The errors for the asymmetry analyses of the events common to more than one sample can be estimated by using these signal to background numbers, the contributions of the various flavours in the sample together with the statistical overlap given in table 3.16. From these numbers the correlation matrix of the five measurements of the heavy flavour asymmetries can be calculated and is given below.

Systematic Errors

The systematic covariance matrix, C^{sys} , can be calculated from the detailed breakdown of systematic errors given in table 3.18. The diagonal element, C_{ii}^{sys} , is the square of the total

	$(A_{\text{FB}}^b)_{\text{lep}}$	$(A_{\text{FB}}^c)_{\text{lep}}$	$(A_{\text{FB}}^b)_D$	$(A_{\text{FB}}^c)_D$	$(A_{\text{FB}}^b)_{\text{jq}}$
$(A_{\text{FB}}^b)_{\text{lep}}$	1.00	0.17	0.02	0.01	0.16
$(A_{\text{FB}}^c)_{\text{lep}}$	0.17	1.00	0.01	0.04	0.02
$(A_{\text{FB}}^b)_D$	0.02	0.01	1.00	-0.27	0.05
$(A_{\text{FB}}^c)_D$	0.01	0.04	-0.27	1.00	0.03
$(A_{\text{FB}}^b)_{\text{jq}}$	0.16	0.02	0.05	0.03	1.00

Table 3.17: Statistical error correlation matrix of the charm and bottom asymmetry measurements of the three analyses.

systematic error for measurement i . If the signed systematic error on result r_i^u due to a source of systematic uncertainty p is written as $s_i(p)$, then an off-diagonal element is given by:

$$C_{ij}^{\text{sys}} = \sum_p s_i(p)s_j(p), \quad (3.31)$$

where the sum is over all sources of uncertainty, p , which are correlated between results i and j .

A detailed listing of the correlated and uncorrelated systematic errors for the measurement on the Z^0 pole is given in table 3.18. For the measurements in all three energy ranges considered the sum of correlated and uncorrelated statistical and systematic errors are summarised in table 3.19. More details about the individual systematic errors of the measurements above and below the Z^0 resonance can be found in [14, 50].

Results

Combining the measurements of the OPAL bottom and charm asymmetries with the averaging procedure described above yields the following results:

$$\begin{aligned} A_{\text{FB}}^b &= 0.039 \pm 0.014 & A_{\text{FB}}^c &= -0.046 \pm 0.022 & \langle E_{\text{cm}} \rangle &= 89.45 \text{ GeV} \\ A_{\text{FB}}^b &= 0.0951 \pm 0.0040 & A_{\text{FB}}^c &= 0.0605 \pm 0.0067 & \langle E_{\text{cm}} \rangle &= 91.22 \text{ GeV} \\ A_{\text{FB}}^b &= 0.120 \pm 0.021 & A_{\text{FB}}^c &= 0.152 \pm 0.020 & \langle E_{\text{cm}} \rangle &= 93.00 \text{ GeV} \end{aligned}$$

The correlation matrix of the combined results for the three energy ranges of the bottom and charm asymmetries is given in the table 3.20. The results for the measurement on the Z^0 pole and the correlation between the bottom and charm asymmetries of the individual measurements are visualised in figure 3.16. The results are compared with the predictions of the Standard Model, where the top mass is varied within the experimental errors and a Higgs mass range from 90 to 260 GeV is considered.

3.5.1 Interpretation of the Results

Energy Dependence

The energy dependence of the forward-backward asymmetries in the Standard Model is determined by the interplay of the γ - and Z^0 -exchange. In addition to the γ - and Z^0 -exchange

	Lepton		D meson		Jet-Charge
	A_{FB}^b	A_{FB}^c	A_{FB}^b	A_{FB}^c	A_{FB}^b
statistical errors					
total statistics	0.0044	0.0059	0.027	0.012	0.0052
statistics uncorrelated	0.0051	0.0061	0.041	0.014	0.0065
statistics correlated	0.0087	0.0232	0.036	0.023	0.0087
systematic errors					
total systematics	0.0020	0.0056	0.0055	2.20	0.0044
individual systematic errors					
Monte Carlo Statistic	0.0008	0.0010	0.0010	0.0005	0.0008
Conversion fraction	0.0000	0.0003			
Muon Decay fraction	0.0000	0.0000			
Net Source dependence	0.0002	0.0013			
Tracking Resolution	0.0006	0.0000			
Theta dependence	0.0008	0.0019			
Lepton background asymmetry	0.0000	0.0026			
Br(b → l ⁻)	0.0001	0.0015			
Br(b → c → l ⁺)	0.0002	0.0010			
Br(b → \bar{c} → l ⁻)	0.0002	0.0023			
Br(b → τ → l ⁻)	0.0001	0.0009			
Br(c → l ⁻)	0.0003	0.0020			
Semilept. model b → l ⁻	0.0001	0.0020			
Semilept. model c → l ⁺	0.0007	0.0008			
Time dependent mixing	0.0004	0.0004			
Jet-charge hemisphere correlation					0.0013
Jet-charge rhos					0.0012
Detector modelling			0.0008	0.0012	0.0030
D ⁺⁺ charm modelling			0.0054	0.0030	
D ⁺⁺ background acceptance			0.0028	0.0009	
D ⁺⁺ background level			0.0062	0.0014	
D ⁺⁺ background asymmetry			0.0023	0.0010	
D ^{*+} charge correlation			0.0186	0.0010	
common systematic errors					
g → c \bar{c}			0.0020	0.0034	
b and c hadron lifetime			0.0023	0.0028	
B decay multiplicity	} 0.0002	} 0.0001	0.0017	0.0016	0.0003
D decay multiplicity			0.0012	0.0011	0.0002
b fragmentation function	0.0001	0.0002	0.0000	0.0000	
c fragmentation function	0.0012	0.0005	0.0005	0.0003	0.0020
AFB QCD corr	0.0002	0.0002	0.0004	0.0003	0.0005

Table 3.18: Overview over the correlated and uncorrelated errors for the on peak measurements of the bottom and charm asymmetries.

	Lepton						D meson						Jet-charge								
	A_{FB}^b		A_{FB}^c		A_{FB}^b		A_{FB}^c		A_{FB}^b		A_{FB}^c		A_{FB}^b		A_{FB}^c		A_{FB}^b		A_{FB}^c		
\sqrt{s} (GeV)	89.45	91.22	93.00	89.55	91.22	93.00	89.45	91.22	93.00	89.45	91.22	93.00	89.45	91.22	93.00	89.45	91.21	93.00	89.45	91.21	93.00
correlated stat.	0.034	0.0087	0.003	0.098	0.0232	0.079	0.145	0.036	0.127	0.098	0.023	0.079	0.084	0.023	0.079	0.084	0.027	0.065	0.027	0.065	0.003
uncorrelated stat.	0.020	0.0051	0.014	0.025	0.0061	0.020	0.162	0.041	0.128	0.060	0.014	0.043	0.065	0.014	0.043	0.065	0.027	0.065	0.027	0.065	0.003
total statistical	0.017	0.0044	0.014	0.024	0.0059	0.020	0.108	0.027	0.090	0.051	0.012	0.041	0.052	0.012	0.041	0.052	0.021	0.052	0.021	0.052	0.002
uncorrelated syst.	0.0017	0.0016	0.0030	0.0044	0.0056	0.0095	0.0249	0.0217	0.0197	0.0071	0.0026	0.0077	0.0024	0.0026	0.0077	0.0024	0.0024	0.0024	0.0024	0.0024	0.0061
correlated syst.	0.0004	0.0012	0.0022	0.0021	0.0006	0.0038	0.0152	0.0037	0.0167	0.0050	0.0048	0.0079	0.0003	0.0048	0.0079	0.0003	0.0003	0.0003	0.0003	0.0003	0.0035
total systematic	0.0017	0.0020	0.0037	0.0049	0.0056	0.0102	0.0292	0.0220	0.0259	0.0087	0.0055	0.0110	0.0024	0.0055	0.0110	0.0024	0.0024	0.0024	0.0024	0.0024	0.0070

Table 3.19: The summary of the systematic and statistical errors of the bottom and charm asymmetries measured at the different centre-of-mass energies.

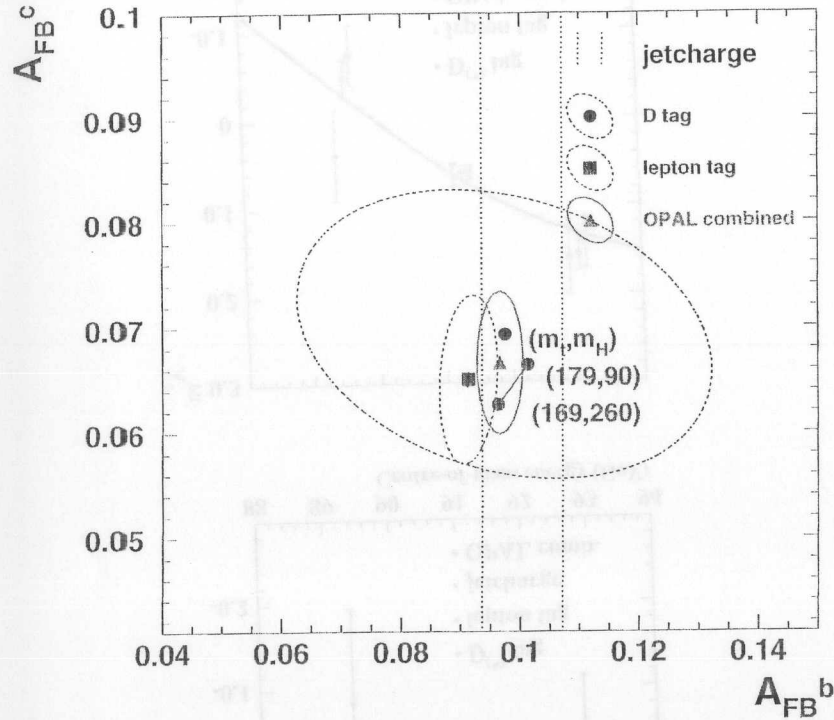


Figure 3.16: The results of the individual bottom and charm asymmetry measurements together with the OPAL combined value. Shown are the 39% confidence level contours in case of the two dimensional fits and the one sigma error band for the jet-charge analysis, which gives information about the bottom asymmetry only.

	$A_{FB}^b - 2$	$A_{FB}^c - 2$	$A_{FB}^b \text{peak}$	$A_{FB}^c \text{peak}$	$A_{FB}^b + 2$	$A_{FB}^c + 2$
$A_{FB}^b - 2$	1.000	.123	.013	-.006	.008	-.002
$A_{FB}^c - 2$.123	1.000	.027	.002	.012	-.016
$A_{FB}^b \text{peak}$.013	.027	1.000	.016	.093	-.048
$A_{FB}^c \text{peak}$	-.006	.002	.016	1.000	-.050	.206
$A_{FB}^b + 2$.008	.012	.093	-.050	1.000	.077
$A_{FB}^c + 2$	-.002	-.016	-.048	.206	.077	1.000

Table 3.20: Error correlation matrix of the combined fit to all three measurements for the three energy ranges. The numbers include the statistical and systematic correlations. $A_{FB} - 2$, $A_{FB} \text{peak}$ and $A_{FB} + 2$ denotes the asymmetry measurements at a mean energy of $\sqrt{s} = 89.44$, 91.21 and 92.91 GeV respectively.

graphs in e^+e^- -annihilation, the interference between both production mechanisms contributes in general. On top of the Z^0 resonance the interference vanishes and the Z -graph dominates by 3 orders of magnitude over the γ -exchange graph. By measuring the asymmetries at energies around the Z^0 -resonance, the interplay between the $SU(2)$ and $U(1)$ gauge interaction can be tested and compared to the predictions of the Standard Model. The individual measurements are corrected for QCD effects as described in section 3.4 and subsequently compared to the predictions of the program ZFITTER [3]. Initial and final state photon radiation are included in the Standard Model predictions of ZFITTER, therefore the asymmetry measurements are not corrected for these effects. A top mass of $m_t = 174.1 \pm 4.9$ GeV and $\alpha_s = 0.119 \pm 0.003^{11}$ are used as Standard Model parameters. The mass of the Higgs boson was varied between $90 < m_H < 260$ GeV, where the lower limit is given by the direct searches at LEP2 and the upper limit corresponds to the 95% c.l. of the overall fit to the electroweak data of LEP and SLD [2]. As can be seen from figure 3.17, both the measurements on the Z^0 resonance as well as the off-peak points are in good agreement with the Standard Model predictions for the bottom and charm asymmetries, although the on-peak measurement of the bottom asymmetry is relatively low compared to the expectation.

Extraction of $\sin^2 \theta_W$

In order to extract some of the electroweak parameters of the Standard Model from the measured asymmetries, they have to be corrected for different effects, as mentioned earlier. The measured asymmetries have to be corrected for QED effects as described in section 1.2, i.e. for initial and final state photon radiation as well as for photon exchange in the vertex. Equations 1.6 and 1.7 are tree level formulae valid for the peak of the Z^0 resonance only. LEP, however, was operating at a mean energy, which was not exactly at the Z^0 mass. To correct for this, the measured values are shifted to match exactly the energy of the Z^0 boson mass. This is done using the Standard Model prediction for the energy dependence of the asymmetries according to ZFITTER. Even on top of the Z^0 resonance a small contribution of the γ exchange diagram exists, which has to be subtracted in order to extract the weak couplings or the weak mixing angle. These corrections are summarised in table 3.5.1 for the bottom and charm asymmetries.

The heavy flavour asymmetry measurements performed in the three energy ranges can be

¹¹The experimental error on α_s leads to negligible effects on the Standard Model prediction.

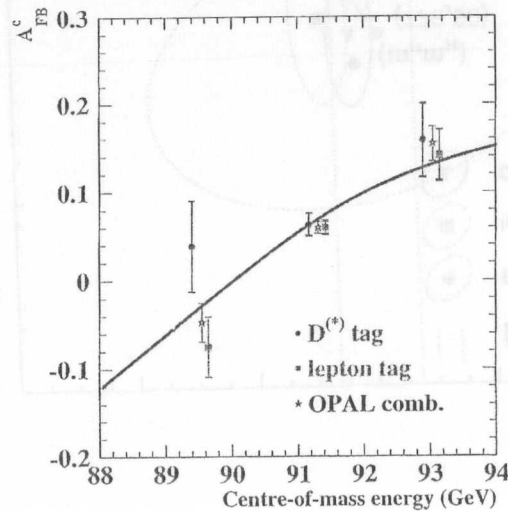
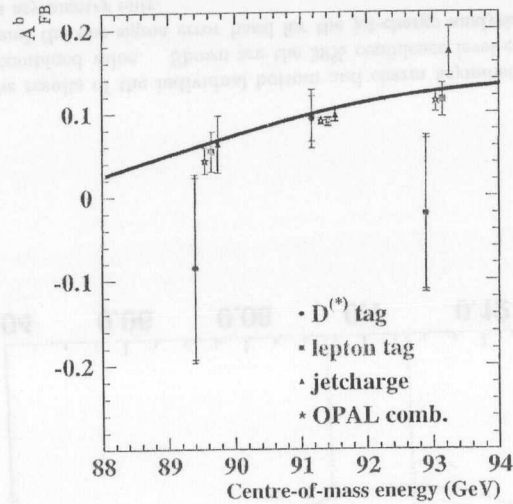


Figure 3.17: Summary of the results for the b and c asymmetries at energies on and around the pole of the Z resonance from different OPAL analyses and their combination. The inner error bars are the statistical errors, the outer ones mark the total error. The dark band shows the range of the Standard Model prediction for a Higgs mass between 90 and 260 GeV and a top mass of 174.1 ± 4.9 GeV.

Source	Shift in A_{FB}^b	Shift in A_{FB}^c
QED corrections	+0.0041	+0.0104
Photon exchange	-0.0003	-0.0008
Centre-of-mass energy	-0.0013	-0.0034

combined into one single measurement for each flavour by extrapolating the off-peak measurements to the peak using the standard model energy dependence predicted by ZFITTER. Here a top mass of 174 GeV and a Higgs mass of 100 GeV was used.

Applying the corrections discussed above and taking the correlations between the measurements into account, the combined value for the bare bottom and charm asymmetries yields

$$A_{FB}^{b,0} = 0.0968 \pm 0.0037 \quad \text{and} \quad A_{FB}^{c,0} = 0.0673 \pm 0.0064 ,$$

where the systematic and statistical errors have been combined in quadrature. The values of the bottom and charm asymmetry are correlated to 1.5%.

According to equation 1.6, the measurements of the quark forward-backward asymmetries A_{FB}^q allow the determination of the product of the asymmetry parameters \mathcal{A}_e of the electrons and \mathcal{A}_q of the quarks. Combining equations 1.6 and 1.2 shows, that from a measurement of the asymmetries the weak mixing angle can be extracted. It is possible to calculate the weak mixing angle $\sin^2 \theta_W^{\text{eff}}$ directly from a measurement of the leptonic asymmetries if lepton universality is assumed. In order to extract $\sin^2 \theta_W^{\text{eff}}$ from the heavy flavour asymmetries, either an input value for the electron asymmetry parameter is needed or the Standard Model relations for the heavy flavour couplings have to be assumed. The latter possibility allows a rather precise extraction of the mixing angle, because no further experimental errors enter. In order to derive the effective leptonic mixing angle, the radiative corrections for the electrons and the charm or bottom quarks, respectively, have to be used as input parameters, as can be seen by combining equations 1.8 and 1.10. They can be taken from the predictions of ZFITTER for example. With this method the results of the determination of the weak mixing angle from the bottom and charm forward-backward asymmetries are

$$A_{FB}^b : \sin^2 \theta_W^{\text{lept,eff}} = 0.23264 \pm 0.00066 \quad \text{and} \quad A_{FB}^c : \sin^2 \theta_W^{\text{lept,eff}} = 0.23300 \pm 0.00150 .$$

Taking into account the correlation of the bottom and charm asymmetries, the average of both measurements yields

$$\sin^2 \theta_W^{\text{lept,eff}} = 0.23270 \pm 0.00060 .$$

According to equation 1.6 the product of the weak coupling constants, i.e. the asymmetry parameter \mathcal{A}_f , can be extracted directly from a measurement of the forward-backward asymmetry A_{FB}^f by putting in the electron couplings. Using the value of $\mathcal{A}_e = 0.1489 \pm 0.0017$ [2], which is the combined result of the measurements performed at LEP and SLD, the bottom and charm asymmetry parameter can directly determined to be

$$\mathcal{A}_b = 0.867 \pm 0.035 \quad \text{and} \quad \mathcal{A}_c = 0.603 \pm 0.058 ,$$

where again the asymmetry parameters are correlated to 1.5%. In the Standard Model, values of $A_b = 0.935 \pm 0.001$ and $A_c = 0.668 \pm 0.003$ are expected assuming a top and Higgs mass of $m_t = 174.1 \pm 4.9$ GeV and $90 < m_H < 260$ GeV, respectively. Whereas the charm asymmetry parameter is in good agreement with the Standard Model, the bottom parameter is about two standard deviations below the expected value. This behaviour, which is even enhanced for the LEP and SLD combined values of the asymmetry parameters, will be discussed in more detail in the following section.

3.5.2 World Averages and Discussion

The heavy flavour forward-backward asymmetries are measured by all four LEP experiments using similar techniques as the ones described in section 3.2. The results of the individual measurements are summarised in figure 3.18 together with the combined result. The measurements at LEP give an average bottom asymmetry of $A_{FB}^b = 0.0990 \pm 0.0021$ and the mean value for the charm quarks is $A_{FB}^c = 0.0709 \pm 0.0044$. The combination of the bottom and charm asymmetry measurements is done by the heavy flavour LEP electroweak working group [2]. The values quoted here are the pole asymmetries, i.e. the results are corrected for QED effects and it is accounted for the photon exchange and interference terms. The QCD corrections have been applied, estimated individually for each of the analyses following the procedure suggested in [45] and explained in section 3.4. The result is a combined value of the three measurements at energies on and about 2 GeV above and below the Z^0 -pole, where the same method has been used as described in section 3.5.1 to transport the result to the energy of the Z-pole. In addition, the prediction of the Standard Model is shown as a function of the mass of the Higgs boson. The individual measurements are in good agreement with each other, and the combined result is comparable with the prediction of the Standard Model, especially if a relatively high mass of the Higgs boson is assumed. This can also be seen in the two dimensional contour plot 3.19 showing the LEP combined bottom and charm asymmetry values and their correlation. On the contrary, a combined fit to worlds electroweak precision data [2] clearly favours a light Higgs boson with an upper limit of 260 GeV at the 95% confidence level¹². The overall chi-square for the fit is 14.9/15 d.o.f., confirming the expectation of the Standard Model with a high probability of 46%. The Standard Model value resulting from this combined electroweak fit for the bottom asymmetry is $A_{FB}^b = 0.1028$ and $A_{FB}^c = 0.0734$ for charm quarks at a Higgs and a top mass of 76 GeV and 171.1 GeV, respectively. Thus the LEP combined result for the bottom asymmetry deviates 1.8σ from the Standard Model electroweak fit. Although being one of the largest deviations from the combined fit for the Standard Model, it could very well be a statistical fluctuation. For a fit of around 20 input parameters, a deviation as high as the observed value for the bottom asymmetry is expected.

The measurements of the heavy flavour forward-backward asymmetries can be used to derive a value for the weak mixing angle. As already explained in section 3.5.1 in order to extract $\sin^2 \theta_W^{\text{lept,eff}}$ from the asymmetries, the Standard Model relation for the hadronic coupling have to be assumed. In figure 3.20 the results of various measurements at LEP and SLC are summarised, from which the leptonic effective weak mixing angle is extracted. From the most recent data a mean LEP value of $\sin^2 \theta_W^{\text{lept,eff}} = 0.23189 \pm 0.00024$ can be derived, which is in reasonable agreement with the SLD measurement of $\sin^2 \theta_W^{\text{lept,eff}} = 0.23109 \pm 0.00029$. The LEP

¹²The mean value for the Higgs mass derived in the fit is 78 GeV, and thus already below the lower limit of approximately 90 GeV resulting from the direct searches [2] at LEP2.

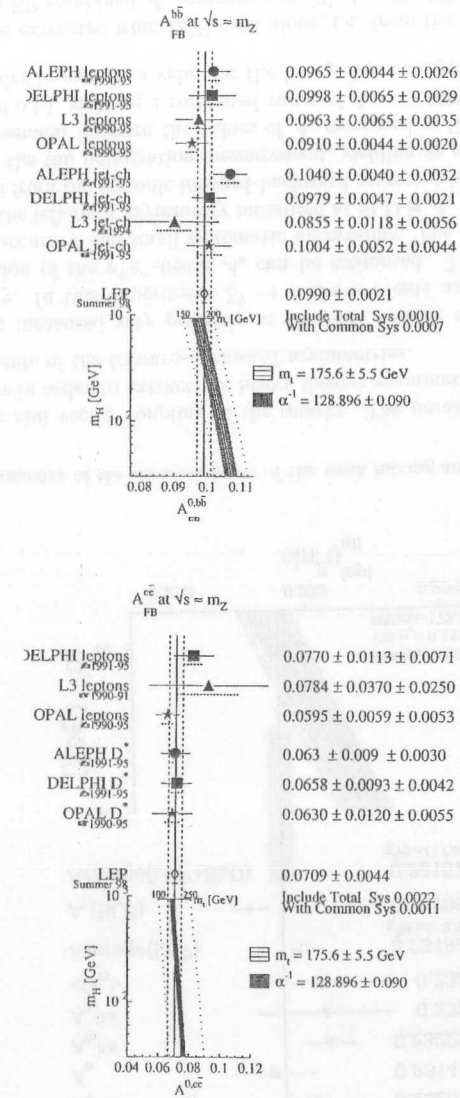


Figure 3.18: Summary of the LEP results for the bottom and charm asymmetries. The results given are the pole asymmetries.

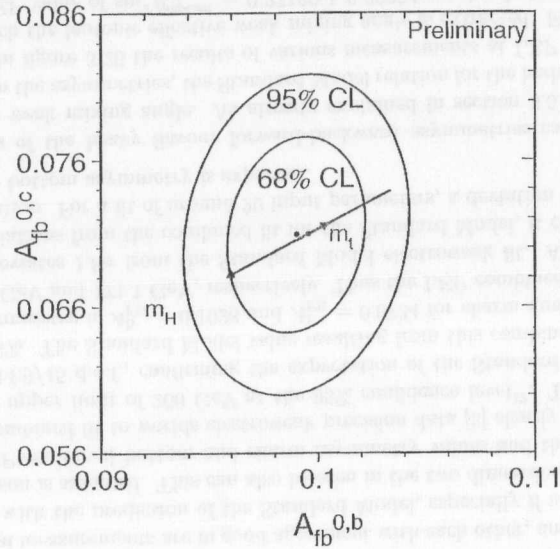


Figure 3.19: The LEP combined result for the bottom and charm forward-backward asymmetries as a two dimensional contour plot. In addition the Standard Model expectation is shown as a function of the Higgs boson and top quark mass.

and SLD average then yields $\sin^2 \theta_W^{\text{lept,eff}} = 0.23157 \pm 0.00018$. These results are summarised in table 3.21. The two most precise contributions, the SLD measurement and the value extracted from the bottom asymmetries at LEP, disagree by about 2.5σ , but the chi-square for the combination of all results shown in figure 3.20 yield a value of $\chi^2/\text{d.o.f.} = 7.6/6$ and thus a probability of around 25%. The values of $\sin^2 \theta_W^{\text{lept,eff}}$ extracted from earlier measurements of LEP and SLD (c.f. for example the values in the summer 1996, summarised in [53]) used to be $\sin^2 \theta_W^{\text{lept,eff}} = 0.23200 \pm 0.00027$ and $\sin^2 \theta_W^{\text{lept,eff}} = 0.23061 \pm 0.00047$, respectively, and thus showed a much stronger deviation.

	$\sin^2 \theta_W^{\text{lept,eff}}$
LEP	0.23189 ± 0.00024
SLD	0.23109 ± 0.00029
combined	0.23157 ± 0.00018

Table 3.21: Summary of the measurements of the effective weak mixing angle performed at LEP and SLD.

The asymmetry parameter \mathcal{A}_q as defined in equation 1.6 measures directly the product of

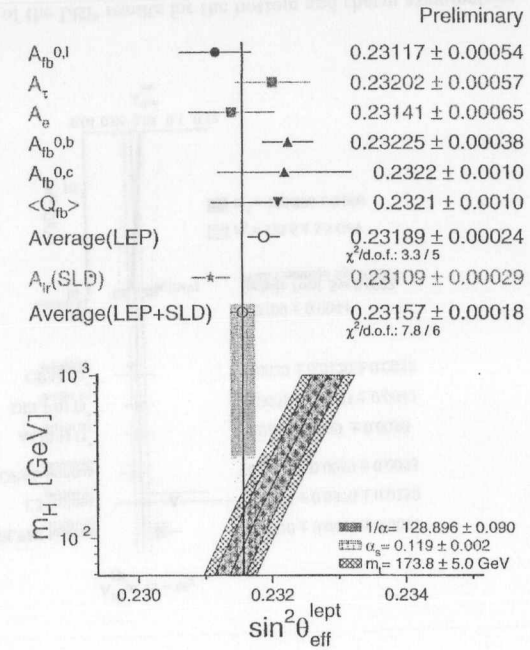


Figure 3.20: Summary of the measurements of the weak mixing angle performed at LEP and SLD.

the axial-vector and vector coupling of the quarks. The parameter \mathcal{A}_e has to be used as an input parameter in order to extract the heavy flavour asymmetry parameters \mathcal{A}_c and \mathcal{A}_b from LEP measurements of the forward-backward asymmetries.

\mathcal{A}_e has been measured very precisely at the SLC collider via a measurement of the left-right asymmetry. In this experiment $Z^0 \rightarrow \text{hadrons}$ events are counted and by making use of the polarisation of the e^+e^- -beam \mathcal{A}_e can be estimated. The result is a measurement of high statistical accuracy and small systematic uncertainty. The electron asymmetry parameter extracted from the left-right asymmetry measured at SLD is $\mathcal{A}_e = 0.1504 \pm 0.0023$. At LEP \mathcal{A}_e can be extracted from the leptonic forward-backward asymmetries assuming lepton universality or directly from the tau polarisation measurement, yielding an average value of $\mathcal{A}_e = 0.1469 \pm 0.0027$. The agreement between the values of \mathcal{A}_e measured at SLC and LEP is good (the chi-square is $2.2/2$ d.o.f.), yielding a combined value of $\mathcal{A}_e = 0.1489 \pm 0.0017$. Two scenarios can be applied in order to extract a value for the heavy flavour asymmetry parameters:

- $\mathcal{A}_{b,c}$ can be extracted from LEP data alone, i.e. from the heavy flavour asymmetries by using the LEP combined \mathcal{A}_e measurement [2] $\mathcal{A}_e = 0.1469 \pm 0.0027$. This yields

$$\mathcal{A}_b = 0.899 \pm 0.025 \quad \text{and} \quad \mathcal{A}_c = 0.644 \pm 0.041.$$

Profiting from the polarisation of the e^+e^- -beam, the heavy flavour asymmetry parameters can be measured directly at SLC via the left-right/forward-backward asymmetries,

yielding values of

$$\mathcal{A}_b = 0.867 \pm 0.035 \quad \text{and} \quad \mathcal{A}_c = 0.647 \pm 0.040.$$

Thus the LEP results can be compared to the values measured directly at SLD, which is done in table 3.22. The results are in good agreement with each other. Both values for \mathcal{A}_b are about one standard deviation low compared to the Standard Model value of $\mathcal{A}_b = 0.935$. The agreement for charm is excellent, both, among the measurements and compared to the Standard Model expectation of $\mathcal{A}_c = 0.668$, although the relative errors are larger compared to the measurements of the bottom quarks.

- Alternatively the world average for $\mathcal{A}_{b,c}$ can be extracted from the measurements of the LEP forward-backward asymmetries with help of the combined value for \mathcal{A}_e from the SLD and LEP measurements, and subsequently the measurements of the asymmetry parameters from SLD are included in the average. The results are

$$\mathcal{A}_b = 0.881 \pm 0.018 \quad \text{and} \quad \mathcal{A}_c = 0.641 \pm 0.028.$$

Again the value for the bottom quarks is low (about 3σ), whereas the results for charm is in good agreement with the expectation of the Standard Model.

	\mathcal{A}_b	\mathcal{A}_c
LEP ($\mathcal{A}_e = 0.1469 \pm 0.0027$)	0.899 ± 0.025	0.644 ± 0.041
SLD	0.867 ± 0.035	0.647 ± 0.040
combined ($\mathcal{A}_e = 0.1489 \pm 0.0017$)	0.881 ± 0.018	0.641 ± 0.028
Standard Model	0.935	0.668

Table 3.22: Summary of the values for the bottom and charm asymmetry parameters as extracted from LEP and SLD measurements. In addition the Standard Model expectation is given, where the input parameters are taken from the best fit to the electroweak data as given in [2].

The discussion above shows, that this deviation of 3σ in the latter scenario is a combined effect of the low value of the bottom forward-backward asymmetry and the low result of the electron asymmetry parameter and could, again, very well be a statistical fluctuation. Nevertheless it is interesting that the largest deviation is found in the third generation of quarks, where the discovery of New Physics is most probably expected. It is worthwhile to study the result found for the bottom asymmetry parameter together with what is found for the partial width of $Z^0 \rightarrow b\bar{b}$, R_b . The experimental result for R_b differed from the expectation of the Standard Model by as much as 3.7σ [23], but today the discrepancy is reduced to a 0.9σ effect by new measurements with higher statistics and fined systematic investigations. It is thus interesting to ask whether the deviation in the partial decay width into $b\bar{b}$ -quark pairs and in the forward-backward asymmetry of the bottom quark together could give a hint to new physics. The deviation in the partial width used to cause a lot of discussion and a variety of possible explanations were suggested in terms of extensions of the Standard Model.

Alternatively to the equations 1.4 and 1.6 of section 1.2, R_b and \mathcal{A}_b can be expressed in terms of the right- and lefthanded coupling constants like

$$\Gamma_{f\bar{f}} \propto (c_L^f)^2 + (c_R^f)^2 \quad \text{and} \quad (3.32)$$

$$\mathcal{A}_f = \frac{(c_L^f)^2 - (c_R^f)^2}{(c_L^f)^2 + (c_R^f)^2}. \quad (3.33)$$

Equation 3.33 is equivalent to

$$\frac{|c_L^f|}{|c_R^f|} = \sqrt{\frac{1 + \mathcal{A}_f}{1 - \mathcal{A}_f}}, \quad (3.34)$$

i.e. the ratio of the left- to righthanded couplings can directly be derived from the asymmetry parameters. Thus, a measurement of the asymmetry gives information about the relative strength of the left- and righthanded coupling parameters. Using the mean value of $\mathcal{A}_b = 0.881 \pm 0.018$ (c.f. table 3.22), the ratio of the left- to righthanded coupling can be extracted to be $|c_L^b|/|c_R^b| = 3.98 \pm 0.35$. From the Standard Model a ration of $|c_L^b|/|c_R^b| = 5.46$ is expected. Together with the R_b measurements which yield a value 0.9σ high compared to the Standard Model, this suggests that the righthanded coupling of the b-quark is higher than expected. None of the popular extensions of the Standard Model, like for example the MSSM (the minimal supersymmetric extension of the Standard Model), could account for these effects of the two measurements R_b and \mathcal{A}_b . It is for example unlikely that the deviations arise from new physics in the form of radiative corrections, because the correction parameter κ_b (c.f. equation 1.8) would have to deviate about 30% from the Standard Model value. The only possible explanation would be an extension, which couples on tree level and influences mainly the righthanded coupling of the third generation of quarks, without contradicting the measurement of R_b . One, although a fairly remote, possibility to explain the deviations in both quantities could be a scalar neutrino ($\tilde{\nu}$) resonance in R-parity violating supersymmetric models [54]. Because in most of the models discussed at presence, the scalar fields of the third generation are lighter than the first two, it would be expected to discover the resonance of the third generation, $\tilde{\nu}_\tau$, at the lowest energy. Assuming that such a $\tilde{\nu}_\tau$ -sneutrino would cause the deviations in R_b and \mathcal{A}_b , it would couple primarily to the $b\bar{b}$ -pairs, i.e. the third generation of quarks. The mass of the sneutrino could be around the mass of the Z^0 boson, resulting in a hidden $\tilde{\nu}$ -resonance in the s-channel. According to [54], the chi-square in a combined fit to the line-shape of the Z^0 and the heavy flavour electroweak observables¹³ could be improved from $\chi^2/\text{d.o.f.} = 60.6/54$ to around $\chi^2/\text{d.o.f.} = 54/51$ by allowing for a sneutrino resonance as described above, which could be interpreted as a slight improvement in the probability for such a scenario. The extracted line-shape parameters from this fit are almost identical to the Standard Modelvalue, except that the value for the hadronic cross-section is reduced by two thirds of a standard deviation. The improvement in the fit probability is mainly due to R_b ($\chi^2/\text{d.o.f.}$ reduced from 4.5 to 0.1) and to \mathcal{A}_b , yielding now a $\chi^2/\text{d.o.f.}$ of 1.4 instead of 2.6 without assuming a sneutrino resonance. Thus the usual line-shape parameters could be extracted with about the same agreement as the Standard Model line-shape fit by a simultaneous improvement in the couplings of the third quark generation.

¹³This analysis is based on the electroweak data of summer 1997, where the deviation of the LEP and SLD average of \mathcal{A}_b compared to the Standard Model was also as large as 3σ and the measured value for R_b differed by about 1.6σ from the expectation.

Chapter 4

Measurement of the Triple Gauge Boson Couplings with the Spin Density Matrix Method

4.1 Introduction

In lowest order, W pairs are produced in e^+e^- collision via the Feynman diagrams depicted in figure 4.1. The production mechanism shown in the first sketch of this figure allows a direct test of the couplings among the three gauge bosons $WW\gamma$ and WWZ . This is an important test of the $SU(2)_L \times U(1)_Y$ gauge invariance of the Standard Model. Whereas the couplings

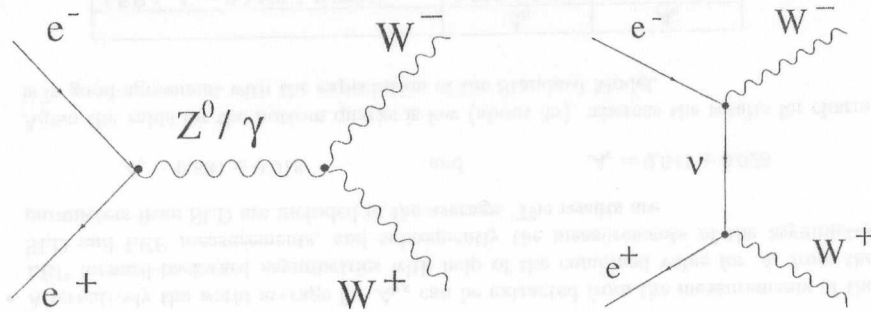


Figure 4.1: Feynman diagrams of W pair production in e^+e^- collision.

of the gauge bosons to fermions have been measured rather precisely, particularly at LEP and SLC, the self coupling of the vector bosons is experimentally not yet very well exploited. The W pair production in the clean environment of an e^+e^- collider is the ideal laboratory for an investigation of the trilinear gauge boson vertices $WW\gamma$ and WWZ .

Although there are indirect tests of the trilinear vector boson vertices and limits on anomalous couplings – mostly from precision tests of the electroweak physics at LEP1 – these tests allow restrictions on single triple gauge coupling (TGC) parameters only and not on the combination of different anomalous coupling parameters. Cancellations between different anomalous

couplings could have inhibited the detection of anomalous triple gauge couplings. Moreover, the deduction of these bounds from virtual contributions in precision measurements is possible only under the assumption of specific models of new physics. Thus, the bounds derived from these indirect tests of the trilinear gauge boson vertex can only serve as an order of magnitude estimate as long as the underlying physics is not specified [55]. Therefore, these indirect tests cannot replace direct measurements of the gauge boson couplings.

In this thesis a method for testing the trilinear gauge boson vertices is described which uses observables closely related to the polarisation of the W bosons, the so-called spin density matrix method. Additional insight into the underlying physics may be gained by visualising these spin-related observables, and a direct comparison of the production of different helicity states of the W pairs can be obtained. Explicit examination of the helicity amplitudes ensures that no cancellations or correlations of anomalous couplings escape detection. Moreover, if any deviations from the Standard Model are found, the measurement of the polarisation of the W would be helpful to disentangle different anomalous couplings. In addition, with the help of the spin density matrix elements the transverse and longitudinally polarised cross-section of the W -production can be derived.

In the following sections, the spin density matrix method is introduced. The extraction of the density matrix elements allows the determination of the contributions of the different helicity states. Comparing the spin density matrix elements with the theoretical predictions allows a model-independent test of the triple gauge couplings and the origin of anomalous couplings could be tracked down if deviations from the Standard Model are detected. Subsequently, a fit is performed in order to quantify the results and either measure or restrict anomalous couplings. Two different methods of accounting for experimental effects are discussed. For this analysis the OPAL data taken in the year 1997 with a centre-of-mass energy of 183 GeV are used. Finally these results are combined with other OPAL measurements and the limits derived are compared to the world averages of triple gauge boson coupling.

4.2 Phenomenology of the Triple Gauge Couplings

4.2.1 The Trilinear Gauge Boson Vertex

The most general Lorentz invariant effective Lagrangian describing the couplings of two charged vector bosons with a neutral one, WWV , with $V = Z, \gamma$ can be split into four components with different behaviour under the transformations of parity (P) and charge conjugation (C) [56, 57]:

$$\mathcal{L}_{\text{eff}}^{WWV} = \mathcal{L}_{C,P}^{WWV} + \mathcal{L}_{\mathcal{C},CP}^{WWV} + \mathcal{L}_{\mathcal{C},P}^{WWV} + \mathcal{L}_{P,C}^{WWV}, \quad (4.1)$$

where the individual components are given by

$$\begin{aligned} \mathcal{L}_{C,P}^{WWV} &= (-i)g_{WWV} \left[g_1^V V^\mu (W_{\mu\nu}^- W^{+\nu} - W_{\mu\nu}^+ W^{-\nu}) + \kappa_V W_\mu^- W_\nu^+ V^{\mu\nu} + \frac{\lambda_V}{m_W^2} V^{\mu\nu} W_\nu^{+\rho} W_{\rho\nu}^- \right] \\ \mathcal{L}_{\mathcal{C},CP}^{WWV} &= g_{WWV} \cdot g_5^V \epsilon_{\mu\nu\rho\sigma} [(\partial^\rho W^{-\mu}) W^{+\nu} - W^{-\mu} (\partial^\rho W^{+\nu})] V^\rho \\ \mathcal{L}_{\mathcal{C},P}^{WWV} &= g_{WWV} \cdot g_4^V W_\mu^- W_\nu^+ (\partial^\mu V^\nu + \partial^\nu V^\mu) \\ \mathcal{L}_{P,C}^{WWV} &= ig_{WWV} \left[\frac{\tilde{\kappa}_V}{2} W_\mu^- W_\nu^+ \epsilon_{\mu\nu\rho\sigma} V_{\rho\sigma} + \frac{\tilde{\lambda}_V}{2m_W^2} W_{\rho\mu}^- W_\nu^{+\mu} \epsilon_{\nu\rho\alpha\beta} V_{\alpha\beta} \right]. \end{aligned} \quad (4.2)$$

Here the former two components are CP conserving, whereas the latter violate CP invariance. For this Lagrangian it is assumed, that the vector bosons couple to effectively massless fermions. Here the overall coupling constants are defined as $g_{WW\gamma} = e$ and $g_{WWZ} = e \cot \theta_W$, where θ_W is the weak mixing angle and the following notation is adopted: $W_{\mu\nu} = \partial_\mu W_\nu - \partial_\nu W_\mu$ and accordingly $V_{\mu\nu} = \partial_\mu V_\nu - \partial_\nu V_\mu$. From equation 4.2 it follows, that in the most general case the triple gauge boson vertex can be described by seven electromagnetic and seven weak coupling parameters. Within the Standard Model, at tree level, the couplings are given by $g_1^Z = g_1^\gamma = \kappa_Z = \kappa_\gamma = 1$, whereas all other couplings vanish. Thus, in the Standard Model only C and P conserving trilinear gauge couplings exist. Throughout this thesis the couplings are expressed as the deviations from the tree-level Standard Model values, using the notation

$$\begin{aligned} \Delta g_1^Z &\equiv (g_1^Z - 1), & \Delta g_1^\gamma &\equiv (g_1^\gamma - 1) \\ \Delta \kappa_Z &\equiv (\kappa_Z - 1), & \Delta \kappa_\gamma &\equiv (\kappa_\gamma - 1). \end{aligned} \quad (4.3)$$

For the electromagnetic coupling to the W bosons, the C and P conserving terms are directly connected with the lowest order terms in a multipole expansion. The charge q_W , the magnetic dipole moment μ_W and the electric quadrupole moment Q_W^e can be related to the CP coupling parameters in equation 4.2 via

$$\begin{aligned} q_W &= eg_1^\gamma \\ \mu_W &= \frac{e}{2m_W}(g_1^\gamma + \kappa_\gamma + \lambda_\gamma) \\ Q_W^e &= -\frac{e}{m_W^2}(\kappa_\gamma - \lambda_\gamma), \end{aligned} \quad (4.4)$$

while the CP-violating parameters are related to the electric dipole moment d_W and magnetic quadrupole moment Q_W^m according to

$$\begin{aligned} d_W &= \frac{e}{2m_W}(\tilde{\kappa}_\gamma + \tilde{\lambda}_\gamma) \\ Q_W^m &= -\frac{e}{m_W^2}(\tilde{\kappa}_\gamma - \tilde{\lambda}_\gamma). \end{aligned} \quad (4.5)$$

4.2.2 Parametrisations of the Triple Gauge Boson Couplings

As already mentioned in section 4.2.1, the most general coupling of the triple gauge boson vertex can be parametrised by altogether 14 different coupling parameters. Due to the limited statistic of W^+W^- -pair production at LEP2 it is desirable to reduce the number of couplings to be tested. For real photons the relation $g_1^\gamma = 1$ can be derived from electromagnetic gauge invariance¹, describing the electric charge of the W-boson to be $q_W = \pm e$ [4]. By restricting to the C and P conserving couplings only, the number of possible deviations from the Standard Model couplings reduces to the following five coupling parameters: $\Delta g_1^Z, \Delta \kappa_Z, \Delta \kappa_\gamma, \lambda_Z, \lambda_\gamma$.

The number of parameters can be further reduced by concentrating on parameters which are not severely constrained by LEP1 or other precision low energy data. Especially vertex extensions, which affect the triple gauge boson vertex already at tree level are unlikely to be compatible with low energy measurements, unless accidental cancellations disturb these indirect derivations of the gauge coupling parameters. Moreover it is desirable to embed the non-standard TGC into a theory which obeys the local $SU(2)_L \times U(1)_Y$ symmetry [55, 58, 59].

A low energy approximation can be expressed with the help of a dimensional analysis of the most general Lagrangian given in equations 4.1 and 4.2. This procedure corresponds to the

¹For $q^2 \neq 0$ deviations are possible because of form factor effects

'linear realisation' [4, 59] of the gauge symmetry and is applicable if a light Higgs particle with a mass lower than around 1000 GeV exists. Then a Taylor expansion in the field dimension d can be performed and the operators describing the physics beyond the Standard Model can be expressed in a power series in v^2/Λ^2 , where v is the vacuum expectation of the Higgs boson and Λ denotes the scale of new physics. In a $SU(2)_L \times U(1)_Y$ invariant theory and with the restriction to operators of dimension six or lower, then there exist only three independent operators to extend the Standard Model triple gauge boson coupling vertex, without affecting the triple gauge boson coupling vertex already at tree level or involving anomalous Higgs couplings. The possible extensions of the Standard Model Lagrangian obeying these constraints are the following:

$$\begin{aligned} \mathcal{L}_W &= g \cdot \alpha_W \frac{1}{6m_W} \hat{W}^\mu \cdot (\hat{W}^\nu_\rho \times \hat{W}^\rho_\mu) \\ \mathcal{L}_{W\Phi} &= ig \cdot \alpha_{W\Phi} \frac{1}{m_W} (D_\mu \Phi)^\dagger \tau \hat{W}^{\mu\nu} (D_\nu \Phi) \\ \mathcal{L}_{B\Phi} &= -ig' \cdot \alpha_{B\Phi} \frac{1}{m_W} (D_\mu \Phi)^\dagger B^{\mu\nu} (D_\nu \Phi), \end{aligned} \quad (4.6)$$

where $\hat{W}_{\mu\nu} = W_{\mu\nu} - gW_\mu \times W_\nu$ are the non-abelian field strength tensors. Here the quadrupole interaction \mathcal{L}_W describes purely transverse vertices of three or more vector bosons. For the dipole interactions $\mathcal{L}_{W\Phi}$ and $\mathcal{L}_{B\Phi}$ also longitudinally degrees of freedom are involved.

The parameters $\alpha_W, \alpha_{W\Phi}$ and $\alpha_{B\Phi}$ can be expressed in terms of the five C and P conserving parameters like [58, 59]

$$\begin{aligned} \alpha_{B\Phi} &= \Delta \kappa_\gamma - \Delta g_1^Z \cos^2 \theta_W \\ \alpha_{W\Phi} &= \Delta g_1^Z \cos^2 \theta_W \\ \alpha_W &= \lambda_\gamma, \end{aligned} \quad (4.7)$$

using the following constraints which arise from gauge invariance:

$$\begin{aligned} \Delta \kappa_Z &= \Delta \kappa_\gamma \tan^2 \theta_W + \Delta g_1^Z \\ \lambda_Z &= \lambda_\gamma. \end{aligned} \quad (4.8)$$

Single parameter extensions like $\mathcal{L}_{W\Phi}$, i.e. $\mathcal{L}_W = \mathcal{L}_{B\Phi} = 0$, can be interpreted as excluding WW scattering amplitudes growing as s^2 [59]. A dipole interaction like $\mathcal{L}_{W\Phi} - \mathcal{L}_{B\Phi}$, i.e. a deviation of g_{ZW} alone, would describe the effects of the novel heavy vector boson triplet with potentially strong self-coupling, but without any couplings to ordinary fermions [58]. According to equation 4.7, in case of a one-parameter model the following parameters are equivalent:

$$\begin{aligned} \alpha_{B\Phi} &\equiv \Delta \kappa_\gamma \\ \alpha_W &= \lambda_\gamma. \end{aligned} \quad (4.9)$$

In reference [55] another model with the additional constraint $\alpha_{B\Phi} = \alpha_{W\Phi}$ is proposed. It is equivalent to

$$\Delta g_1^Z = \Delta \kappa_\gamma^{(HISZ)} / (2 \cos^2 \theta_W), \quad (4.10)$$

leading to a reduced parameter set of $\Delta \kappa_\gamma^{(HISZ)}$ and λ_γ . This scenario might naturally be expected in a composite Higgs model [55].

In the absence of a light Higgs boson a non-linear realisation of the symmetry breakdown has to be assumed. Then the dimensional analysis cannot be employed, because v and Λ are no longer independent. Nevertheless the considerations of a 'naive dimensional analysis' show,

that the parameters Δg_1^2 , $\Delta \kappa_\gamma$ and $\Delta \kappa_Z$ (and thus $\alpha_{W\Phi}$ and $\alpha_{B\Phi}$) would be expected to be the dominant ones, whereas here the λ_γ and λ_Z (and correspondingly α_W) terms are negligible.

The analogous considerations with respect to the dimensional analysis and the gauge invariance as for the C and P conserving parts of the Lagrangian can be carried out for the CP-violating parts [60]. In that case the restriction to $SU(2)_L \times U(1)_Y$ -invariant operators of dimension six lead to two possible CP-violating extensions of the Standard Model:

$$\begin{aligned}\tilde{\mathcal{L}}_{BW} &= gg' \cdot \tilde{\alpha}_{BW} \frac{1}{2m_W^2} \Phi^{\dagger \frac{\tau}{2}} \cdot \hat{W}^{\mu\nu} \Phi B_{\mu\nu} \\ \tilde{\mathcal{L}}_W &= g \cdot \tilde{\alpha}_W \frac{1}{m_W^2} \frac{1}{3!} (\hat{W}_\rho^\mu \times \hat{W}_\nu^\rho) \cdot \frac{1}{2} \epsilon^{\mu\nu\rho\sigma} \hat{W}_\sigma^\rho.\end{aligned}\quad (4.11)$$

Here the parameters $\tilde{\alpha}_{BW}$ and $\tilde{\alpha}_W$ are related to the CP-violating parameters in equation 4.2 via

$$\begin{aligned}\tilde{\alpha}_{BW} &= \tilde{\kappa}_\gamma \\ \tilde{\alpha}_W &= \tilde{\lambda}_\gamma,\end{aligned}\quad (4.12)$$

with the following constraints from gauge invariance:

$$\begin{aligned}\tilde{\kappa}_Z &= -\tan^2 \theta_W \tilde{\kappa}_\gamma \\ \tilde{\lambda}_Z &= \tilde{\lambda}_\gamma.\end{aligned}\quad (4.13)$$

4.2.3 W-Pair Production and Polarisation of the W Bosons

In the following two paragraphs the phenomenology of the W-pair production and the trilinear gauge boson vertex will be briefly and qualitatively summarised, before a more detailed and formal description will be given.

As already mentioned three different graphs contribute to the W-pair production. In only two of them the triple gauge boson vertex is involved. For an investigation of the polarisation properties of the W bosons these contributions have to be disentangled. A simple method of testing the triple gauge boson vertex is the investigation of the total W-pair production cross-section, as will be explained in the following paragraph. Each of the three production mechanisms on its own would show a divergent behaviour in the cross-section, i.e. a rise proportional to s or even s^2 . Only the sum of all contributions has a good high energy behaviour. This is because the steeply rising terms of the cross-section of the individual production mechanisms cancel. This behaviour is called 'gauge cancellations' and the level of cancellation depends on the centre-of-mass energy. Anomalous couplings would alter this gauge cancellations and cause a violation of unitarity, if not at higher energies new physics comes into play. Possible differences between the Standard Model expectation and new physics would be more pronounced for energies well above the W-pair production threshold, where the affected terms are already cancelled in the Standard Model.

Another method to distinguish the individual production mechanisms is to investigate the distribution in the W production angle θ of the W^- compared to the incoming electron. For example the t -channel exchange shows a forward peaked structure in the production angle θ , which is typical for a t -channel process. In addition, the polarisation of the W-pairs is different for the individual contributions. Consequently additional information on the trilinear gauge boson vertex can be gained from the helicity of the W bosons. The polarisation of the

instantaneously decaying W bosons can be determined from their decay products since the well-known V-A structure of the W decay can be utilised as a polarisation analyser. Experimentally, the observables used for this purpose are the W decay angles, i.e. the polar and azimuthal angle $\cos \theta^*$ and ϕ^* of each of the fermions resulting from a W decay in the W rest frame. The relative contribution of the different helicity states varies as a function of the W production angle θ . Thus in the event shape analysis the five-fold differential cross-section $d\sigma/d \cos \theta_W d \cos \theta_{W^-}^* d\phi_{W^-}^* d \cos \theta_{W^+}^* d\phi_{W^+}^*$ is investigated.

The W boson, carrying one unit of angular momentum, has three possibilities to adjust its spin, resulting in three helicity states $\tau_W = \pm 1$ or 0. In the following τ_- and τ_+ denote the helicity states of the W^- and W^+ , respectively. For the reaction $e^-(\lambda)e^+(\lambda') \rightarrow W^-(\tau_-)W^+(\tau_+)$ there are nine different helicity amplitudes $\mathcal{F}_{\tau_-\tau_+}^{(\lambda)}$ for each of the two possible helicity states of the e^+e^- system ($\lambda = -\lambda' = \pm 1/2$)².

The helicity amplitudes $\mathcal{F}_{\tau_-\tau_+}^{(\lambda)}$ for the process $e^+e^- \rightarrow W^+W^-$ are given by the sum over all contributing production mechanisms

$$\mathcal{F}_{\tau_-\tau_+}^{(\lambda)} = \mathcal{F}_\gamma + \mathcal{F}_Z + \mathcal{F}_\nu. \quad (4.14)$$

The dominant angular dependence of the helicity amplitudes originates from the rotation of the angular momentum of the W^+W^- system compared to the e^+e^- initial state. It can be expressed with the help of the spin rotation d -functions (see for example [38]). The reduced amplitudes $\tilde{\mathcal{F}}$ are defined as

$$\mathcal{F}_{\tau_-\tau_+}^{(\lambda)}(\theta) = \sqrt{2}\lambda e^2 \tilde{\mathcal{F}}_{\tau_-\tau_+}^{(\lambda)}(\theta) d_{\lambda, \Delta\tau}^{J_0}(\theta), \quad (4.15)$$

where J_0 is the lowest angular momentum contributing to the process and $\Delta\tau = \tau_- - \tau_+$. For $(\tau_+, \tau_-) = (\pm, \mp)$, i.e. a spin of $\Delta\tau = 2$, only the t -channel neutrino exchange contributes because of angular momentum conservation. In the limit of massless fermions the electron has to be lefthanded ($\lambda = -1/2$) for this configuration. The corresponding amplitude is

$$\mathcal{F}_{\tau_-(\tau_+ = -\tau_-)}^{(-1/2)}(\theta) = -\sqrt{2}e^2 \frac{-\sqrt{2}}{\sin^2 \theta_W} \frac{1}{1 + \beta^2 - 2\beta \cos \theta} (\tau_-) \sin \theta (1 - (\tau_-) \cos \theta)/2, \quad (4.16)$$

where β is the velocity of the W boson $\beta = \sqrt{1 - m_W^2/s}$. For all other helicity amplitudes there are also contributions from the s -channel Z^0 - and γ -exchange. The reduced amplitudes $\tilde{\mathcal{F}}$ are then given in the limit of massless fermions by

$$\begin{aligned}\tilde{\mathcal{F}}_\gamma &= -\beta A_{\tau_-\tau_+}^\gamma \\ \tilde{\mathcal{F}}_Z &= \beta A_{\tau_-\tau_+}^Z \left[(1 - \delta_{\lambda, -1/2}) \frac{1}{2 \sin^2 \theta_W} \right] \frac{s}{s - m_Z^2} \\ \tilde{\mathcal{F}}_\nu &= (\delta_{\lambda, -1/2}) \frac{1}{2\beta \sin^2 \theta_W} \left[B_{\tau_-\tau_+} - \frac{1}{1 + \beta^2 - 2\beta \cos \theta} C_{\tau_-\tau_+} \right].\end{aligned}\quad (4.17)$$

The subamplitudes A , B and C are given in table 4.1.

The helicity amplitude for $\Delta\tau = 2$ (c.f. equation 4.17 and table 4.1) shows a good high energy behaviour (i.e. non-divergent), whereas the contributions from the individual feynman graphs involving longitudinally polarised (i.e. $\tau_W = 0$) W bosons grow with the energy. In the

²In the limit where the electron and positron mass is neglected

(τ_+, τ_-)	$\Delta\tau$	$A_{\tau_-\tau_+}^V$	$B_{\tau_-\tau_+}$	$C_{\tau_-\tau_+}$	$d_{\lambda, \Delta\tau}^{J_0}$
(++)	0	$g_1^V + 2\gamma^2\lambda_V + (i/\beta)(\bar{\kappa}_V + \bar{\lambda}_V - 2\gamma^2\bar{\lambda}_V)$	1	$1/\gamma^2$	$-\sigma \sin \theta / \sqrt{2}$
(---)	0	$g_1^V + 2\gamma^2\lambda_V - (i/\beta)(\bar{\kappa}_V + \bar{\lambda}_V - 2\gamma^2\bar{\lambda}_V)$	1	$1/\gamma^2$	$-\sigma \sin \theta / \sqrt{2}$
(00)	0	$g_1^V + 2\gamma^2\kappa_V$	$2\gamma^2$	$2/\gamma^2$	$-\sigma \sin \theta / \sqrt{2}$
(+0)	1	$\gamma(f_3^V - ig_4^V + \beta g_5^V + (i/\beta)(\bar{\kappa}_V - \bar{\lambda}_V))$	2γ	$2(1 + \beta)/\gamma$	$(1 + \sigma \cos \theta) / 2$
(0-)	1	$\gamma(f_3^V + ig_4^V + \beta g_5^V - (i/\beta)(\bar{\kappa}_V - \bar{\lambda}_V))$	2γ	$2(1 + \beta)/\gamma$	$(1 + \sigma \cos \theta) / 2$
(0+)	-1	$\gamma(f_3^V + ig_4^V - \beta g_5^V + (i/\beta)(\bar{\kappa}_V - \bar{\lambda}_V))$	2γ	$2(1 - \beta)/\gamma$	$(1 - \sigma \cos \theta) / 2$
(-0)	-1	$\gamma(f_3^V - ig_4^V - \beta g_5^V - (i/\beta)(\bar{\kappa}_V - \bar{\lambda}_V))$	2γ	$2(1 - \beta)/\gamma$	$(1 - \sigma \cos \theta) / 2$

Table 4.1: Subamplitudes A, B and C for the reduced helicity amplitudes $\bar{\mathcal{F}}$ for processes with a transfer of the total angular momentum of $J_0 = 1$. Here γ is defined as $\gamma = \sqrt{s}/2m_W$ and f_3^V denotes the combination of coupling parameters $f_3^V = g_1^V + \kappa_V + \bar{\lambda}_V$. In the Standard Model $g_1^V = 1$ for $V = Z^0, \gamma$, whereas all other coupling constants vanish.

Standard Model gauge cancellations between the various production mechanisms ensure a good high energy behaviour. Within the Standard Model the subamplitudes A^Z and A^γ are equal and thus the ‘electromagnetic’ terms in equation 4.17 cancel except for the difference between the photon and Z Boson propagator. Similarly, the purely weak term of the Z-exchange graph (i.e. the second term of $\bar{\mathcal{F}}_Z$) and the first term of the t -channel contribution, $\bar{\mathcal{F}}_\nu$, cancel in their asymptotic ($\gamma \rightarrow \infty$) form. The second term in the ν -exchange graph converges even in the high energy limit. For energies near the WW-production threshold, and thus for energies relevant for LEP2 analyses, these terms are not yet totally cancelled. Numerically, at a centre-of-mass energy of $\sqrt{s} = 183$ GeV, approximately 65% of the γ exchange amplitude is cancelled by the according ‘electromagnetic’ term of the Z exchange, whereas only 30% of the ‘weak isovector part’ of the Z exchange is cancelled by the ν exchange contribution, as can be seen from equation 4.17 and table 4.1. Therefore the investigation of the total cross-section of the W production, where the effects of the cancellation becomes directly visible, are expected to be less sensitive to anomalous couplings than for higher energies. On the other hand the W-pair production cross-section is not yet totally dominated by the helicity combination $(-+)$ from the t -channel ν -exchange diagram. Interference terms between the ν -exchange graph and graphs involving the triple gauge boson vertex would enhance any differences from the Standard Model and the experimental sensitivity to measure the coupling parameters is increased. A detailed analysis of the helicity amplitudes of the W production thus provides useful information in addition to the measurement of the total cross-section.

The various helicity cross-sections (or combinations) as a function of the W^- production angle $\cos \theta$ are shown for an unpolarised e^+e^- initial state in figure 4.2 a). The interferences between the different production mechanisms of the individual W helicity states are clearly visible and help to discriminate between the various helicity states, i.e. the contributions of the longitudinally polarised W bosons is enhanced by the interference with the dominant ν exchange contribution. This characteristic behaviour allows to disentangle the contributions of possible different anomalous couplings. Therefore, an analysis of the W polarisation should be established with observables closely related to the helicity amplitudes and as a function of the

W production angle θ .

In addition to the helicity amplitudes with Standard Model couplings in figure 4.2a), the amplitudes for various anomalous couplings are shown in figure 4.2b) to d). For figure 4.2b) Δg_1^Z is varied ($\Delta g_1^Z \cot \theta_W = 2$), in figure 4.2c) an anomalous magnetic dipole moment with $\Delta \kappa_\gamma = 2, \Delta \kappa_Z = -2 \tan \theta_W$ and in figure 4.2d) an electric quadrupole moment with $\lambda_\gamma = 2, \lambda_Z = 2 \tan \theta_W$ is assumed. In each case the anomalous couplings which are not explicitly mentioned are chosen to be zero. Although the total differential cross-sections show only small variations for the various anomalous couplings, the effects are clearly enhanced in the individual helicity amplitudes. Both their shape as well as the normalisation show a distinctive behaviour.

With the help of the well known V-A structure of the W decay into a fermion pair, the angular distribution of the W decay can be used as a polarisation analyser in order to determine the helicity of the W boson. This is done by measuring the polar and azimuthal W decay angles θ^* and ϕ^* in the rest frame of the W boson. In the following the convention from [58] is adopted: θ^* and ϕ^* define the angles between the flight direction of the W boson and the down-type fermion, i.e. between the boson and the $e^+, \mu^+, \tau^+, \bar{d}$ or \bar{s} quark in case of the W^- and the e^-, μ^-, τ^-, d or s quark in case of the W^+ boson. The angles are then defined in a right-handed system, which is oriented such, that the W flight direction coincides with the z -axis and the y -axis is perpendicular to the $e^+e^- - W^+W^-$ -plane. This procedure is visualised in figure 4.3.

The decay amplitudes \mathcal{M}_τ of the decay of a W boson with helicity τ can be written as

$$\mathcal{M}_\tau = \frac{em_W}{\sqrt{2} \sin \theta_W} \ell_\tau(\theta^*, \phi^*), \quad (4.18)$$

where the angular dependence is given by $\ell_\tau(\theta^*, \phi^*) = \sqrt{2} d_{1,\tau}^1 e^{i\tau\phi^*}$. Thus the angular dependence of the W decay $W \rightarrow f\bar{f}$ is contained in the so-called D -functions

$$D_{\tau\tau'}(\theta^*, \phi^*) = \ell_\tau(\theta^*, \phi^*) \ell_{\tau'}^*(\theta^*, \phi^*), \quad (4.19)$$

which are summarised below.

$$\begin{aligned} D_{++} &= \frac{1}{2}(1 + \cos^2 \theta^*) - \cos \theta^* \\ D_{--} &= \frac{1}{2}(1 + \cos^2 \theta^*) + \cos \theta^* \\ D_{00} &= \sin^2 \theta^* \\ D_{+-} &= \frac{1}{2} \sin^2 \theta^* e^{2i\phi^*} \\ D_{+0} &= \frac{1}{2} \sqrt{2} \sin \theta^* e^{+i\phi^*} (\cos \theta^* - 1) \\ D_{-0} &= \frac{1}{2} \sqrt{2} \sin \theta^* e^{-i\phi^*} (-\cos \theta^* - 1) \end{aligned} \quad (4.20)$$

The information of the W production and decay is comprised in the five-fold differential cross-section $d\sigma/(d \cos \theta_W d \cos \theta_{W^-}^* d \phi_{W^-}^* d \cos \theta_{W^+}^* d \phi_{W^+}^*)$, where $\cos \theta$ denotes the production angle of the W and $\theta_{W^\pm}^*$ and $\phi_{W^\pm}^*$ are the decay angles of the W^- and W^+ bosons, respectively. Then the five-fold differential cross-section can be written in terms of the W production amplitudes $\mathcal{F}_{\tau_-\tau_+}^{(\lambda)}$ and the D -functions in the narrow W-width approximation

$$\begin{aligned} \frac{d^5 \sigma(e^+e^- \rightarrow W^+W^- \rightarrow f_1 \bar{f}_2 f_3 \bar{f}_4)}{d \cos \theta_W d \cos \theta_{W^-}^* d \phi_{W^-}^* d \cos \theta_{W^+}^* d \phi_{W^+}^*} &= \frac{\beta}{128\pi s} \left(\frac{3}{8\pi} \right)^2 Br(W \rightarrow f_1 \bar{f}_2) Br(W \rightarrow f_3 \bar{f}_4) \\ &\times \sum_{\lambda \tau_-\tau_+\tau_-\tau_+} \mathcal{F}_{\tau_-\tau_+}^{(\lambda)} (\mathcal{F}_{\tau_-\tau_+}^{(\lambda)})^* \times D_{\tau_-\tau_+}(\theta_{W^-}^*, \phi_{W^-}^*) D_{\tau_+\tau_+}(\pi - \theta_{W^+}^*, \phi_{W^+}^* + \pi) \end{aligned} \quad (4.21)$$

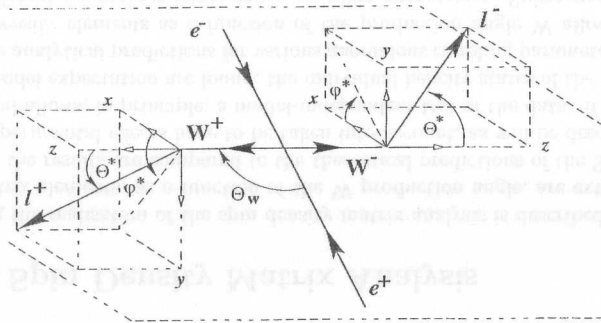


Figure 4.3: An illustration of the definitions of the W production and decay angles.

4.2.4 Spin Density Matrices

In the following section the spin density matrix element method will be explained. The aim of the analysis is to extract the information of the helicity states of the W bosons as a function of the W production angle θ . In this method the information about the trilinear gauge couplings contained in the total W-pair production cross-section will not be utilised. Therefore this analysis, which relies on differential angular distributions only, can finally be combined with the event rate analysis.

The spin density matrix elements are normalised products of the helicity amplitudes and describe the polarisation of the W boson pair. The elements of the two-particle joint density matrix are defined by

$$\rho_{\tau_-\tau'_-\tau_+\tau'_+}(\cos\theta) = \frac{\sum_{\lambda} \mathcal{F}_{\tau_-\tau_+}^{(\lambda)} (\mathcal{F}_{\tau'_-\tau'_+}^{(\lambda)})^*}{\sum_{\lambda\tau_+\tau_-} |\mathcal{F}_{\tau_-\tau_+}^{(\lambda)}|^2}. \quad (4.22)$$

Altogether, the W^+W^- system has 81 density matrix elements. With the normalisation

$$\sum_{\tau_+\tau_-} \rho_{\tau_-\tau_+\tau_+\tau_-} = 1, \quad (4.23)$$

80 of these are independent. This number reduces to 35 elements in an CP conserving theory, as is described in [58]. Even with the expected full LEP 2 statistics (500 pb⁻¹ per experiment) it is illusive to extract all two-particle joint density matrix elements of the WW system. It is possible to reduce the number of observables by considering the W bosons individually. Summing over all possible helicity states of the second W gives the so-called single W spin density matrix. Here the relation for the single W matrix elements of the W^- boson is given as an example:

$$\rho_{\tau_-\tau'_-}^{W^-}(\cos\theta) = \sum_{\tau_+} \rho_{\tau_-\tau'_-\tau_+\tau_+}. \quad (4.24)$$

The matrix $\rho_{\tau\tau'}$ is hermitian, thus having six independent matrix elements. The density elements will be extracted as a function of $\cos\theta$, since the helicity amplitudes and thus the density

elements depend strongly on the W production angle as can be seen from figure 4.2. The diagonal elements $\rho_{\tau\tau}$ of the spin density matrix can be interpreted as the probability to produce a W boson with helicity τ . Therefore, they are normalised to unity:

$$\sum_{\tau_{\pm}} \rho_{\tau_{\pm}\tau_{\pm}}^{W_{\pm}} = 1. \quad (4.25)$$

Note that in general the off-diagonal elements are complex. For CP-conserving theories, however, the imaginary parts vanish. This will be described in more detail in section 4.2.5. In this analysis, where the single W spin density matrices are reconstructed, the spin correlations between the two W bosons are not considered. The resulting loss in sensitivity is very small. This issue will be discussed in section 4.6.

The three-fold differential cross-section for the W production and decay angles of the W^- boson as an example is given in terms of the single W density matrix elements by

$$\frac{d\sigma(e^+e^- \rightarrow W^+ + f\bar{f})}{d\cos\theta d\cos\theta_W^* d\phi_{W^-}^*} = \frac{d\sigma(e^+e^- \rightarrow W^+W^-)}{d\cos\theta} (\text{Br}) \left(\frac{3}{8\pi}\right) \sum_{\tau_-\tau'_-} \rho_{\tau_-\tau'_-}^{W^-}(\cos\theta) D_{\tau_-\tau'_-}(\cos\theta_{W^-}^*, \phi_{W^-}^*). \quad (4.26)$$

Here (Br) denotes the branching ratio $\text{Br}_{W^- \rightarrow f\bar{f}}$ of the W^- decay, from which the density matrix is extracted.

The theoretical predictions for the single W spin density matrix elements as functions of the anomalous couplings can be derived from the analytical expressions of the helicity subamplitudes in table 4.1, equations 4.15, 4.17, 4.22 and 4.24. They are given explicitly in [58, 61].

As a summary of the description above, the information contained in the three-fold differential cross-section of the production and decay angles of the W boson can be transformed into nine projections, the spin density matrix elements. These are the six real parts and three imaginary parts of the matrix, taking into account that the density matrix is hermitian. These observables are physical meaningful and represent the smallest set of observables which contain all information about the helicity of one W boson.

4.2.5 Test of CP-Invariance

An examination of the reaction $e^+e^- \rightarrow W^+W^-$ provides a genuine experimental test of CP-invariance, which is entirely independent of any theoretical assumptions [58, 62]. In the Standard Model CP violation is only present via the Kobayashi Maskawa phase, which affects this reaction only at two-loop order. These effects are too small ($\mathcal{O} = 10^{-8}$) to be detected with the precision of the LEP2 program. Thus if any signals of CP violation are observed, this would unambiguously be a sign of new physics. But the Lagrangian \mathcal{L} describing the most general triple gauge coupling vertex as given in equations 4.1, 4.2 allows for CP violation. There exist very stringent bounds on CP-violation in the electromagnetic interaction, which can be derived from limits on the electric dipole moments [63, 64]. If the SU(2) weak isospin symmetry is valid, CP violation is neither expected in the weak sector. Therefore, CP violation in the trilinear gauge coupling is theoretically disfavoured. On the other hand there are no measurements which exclude CP-violation in the weak sector and the indirect limits in the electromagnetic sector cannot replace direct measurements. It is thus of great importance to confirm the expectation of CP conservation in the triple gauge couplings.

Within the formalism of spin density matrix elements, a very simple test of CP-invariance in W-pair production can be performed, which will be shown in the following.

CPT invariance implies

$$\mathcal{F}_{\tau^-\tau^+}^{(\lambda)} = (\mathcal{F}_{(-\tau^+)(-\tau^-)}^{(\lambda)})^*. \quad (4.27)$$

From this at tree-level for the single-W spin density matrix element directly follows

$$\rho_{\tau\tau'}^{W^-} = (\rho_{(-\tau)(-\tau')}^{W^+})^*. \quad (4.28)$$

On the other hand, a CP conserving theory implies for the helicity amplitudes

$$\mathcal{F}_{\tau^-\tau^+}^{(\lambda)} = \mathcal{F}_{(-\tau^+)(-\tau^-)}^{(\lambda)}, \quad (4.29)$$

and as a consequence for the density elements

$$\rho_{\tau\tau'}^{W^-} = \rho_{(-\tau)(-\tau')}^{W^+}. \quad (4.30)$$

Following equation 4.30 a very simple test of CP invariance can be derived through the following relations:

$$\begin{aligned} \text{Im}(\rho_{+-}^{W^-}) - \text{Im}(\rho_{-+}^{W^+}) &= 0 \\ \text{Im}(\rho_{+0}^{W^-}) - \text{Im}(\rho_{-0}^{W^+}) &= 0 \\ \text{Im}(\rho_{-0}^{W^-}) - \text{Im}(\rho_{+0}^{W^+}) &= 0. \end{aligned} \quad (4.31)$$

Any deviations from equations 4.31 directly imply CP violation. On the other hand, following equation 4.28, the presence of loop effects can be tested by comparing the imaginary parts according to

$$\text{Im}(\rho_{\tau\tau'}^{W^-}) + \text{Im}(\rho_{-\tau-\tau'}^{W^+}) = 0. \quad (4.32)$$

A deviation from zero would give an estimate of (CP conserving and violating) loop effects, whereas any non-zero CP-violating tree level contributions would cancel.

The CP test described in this section is much simpler compared to a full analysis, which would also take the real parts of the density elements and the angular distribution of the W production angle into account. Nevertheless this simple test has similar sensitivity, because the CP-violating parameters enter linearly in the imaginary parts of the spin density matrix elements, whereas for the real parts the dependence is quadratically. Therefore, and for the sake of simplicity the CP-violating TGC parameters are extracted from the imaginary parts only.

4.3 The Spin Density Matrix Analysis

In the following the realisation of the spin density matrix analysis is described. In a first step the density matrix elements, as a function of the W production angle, are extracted from the data. Secondly, the results are compared to the theoretical predictions of the Standard Model. To do so the experimental effects have to be taken into account, as will be described in section 4.4. This method allows, in principle, a model-independent test of the data. If deviations from the Standard Model expectation are found, the individual helicity states of the W boson can be compared to the analytical predictions for various anomalous coupling parameters. The specific shapes of the density elements as a function of the production angle W allow to distinguish between the different anomalous triple gauge coupling parameters. Subsequently, in order to quantify the agreement between the data and the theoretical prediction, a fit is performed for various models and the anomalous coupling parameters can either be measured or restricted.

4.3.1 Data Sample and Angular Reconstruction

For the analysis described in the following only the so-called ‘semi-leptonic’ channel $WW \rightarrow qq\ell\nu$ is used. About 43% of the total W^+W^- decay cross-section is expected to contribute to this modus. Measuring the direction of the jets of the hadronically decaying W by summing over the jet momenta and applying momentum conservation, the direction of the W bosons can be reconstructed. This is done with the help of a kinematic fit: from the measured lepton and jet momenta and their errors the momentum vectors of the W bosons are determined by constraining the total energy to the centre-of-mass energy and the total momentum to zero.

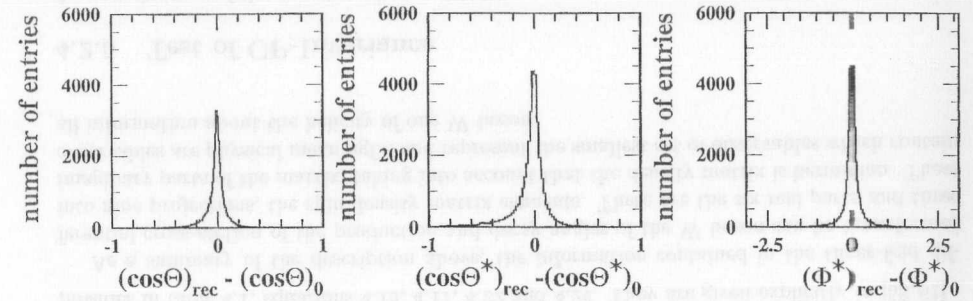


Figure 4.4: The angular resolution for the W production and decay angles as determined from the Monte Carlo (EXCALIBUR).

The charge of the lepton from the leptonically decaying W can be used to distinguish the W^- and the W^+ boson. In case of a τ lepton the charge of the W boson can be derived by the charge(s) of the τ lepton decay products. Because of the missing information due to the additional neutrino(s) of the τ decay further constraints have to be assumed to fully reconstruct these events. According to [65] the direction of the τ lepton can be reasonably approximated by the direction of the visible τ decay products. Doing so and with the constraints from energy and momentum conservation in a kinematic fit the W production and decay angles can be reconstructed as in the case of the electron and muon decay. Via the measured charge of the lepton candidate, the fermion can be distinguished easily from the anti-fermion, and thus the decay angles of the leptonically decaying W can be reconstructed unambiguously. This is not the case for the hadronically decaying W, where the quark and the anti-quark cannot be distinguished without applying additional techniques for the determination of the hadronic charges like jet-charges, for which the efficiency for measuring the charge of the quark jets correctly is relatively low (around 70%) and would give only very modest statistical improvement. Therefore such techniques are not applied here and consequently only folded angular distributions are accessible for the hadronically decaying W. Theoretically, these folded, or symmetrised, angular distributions can be derived from the true angles by using the following relations, depending on the value of the polar angle $\cos\theta^*$ of the W decay:

$$\begin{aligned} \cos\theta^* > 0 &\rightarrow (\cos\theta^*, \phi^*) \\ \cos\theta^* < 0 &\rightarrow (-\cos\theta^*, \phi^* + \pi). \end{aligned} \quad (4.33)$$

Fully hadronic decays, $W^+W^- \rightarrow q\bar{q}q\bar{q}$, which are expected to contribute with 46% to the total W^+W^- -decay cross-section are difficult to reconstruct and therefore expected to have relatively little impact on the measurement of the triple gauge boson coupling as will be explained in the following. The selection is expected to be less pure than for the semileptonic case, because of the high background from multi-jet final states in $e^+e^- \rightarrow (Z^0/\gamma)^* \rightarrow q\bar{q}(\gamma)$ events. Moreover hard gluon radiation will complicate the selection. An additional problem is that the jets cannot unambiguously be assigned to the W bosons. The most severe problem for measurements of the triple gauge boson coupling is the poor reconstruction of both the W production and decay angles. Neither the W^+ boson can be distinguished from the W^- boson nor the W -decay jets originating from the quark or anti-quark can be identified without additional techniques to determine the charge of the jets or the W bosons. As mentioned, these techniques are quite limited in their performance. Therefore the useful information in an analysis of the angular distribution is strongly diluted and the channel is expected to contribute relatively little compared to the semi-leptonic channel, despite the fact that it has the largest cross-section of all the channels. The fully hadronic channel has been analysed in a separate analysis using a binned likelihood fit and its results are combined with these from the spin density matrix analysis for the $q\bar{q}\ell\bar{\nu}$ channel in section 4.7.

Approximately 11% of the W -pairs are expected to decay through the fully leptonic channel $W^+W^- \rightarrow l^+\nu_l l^-\bar{\nu}_l$. In this channel the momenta of the two neutrinos are unknown. Applying momentum and energy conservation and forcing the two W bosons to a fixed mass m_W allows the reconstruction of the two neutrino momenta, in case of the two leptons being an electron or muon. The quadratic nature of the mass constraint results in a twofold ambiguity in the reconstruction of the five angles, which implicates a loss in sensitivity for measuring anomalous couplings. Because of these problems together with the low cross-section, this channel as well is expected to have a low impact compared to the semileptonic decay channel. Events with at least one W -decay via the τ -channel cannot be reconstructed because of the missing information of the additional neutrino(s) in the τ decay. As for the fully hadronic channel a separate analysis has been performed for this channel and the results will be combined with these of the spin density matrix method in section 4.7. The results of the spin density matrix analysis of the $WW \rightarrow q\bar{q}\ell\nu$ channel can subsequently be combined with the results from the event-rate analysis and from other channels. This will be described in section 4.7.

4.3.2 Monte Carlo Samples

Different Monte Carlo generators are used in order to simulate the physics processes of the W^+W^- -pair production and their backgrounds. In the following the generators, which are used for the analysis of the triple gauge boson coupling, are introduced briefly and the main features are summarised.

- EXCALIBUR [66] can be used either in a full 4-fermion mode, where all CC and NC final states are generated, or as a CC03 (c.f. section 1.3) generator (optionally, any graphs or combination can be switch on and off). QCD corrections, finite W width and the masses of the fermions are incorporated. For initial state radiation (ISR) a simplified simulation is implemented, where only single photon radiation without transverse momentum is taken into account. Anomalous triple gauge couplings can be switched on, with all CP-conserving anomalous

coupling parameters settable. This Monte Carlo generator is mostly used in order to produce samples with anomalous couplings in the various models examined, including simulation of the OPAL detector.

- KORALW [67] can be used in the CC03 mode or, alternatively, all charged current diagrams (CC11) can be produced. They are generated using the GRACE package [68]. The matrix elements are calculated for massless fermions, but optionally kinematics with massive fermions can be used. The finite W width is incorporated and Coulomb corrections can be switched on. The main advantage compared to EXCALIBUR is a careful implementation of ISR, including multiple photon emission and finite transverse momenta of the photons. The fully simulated OPAL samples are produced in the CC03 mode and without anomalous couplings. No anomalous couplings are settable.
- PYTHIA [69] is mostly used in order to produce Standard Model WW (CC03) samples to cross-check the EXCALIBUR or KORALW samples. Only single classes of events, like WW or ZZ samples, can be produced, PYTHIA does not allow for full 4-fermion samples including the interference terms. No anomalous couplings can be set.
- grc4f [70] is able to generate all 4-fermion processes without any kinematic cuts. It is based on the GRACE package [68], which computes Feynman diagrams automatically. Therefore the calculation is considered to be the most complete and reliable. The fermion masses are finite, QCD and Coulomb corrections are included. For handling ISR two possibilities exist: either a structure function formalism or a parton shower algorithm is used. The latter may also be used in order to implement final state radiation. In principle any anomalous triple gauge couplings can be set. The price to pay for all these advantages is that the grc4f program is very slow. Therefore fully simulated samples are only used by OPAL in order to produce reliable 4-fermion samples with Standard Model couplings and the according CC03 samples as counterparts in order to investigate possible 4-fermion effects.

The fragmentation and hadronisation is done with the JETSET [10] Monte Carlo while HERWIG [49] is used for systematic studies. For the decays of τ -leptons the program TAUOLA [71] is used, which models hadronic decays of the τ including the relevant resonances.

Various samples of fully simulated Monte Carlo events, both the Standard Model processes and samples with anomalous triple gauge boson couplings, are used for the spin density matrix analysis or systematic checks. They are summarised in tables 4.3, 4.4 and 4.5. All Standard Model samples, generated with the different Monte Carlo programs, are summarised in table 4.3. In table 4.4 samples with anomalous couplings are listed, where only the CC03 diagrams of the W^+W^- -pairs are produced with the EXCALIBUR generator. In table 4.5 the samples produced in the 4-fermion mode of the EXCALIBUR generator are summarised. All 4-fermion processes, which are sensitive to anomalous couplings are produced, including interferences between these processes. The $e\ell\ell$ and $e\ell\bar{q}$ final states are independent of anomalous couplings, therefore they are not included in these samples.

Run	Quantity	Physics process	Generator	\sqrt{s}
5762	100k	WW	PYTHIA	184 GeV
6843	100k	WW	EXCALIBUR	184 GeV
5033	150k	WW	HERWIG	184 GeV
6640	157k	WW	grc4f	184 GeV
7322	50k	WW	KORALW	183 GeV
7323	100k	WW	KORALW	183 GeV
6900	100k	WW	PYTHIA	183 GeV
7352	100k	WW	EXCALIBUR	183 GeV
7337	78k	WW	grc4f	183 GeV
5795	80k	4f \rightarrow qqqq	grc4f	184 GeV
6850	82k	4f \rightarrow llqq	grc4f	184 GeV
6851	261k	4f \rightarrow eeqq	grc4f	184 GeV
7051	39k	4f \rightarrow qqqq	grc4f	183 GeV
7050	41k	4f \rightarrow llqq	grc4f	183 GeV
7055	134k	4f \rightarrow eeqq	grc4f	183 GeV
6859	170k	4f (TGC sensitive)	EXCALIBUR	184 GeV
7330	100k	4f (TGC sensitive)	EXCALIBUR	183 GeV
5050	500k	Z/ γ \rightarrow q \bar{q}	PYTHIA	183 GeV
1124	150k	Z/ γ \rightarrow q \bar{q}	HERWIG	184 GeV
1126	170k	$\gamma\gamma$ \rightarrow q \bar{q} (tagged)	HERWIG	184 GeV

Table 4.3: The Monte Carlo samples without anomalous couplings used in this analysis.

4.3.3 Event Selection

WW \rightarrow qql ν events are characterised by two well-separated hadronic jets, missing energy due to the unobserved neutrino and a high momentum lepton. In case of the electron or muon channel, the lepton can be directly identified, whereas for tau events the signature is an additional jet with low multiplicity. The missing momentum of the neutrino resulting from the W decay is expected to be less well defined in this case due to the additional neutrino(s) from the τ decay.

Because of the similar signature of the three different channels in the semi-leptonic W-pair decays, a common event selection [72, 73]. is performed, which proceeds in four steps:

- **Identification of the candidate Lepton**

In case of the electron and muon channel, WW \rightarrow qql ν , l = e, μ , no explicit lepton identification is required, in order to maximise the efficiency. Instead, the track in the event which is, according to a likelihood calculation, most consistent with being an electron or muon from a W decay is chosen as a lepton candidate. This selection is based on a set of variables, like the specific energy loss in the jet chamber or the matching between the hits in the central detector and the muon chambers. This information is combined with variables like energy and isolation, which help to identify tracks coming from a leptonic W decay.

In case of the tau channel the track (or tracks) most consistent with being from the leptonic decays W \rightarrow $\tau\bar{\nu}_\tau \rightarrow (e\bar{\nu}_e\nu_\tau)\bar{\nu}_\tau$, W \rightarrow $\tau\bar{\nu}_\tau \rightarrow (\mu\bar{\nu}_\mu\nu_\tau)\bar{\nu}_\tau$ and from the hadronic decays W \rightarrow $\tau\bar{\nu}_\tau \rightarrow (\pi^\pm(n\pi^0)\nu_\tau)\bar{\nu}_\tau$ and W \rightarrow $\tau\bar{\nu}_\tau \rightarrow (2\pi^\pm\pi^\mp\nu_\tau)\bar{\nu}_\tau$ is identified, using the

Run	Quantity	\sqrt{s}	anomalous couplings
6844	50k	184 GeV	$\alpha_{W\Phi} = +2$
6845	50k	184 GeV	$\alpha_{W\Phi} = -2$
6846	50k	184 GeV	$\alpha_{B\Phi} = +2$
6847	50k	184 GeV	$\alpha_{B\Phi} = -2$
6848	50k	184 GeV	$\alpha_W = +2$
6849	50k	184 GeV	$\alpha_W = -2$
7353	50k	183 GeV	$\alpha_{W\Phi} = +2$
7354	50k	183 GeV	$\alpha_{W\Phi} = +1$
7392	50k	183 GeV	$\alpha_{W\Phi} = +0.5$
7393	50k	183 GeV	$\alpha_{W\Phi} = -0.5$
7355	50k	183 GeV	$\alpha_{W\Phi} = -1$
7356	50k	183 GeV	$\alpha_{W\Phi} = -2$
7357	50k	183 GeV	$\alpha_W = +2$
7358	50k	183 GeV	$\alpha_W = +1$
7394	50k	183 GeV	$\alpha_W = +0.5$
7395	50k	183 GeV	$\alpha_W = -0.5$
7359	50k	183 GeV	$\alpha_W = -1$
7360	50k	183 GeV	$\alpha_W = -2$
7361	50k	183 GeV	$\alpha_{B\Phi} = +2$
7362	50k	183 GeV	$\alpha_{B\Phi} = +1$
7396	50k	183 GeV	$\alpha_{B\Phi} = +0.5$
7397	50k	183 GeV	$\alpha_{B\Phi} = -0.5$
7363	50k	183 GeV	$\alpha_{B\Phi} = -1$
7364	50k	183 GeV	$\alpha_{B\Phi} = -2$
7794	50k	183 GeV	$\Delta g_1^Z = +2$
7795	50k	183 GeV	$\Delta g_1^Z = +1$
7796	50k	183 GeV	$\Delta g_1^Z = -1$
7797	50k	183 GeV	$\Delta g_1^Z = -2$
7367	50k	183 GeV	$\Delta\kappa_\gamma = +1$
7368	50k	183 GeV	$\Delta\kappa_\gamma = -1$
7798	50k	183 GeV	$\Delta\kappa_\gamma(\text{HISZ}) = +2$
7799	50k	183 GeV	$\Delta\kappa_\gamma(\text{HISZ}) = +1$
7800	50k	183 GeV	$\Delta\kappa_\gamma(\text{HISZ}) = -1$
7801	50k	183 GeV	$\Delta\kappa_\gamma(\text{HISZ}) = -2$
7369	20k	183 GeV	$\Delta\kappa_\gamma = \lambda_\gamma = +1$
7370	20k	183 GeV	$\Delta\kappa_\gamma = \lambda_\gamma = -1$
7371	20k	183 GeV	$\alpha_{W\Phi} = +1$ and $\alpha_W = +1$
7372	20k	183 GeV	$\alpha_{W\Phi} = +1$ and $\alpha_{B\Phi} = +1$
7373	20k	183 GeV	$\alpha_{B\Phi} = +1$ and $\alpha_W = +1$

Table 4.4: The Monte Carlo samples with anomalous couplings, produced with the EXCALIBUR generator in the WW (CC03) mode.

same information as for the electron and muon channel, and in addition variables identifying the tau decay products, like for example the mass of all tracks and clusters within

Run	Quantity	\sqrt{s}	anomalous couplings
7331	50k	183 GeV	$\alpha_{W\Phi} = +2$
7827	50k	183 GeV	$\alpha_{W\Phi} = +1$
7828	50k	183 GeV	$\alpha_{W\Phi} = -1$
7332	50k	183 GeV	$\alpha_{W\Phi} = -2$
7333	50k	183 GeV	$\alpha_W = +2$
7831	50k	183 GeV	$\alpha_W = +1$
7832	50k	183 GeV	$\alpha_W = -1$
7334	50k	183 GeV	$\alpha_W = -2$
7335	50k	183 GeV	$\alpha_{B\Phi} = +2$
7829	50k	183 GeV	$\alpha_{B\Phi} = +1$
7830	50k	183 GeV	$\alpha_{B\Phi} = -1$
7336	50k	183 GeV	$\alpha_{B\Phi} = -2$
7823	50k	183 GeV	$\Delta g_1^Z = +2$
7824	50k	183 GeV	$\Delta g_1^Z = +1$
7825	50k	183 GeV	$\Delta g_1^Z = -1$
7826	50k	183 GeV	$\Delta g_1^Z = -2$
7837	50k	183 GeV	$\Delta \kappa_\gamma = +2$
7838	50k	183 GeV	$\Delta \kappa_\gamma = +1$
7839	50k	183 GeV	$\Delta \kappa_\gamma = -1$
7840	50k	183 GeV	$\Delta \kappa_\gamma = -2$
7833	50k	183 GeV	$\Delta \kappa_\gamma(\text{HISZ}) = +2$
7834	50k	183 GeV	$\Delta \kappa_\gamma(\text{HISZ}) = +1$
7835	50k	183 GeV	$\Delta \kappa_\gamma(\text{HISZ}) = -1$
7836	50k	183 GeV	$\Delta \kappa_\gamma(\text{HISZ}) = -2$

Table 4.5: The Monte Carlo samples with anomalous couplings, produced with the EXCALIBUR generator in the 4-fermion mode. The cell and $eeq\bar{q}$ final states are not included in these samples.

a 200 mrad cone around the track.

• Preselection

Preselection cuts are applied to remove the main contribution from background events, like two-photon and $(Z^0/\gamma)^* \rightarrow q\bar{q}(\gamma)$ events. For each channel a slightly different preselection is used, where for example the energy of the lepton candidate, the visible energy or the energy of the highest energetic photon are used. Details may be found in [72]. For $W^+W^- \rightarrow q\bar{q}\tau\bar{\nu}_\tau$ events four different preselections are performed for the four channels.

• Relative Likelihood Selection

Relative likelihoods are used to distinguish signal $W^+W^- \rightarrow q\bar{q}l\bar{\nu}_l$ events from background. The main background after the preselection are $(Z^0/\gamma)^* \rightarrow q\bar{q}(\gamma)$ events. To distinguish signal from background contributions a set of variables like the energy of the lepton candidate, the lepton identification probability or the angle between the lepton track and the missing momentum vector is used. All variables are summarised in [72]. The likelihood, $\mathcal{L}^{qq\ell\bar{\nu}}$, for being a $q\bar{q}l\bar{\nu}_l$ event is calculated as the product of probabilities for the individual variables, and is subsequently compared to the likelihood, $\mathcal{L}^{q\bar{q}}$, of being

a background event. Events are finally selected if the relative likelihood

$$\mathcal{L}^{qq\ell\bar{\nu}} = \frac{\mathcal{L}^{qq\ell\bar{\nu}}}{\mathcal{L}^{q\bar{q}\ell\bar{\nu}} + f \times \mathcal{L}^{q\bar{q}}}$$

exceeds a certain cut value. Here the normalisation factor, f , is the ratio of preselected background to signal cross-sections from Monte Carlo. For the electron and muon channel a relative likelihood of $\mathcal{L}^{qqe\bar{\nu}} > 0.5$ or $\mathcal{L}^{qq\mu\bar{\nu}} > 0.5$ is sufficient, whereas $W^+W^- \rightarrow q\bar{q}\tau\bar{\nu}_\tau$ events are selected if the relative likelihood $\mathcal{L}^{qq\tau\bar{\nu}}$ is greater than 0.75.

• Event categorisation

After applying the preselection and performing the relative likelihood selection for the $W^+W^- \rightarrow q\bar{q}e\bar{\nu}_e$ and $W^+W^- \rightarrow q\bar{q}\mu\bar{\nu}_\mu$ channels, approximately 25% of the $W^+W^- \rightarrow q\bar{q}\tau\bar{\nu}_\tau$ events are selected. Therefore the events passing the $W^+W^- \rightarrow q\bar{q}e\bar{\nu}_e$ and $W^+W^- \rightarrow q\bar{q}\mu\bar{\nu}_\mu$ selections are re-classified by additional likelihoods in order to recognise $W^+W^- \rightarrow q\bar{q}\tau\bar{\nu}_\tau$ events. This procedure results in a better angular resolution for the leptonic decay angles of the W, because the additional neutrinos from the τ -decays are taken into account properly. The predominant $W^+W^- \rightarrow q\bar{q}\tau\bar{\nu}_\tau$ contamination in the $q\bar{q}e\bar{\nu}_e$ and $q\bar{q}\mu\bar{\nu}_\mu$ selection arises from tau-decays into an one prong hadronic state, an electron or muon plus neutrino(s), respectively. Therefore two different likelihoods are applied to events selected in the $W^+W^- \rightarrow q\bar{q}e\bar{\nu}_e$ and $W^+W^- \rightarrow q\bar{q}\mu\bar{\nu}_\mu$ channel to classify the candidates either as $W^+W^- \rightarrow q\bar{q}e\bar{\nu}_e$ and $W^+W^- \rightarrow q\bar{q}\mu\bar{\nu}_\mu$ events, or to identify $W^+W^- \rightarrow q\bar{q}\tau\bar{\nu}_\tau$ events in the channels $W \rightarrow \tau\bar{\nu}_\tau \rightarrow (\pi^\pm(n\pi^0)\nu_\tau)\bar{\nu}_\tau$ or $W \rightarrow \tau\bar{\nu}_\tau \rightarrow (e\bar{\nu}_e\nu_\tau)\bar{\nu}_\tau$ and $W \rightarrow \tau\bar{\nu}_\tau \rightarrow (\mu\bar{\nu}_\mu\nu_\tau)\bar{\nu}_\tau$ respectively. For these likelihoods the same variables as for the relative likelihood selections for $q\bar{q}e\bar{\nu}_e$ and $q\bar{q}\mu\bar{\nu}_\mu$ events are used.

The following background processes have to be considered in the selection of the semileptonic decay of the W-pairs:

• $(Z^0/\gamma)^* \rightarrow f\bar{f}$

is the most important background contribution in the $q\bar{q}\tau\bar{\nu}_\tau$ channel, but it is also relevant in the other two semileptonic channels. On average, the cross-section is reduced about a factor of 1000 after the selection for the angular analysis.

• Two-photon production

is the process with the largest cross-section (c.f. section 1.2). In most of the cases the photons are quasi-real, so that the cross-section reduces significantly, when minimal mass in the GeV-range is required for the fermion system originating from the photons. In this sense the two-photon processes are relatively easy to distinguish from the events, where gauge bosons are produced resonantly. Only in the $W^+W^- \rightarrow q\bar{q}e\bar{\nu}_e$ channel a significant fraction of these processes remain in the selected events.

• Single resonant W production

is a potentially serious background for the investigation of the triple gauge boson vertex. Here identical final states as in the W-pair production can be produced, which leads to interferences between the reaction $e^+e^- \rightarrow We\nu \rightarrow f\bar{f}e\nu$ and the CC03 diagrams of the W-pair production. Experimentally those two processes can be distinguished in a good fraction of cases, i.e. when a quasi-real photon is radiated off and thus the electron

(or positron) escapes detection. But in case that the electron is found in the detector, the contribution of $ff\nu$ final states in W -pair production cannot be disentangled from single- W production: this background is especially dangerous for the investigation of the trilinear gauge boson coupling, because of its contribution from non-abelian 4-fermion processes. For this production mechanism the background contains the same vertex as should be investigated in the signal. The background could be reduced by a factor of 15 due to the selection and the additional cuts applied for the angular analysis. Because only a very small fraction of the single W -events remain in the sample (for 57pb^{-1} 2.6 events are selected), the dependence on anomalous couplings is neglected for this analysis.

- **Z-pair production**

comes into play at energies above the production threshold of ≈ 182 GeV. But the cross-section is significantly smaller than that for W -pair production as discussed in section 1.3. The accepted cross-section is reduced by a factor of about 15 compared to the Z -pair cross-section.

- **Single Z^0 production**

is especially important in the $q\bar{q}e\bar{\nu}_e$ and $q\bar{q}\tau\bar{\nu}_\tau$ channel. Analogously to the single W -production, usually one of the electrons in the final state escapes detection. This process does not interfere with W -pair production, apart from the $e^+e^-\nu_e\bar{\nu}_e$ final state.

All processes except the first two mentioned are part of the so-called 4-fermion background. In principle a full 4-fermion analysis has to be performed in order to account for the interference effects between the individual signal- and background processes (c.f. section 1.3). This is done in case of the total cross-section analysis (c.f. [73]). Therefore the background cross-section given in table 4.6 is categorised via its final states instead of the underlying physics process. The analysis described in this thesis is based on the CC03 processes. Possible systematic effects and biases because of this simplification are small compared to the statistical error and will be discussed in section 4.5.4.

The efficiency for the $W^+W^- \rightarrow q\bar{q}l\bar{\nu}_l$ selection is 85.7%, with a purity of 89.6%. Thus for OPAL's integrated luminosity of $(56.56 \pm 0.27)\text{pb}^{-1}$ the expected number of events is 374.1 ± 8.6 , while 362 are observed in total. Of those, 140 are selected as $W^+W^- \rightarrow q\bar{q}e\bar{\nu}_e$, 118 as $W^+W^- \rightarrow q\bar{q}\mu\bar{\nu}_\mu$ and 104 as $W^+W^- \rightarrow q\bar{q}\tau\bar{\nu}_\tau$ events. The error given on the number of expected events include systematic uncertainties from the efficiency, luminosity, beam energy, WW cross-section (2%) and m_W . The cross contamination between W^+W^- events from different topologies is taken into account in the spin density matrix analysis and thus the dependence of this sort of background to possible anomalous couplings is included in the analysis. The different background sources with their accepted cross-sections are summarised in table 4.6.

For the angular analysis a number of additional requirements are applied in addition to this selection in order to further reduce the background and to assure a reliable reconstruction of the event kinematics.

For events in the $W^+W^- \rightarrow q\bar{q}e\bar{\nu}_e$ and $W^+W^- \rightarrow q\bar{q}\mu\bar{\nu}_\mu$ channels a kinematic fit with three constraints is applied, where energy and momentum conservation are employed and the mass of the two W bosons is constrained to the world average of the W mass value, $m_W = 80.40 \text{ GeV}/c^2$ [74], within the W -width. The results of the fit are then used to reconstruct the W production and decay angles, if the fit probability exceeds a value of 0.001. For events failing this requirement a kinematic fit with energy and momentum conservation but without

Source	Accepted background cross-sections (fb)		
	Event Selection $W^+W^- \rightarrow$		
	$q\bar{q}e\bar{\nu}_e$	$q\bar{q}\mu\bar{\nu}_\mu$	$q\bar{q}\tau\bar{\nu}_\tau$
$q\bar{q}q\bar{q}$	1 ± 2	1 ± 2	7 ± 7
$q\bar{q}e\bar{\nu}_e$	91 ± 58	3 ± 3	76 ± 7
$q\bar{q}\ell^+\ell^-$	66 ± 19	25 ± 5	70 ± 12
$q\bar{q}\nu\bar{\nu}$	0 ± 0	0 ± 0	9 ± 2
$l\bar{\nu}_l\nu_l$	0 ± 0	0 ± 0	0 ± 0
$\ell^+\ell^-\ell^+\ell^-$	0 ± 0	0 ± 0	0 ± 0
$Z^0/\gamma \rightarrow q\bar{q}$	53 ± 10	29 ± 5	184 ± 22
$Z^0/\gamma \rightarrow \ell^+\ell^-$	2 ± 1	1 ± 1	6 ± 1
Two Photon	13 ± 13	0 ± 0	5 ± 5
Combined	226 ± 63	59 ± 8	357 ± 28

Table 4.6: Background cross-sections for the 183 GeV W^+W^- selections in fb.

the mass constraint is performed. They pass if the fit probability is greater than 0.001. These additional requirements rejects about 2% of the signal events and 10% of the background.

For the tau channel all events passing the selection are used, if in addition a kinematic fit requiring energy-momentum conservation and equality between the masses of the hadronic and the leptonic systems converges with a fit probability greater than 0.001. The cosine of the angles between the two hadronic jets is required to be lower than -0.2 , and the angle between the tau and the closest jet should be greater than 20 degrees. These cuts reject 20% of the signal and 42% of the background. These cuts were also imposed to suppress $q\bar{q}\tau\bar{\nu}_\tau$ events which are correctly identified as belonging to this decay channel, where, however, the tau decay products are not identified correctly, leading to a wrong estimate of the tau flight direction. The fraction of these events is reduced from 13% to 8.5% of the $q\bar{q}\tau\bar{\nu}_\tau$ sample by these additional cuts. With these requirements 322 events are selected, 135 as $W^+W^- \rightarrow q\bar{q}e\bar{\nu}_e$, 115 as $W^+W^- \rightarrow q\bar{q}l\bar{\nu}_l$ and 72 as $W^+W^- \rightarrow q\bar{q}\tau\bar{\nu}_\tau$ candidates.

4.3.4 Extraction of the Spin Density Matrix Elements

In principle there are two different possibilities to extract the single W spin density matrices from data. Expressing the angular distributions of the production and decay of the W boson in terms of the density matrix elements as given in equation 4.26 allows the determination by a maximum likelihood fit to the angular distributions of the W decay [4].

The method used in this analysis is the extraction with the help of projection operators [61]. The single W spin density matrices $\rho_{rr'}$ can be extracted from W -pair decays using the threefold differential cross-section $d\sigma/d\cos\theta d\cos\theta^* d\phi^*$ by

$$\rho_{rr'}^{W^-}(\cos\theta) \frac{d\sigma(e^+e^- \rightarrow W^+W^-)}{d\cos\theta} = \frac{1}{\text{Br}_{W^- \rightarrow \bar{f}f}} \int \int \frac{d\sigma(e^+e^- \rightarrow W^+\bar{f}f)}{d\cos\theta d\cos\theta_W^* d\phi_W^*} \Lambda_{rr'}(\theta^*, \phi^*) d\cos\theta_W^* d\phi_W^* \quad (4.34)$$

where $\Lambda_{rr'}$ is a suitable projection operator for extracting the spin density matrix element $\rho_{rr'}$. In equation 4.34 the extraction of the spin density matrix elements of the W^- boson is shown

as an example. The projection operators reflect the standard V-A couplings of the fermions to the W boson in the W decay. They can be derived from equation 4.26 by integrating over the two W decay angles and using the normalisation relation of the D-functions

$$\int_{-1}^{+1} \int_{-\pi}^{+\pi} D_{\tau\tau'}(\theta^* \phi^*) d \cos \theta^* d \phi^* = \frac{8\pi}{3} \delta_{\tau\tau'}.$$

Expressions for the projectors [61] are summarised below and the functional forms are shown in figure 4.5.

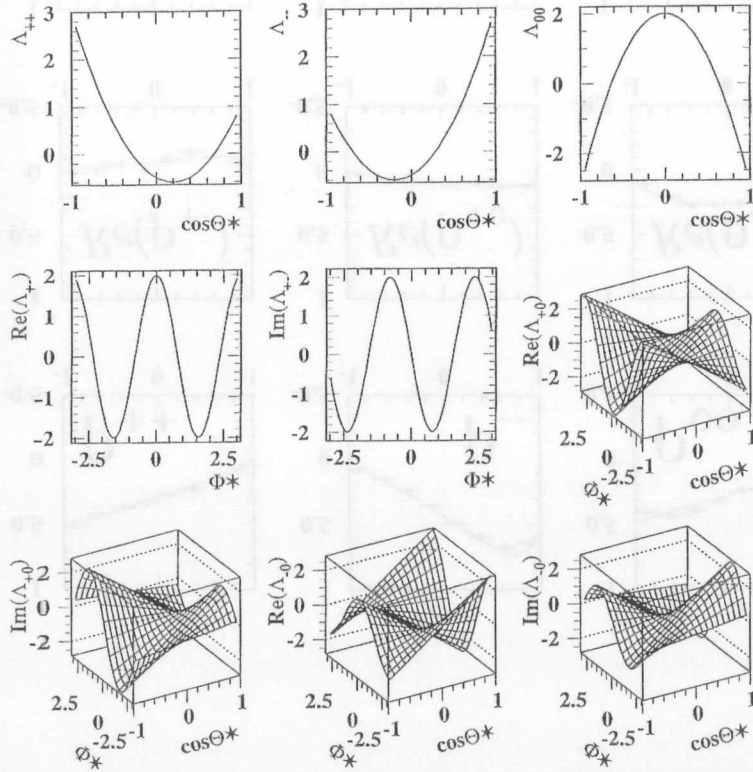


Figure 4.5: The projection functions

$$\begin{aligned} \Lambda_{\pm\pm}^{W+} &= \Lambda_{\mp\mp}^{W-} = \frac{1}{2}(5 \cos^2 \theta^* \mp 2 \cos \theta^* - 1) \\ \Lambda_{00}^{W+} &= \Lambda_{00}^{W-} = 2 - 5 \cos^2 \theta^* \\ \Lambda_{+-}^{W+} &= \Lambda_{-+}^{W-} = 2 \exp(2i\phi^*) \\ (\Lambda_{+0}^{W+})^* &= -\Lambda_{\pm 0}^{W-} = \frac{8}{3\pi\sqrt{2}}(1 \mp 4 \cos \theta^*) \exp(\mp i\phi^*) \end{aligned} \quad (4.35)$$

The resulting density matrix elements are functions of $\cos \theta$.

The method of extracting the spin density matrix elements from data is described in the following. For each event i there is a measurement of the W production angle $\cos \theta_i$ and the W decay angles $\cos \theta_i^*$ and ϕ_i^* . According to equation 4.34, the spin density matrix element of a certain bin k of $\cos \theta$ is then obtained by

$$\rho_{\tau\tau'}^k = \frac{1}{N_k} \sum_{i=1}^{N_k} \Lambda_{\tau\tau'}(\cos \theta_i^*, \phi_i^*). \quad (4.36)$$

Here, the sum runs over all events i in bin k of $\cos \theta$, N_k is the total number of events in this particular bin of $\cos \theta$, and $\Lambda = \Lambda(\cos \theta^*, \phi^*)$ is the value of the projection operator at $\cos \theta_i^*$ and ϕ_i^* of event i .

The error on the spin density matrix element $\rho_{\tau\tau'}^k$ can then be obtained by

$$\sigma(\rho_{\tau\tau'}^k) = \sqrt{\frac{1}{N_k(N_k - 1)} \sum_{i=1}^{N_k} (\Lambda_{\tau\tau'}(\cos \theta_i^*, \phi_i^*) - \rho_{\tau\tau'}^k)^2}. \quad (4.37)$$

The different spin density matrix elements are correlated in a given bin of $\cos \theta$. However, for different bins of $\cos \theta$ they are uncorrelated. The covariance between the two spin density matrix elements $\rho_{\tau\tau'}^k$ and $\rho_{\lambda\lambda'}^k$ can be estimated according to

$$\text{cov}(\rho_{\tau\tau'}^k, \rho_{\lambda\lambda'}^k) = \frac{1}{N_k(N_k - 1)} \left(\sum_{i=1}^{N_k} (\Lambda_{\tau\tau'}(\cos \theta_i^*, \phi_i^*) - \rho_{\tau\tau'}^k) (\Lambda_{\lambda\lambda'}(\cos \theta_i^*, \phi_i^*) - \rho_{\lambda\lambda'}^k) \right) \quad (4.38)$$

Using all projection operators given in equation 4.35, three real diagonal and six off-diagonal spin density matrix elements with a real and an imaginary part can be extracted from the data set and the errors and correlations can be determined. However, the single W spin density matrix is hermitian, therefore only three off-diagonal elements are independent.

The spin density matrix elements extracted from a Monte Carlo sample on generator level (Run 5762) of 100000 WW events at a centre-of-mass energy of 184 GeV is shown together with the Born level prediction in figure 4.6. In table 4.7, the correlations between all nine spin density matrix elements integrated over the whole $\cos \theta$ range are given. The correlations do not depend strongly on $\cos \theta$, and, therefore, can be regarded as typical values for all bins in $\cos \theta$.

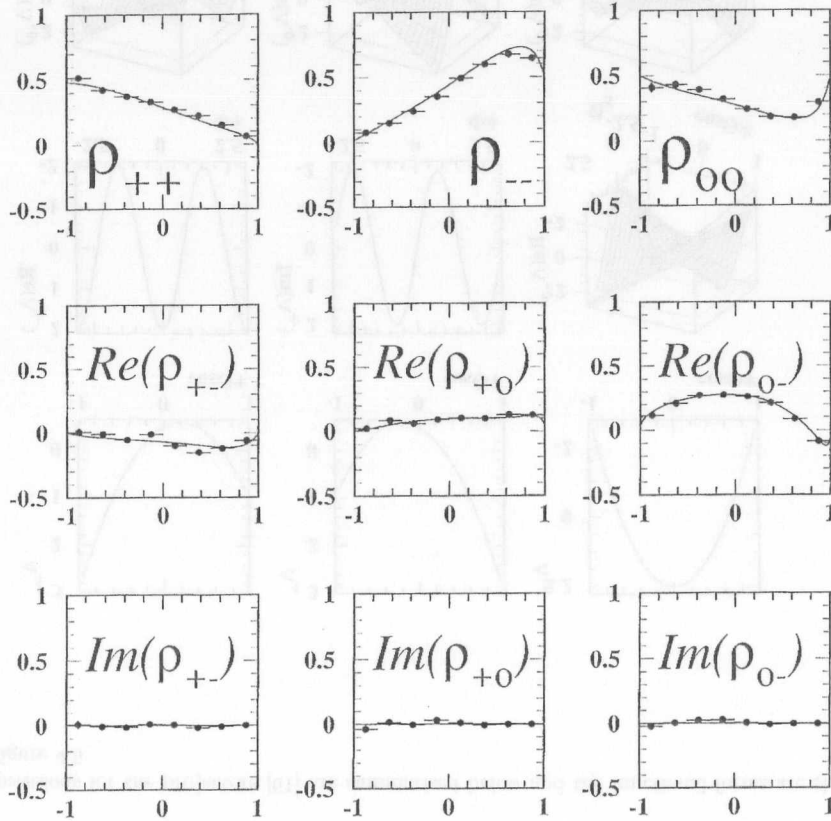


Figure 4.6: The spin density matrix elements extracted from the leptonically decaying W of a generator level Monte Carlo sample are shown. Overlaid are the Born level predictions of the Standard Model.

	ρ_{++}	ρ_{--}	ρ_{00}	$\text{Re}(\rho_{+-})$	$\text{Im}(\rho_{+-})$	$\text{Re}(\rho_{+0})$	$\text{Im}(\rho_{+0})$	$\text{Re}(\rho_{0-})$	$\text{Im}(\rho_{0-})$
ρ_{++}	1.00	0.29	-0.75	0.01	0.00	0.12	0.00	-0.11	0.00
ρ_{--}	0.29	1.00	-0.86	0.02	0.01	-0.14	0.00	0.04	-0.01
ρ_{00}	-0.75	-0.86	1.00	-0.02	0.01	0.03	0.00	0.03	0.02
$\text{Re}(\rho_{+-})$	0.01	0.02	-0.02	1.00	0.00	0.07	0.00	0.07	0.00
$\text{Im}(\rho_{+-})$	0.00	0.01	0.01	0.00	1.00	-0.01	0.08	0.00	-0.05
$\text{Re}(\rho_{+0})$	0.12	-0.14	0.03	0.07	-0.01	1.00	0.00	-0.73	0.00
$\text{Im}(\rho_{+0})$	0.00	0.00	0.00	0.00	0.08	0.00	1.00	0.00	0.69
$\text{Re}(\rho_{0-})$	-0.11	0.04	0.03	0.07	0.00	-0.73	0.00	1.00	0.01
$\text{Im}(\rho_{0-})$	0.00	0.00	0.00	0.00	-0.05	0.00	0.71	0.00	1.00

Table 4.7: Correlations between the different spin density matrix elements as determined from the Monte Carlo Run 5762.

4.3.5 What can be gained from Folded Angular Distributions

For hadronic decays of the W boson, where the quark cannot be distinguished from the anti-quark without additional information like jet-charge, only the folded angular distributions of $\cos \theta^*$ and ϕ^* are directly available. The folded distributions can be identified with the symmetric³ part of the angular distributions [58], whereas no information about the anti-symmetric part is accessible. Six out of nine spin density matrix elements (or combinations of them) can be extracted from the folded angular distributions, as will be shown in the following. The projection operators can be split into a symmetric and anti-symmetric part, as given in table 4.8. The symmetric part of the spin density matrix element can be extracted from the symmetric

Projection Operator	Symmetric Part	Anti-Symmetric Part
$\Lambda_{\pm\pm}^{W+} = \Lambda_{\mp\mp}^{W-}$	$\frac{1}{2}(5 \cos^2 \theta^* - 1)$	$\frac{1}{2} \mp \cos \theta^*$
$\Lambda_{00}^{W+} = \Lambda_{00}^{W-}$	$2 - 5 \cos^2 \theta^*$	-
$\Lambda_{+-}^{W+} = \Lambda_{-+}^{W-}$	$2 \exp(2i\phi^*)$	-
$(\Lambda_{\mp 0}^{W+})^* = -\Lambda_{\pm 0}^{W-}$	$\frac{8}{3\pi\sqrt{2}}(\mp 4 \cos \theta^* \exp(\mp i\phi^*))$	$\frac{8}{3\pi\sqrt{2}} \exp(\mp i\phi^*)$

Table 4.8: The symmetric and anti-symmetric parts of the projection operators

part of the angular distribution together with the symmetric part of the projection operator.

A symmetric (anti-symmetric) projection operator affects the symmetric (anti-symmetric)

³symmetric/anti-symmetric under the transformation

$$\begin{aligned} \cos \theta^* &\rightarrow -\cos \theta^* \\ \phi^* &\rightarrow \phi^* + \pi. \end{aligned}$$

angular distribution only, because the integral over an anti-symmetric function vanishes, *i.e.*

$$\begin{aligned}
\rho_{\tau\tau'} \frac{d\sigma}{d\cos\theta} &= \frac{1}{\text{Br}_{W\rightarrow\text{ff}}} \int_{-1}^{+1} \int_{-\pi}^{+\pi} \left(\frac{d\sigma}{d3a} \Lambda \right) d\cos\theta^* d\phi^* \\
&= \frac{1}{\text{Br}_{W\rightarrow\text{ff}}} \int_{-1}^{+1} \int_{-\pi}^{+\pi} \left(\left(\frac{d\sigma}{d3a} \right)^{(s)} + \left(\frac{d\sigma}{d3a} \right)^{(a)} \right) (\Lambda^{(s)} + \Lambda^{(a)}) d\cos\theta^* d\phi^* \\
&= \frac{1}{\text{Br}_{W\rightarrow\text{ff}}} \int_{-1}^{+1} \int_{-\pi}^{+\pi} \left(\left(\frac{d\sigma}{d3a} \right)^{(s)} \Lambda^{(s)} + \left(\frac{d\sigma}{d3a} \right)^{(a)} \Lambda^{(a)} + \left(\frac{d\sigma}{d3a} \right)^{(s)} \Lambda^{(a)} + \left(\frac{d\sigma}{d3a} \right)^{(a)} \Lambda^{(s)} \right) d\cos\theta^* d\phi^* \\
&= \frac{1}{\text{Br}_{W\rightarrow\text{ff}}} \int_{-1}^{+1} \int_{-\pi}^{+\pi} \left(\left(\frac{d\sigma}{d3a} \right)^{(s)} \Lambda^{(s)} + \left(\frac{d\sigma}{d3a} \right)^{(a)} \Lambda^{(a)} \right) d\cos\theta^* d\phi^*, \tag{4.39}
\end{aligned}$$

where $\frac{d\sigma}{d3a}$ is used as an abbreviation for $d\sigma/d\cos\theta d\cos\theta^* d\phi^*$. The following combinations of spin density matrix elements can be extracted from folded angular distributions, because the according combinations of projection operators can be expressed in symmetric parts of the projection operators only.

$$\rho_{++} + \rho_{--}, \quad \rho_{00}, \quad \text{Re}(\rho_{+-}), \quad \text{Im}(\rho_{+-}), \quad \text{Re}(\rho_{+0} - \rho_{-0}), \quad \text{Im}(\rho_{+0} + \rho_{-0}),$$

where the combination $\rho_{++} + \rho_{--}$ and the spin density matrix element ρ_{00} are fully anticorrelated. As an example it is shown explicitly how the combination $\text{Re}(\rho_{+0} - \rho_{-0})$ can be extracted from the folded distribution only:

$$\begin{aligned}
\text{Re}(\rho_{+0} - \rho_{-0}) \frac{d\sigma}{d\cos\theta} &= \frac{1}{\text{Br}_{W\rightarrow\text{ff}}} \int \int \frac{d\sigma}{d3a} (\text{Re}(\Lambda_{+0}) - \text{Re}(\Lambda_{-0})) d\cos\theta^* d\phi^* \\
&= \frac{1}{\text{Br}_{W\rightarrow\text{ff}}} \int \int \left(\left(\frac{d\sigma}{d3a} \right)^{(s)} + \left(\frac{d\sigma}{d3a} \right)^{(a)} \right) 2\text{Re}(\Lambda_{-0}^{(s)}) d\cos\theta^* d\phi^* \tag{4.40} \\
&= 2 \frac{1}{\text{Br}_{W\rightarrow\text{ff}}} \int \int \left(\frac{d\sigma}{d3a} \right)^{(s)} \text{Re}(\Lambda_{-0}^{(s)}) d\cos\theta^* d\phi^*
\end{aligned}$$

4.3.6 Extraction of the Anomalous TGC

In order to compare the spin density matrix elements extracted from the data with the theoretical predictions and to measure the triple gauge boson coupling parameters a χ^2 -fit is performed. In the following section the main issues of the fit are demonstrated. For this purpose the spin density matrix elements extracted from generator level Monte Carlo are directly compared to their analytical Born level expressions. The treatment of the experimental effects will be described in section 4.4.

According to equation 4.34 the density matrix elements as a function of the W production angle $\cos\theta$ are normalised to the differential cross-section $d\sigma/d\cos\theta$, *i.e.* only the information about the relative contribution of the various helicity states is accessible. Therefore, additional information can be utilised by including the differential cross-sections $d\sigma/d\cos\theta$ in the χ^2 -fit. Consequently, the spin density matrix of the leptonically and hadronically decaying W boson can be used independently⁴ together with the angular information of the W production. Single parameters or combinations of anomalous trilinear gauge couplings are the free parameters in the fit.

As can be seen from equation 4.25 and table 4.7, the diagonal elements of the spin density matrix are highly correlated. Therefore, only two of the three diagonal elements have been

⁴Although in the method described here (the single-W spin density matrix analysis) the spin correlations between the two W bosons are neglected. The resulting loss in sensitivity is small, *c.f.* section 4.6.

used in the fit. The following list summarises the information used in the fit to extract the coupling parameters:

$$\begin{aligned}
W^- &: \cos\theta \\
W_{\text{lep}} &: \rho_{--}, \rho_{00}, \rho_{+-}, \rho_{+0}, \rho_{-0} \\
W_{\text{had}} &: \rho_{00}, \rho_{+-}, \text{Re}(\rho_{+0} - \rho_{-0}), \text{Im}(\rho_{+0} + \rho_{-0}).
\end{aligned}$$

The correlations between the density elements are taken into account. In principle the correlations between the individual matrix elements can be estimated directly from data. But because of the limited statistics of the present data samples, this would introduce a large statistical component into the correlation estimate. Therefore, the correlations are taken from the Monte Carlo. In general, the correlations depend on possible anomalous couplings. In table 4.9 a comparison is shown, where two generator level Monte Carlo samples with anomalous couplings have been analysed. The fit was performed using the correct correlations as determined from the Monte Carlo sample with the anomalous couplings and then repeated using the Standard Model correlations. As can be seen from table 4.9, the differences in the fit results are tiny, *i.e.* the systematic effects error for taking the Standard Model correlations is negligible, even for relatively large anomalous couplings.

	correct correlations	Standard Model correlations
Run 6844	2.009 ± 0.021	2.009 ± 0.021
Run 6845	$-2.084 \begin{smallmatrix} +0.051 \\ -0.054 \end{smallmatrix}$	$-2.081 \begin{smallmatrix} +0.051 \\ -0.054 \end{smallmatrix}$

Table 4.9: The results of the χ^2 -fit to Monte Carlo samples with anomalous couplings, where the ‘true’ correlations or the Standard Model correlations are used.

4.3.7 Comparison of the Sensitivity to Anomalous TGC

In the following section the relative contributions of the different angular distributions to the overall error on the determination of the triple gauge couplings are investigated. In table 4.10, the results of the fit to a PYTHIA Monte Carlo sample (Run 5762) are given for the fit of the spin density matrices of the leptonically and hadronically decaying W and the W production angle.

Although the error of the fit is only reduced by 10 - 30 % by including the information of the decay angles of the W, this information turns out to be essential to constrain the fit to the ‘true’ minimum. Because of the particular shape of the angular distribution for different triple gauge coupling parameters, it may happen that the χ^2 -curve of a Standard Model sample has a second minimum for a non-Standard Model value of the coupling parameter. Especially in the W Φ model the information of the decay angles helps to avoid these ambiguities in the fit result. This can be demonstrated by studies using a number of Monte Carlo subsamples with luminosities similar to that of the OPAL data of about 57pb^{-1} . Figure 4.7 a) and b) show the fit results for 120 fits to the $\alpha_{W\Phi}$ parameter, where $\cos\theta$ only or $\cos\theta$ plus the information of the W decay angles have been used, respectively. Whereas in case a) the correct value for

	$\alpha_{B\Phi}$	$\alpha_{W\Phi}$	α_W
$\cos\theta$	+0.000 ^{+0.046} _{-0.045}	+0.000 ± 0.008	-0.003 ± 0.014
ρ_{lep}	-0.106 ^{+0.058} _{-0.054}	-0.003 ± 0.018	-0.019 ^{+0.025} _{-0.029}
ρ_{had}	+0.129 ^{+0.122} _{-0.115}	-0.027 ^{+0.026} _{-0.027}	+0.103 ^{+0.075} _{-0.072}
all	-0.042 ^{+0.035} _{-0.034}	-0.002 ± 0.007	-0.003 ± 0.012

Table 4.10: Comparison of the sensitivity of the individual angular distributions to anomalous couplings, determined from the Monte Carlo Run 5762.

$\alpha_{W\Phi}$ is fitted in 55% of the cases, in case b) in all fits except one the Standard Model value is reproduced within its errors.

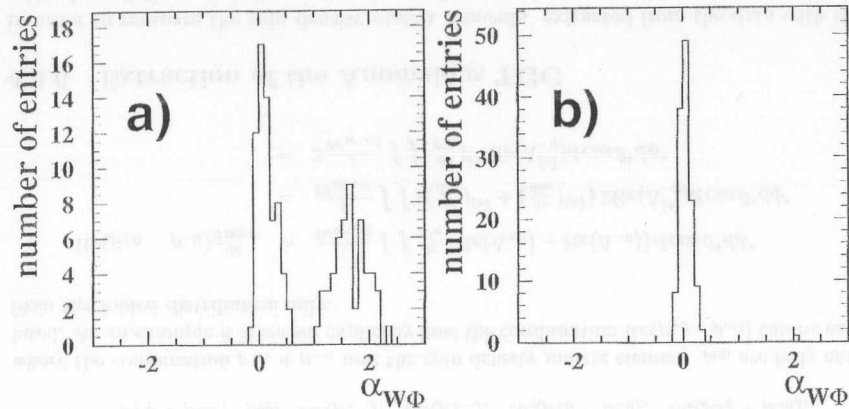


Figure 4.7: Fit results in the $W\Phi$ model for 120 fits to small Monte Carlo samples, where the $\cos\theta$ only (a) or all angular information (b) is used.

4.4 Extracting TGC including Experimental Effects

The theoretical predictions for the helicity amplitudes and density matrix elements in reference [58, 61] are Born level approximations and do not include neither effects of initial state radiation (ISR) nor the finite width of the W decay. Moreover, there are a number of experimental effects which disturb the reconstruction of the angular distributions and, thus, lead to deviations from the true spin density matrix elements when extracted from data. The most important effects are the angular resolution, the finite selection efficiency and detector acceptance. In addition, background contributions have to be taken into account.

In the following two different methods will be presented to handle experimental effects. The first strategy is to ‘correct’ the data such, that the ‘true’ density matrix elements, i.e. without

any experimental effects, can be reconstituted. Then the spin density matrix elements can be compared to the Born level analytical expressions. The main advantage is that with this method the density elements can be visualised and the corrected data can directly be compared to the theoretical expressions ‘by eye’. In such a way a model-independent test of the trilinear gauge coupling is possible. This correction method is done with the help of a Standard Model Monte Carlo and thus the experimental effects for any possible anomalous couplings are only described approximately. Therefore this method is suitable for a quantitative analysis of the trilinear gauge couplings with reservations only.

The idea of the second approach is to reconstruct the angular distributions and density elements from the data without any correction for experimental effects. Subsequently these distributions are compared with the adequate distributions taken from fully simulated Monte Carlo. Because only a limited number of fully simulated data samples (with a small number of different anomalous coupling parameters) is available, a reweighting technique is used to produce samples with a continuous spectrum of anomalous couplings, which is necessary in order to perform a fit to the data. For this method the experimental effects are handled exactly for any anomalous couplings. But since the extracted spin density elements cannot directly be compared to the theoretical predictions, thus the visualisation of the physics behind is intangible. In the following these two analysis techniques are described.

4.4.1 The ‘naive’ Method: Correction of the Data

In the following sections various experimental effects and the correction procedures applied to the data to account for possible biases are discussed.

ISR and finite W Width

The description of the angular distributions of the W decay, c.f. equation 4.26, and, consequently, the projection operators given in equation 4.35 as well, do not include the effects of ISR and the finite W width. Therefore, systematic differences are expected when the density elements derived from the data are compared to the Born level formulas. A bias may be introduced if the method is blindly adopted without accounting for these effects. According to studies in [4], the effect due to the W width is one order of magnitude smaller than that of the ISR, and is, therefore, negligible.

According to the EXCALIBUR Monte Carlo, the mean energy of the initial state photons is 1.6 GeV. To first order the overall effect of ISR is a reduction of the centre-of-mass energy. Because the W^+W^- system is boosted after initial state radiation, the angular distributions are affected as well. Consequently, the effects of ISR can, at least partly, be compensated by reducing the centre-of-mass energy for the theoretical predictions of the density matrices and the differential cross-section in the χ^2 fit. In order to estimate the effects due to ISR, the centre-of-mass energy in the fit is reduced in steps of 1 GeV, fitting a PYTHIA Monte Carlo sample. The results are listed in table 4.11. In addition the results of the fit with an energy reduced by the mean initial state photon energy is quoted. This procedure is repeated with the EXCALIBUR and, because of its accurate description of photon radiation, the KORALW Monte Carlo.

Comparing the results of the different Monte Carlo generators of table 4.11, it is clearly visible that an overall reduction of the centre-of-mass energy helps to reduce systematic shifts

$\sqrt{s}[\text{GeV}]$	$\alpha_{B\Phi}$	$\alpha_{W\Phi}$	α_W
PYTHIA MC Run 5762 (184 GeV)			
184.0	-0.175 ± 0.031	-0.037 ± 0.007	-0.069 ± 0.011
183.0	-0.129 ± 0.032	-0.023 ± 0.007	-0.043 ± 0.012
182.0	-0.074 ± 0.034	-0.009 ± 0.007	-0.017 ± 0.013
181.0	-0.007 ± 0.037	0.006 ± 0.007	0.012 ± 0.012
182.4	-0.103 ± 0.033	-0.016 ± 0.007	-0.029 ± 0.012
EXCALIBUR MC Run 6843 (184 GeV)			
184.0	-0.171 ± 0.030	-0.029 ± 0.007	-0.066 ± 0.011
183.0	-0.123 ± 0.031	-0.015 ± 0.007	-0.040 ± 0.012
182.0	-0.063 ± 0.034	-0.001 ± 0.007	-0.013 ± 0.012
181.0	0.001 ± 0.039	0.015 ± 0.007	0.017 ± 0.013
182.4	-0.094 ± 0.032	-0.008 ± 0.007	-0.026 ± 0.012
KORALW MC Run 7323 (183 GeV)			
183.0	-0.206 ± 0.030	-0.026 ± 0.007	-0.055 ± 0.012
182.0	-0.152 ± 0.032	-0.011 ± 0.007	-0.027 ± 0.012
181.0	-0.086 ± 0.036	-0.005 ± 0.007	0.025 ± 0.013
180.0	0.016 ± 0.041	0.021 ± 0.007	0.034 ± 0.013
181.4	-0.114 ± 0.034	-0.002 ± 0.007	-0.009 ± 0.013

Table 4.11: The fit results of generator level fits to fully simulated data, where the centre-of-mass energy in the χ^2 -fit is stepwise reduced, in order to account for ISR. All the samples used here are Standard Model Monte Carlo.

due to ISR, although this simplified method cannot correct perfectly for ISR. If, for example, the energy in the χ^2 -fit is reduced by 1.6 GeV, i.e. the mean energy of the initial state photons, the bias due to ISR vanishes for the $\alpha_{W\Phi}$ and α_W model. Whereas for the $\alpha_{B\Phi}$ model there is still a shift visible, but compared to the fits using the nominal centre-of-mass energy, it is reduced by a factor of two.

It has been confirmed by generator level studies with the EXCALIBUR program, that the variations seen in the tests described above are really due to ISR. The EXCALIBUR generator allows to switch off ISR. Thus two samples of Standard Model (i.e. without anomalous couplings) EXCALIBUR Monte Carlo has been generated without detector simulation, of which in one the initial state radiation was set to zero, whereas the other one included the effects of ISR. The samples were generated with a centre-of-mass energy of 183 GeV. After extraction of the spin density matrix elements of both samples the χ^2 -fit was performed. The fit of the test sample without ISR returns the generated Standard Model value for the TGC without any bias, whereas the fitted value for the sample with ISR gives a non-zero value for the coupling parameters, comparable to those in table 4.11.

Overall, the effects of ISR can be significantly reduced by lowering the centre-of-mass energy by the mean energy of the initial state photons. Note that the effects of ISR (i.e. the bias seen by comparing data or Monte Carlo including ISR with Born level approximations of the density elements) are expected to be different for samples with anomalous couplings, because the angular distributions will be affected differently by the recoil of the initial state photon.

Acceptance and Angular Resolution

In figure 4.8, the angular distributions derived from the EXCALIBUR sample (Run 7352) in $\cos\theta, \cos\theta^*$ and ϕ^* of the leptonically decaying are shown for all events and the true Monte Carlo angles. Overlaid are the distributions, where selected events only are used and where the angles are either reconstructed as they are in data or those from the Monte Carlo information has been used, respectively. Comparing the distributions for all and for the selected events only shows, that the selection biases the angular distributions. This bias is introduced because of the finite detector acceptance and the selections cuts. Moreover, the finite angular resolution introduces an additional bias in the angular distributions.

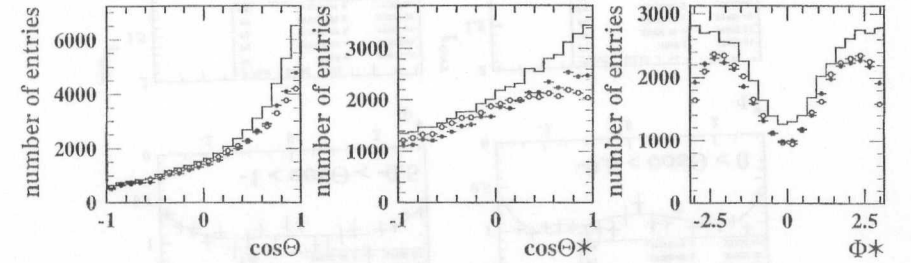


Figure 4.8: The angular distributions of the three angles $\cos\theta$, $\cos\theta^*$ and ϕ^* . The histogram represents the 'truth', where the Monte Carlo angles for all events are shown, the open circles and the black dots mark the distributions of the Monte Carlo and the reconstructed angles, respectively, for selected events only.

In the following a method to account for these experimental effects is described. The method adopted here is an expanded acceptance correction. A finite acceptance can easily be taken into account by introducing a correction, which is given by the ratio of the appropriate distribution of the selected events to that of all events. This approach is adopted here in order to account not only for the finite detector acceptance, but for the bias due to selection cuts and angular resolutions as well. It is clear that this simplistic attempt cannot be exact and cannot account perfectly for the different experimental effects. But in view of the limited statistics of the data taken in 1997, the method seems to be warrantable as will be shown in the following. Especially a dependence in the selection efficiency on the angular distributions will cause a bias when large anomalous couplings are determined.

The binning in $\cos\theta$ in the density matrices corresponds to the binning for the correction functions. The correction functions for a certain bin of $\cos\theta$, k , are defined as

$$f_k^{\text{corr}} = \left(\frac{d\sigma}{d\cos\theta^* d\phi^*} \right)_{\text{rec}} / \left(\frac{d\sigma}{d\cos\theta^* d\phi^*} \right)_{\text{true}}, \quad (4.41)$$

where *true* and *rec* denotes the differential cross-section of the simulation before and after the selection and reconstruction. In those cases, where only one dimensional distributions in $\cos\theta^*$ or ϕ^* are used to extract the density elements (c.f. equations 4.35), a polynomial is fitted to

the correction distributions, and the value of this function for the corresponding value of $\cos\theta^*$ or ϕ^* is used to correct the data. In the 2-dimensional case the fit gives unsatisfactory results, and therefore, the correction is done in a binned way. The fitted functions used for the combined efficiency and angular resolution correction including the fit parameters are shown in figure 4.9 for four different bins of $\cos\theta$.

The density matrix elements are then obtained according to

$$\rho_{\tau\tau'}^k = \frac{1}{N_k} \sum_{i=1}^{N_k} \frac{1}{f_k^{\text{corr}}} \Lambda_{\tau\tau'}(\cos\theta_i^*, \phi_i^*), \quad (4.42)$$

where f_k^{corr} is the efficiency correction of bin k in $\cos\theta$. The errors and correlations are estimated analogically.

In figure 4.10 the spin density matrix elements, extracted from the KORALW Monte Carlo sample on generator level are compared to those, where only the selected events with the reconstructed angles are used. In the latter case the correction for acceptance and angular resolution as derived from the EXCALIBUR Monte Carlo was applied. Note that the differences between both distributions in figure 4.10 contain a statistical component in addition to the possible systematic differences due to the efficiency and angular resolution correction, because the statistical overlap between the samples is 85% only. In order to quantify the differences, fits for anomalous couplings have been performed using Standard Model Monte Carlo samples. The results are summarised in table 4.12. The resulting differences between the fits to the generator level and corrected Monte Carlo are small.

	KORALW Monte Carlo		
	$\alpha_{B\Phi}$	$\alpha_{W\Phi}$	α_W
generator level	-0.114 ± 0.034	-0.002 ± 0.007	-0.009 ± 0.013
detector level (corrected with EXCALIBUR)	$-0.076^{+0.040}_{-0.039}$	-0.011 ± 0.008	$-0.040^{+0.014}_{-0.013}$

Table 4.12: Comparison of the χ^2 fit results for the full Monte Carlo information (generator level) with the sample of selected events only, where the reconstructed angles have been used and the selection efficiency and resolution correction have been applied. The correction have been extracted from Monte Carlo samples generated with the EXCALIBUR program.

In addition, the density elements have been extracted from Monte Carlo samples including anomalous couplings, but using a Standard Model Monte Carlo sample to determine the correction function. Here a bias is expected, because the correction functions are determined from a Standard Model Monte Carlo sample. The correction functions determined from samples including anomalous couplings are different from the Standard Model corrections mostly because the efficiency and resolution depends in general on the angular distributions and thus on the anomalous couplings. These investigations are summarised in figure 4.11 for different samples. These comparisons show that, especially for large anomalous couplings, a bias is introduced if the acceptance and resolution corrections is extracted from a Standard Model Monte Carlo. The discrepancy between the input and the fitted value for the coupling parameters show a

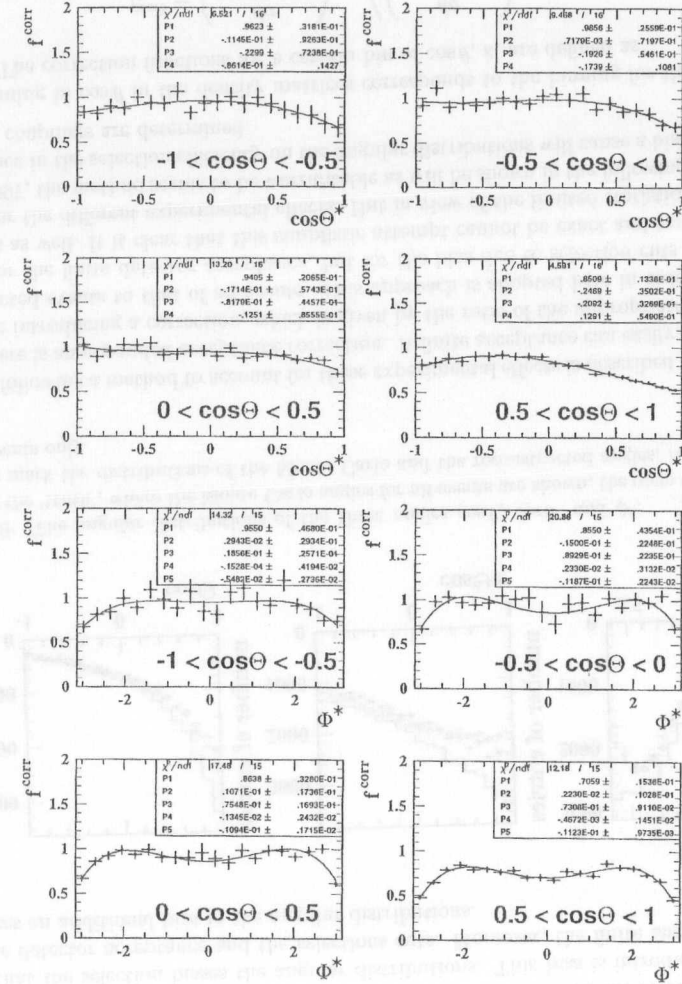


Figure 4.9: The acceptance and resolution corrections for four bins in $\cos\theta$. Shown are the correction functions in $\cos\theta^*$ and ϕ^* , where a third and fourth degree polynomial is used to fit the correction factors, respectively.

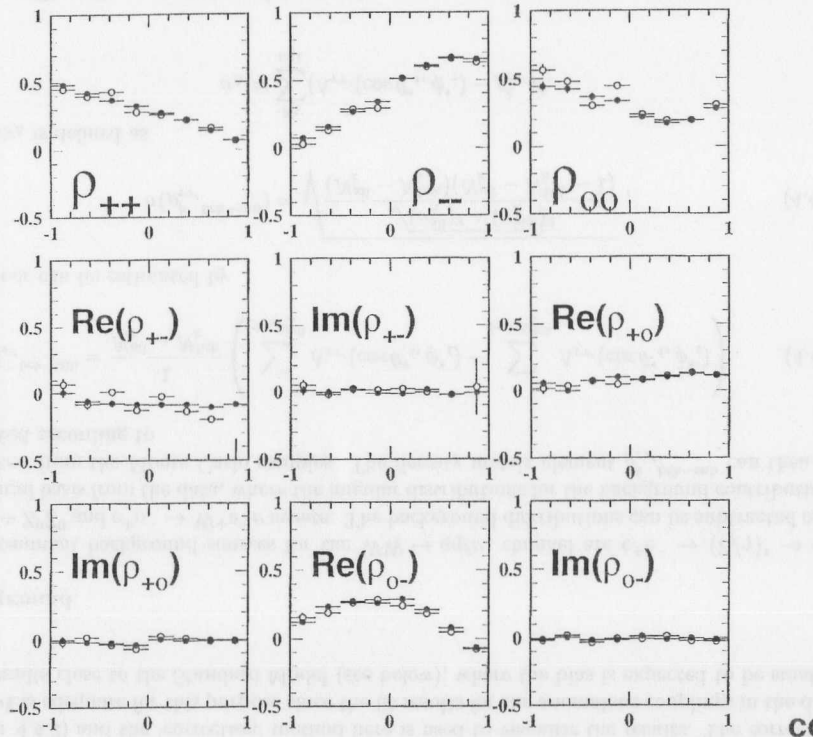


Figure 4.10: The density elements extracted from the KORALW Monte Carlo on generator level (open circles) compared to those, where selected events only and the reconstructed angles are used and the correction (derived from the EXCALIBUR sample) has been applied (black dots).

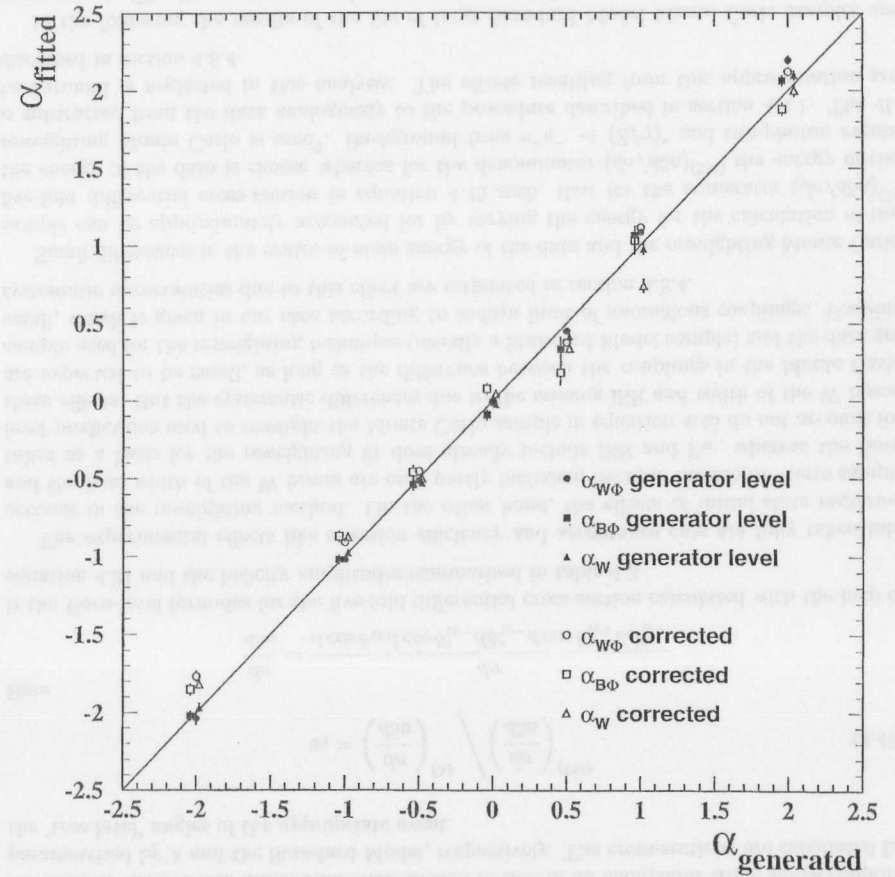


Figure 4.11: Summary of the bias checks for the methods which corrects the data to tree level (open symbols). For a comparison the results for the generator level fits of the same samples are shown (black symbols). The line corresponds to an unbiased analysis.

non-linear behaviour on the dependence on the anomalous coupling, such that a bias-correction seems to be difficult. Especially in the $B\Phi$ model the bias is relatively large.

An alternative correction of the data to tree-level distributions would be a real unfolding technique. This would avoid the disadvantages mentioned above, but the ‘unfolding’ would have to be done in a binned way in a five dimensional space, because of the correlations of the five angles $\cos\theta$, $(\cos\theta)_{W^-}$, $(\phi)_{W^-}$, $(\cos\theta)_{W^+}$ and $(\phi)_{W^+}$. This would not only cause severe Monte Carlo statistics problems but also a loss in the statistical power of the analysis, because the extraction of the density matrices would no longer be unbinned in $\cos\theta^*$ and ϕ^* . Instead, a reweighting technique will be employed to get the quantitative results of this analysis (c.f. section 4.4.2) and the ‘correction’ method here is used to visualise the results. The correction method is adequate for this purpose since the fit results for the anomalous couplings in the data give results close to the Standard Model (see below), where the bias is expected to be small.

Background

The dominant background sources for the $WW \rightarrow qq\ell\nu$ channel are $e^+e^- \rightarrow (Z/\gamma)^* \rightarrow q\bar{q}$, $e^+e^- \rightarrow Z^0Z^0$ and $e^+e^- \rightarrow W^+e^-\nu$ events. The background distributions can be subtracted on a statistical basis from the data, where the angular distributions for the background contributions are taken from the Monte Carlo samples. The density matrix element $\rho_{\tau\tau'}^k{}^{\text{bck-sub}}$ can then be extracted according to

$$\rho_{\tau\tau'}^k{}^{\text{bck-sub}} = \frac{1}{N_k^{\text{all}} - N_k^{\text{bck}}} \left(\sum_{i=1, N_k^{\text{all}}} \Lambda_{\tau\tau'}(\cos\theta_i^*, \phi_i^*) - \sum_{i=1, N_k^{\text{bck}}} \Lambda_{\tau\tau'}(\cos\theta_i^*, \phi_i^*) \right). \quad (4.43)$$

The error can be estimated by

$$\sigma(\rho_{\tau\tau'}^k{}^{\text{bck-sub}}) = \sqrt{\frac{\sqrt{(\sigma_\Lambda^{\text{all}})^2 + (\sigma_\Lambda^{\text{bck}})^2}}{(N_k^{\text{all}} - N_k^{\text{bck}})(N_k^{\text{all}} - N_k^{\text{bck}} - 1)}}, \quad (4.44)$$

where σ_Λ is defined as

$$\sigma_\Lambda = \sum_{i=1}^{N_k} (\Lambda_{\tau\tau'}(\cos\theta_i^*, \phi_i^*) - \rho_{\tau\tau'}^k)^2.$$

4.4.2 The Reweighting Method

In order to reduce the bias introduced by handling the experimental effects, an alternative procedure has been developed to extract and fit the density matrix elements. In this method the angular distributions and density elements are directly reconstructed in data, without any correction for experimental effects. Subsequently these distributions are compared in a χ^2 -fit to the corresponding distributions taken from fully simulated data, which are produced by a reweighting technique. By this procedure the experimental effects are included (nearly) exactly, and therefore no bias is expected, even for large anomalous couplings. At the same time the statistical advantage of extracting the density matrix elements in an unbinned way in $\cos\theta^*$ and ϕ^* is preserved.

Each selected event i in a fully simulated Standard Model Monte Carlo sample is weighted by a factor w_i in order to reproduce a sample of any anomalous coupling parameter λ (in one of the appropriate models). These weights can be interpreted as the probability that an event is produced in a certain phase space point (with the angles $\cos\theta$, $\cos\theta_{W^-}^*$, $\phi_{W^-}^*$, $\cos\theta_{W^+}^*$ and $\phi_{W^+}^*$) assuming an anomalous coupling λ divided by the probability that this event is produced at the same phase space point within the Standard Model. Thus these weights w_i are calculated by the ratio of the five-fold differential cross-section in case of an anomalous triple gauge coupling parametrised by λ and the Standard Model, respectively. The cross-sections are calculated for the ‘tree level’ angles of the appropriate event.

$$w_i = \left(\frac{d\sigma}{d5a} \right)^{(\lambda)} / \left(\frac{d\sigma}{d5a} \right)^{(\text{SM})}. \quad (4.45)$$

Here

$$\frac{d\sigma}{d5a} = \frac{d\sigma}{d\cos\theta_W d\cos\theta_{W^-}^* d\phi_{W^-}^* d\cos\theta_{W^+}^* d\phi_{W^+}^*}$$

is the Born-level formulas for the five-fold differential cross-section calculated with the help of equation 4.21 and the helicity amplitudes summarised in table 4.2.

The experimental effects like selection efficiency and acceptance cuts are fully taken into account in the reweighting method. On the other hand, the effects of initial state radiation and the final width of the W boson are only partly included, because the Monte Carlo sample taken as a basis for the reweighting fit does already include ISR and Γ_W , whereas the Born level predictions used to reweight the Monte Carlo sample in equation 4.45 do not account for these effects. But the systematic differences due to the missing ISR and width of the W boson are expected to be small, as long as the difference between the couplings in the Monte Carlo sample used for the reweighting technique (usually a Standard Model sample) and the data are small, which is given in our case according to today's limit of anomalous couplings. Possible systematic uncertainties due to this effect are estimated in section 4.5.4.

Small differences in the centre-of-mass energy of the data and the reweighting Monte Carlo sample can be approximately accounted for by varying the energy for the calculation of the five-fold differential cross-section in equation 4.45 such, that for the numerator $(d\sigma/d5a)^{(\lambda)}$ the energy of the data is chosen whereas for the denominator $(d\sigma/d5a)^{(\text{SM})}$ the energy of the reweighting Monte Carlo is used⁵. Background from $e^+e^- \rightarrow (Z/\gamma)^*$ and two-photon events is subtracted from the data analogously to the procedure described in section 4.4.1. The 4f-background is neglected in this analysis. The effects resulting from this approximation are discussed in section 4.5.4.

In the following the results of the fits of large Standard Model Monte Carlo samples are summarised. The EXCALIBUR sample generated at 183 GeV has been chosen as a test sample. Various samples have been used as the reweighting Monte Carlo. In order to check the method to account for differences in energy between the reweighting Monte Carlo and data, the EXCALIBUR sample generated with 183 GeV has been fitted with an EXCALIBUR sample of 184 GeV as a reweighting Monte Carlo and applying the correction described above. The results are given in the last row of table 4.13 and they do not show any bias within the statistical significance of these tests.

⁵For fits on generator level this is an exact approach, whereas for fit including experimental effects this gives a reasonable approximation.

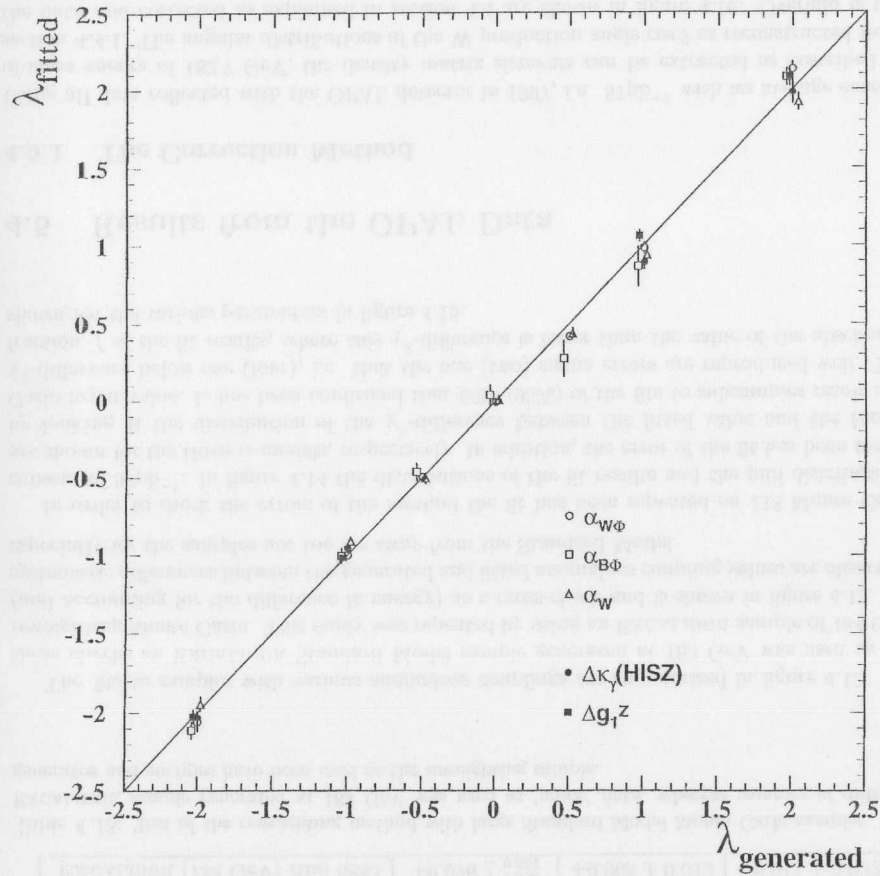


Figure 4.12: Summary of the bias checks for the reweighting method. All samples are generated with the EXCALIBUR Monte Carlo at a centre-of-mass energy of 183 GeV. The line corresponds to an unbiased analysis.

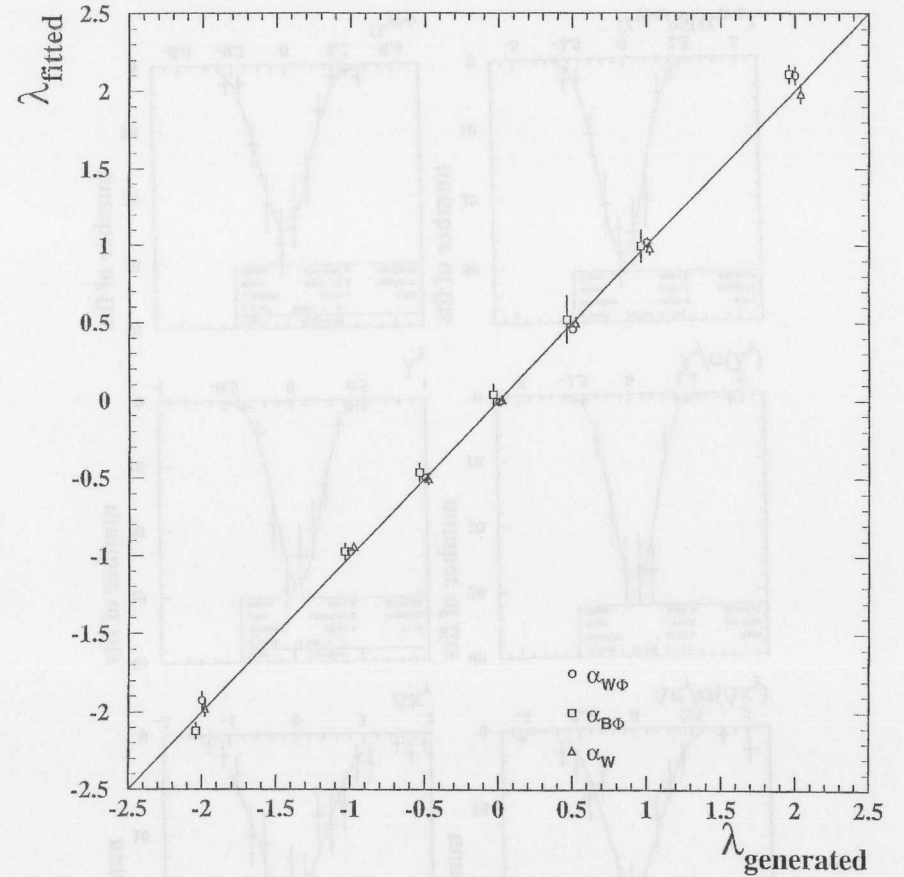


Figure 4.13: Summary of the bias checks for the reweighting method. The samples with anomalous couplings are EXCALIBUR samples generated at 183 GeV, whereas for the reweighting an EXCALIBUR Monte Carlo at 184 GeV was used. The line corresponds to an unbiased analysis.

Rewighting MC	$\alpha_{B\Phi}$	$\alpha_{W\Phi}$	α_W
PYTHIA Run 6900	$+0.028^{+0.068}_{-0.064}$	$+0.003 \pm 0.012$	$+0.009 \pm 0.021$
KORALW Run 7323	$+0.035^{+0.066}_{-0.070}$	$+0.012 \pm 0.012$	$+0.002 \pm 0.022$
grc4f Run 7337	$+0.003 \pm 0.069$	-0.022 ± 0.013	-0.031 ± 0.017
EXCALIBUR (184 GeV) Run 6843	$+0.076^{+0.068}_{-0.064}$	$+0.005 \pm 0.012$	$+0.011 \pm 0.022$

Table 4.13: Test of the reweighting method with large Standard Model Monte Carlo samples. The EXCALIBUR sample generated at 183 GeV was used as 'mock' data, whereas samples of different generator and energies have been used as the reweighting sample.

The fits to samples with various anomalous couplings are summarised in figure 4.12. For these checks an EXCALIBUR Standard Model sample generated at 183 GeV was used as the reweighting Monte Carlo. This study was repeated by using an EXCALIBUR sample of 184 GeV (and accounting for the difference in energy) as a cross-check and is shown in figure 4.13. No systematic differences between the generated and fitted anomalous coupling values are observed, especially for the samples not too far away from the Standard Model.

In order to check the errors of the method the fit has been repeated on 118 Monte Carlo subsets of 57pb^{-1} . In figure 4.14 the distributions of the fit results and the pull distributions are shown for the three α -models, respectively. In addition, the error of the fit has been tested by looking at the distribution of the χ^2 -difference between the fitted value and the Monte Carlo input value. It has been confirmed that 68% (95%) of the fits to subsamples result in a χ^2 -difference below one (four), i.e. that the one (two) sigma errors are reproduced well. The fraction f of the fit results, where this χ^2 -difference is lower than the value of the abscissa is shown for the various parameters in figure 4.15.

4.5 Results from the OPAL Data

4.5.1 The Correction Method

Using all data collected with the OPAL detector in 1997, i.e. 57pb^{-1} with an average centre-of-mass energy of 182.7 GeV, the density matrix elements can be extracted as described in section 4.4.1. The angular distributions of the W production angle $\cos\theta$ as reconstructed from the data and corrected as explained in section 4.4 are shown in figure 4.16. Overlaid is the Standard Model Monte Carlo distribution normalised to the number of expected events and the background contribution. In figure 4.17 and 4.18 the spin density elements are shown as a function of $\cos\theta$, extracted from the leptonic and hadronic W decay angles, respectively.

The data is corrected with the help of a Standard Model Monte Carlo sample in order to account for experimental effects as described in section 4.4.1. Overlaid are the (Born level) distributions as expected in the Standard Model and in addition the predictions for anomalous couplings of $\Delta g_1^2 = \pm 1$. The data are in good agreement with the Standard Model expectation. The results of a fit to these corrected curves with their statistical errors for the different triple gauge boson coupling parameters are given in table 4.14. For these measurements the angular

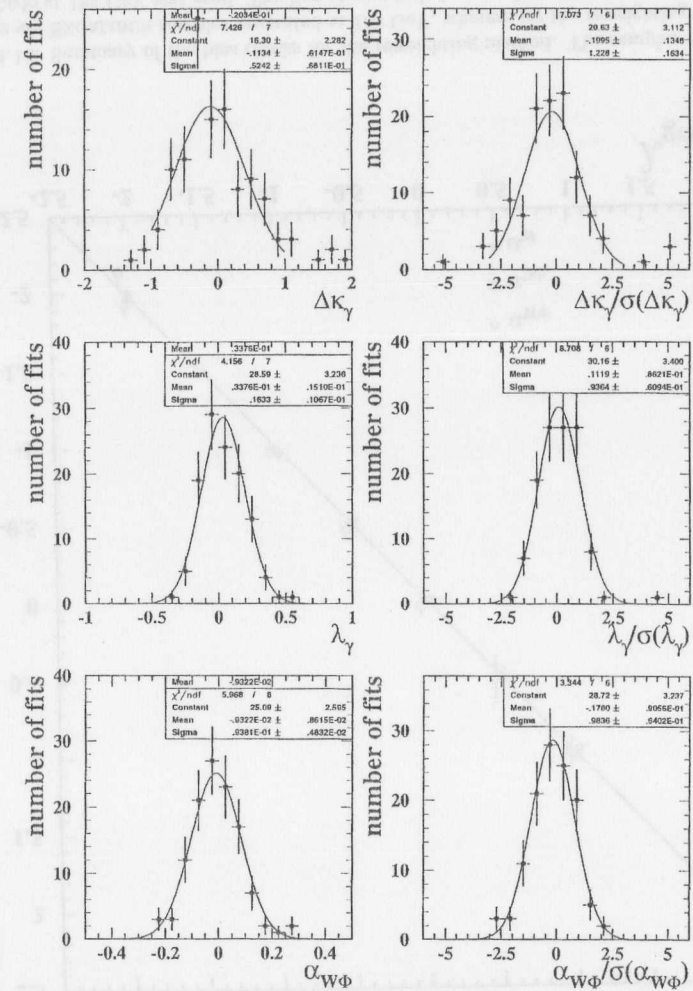


Figure 4.14: Fit results of 118 subsamples of the EXCALIBUR Monte Carlo with luminosities corresponding to 57pb^{-1} . The widths of the distributions of the results (left side) represent the expected error of the analysis for the corresponding coupling parameter. For these tests the statistical error of the reweighting Monte Carlo sample is included in the statistical fit errors, which will not be the case for the analysis of the data. Thus the expected error shown in table 4.15 are slightly smaller than the width of the distributions here. The width of the pull distributions (right side) shall be compatible with unity for correct errors.

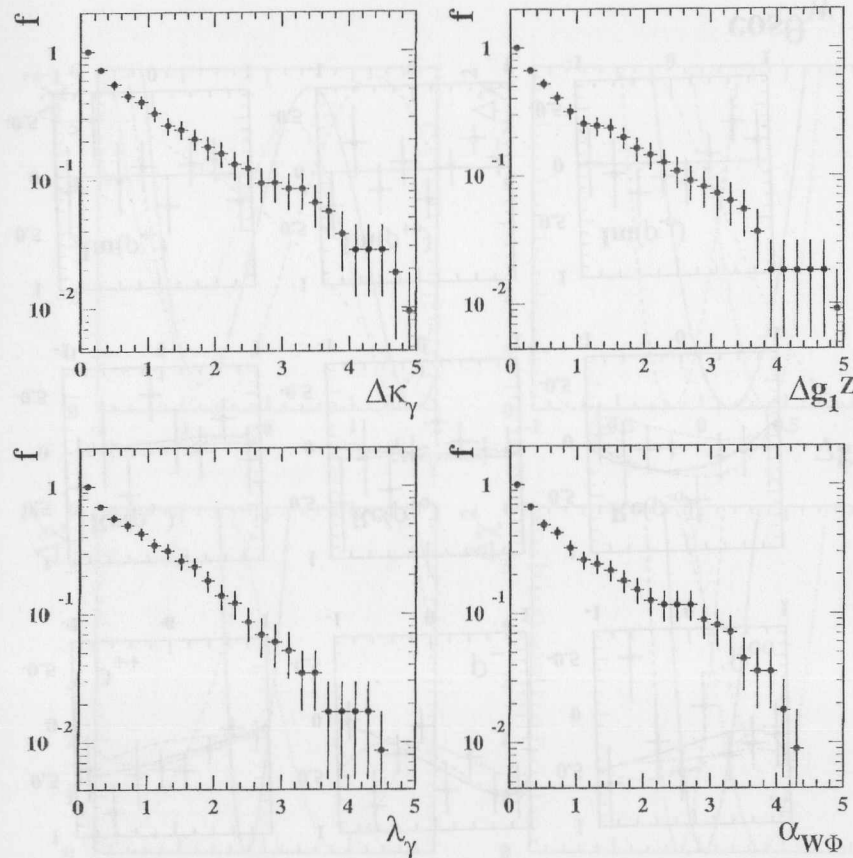


Figure 4.15: The fraction f of the fit results, where the χ^2 -difference between the fitted value and the Monte Carlo input value is below the value of the abscissa. The test is based on 118 subsamples of the EXCALIBUR Monte Carlo with luminosities of 57pb^{-1} . At an anomalous coupling parameter of one, the fraction f is expected to be 0.32, whereas for a value of four a fraction of below 0.05 confirms the correct error estimate of the fit.

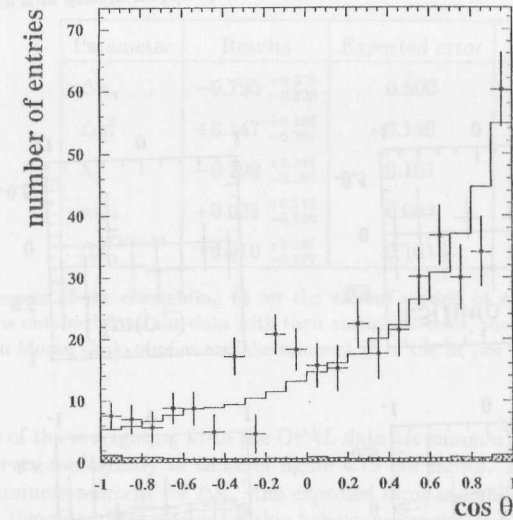


Figure 4.16: The differential cross-section reconstructed from data. Overlaid is the Standard Model expectation and the expected background contribution.

information of the W production and decay angles have been used, as described in section 4.4.1. The χ^2 -curves determined in the fit for the various triple gauge boson coupling parameters are

Parameter	Results
$\Delta\kappa_\gamma$	$-0.776^{+0.352}_{-0.302}$
Δg_1^Z	$+0.170^{+0.193}_{-0.203}$
λ_γ	$-0.211^{+0.165}_{-0.151}$
$\alpha_{W\Phi}$	$+0.027^{+0.111}_{-0.102}$
$\Delta\kappa_\gamma^{(HISZ)}$	$-0.007^{+0.174}_{-0.165}$

Table 4.14: Results and statistical errors of the χ^2 -fits to the corrected distributions.

shown in figure 4.19.

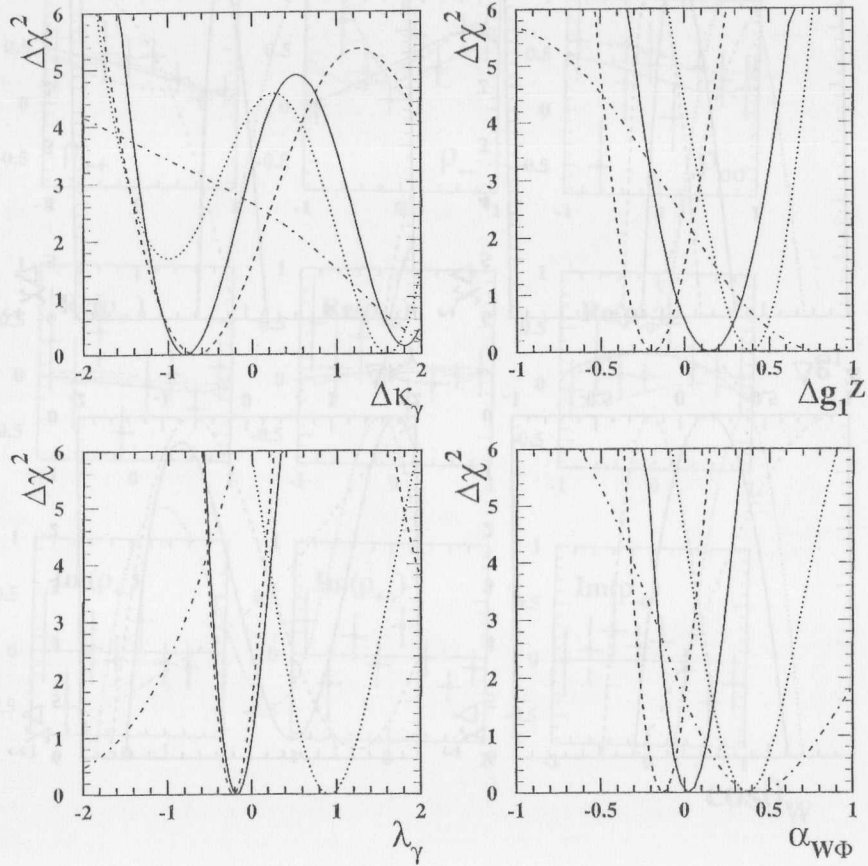


Figure 4.20: The χ^2 -curves for the reweighting fit to the OPAL data. For the explanation of the different curves see figure (4.19).

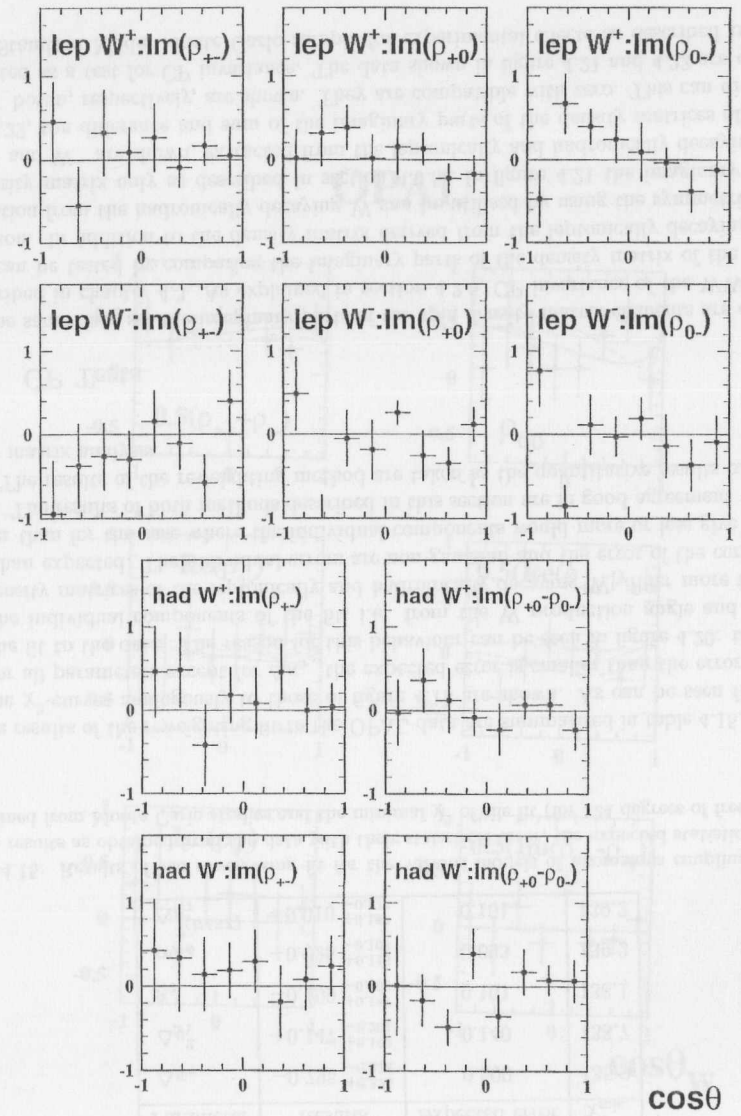


Figure 4.21: The imaginary parts of the density matrices determined from data. The line indicated the Standard Model expectation.

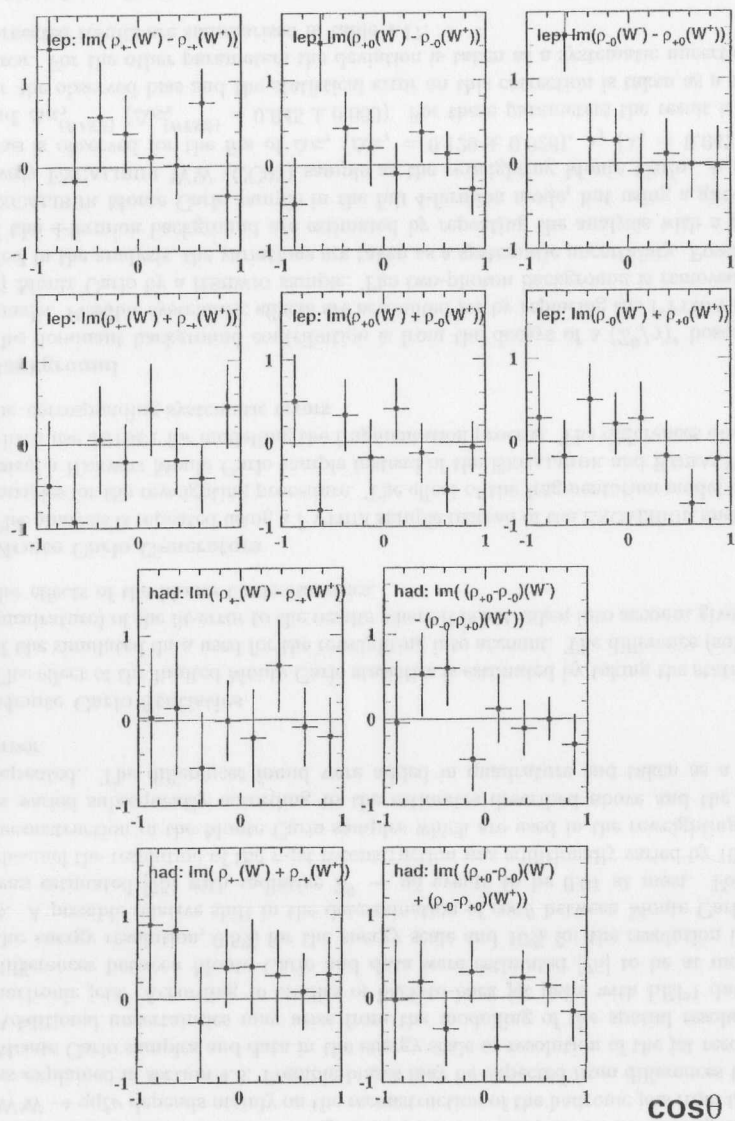


Figure 4.22: The differences and sums of the imaginary parts of the density matrices determined from data. For a CP-conserving triple gauge boson vertex the differences should be compatible with zero. Possible deviations from zero for the sums of imaginary parts indicate the presence of loop effects.

technique as described in section 4.4.2, where the correlations between the density elements are taken from the Monte Carlo. The χ^2 -curves determined in the fit are shown in figure 4.23.

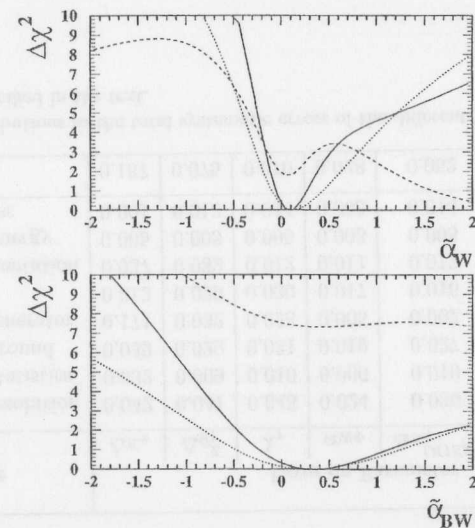


Figure 4.23: The χ^2 -curves for the fit to CP violating TGC parameters, where $\Delta\chi^2 = \chi^2 - \chi^2_{\min}$. The dashed and dotted curves show the results from the information of the leptonically and hadronically decaying W, respectively and the solid curves the combination.

The correlations between the CP-conserving and violating parameters are expected to be small, because for these fit only the imaginary parts of the density matrices are used, whereas the real parts and the differential cross-sections, where the largest sensitivity for the CP-conserving parameters is present, are not included. The results of these fits are

$$\begin{aligned}\tilde{\alpha}_W &= 0.086^{+0.178}_{-0.141} \\ \tilde{\alpha}_{BW} &= 0.327^{+0.773}_{-0.562}.\end{aligned}$$

4.5.4 Systematic Error Studies

In the following, possible sources of systematic uncertainties for the analysis of triple gauge coupling measurements are pointed out and the methods of estimating these systematic errors are discussed. In table 4.16 the results of these studies are summarised and estimates for the

overall uncertainty for the various models of anomalous couplings are given. The systematic errors quoted here are those of the reweighting fit.

- **Jet Reconstruction**

The reconstruction of the five angles used for the analysis of the semileptonic channel $WW \rightarrow qq\ell\nu$ depends mainly on the reconstruction of the hadronic jets from the W decay as explained in section 4.3. Possible biases may be expected from differences between the Monte Carlo samples and data in the energy scale or resolution of the jet reconstruction. Additional uncertainties may arise from the modelling of the spatial resolution of the hadronic jets. According to studies of back-to-back jet pairs with LEP1 data, possible differences between Monte Carlo and data were estimated [75] to be at most 10% for the energy resolution, 0.5% for the energy scale and 10% for the resolution in $\cos\theta$ and ϕ . A possible relative shift in the determination of $\cos\theta$ between Monte Carlo and data was estimated [75] with radiative $Z^0 \rightarrow q\bar{q}$ events to be 0.01 at most. For the $q\bar{q}\tau\nu$ channel the resolution of the τ -jet reconstruction was additionally varied by 10%. The jet reconstruction in the Monte Carlo samples which are used in the reweighting procedure is varied subsequently according to the estimates described above and the analysis is repeated. The differences found were added in quadrature and taken as a systematic error.

- **Monte Carlo Statistics**

The effect of the limited Monte Carlo statistics is estimated by taking the statistical error of the simulated data used for the reweighting into account. The difference (subtracted in quadrature) of the fit-error to the results where it is not taken into account gives explicitly the effects of the Monte Carlo statistics.

- **Monte Carlo Generators**

The analysis is repeated using a PYTHIA sample instead of the EXCALIBUR and KORALW samples for the reweighting procedure. The effect of the fragmentation model is tested by using a HERWIG Monte Carlo sample instead of the EXCALIBUR and KORALW samples, which use JETSET for modelling the fragmentation process. The differences observed give the corresponding systematic errors.

- **Background**

The dominant background contribution is from the decays of a $(Z^0/\gamma)^*$ boson into two quarks. Possible systematic effects are accounted for by replacing the PYTHIA $(Z^0/\gamma)^* \rightarrow q\bar{q}$ Monte Carlo by a HERWIG sample. The two-photon background is removed and doubled in the analysis, the variations are taken as a systematic uncertainty. Possible effects of the 4-fermion background are estimated by repeating the analysis with a grc4f and EXCALIBUR Monte Carlo sample in the full 4-fermion mode, but using a grc4f respectively EXCALIBUR WW (CC03) sample as the reweighting Monte Carlo. A significant bias is observed for the fits of $\Delta\kappa_\gamma$ ($\Delta\kappa_\gamma = 0.129 \pm 0.026$), λ_γ ($\lambda_\gamma = 0.042 \pm 0.009$), and $\Delta\kappa_\gamma^{(HISZ)}$ ($\Delta\kappa_\gamma^{(HISZ)} = 0.045 \pm 0.009$). For these parameters the result is corrected for the observed bias and the statistical error on this correction is taken as a systematic error. For the other parameters the deviation is taken as a systematic uncertainty. The corrected results are summarised in table 4.17.

- **Initial State Radiation**

As already pointed out in section 4.4 the effects of ISR are not fully implemented in

the reweighting technique, and small systematic uncertainties might be possible. These 'second order' effects due to ISR are estimated by using a Monte Carlo sample with anomalous coupling (i.e. that one of the list in table 4.4, which is nearest to the fit result from data in the appropriate model) instead of a Standard Model sample in the reweighting procedure. The observed differences are taken as a systematic error.

- **W mass and LEP beam energy**

The effects of varying the LEP beam energy within its errors ($\Delta E_{\text{beam}} = 30\text{MeV}$) and the uncertainty in the W mass measured at the TEVATRON ($\Delta m_W = 90\text{MeV}$) is estimated with the help of the reweighting procedure. The effects caused by a variation of the LEP beam energy or the W boson mass can be incorporated in the Monte Carlo sample used for the reweighting method by changing the variables in the cross-section of the denominator, which is used for estimating the weighting factors, c.f. equation 4.45.

The results of these systematic studies are summarised for the various triple gauge boson coupling parameters in table 4.16. As can be seen from the results given in table 4.16, one of the largest systematic uncertainties is due to the different Monte Carlo generators. However, the method used to determine the error due to this uncertainty contains a large statistical component.

Source	Error on Parameter						
	$\Delta\kappa_\gamma$	Δg_γ^Z	λ_γ	$\alpha_{W\Phi}$	$\Delta\kappa_\gamma^{(HISZ)}$	$\bar{\alpha}_W$	$\bar{\alpha}_{BW}$
Jet Resolution	0.042	0.041	0.043	0.024	0.036	0.009	0.059
MC Statistics	0.032	0.009	0.010	0.006	0.010	0.012	0.038
Background	0.039	0.029	0.031	0.019	0.027	0.018	0.071
MC generator	0.171	0.032	0.028	0.005	0.002	0.012	0.008
ISR	0.012	0.029	0.030	0.017	0.016	-	-
Fragmentation	0.037	0.032	0.012	0.011	0.012	0.003	0.061
LEP energy	0.005	0.003	0.005	0.003	0.005	0.001	0.001
W mass	0.001	0.013	0.014	0.008	0.014	0.001	0.004
Total	0.187	0.075	0.070	0.028	0.052	0.026	0.117

Table 4.16: Contributions to the total systematic errors of the different TGC parameters due to the various sources specified in the text.

4.5.5 Determination of the Longitudinally Polarised Cross-Section

The spin density matrix elements can be combined with the $\cos\theta$ angular distribution and a measurement of the total W-production cross-section (c.f. section 4.6 or reference [73]) to determine the differential cross-section for the production of transversely polarised W bosons, $e^+e^- \rightarrow W_T W$, and longitudinally polarised W bosons, $e^+e^- \rightarrow W_L W$, where in either case the second W can have any helicity. The W-pair production cross-section is measured [73] to be $\sigma_{WW} = 15.43 \pm 0.61(\text{stat.}) \pm 0.50(\text{sys.}) \text{ pb}$, assuming that the angular distributions of the W-pair production and decay, as well as their branching fractions, behave according to the

Standard Model. The semi-inclusive cross-sections $d\sigma(W_{T,L})/d\cos\theta$ can be derived from the diagonal density matrix elements, which directly give the probability to produce a W boson with a certain helicity, by the multiplication with the differential cross-section measurement normalised to the measurement of the total W-production cross-section. For this purpose the spin density matrix elements and the $\cos\theta$ distribution are corrected for experimental effects as described in section 4.4.1, i.e. the background is subtracted and it is accounted for efficiency and resolution effects. The systematic errors are determined as described for the reweighting technique. For the evaluation of an additional systematic uncertainty, the Standard Model Monte Carlo sample used for the correction of the experimental effects, is replaced with samples generated with $\Delta g_1^Z = \pm 1$. This resulting difference should cover all possible systematic effects from model-dependences of the correction procedure, keeping in mind the fit results and the small differences between the 'naive' correction procedure and the reweighting fit. The resulting

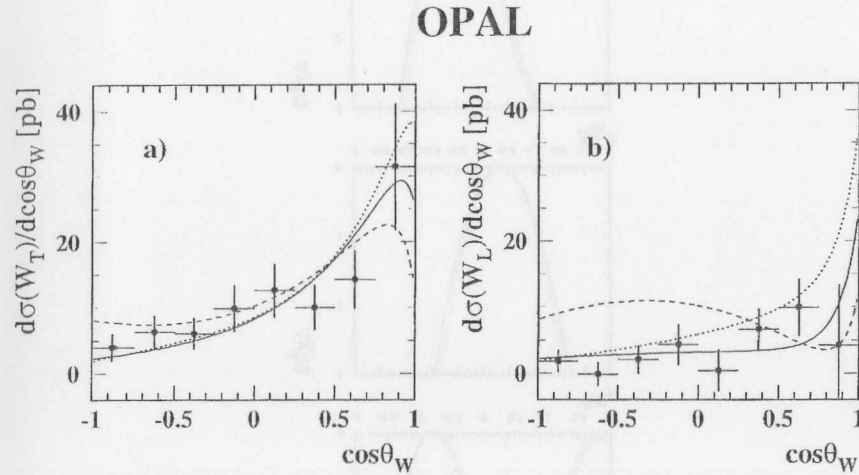


Figure 4.24: Differential cross-section to produce a) a transversely polarised W and b) a longitudinally polarised W in a W-pair event, where the second W can have any polarisation. The points represent the data and the solid (dotted, dashed) lines show the prediction of the Standard Model ($\Delta g_1^Z = +1, -1$). The error bars include statistical and systematic uncertainties, expect for a total normalisation error of 4.6% associated with the total cross-section measurement.

distributions for the transversely and longitudinally polarised cross-section are shown in figure 4.24. Overlaid are the Standard Model expectation as derived from the Born-level formulae of the helicity amplitudes given in table 4.2 in addition with the curves for an anomalous coupling of $\Delta g_1^Z = \pm 1$. As can be seen from figure 4.24, the measurement is in good agreement with the Standard Model. Integrating over these cross-sections, the overall fraction of longitudinally polarised W bosons is determined to be $0.242 \pm 0.091 \pm 0.023$. The systematic error is dominated by uncertainties in the jet resolution (0.017) and the Monte Carlo generator (0.015). The expected value for the Standard Model is 0.272, whereas for an anomalous coupling of the Δg_1^Z parameter of +1 or -1, this fraction is expected to be 0.393 and 0.405, respectively.

4.5.6 Summary

The final results of the spin density matrix analysis of the angular distributions is summarised in table 4.17, where the bias correction due to the 4-fermion effects and the systematic uncertainties are included. The χ^2 -curves for the fit results including the systematic error are

Parameter	Results
$\Delta\kappa_\gamma$	$-0.67 \pm_{-0.33}^{+0.38} \pm 0.19$
Δg_1^Z	$+0.15 \pm 0.20 \pm 0.08$
λ_γ	$-0.16 \pm_{-0.17}^{+0.19} \pm 0.07$
$\alpha_{W\Phi}$	$+0.03 \pm_{-0.11}^{+0.12} \pm 0.03$
$\Delta\kappa_\gamma^{(HSZ)}$	$-0.04 \pm_{-0.18}^{+0.19} \pm 0.05$
$\tilde{\alpha}_W$	$+0.09 \pm_{-0.14}^{+0.18} \pm 0.03$
$\tilde{\alpha}_{BW}$	$+0.33 \pm_{-0.56}^{+0.77} \pm 0.12$

Table 4.17: Results of the reweighting fit including bias correction for 4-fermion effects and systematic errors.

shown in figure 4.25 for the triple gauge boson coupling parameter $\Delta\kappa_\gamma$, Δg_1^Z and λ_γ . The dashed curves show the χ^2 -curves for the statistical errors only. The integrated fraction of the production of longitudinally polarised W bosons is determined to be $0.242 \pm 0.091 \pm 0.023$, where in the Standard Model a value of 0.272 is expected.

4.6 Comparison of Different Methods to Measure TGC

There are three different techniques for the determination of the trilinear gauge coupling, which have been proposed in [4] and are all employed by the OPAL collaboration. In addition to the spin density matrix method, the maximum likelihood technique and the method of optimal observables have been used in [73, 75]. In the following these techniques are briefly introduced and their features are discussed.

4.6.1 The Maximum Likelihood Method

The maximum likelihood method was applied in [75, 76] in order to determine the OPAL results for the TGC angular analysis. Here the distributions of the angular distributions are directly used in a maximum likelihood fit. In order to handle detector and resolution effects, a binned fit has been chosen. The likelihood distribution is obtained in several steps. As a first step the expected cross-section σ_i^{gen} is parametrised in each bin as a function of an anomalous coupling parameter λ , making use of the quadratic dependence upon λ . Here large samples of generator level EXCALIBUR Monte Carlo are used, where the effects of ISR and the finite width of the W boson are included. Subsequently the detector and resolution effects as well as the contribution

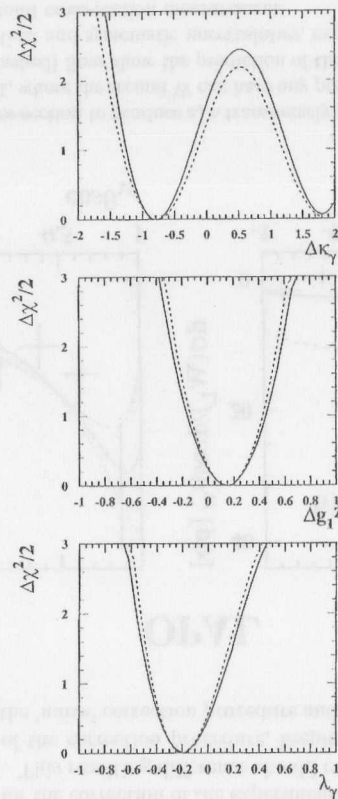


Figure 4.25: The χ^2 -curves for the fit results including the systematic errors (solid curve). The dashed curves show the χ^2 for the statistical errors only.

of other W^+W^- decay channels are included using samples of fully simulated Standard Model Monte Carlo events. Correction factors c_{ki} are calculated, which describe the migration of events of bin i on generator level to be reconstructed due to experimental effects in bin k . Then the expected observed cross-section for each bin k is given by

$$\sigma_k^{\text{WW}}(\lambda) = \sum_i c_{ki} \sigma_i^{\text{gen}}(\lambda). \quad (4.46)$$

After adding the expected cross-section from background events, the probability for observing the number of events seen in the data for each bin is calculated using Poisson statistics. Then the anomalous coupling parameters can be determined by minimising the logarithm of the likelihood function. This method allows for all effects like Γ_W , ISR, detector acceptance and angular resolution.

If both the production angle θ as well as the four decay angles of the W bosons are included, the fit has to be performed in a five-dimensional space. In order not to run into severe Monte Carlo statistics problems for the determination of the migration matrix, an appropriate binning have to be chosen. Because the information contained in the decay angles of the hadronically decaying W boson is very limited, they were omitted from the analysis in [73, 75] in order to allow for smaller binning in the other angles, which are known to be of higher relevance for a TGC analysis. A binning of 20 bins in $\cos\theta$, 10 bins in $\cos\theta^*$ and 5 bins in ϕ^* have been chosen. Here the drawback of this method becomes clear: if the angles of the hadronically decaying W are included and/or a less coarser binning is chosen in order to increase the statistical precision of the analysis, the amount of fully simulated Monte Carlo events needed for this method becomes huge. Thus the technique is statistically less powerful, although it uses directly the ‘canonical’ observables, i.e. the production and decay angles of the W boson, and thus no loss of information from the method itself is expected.

4.6.2 The Method of Optimal Observables

In the method of optimal observables the multi-dimensional space of the five angles is projected into a single observable with maximal sensitivity to a possible deviation of the triple gauge couplings. The optimal observable for any TGC parameter λ is constructed for each event by differentiating the differential cross-section for the event with respect to the coupling λ evaluated at the Standard Model value $\lambda = 0$ and normalising to the Standard Model cross-section according to

$$\mathcal{O}_i = \frac{1}{\sigma_i^{\text{SM}}} \left. \frac{d\sigma_i(\alpha)}{d\alpha} \right|_{\alpha=0}. \quad (4.47)$$

Thus for each of the trilinear gauge coupling parameters an optimal observable is defined. All other couplings are assumed to have the Standard Model values. Subsequently a binned maximum likelihood fit is performed, comparing the optimal observable distributions determined from the data to those derived from fully simulated Monte Carlo samples. In order to produce the full spectrum of distributions with all intermediate anomalous coupling parameters in addition to those listed in tables 4.4 and 4.5, a reweighting technique is applied, similar to that described in section 4.4.2. All experimental effects are incorporated in this method. It has been shown that for a differential cross-section which is linear in the parameter to be determined, the sensitivity of the optimal observable is the same as for a multi-dimensional maximum likelihood fit. However, the W-pair production cross-section is quadratic in the coupling parameters,

thus a loss of sensitivity is expected in principle if the observables are constructed without the quadratic term, i.e. the next term of the expansion of equation 4.47, see reference [4] for details. But it turns out that the loss is marginal, because the quadratic terms are suppressed as long as the deviations of the couplings from zero are small. In [73], the spectrum of optimal observables is divided into 30 bins, thus no loss in sensitivity due to coarse binning is expected. The method of optimal observables is solely used for one-dimensional fits. Because for each TGC parameter a different observable is needed, the method is less convenient for multi-dimensional fits. Here the same sort of problem as for the maximum likelihood analysis arises, because the number of bins would have to be reduced for the two-, three- or even more-dimensional fits, resulting in a loss of sensitivity.

4.6.3 Comparison of the Methods

In order to compare the different methods for analysing the trilinear gauge boson vertex, the main features of the spin density matrix method will be summarised. In this method the five-dimensional space in the production and decay angles is decomposed into the $\cos\theta$ distribution and two hermitian spin density matrices of the single W bosons. The differential cross-section in $\cos\theta$ is independent of the spin density matrices, because the elements are normalised to the $\cos\theta$ distribution, allowing for information of the relative contribution of the helicity states. Each of the hermitian spin density matrices consists of altogether six different elements, of which three are real and three are complex in general. The elements corresponds to one-dimensional projections of the three-dimensional angular space (i.e. the production and decay angles of one W boson). The elements of such a density matrix are correlated. The spin correlations between both W bosons are disregarded in this analysis, resulting in a small loss of sensitivity, c.f. section 4.3.

The spin density elements are the smallest set of projections which can be done in a model independent way. Then the problems with binning and Monte Carlo statistics are avoided without loss of generality. The advantage of the spin density matrix method is the direct connection of the observables to physical quantities, i.e. the polarisation of the W bosons. In this way physical meaningful quantities, like for example the cross-section of the transversely and longitudinally polarised W bosons can directly be derived. Moreover, in principle a model-independent analysis of the trilinear gauge boson vertex is possible. Through the decomposition of the multi-dimensional space into one-dimensional projections it is relatively easy to follow the intermediate steps of the analysis, i.e. the density matrix elements are something to look at. The origin of possible deviations from the Standard Model expectation can be detected by the visualisation of the observables. In this way different anomalous couplings can be distinguished.

With the maximum likelihood technique a model-independent analysis is possible as well, although a judgement 'by eye' is less clear in the multi-dimensional space. In the optimal observable method the assumptions of the coupling parameter to be investigated enter already in the construction of the observables, thus the analysis is model-dependent.

As already pointed out in the description of the individual methods, the best sensitivity can be reached when a minimal amount of information is lost through the method itself and the binning. In this sense the method of optimal observable and the spin density method are advantageous compared to the maximum likelihood fit, although both methods lose in principle sensitivity because of the projections performed – the optimal observable method due to the neglect of the quadratic terms and the spin density matrix method due to the neglect of the

spin correlations between the two W bosons. But these disadvantages are superseded by the statistical gain obtained through the use of projections, which overcomes the binning problems in a high-dimensional space. Though, the loss in the spin density matrix method where single W matrices are used is larger compared to the optimal observable method. In table 4.18 the expected errors for a data sample of 57pb^{-1} for the different methods are summarised [73]. They are estimated from test with small Monte Carlo samples.

Method	$\Delta\kappa_\gamma$	Δg_1^Z	λ_γ
Maximum Likelihood	± 0.56	± 0.16	± 0.19
Optimal Observables	± 0.48	± 0.14	± 0.15
Spin Density Matrix	± 0.50	± 0.14	± 0.16

Table 4.18: The errors for three different TGC parameters as expected from a sample of 57pb^{-1} , corresponding to the luminosity of the data taken at 183 GeV.

4.7 Combination with other OPAL Measurements

4.7.1 The Analysis of the $q\bar{q}q\bar{q}$ and $l\bar{\nu}l\nu$ Channels

In addition to the analysis of the $q\bar{q}l\bar{\nu}$ channel, the $q\bar{q}q\bar{q}$ and $l\bar{\nu}l\nu$ channels have also been investigated using the data taken at an energy of 183 GeV in reference [73].

The signature for the fully hadronic $W^+W^- \rightarrow q\bar{q}q\bar{q}$ events is typically a four-jet topology. The selection is performed in two stages using a cut based preselection followed by a likelihood selection. Topological variables as, for example, the sphericity of the event or the DURHAM jet resolution parameter as well as the visible energy or the energy of the most energetic electromagnetic cluster are used to distinguish $W^+W^- \rightarrow q\bar{q}q\bar{q}$ events from the main background source arising from hadronic $(Z^0/\gamma)^* \rightarrow q\bar{q}$ events. The event reconstruction of the fully hadronic channel for a TGC analysis using the angular distributions is complicated by the ambiguity in the choice of the correct di-jet combination and by uncertainties in the determination of the W charge. Therefore, in that analysis only the angular distribution of the W production angle $\cos\theta$ is used. The di-jet combination is chosen by a likelihood algorithm with input variables like the di-jet invariant mass, the rescaled beam energy, the jet-charges of the two W candidates and the results of kinematic fits to the momenta and energies of the jets. The probability to choose the correct jet-pairing is about 78% for a centre-of-mass energy of 183 GeV. In order to determine the charge of the W bosons a jet-charge algorithm is applied, where the charged tracks of the two jets paired to belong to one W boson are used. The probability of a correct assignment of the W charges, once the correct jet pairing has been chosen, is about 76%. The triple gauge coupling parameters are determined in a binned maximum likelihood fit, taking into account all experimental effects like acceptance, resolution, incorrect jet pairing and incorrect determination of the W charge. The incorrect jet pairing, the wrong determination of the W charge as well as the restriction to the W production angular information decrease the sensitivity to possible anomalous couplings compared to the analysis of the $W^+W^- \rightarrow q\bar{q}l\bar{\nu}$ channel. Thus the expected error of the TGC analysis of the fully hadronic

channel is by a factor two to three larger than for the semileptonic channel. The results of the $W^+W^- \rightarrow q\bar{q}l\bar{\nu}_l$ angular analysis and the expected errors are summarised in table 4.19. For comparison the results and the expected errors of the spin density matrix method of the

Results	$\Delta\kappa_\gamma$	Δg_1^Z	λ_γ
$W^+W^- \rightarrow q\bar{q}l\bar{\nu}_l$ without systematics	$-0.67^{+0.38}_{-0.33}$	$+0.15 \pm 0.20$	$-0.16^{+0.19}_{-0.17}$
$W^+W^- \rightarrow q\bar{q}l\bar{\nu}_l$ expected errors	± 0.50	± 0.14	± 0.16
$W^+W^- \rightarrow q\bar{q}l\bar{\nu}_l$ with systematics	$-0.67^{+0.45}_{-0.36}$	$+0.14^{+0.22}_{-0.21}$	$-0.17^{+0.19}_{-0.18}$
$W^+W^- \rightarrow q\bar{q}q\bar{q}$ without systematics	$+1.15^{+1.28}_{-1.25}$	$+0.68^{+0.91}_{-0.64}$	$+0.76^{+0.78}_{-0.67}$
$W^+W^- \rightarrow q\bar{q}q\bar{q}$ expected errors	± 1.13	± 0.43	± 0.52
$W^+W^- \rightarrow q\bar{q}q\bar{q}$ with systematics	$+1.16^{+1.39}_{-1.34}$	$+0.73^{+0.88}_{-0.72}$	$+0.79^{+0.79}_{-0.78}$
$W^+W^- \rightarrow l\bar{\nu}_l l\nu_l$ without systematics	$-1.00^{+0.94}_{-0.92}$	$-0.79^{+0.56}_{-0.69}$	$-0.29^{+0.34}_{-0.38}$
$W^+W^- \rightarrow l\bar{\nu}_l l\nu_l$ expected errors	± 1.08	± 0.71	± 0.41
$W^+W^- \rightarrow l\bar{\nu}_l l\nu_l$ with systematics	$-0.74^{+1.23}_{-1.16}$	$-0.76^{+0.70}_{-0.79}$	$-0.23^{+0.35}_{-0.39}$

Table 4.19: Summary of the results of the event shape analysis of the three different channels. The results with statistical errors only, the expected statistical errors as determined from the Monte Carlo and the results including the systematic errors are given.

$W^+W^- \rightarrow q\bar{q}l\bar{\nu}_l$ channel are repeated. Details of the $W^+W^- \rightarrow q\bar{q}q\bar{q}$ analysis can be found in [73].

Fully leptonic events $W^+W^- \rightarrow l^+\nu_l l^-\bar{\nu}_l$ are identified as two acoplanar charged leptons with missing transverse momentum. The purity of the selection is found to be above 99%, thus the background is negligible and is not considered further. While in a $W^+W^- \rightarrow l^+\nu_l l^-\bar{\nu}_l$ event there are at least two undetected neutrinos, the W production and decay angles can still be reconstructed in the small-width and no-ISR approximation for $l = \mu$ or e . There remains an two-fold ambiguity in the reconstruction of the production angle of the W boson as well as for the polar angles of the W decays. It corresponds to a reflection ambiguity for the two neutrinos in the plane defined by the two charged lepton momentum vectors. For events involving one or two τ -leptons and thus (an) additional undetected neutrino(s) this method of reconstructing the angles cannot be applied. Therefore additional cuts are applied for the event shape analysis in order to suppress the contribution of $W \rightarrow \tau\nu$ events. The number of electromagnetic clusters of the lepton candidate and simple requirements of electron and muon identification, for example, are used to distinguish electron and muon candidates from tau events. After applying these additional cuts, the contamination of the $W^+W^- \rightarrow l^+\nu_l l^-\bar{\nu}_l$ selection with $W \rightarrow \tau\nu$ events is below 10%. The method of reconstructing the production and decay angles of the W bosons is complicated by experimental effects, the finite width of the W and ISR. Therefore it may happen that some events do not have a physical solution for the angular reconstruction since a complex momentum of the neutrino results. These events can be recovered by taking the nearest real solution, setting the complex part of the neutrino momentum to zero. The trilinear gauge coupling parameters are extracted in an unbinned maximum likelihood fit. For the events with two solutions for the W production and the polar

decay angles the average of the differential cross sections at the two solutions is used. As discussed in section 4.4.1 it is not possible in an unbinned analysis to fully take into account the experimental effects. Therefore in this analysis a bias is expected. This bias is estimated using large samples of Monte Carlo events and a correction is applied to the results determined in the data. The method is cross-checked by tests with subsamples of similar statistics to the data. The results of the analysis and the expected errors of the $W^+W^- \rightarrow l^+\nu_l l^-\bar{\nu}_l$ analysis of the angular distribution are summarised in table 4.19.

It is interesting that the errors of the fully leptonic channel are comparable to those of the hadronic channel, although the branching fraction of the fully leptonically decaying W-pairs is about four times smaller than for the other two channels. The loss in statistics is compensated by the good reconstruction of the angles despite of the undetected neutrinos and the statistical gain by using the angular information without the loss due to binning. Details and the investigation of systematic uncertainties may be found in [73].

4.7.2 The Analysis of the Total Cross-section

In addition to the investigation of the angular distributions, the total cross-section of the W-pair production is sensitive to a measurement of the trilinear gauge boson vertex. In order to extract the TGC parameters, the number of observed events is compared to the expected cross-section, which is parametrised as a second polynomial in the trilinear gauge coupling parameters. The coefficients of the polynomial are estimated from the expected number of events at various anomalous couplings, which are calculated with the program GENTLE [77]. Here the Standard Model values for the W branching fractions are used. The background, which originates predominantly from $(Z^0/\gamma)^* \rightarrow q\bar{q}$ events, is assumed to be independent of anomalous trilinear gauge couplings. For the total cross-section analysis the same selections are used as described above for the $q\bar{q}q\bar{q}$ and $l\bar{\nu}_l l^-\nu_l$ channel and in section 4.3.3 for the $q\bar{q}l\bar{\nu}_l$ channel, but without the additional requirements imposed to obtain good angular resolutions. The selection efficiency is found to slightly depend on the TGC parameters. This dependence is estimated using various samples of EXCALIBUR Monte Carlo generated with anomalous couplings. Subsequently the number of observed events are compared to the prediction in a likelihood fit. The theoretical uncertainty in the expected number of events are estimated by comparing the prediction from the GENTLE and the EXCALIBUR programs. Moreover the systematic uncertainties arising from the LEP centre-of-mass energy and luminosity, the measured W-mass, the selection efficiencies and backgrounds are taken into account. The individual systematic errors are of the order of 0.1 to 2%.

4.7.3 Combined Results

In the following section the information obtained from the spin density matrix analysis will be combined with the analyses of the other two channels and the total cross-section analysis.

In figure 4.26 the likelihood curves for the angular analysis with the spin density matrix method and for the results of the total cross-section measurement for the $W^+W^- \rightarrow q\bar{q}l\bar{\nu}_l$ channel are shown for fits to the gauge coupling parameters $\Delta\kappa_\gamma$, Δg_1^Z and λ_γ . For this comparison the χ^2 -curves as determined in the density matrix analysis are transformed into log likelihood-curves. In addition the combined results for the semileptonic channel are given, which are

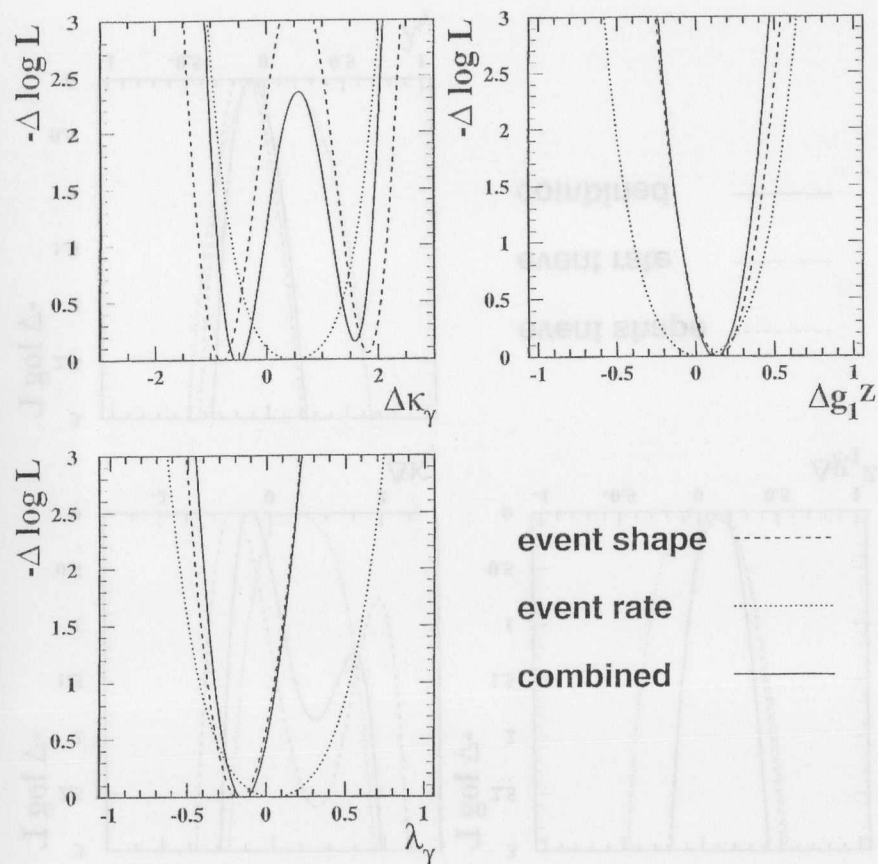


Figure 4.26: The log likelihood curves of the event rate and spin density matrix method of the $qq\bar{l}\nu$ channel together with that of the combined results for the $qq\bar{l}\nu$ channel, given for the three parameters $\Delta\kappa_\gamma$, Δg_1^Z and λ_γ .

determined by summing the log likelihood curves of the event shape and event rate analyses. The values of the observed minima in the logarithm of the likelihood curves with the one sigma errors and the values for the 95% confidence level limits as determined from the combination are given in table 4.20. The TGC results of the three channels are combined by summing the

	$\Delta\kappa_\gamma$	Δg_1^Z	λ_γ
Combined result	$-0.47 \pm_{0.31}^{0.74}$	$+0.12 \pm_{0.20}^{0.21}$	$-0.12 \pm_{0.19}^{0.18}$
95% c.l. limits	[-0.95, 1.96]	[-0.23, 0.46]	[-0.46, 0.17]

Table 4.20: Combined results from the event rate and spin density matrix analysis for the $qq\bar{l}\nu$ channel for the three TGC parameters $\Delta\kappa_\gamma$, Δg_1^Z and λ_γ .

individual log likelihood curves. The correlation between the systematic errors of the three channels is neglected, since most of the important sources of systematic errors, especially for the angular analysis, are relevant to a particular channel and are not common to all three of them. The likelihood curves of the combination of the three channels for the three coupling parameters are shown in figure 4.27. The relative contribution to the final result of the shape analysis and the event rate information can be read of figure 4.27. The combined results, i.e. the one standard deviation errors and the 95% c.l. limits from all three channels are given in table 4.21. In figure 4.28 the relative contributions of the three channels to the combined result is visualised.

	$\Delta\kappa_\gamma$	Δg_1^Z	λ_γ
Combined result	$-0.32 \pm_{0.30}^{0.38}$	$+0.11 \pm_{0.14}^{0.13}$	$-0.07 \pm_{0.14}^{0.12}$
95% c.l. limits	[-0.82, 1.68]	[-0.15, 0.38]	[-0.32, 0.18]

Table 4.21: Combined results of all three channels for the three TGC parameters.

4.8 Present Constraints on TGC Parameters

In this section the worlds data on triple gauge coupling parameters are summarised and combined and the results of the present work is put into perspective.

Another experimental possibility to investigate the trilinear gauge coupling at LEP is single W production. The production mechanism via the *non-abelian fusion* diagram (c.f. figure 1.3) involves the $WW\gamma$ vertex. Thus through the investigation of the single W production the $WW\gamma$ couplings can be measured directly, in contrast to the W-pair production, where both, the WWZ and the $WW\gamma$ vertex is involved. Using the dependence of the single W production cross-section on the $WW\gamma$ couplings (and the restriction to CP-conserving couplings obeying gauge invariance as discussed in section 4.2.2), limits of the triple gauge coupling parameters $\Delta\kappa_\gamma$ and λ_γ can be derived. Although the cross-section for the single W production is suppressed by a factor of around 25 compared to the W-pair production, the sensitivity, especially to the

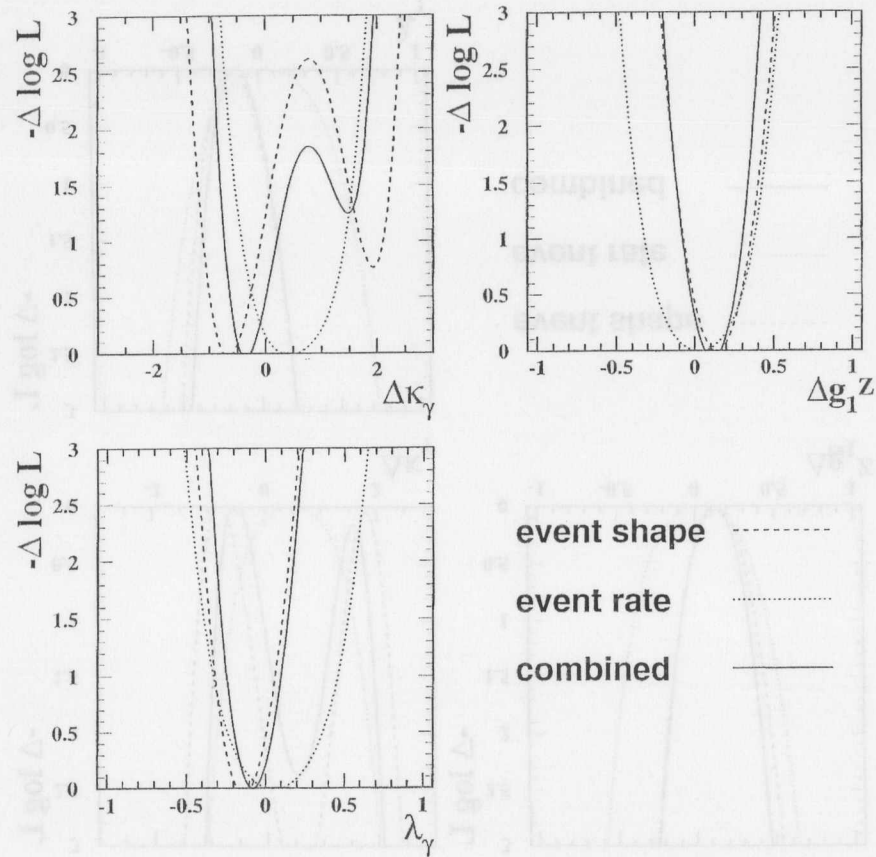


Figure 4.27: The likelihood curves of the event shape and event rate analyses, both combined for all channels and the overall combined results for the parameters $\Delta\kappa_\gamma$, Δg_1^Z and λ_γ .

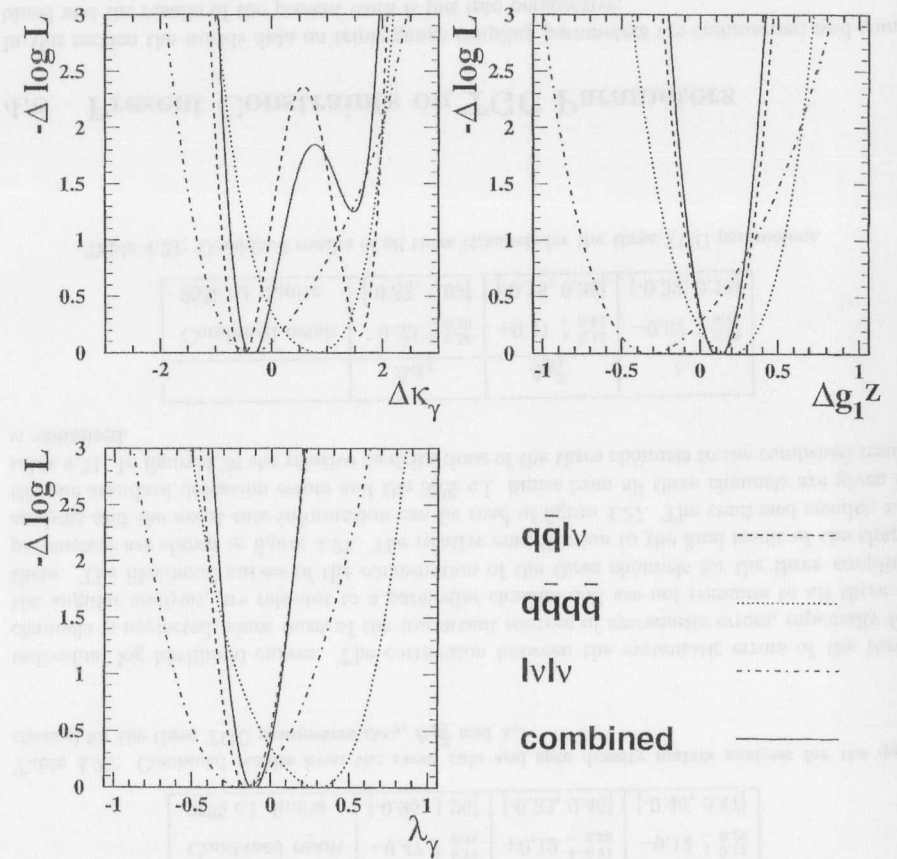


Figure 4.28: The likelihood curves of the three channels individually and the combined results for the three trilinear gauge coupling parameters.

$\Delta\kappa_\gamma$ parameter, is relatively high. This is because the contributions from other production mechanisms, where no trilinear gauge coupling is involved but the same final state is produced, is smaller than for the W-pair production. Especially, diagrams where non-resonant (W-boson) final states are produced populate a different phase-space region than the signal and can be thus suppressed by kinematic cuts. The parameters κ_γ and λ_γ can typically be restricted to be $|\kappa_\gamma| < 1$ to $|\kappa_\gamma| < 1.5$ and $|\lambda_\gamma| < 1.5$ at the 95% confidence level for such an analysis. Such an analysis is performed by ALEPH, DELPHI and L3. OPAL has not yet a single W analysis performed with the data taken at 183 GeV.

There exists a process at LEP2, namely $e^+e^- \rightarrow \bar{\nu}\nu\gamma$, where exclusively the $WW\gamma$ vertex is involved and thus the anomalous coupling parameters of the $WW\gamma$ coupling can be distinguished unambiguously from the WWZ contribution. In this process the incoming electron and positron radiate virtual W bosons at a $W\ell\nu$ -vertex, and the W bosons subsequently fuse into a photon. The sensitivity of such an analysis to the anomalous couplings is for the parameters $\Delta\kappa_\gamma$ about the same as for the $q\bar{q}q\bar{q}$ channel in the W-pair production and for λ_γ about a factor of two less sensitive than the $q\bar{q}q\bar{q}$ channel. The data taken at 183 GeV are analysed for this process from ALEPH and DELPHI.

The trilinear gauge coupling parameters have been measured by all four LEP experiments. Here the results from the analyses at centre-of-mass energies of 161, 172 and 183 GeV are summarised. All channels, which are sensitive to anomalous triple gauge couplings are combined, i.e. the W-pair and single W analyses as well as the analysis of the single photon final state. The results for the one-parameter fits to the coupling parameters $\Delta\kappa_\gamma$, Δg_1^Z and λ_γ from the different experiments are summarised in figure 4.29 and listed in table 4.22. In the figure the likelihood curves of the individual experiments are shown together with the combination, as done by the LEP electroweak working group. In figure 4.30 the LEP combined results for the two-dimensional fits to combinations of the three coupling parameters $\Delta\kappa_\gamma$, Δg_1^Z and λ_γ are given. Since the single W production analysis is especially sensitive to the $\Delta\kappa_\gamma$ parameter, the limit derived by OPAL for this coupling parameter is less stringent than for the other parameters. For the results of the other coupling parameters most of the experiments perform similarly with OPAL having slightly better overall errors than the others. OPAL is the only experiment, which has analysed the data with different methods and the measurement of the spin density matrices and the subsequent derivation of the cross-section for longitudinally and transversely polarised W bosons as described in this thesis are therefore unique. None of the experiments has performed an analysis with the data taken at 183 GeV on the CP violating couplings as the one described in section 4.5.3. For the results of this section to be published the production of Monte Carlo with CP violation is needed in order to cross-check the analysis.

At the TEVATRON $p\bar{p}$ -collider, running at a centre-of-mass energy of $\sqrt{s} = 1.8$ TeV, trilinear gauge couplings are also investigated. The analysis of the D0 experiment⁶ is based on approximately 100pb^{-1} of data. In this analysis the production of WW , $W\gamma$ and WZ pairs are investigated. For the WW and $W\gamma$ production the W decays are considered in the channels $W \rightarrow (e/\mu)\nu$. In addition, decays of the WW and WZ pairs into the $q\bar{q}e\nu$ final state are included. To take into account the unitarity constraint, the anomalous coupling parameters are modified by form factors with a scale Λ according to $\lambda(\hat{s}) = \lambda/(1 - \hat{s}/\Lambda^2)^2$, where \hat{s} is the square of the invariant mass of the gauge boson pair. The D0 experiment has analysed

⁶The D0 experiment is leading in this field. The results of CDF are not competitive and are therefore not quoted here.

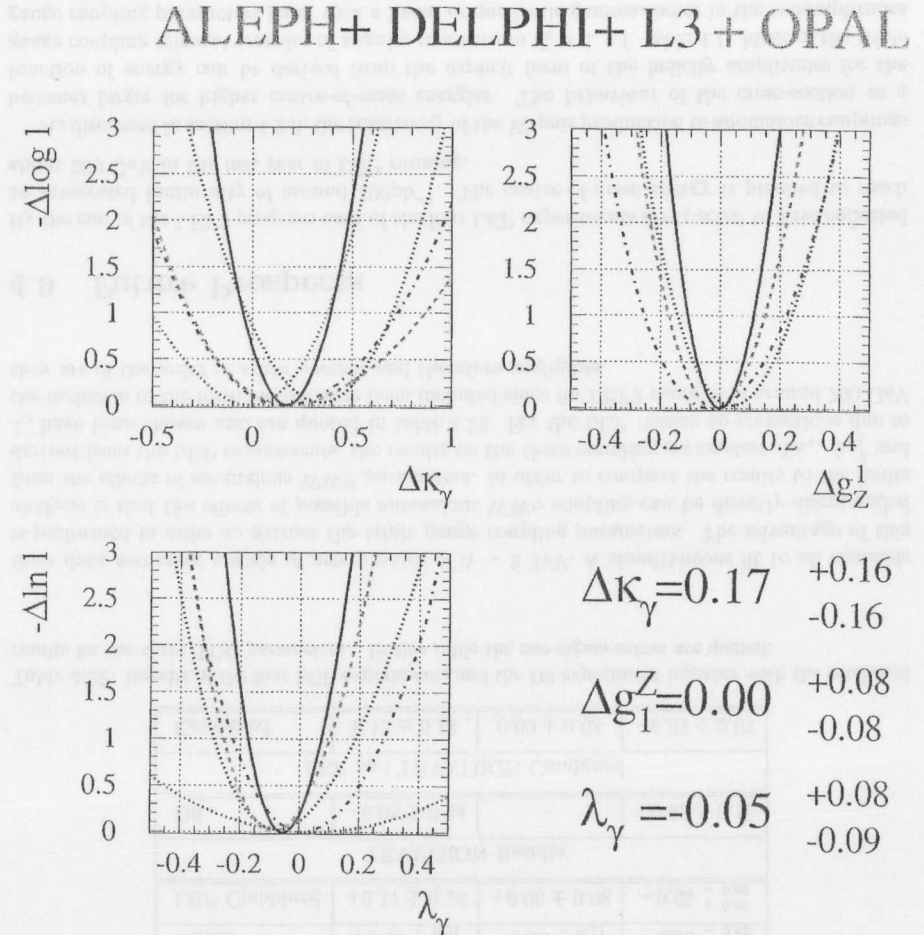


Figure 4.29: The likelihood curves of the combined results of the four LEP experiments for the analysis of the triple gauge coupling parameters $\Delta\kappa_\gamma$, Δg_1^Z and λ_γ . In addition the likelihood curves for the results of each of the four experiments are shown. The combination has been done by the LEP electroweak working group.

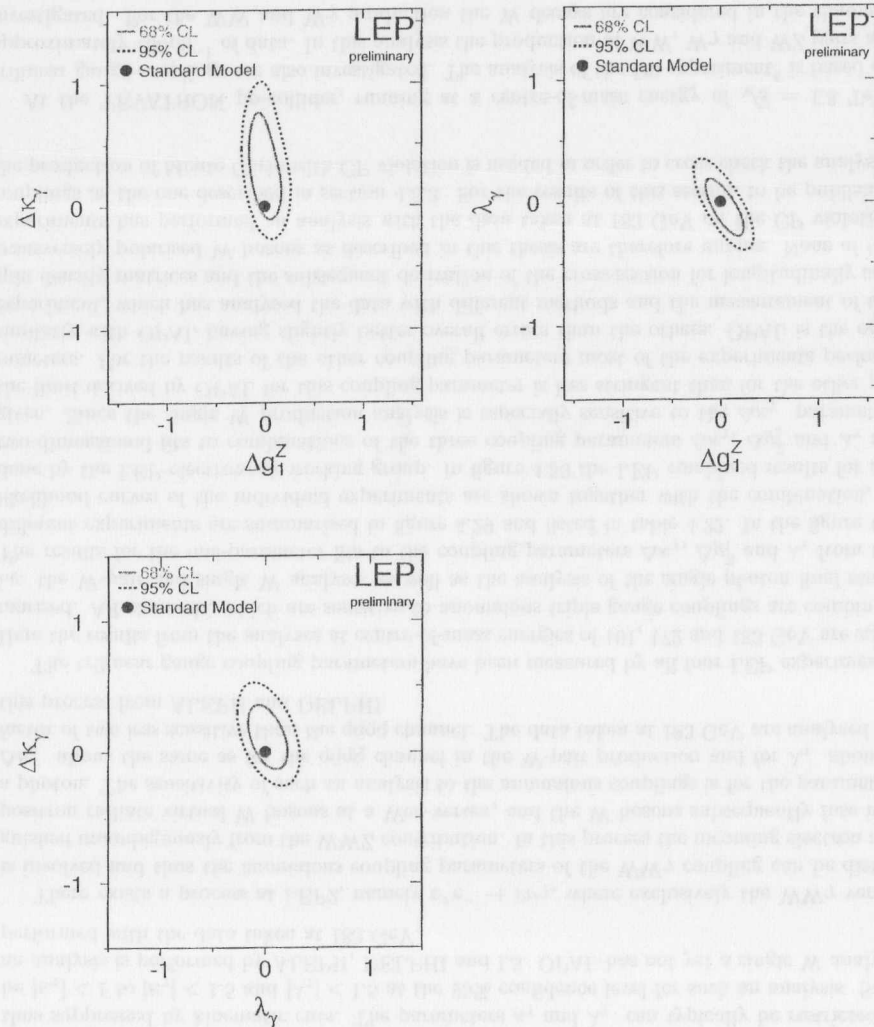


Figure 4.30: The LEP combined results for two-dimensional fits to the three coupling parameters. Shown are the 68% and 95% confidence contours.

	$\Delta\kappa_\gamma$	Δg_1^Z	λ_γ
LEP Results			
ALEPH	$-0.02^{+0.28}_{-0.39}$	–	$+0.05^{+0.50}_{-0.51}$
DELPHI	$+0.34^{+0.26}_{-0.28}$	$+0.04 \pm 0.14$	$-0.07^{+0.19}_{-0.16}$
L3	$+0.16^{+0.40}_{-0.35}$	$-0.03^{+0.18}_{-0.16}$	$+0.01^{+0.19}_{-0.17}$
OPAL	$+0.19^{+0.47}_{-0.37}$	$-0.02^{+0.12}_{-0.11}$	$-0.08^{+0.13}_{-0.12}$
LEP Combined	$+0.17 \pm 0.16$	$+0.00 \pm 0.08$	$-0.05^{+0.08}_{-0.09}$
TEVATRON Results			
D0	-0.08 ± 0.34	–	$+0.00 \pm 0.10$
LEP and TEVATRON Combined			
Combined	0.13 ± 0.14	0.00 ± 0.08	-0.03 ± 0.07

Table 4.22: Results of the four LEP experiments and the D0 experiment together with the combined results for the three TGC parameters. In this table the one sigma errors are quoted.

their data assuming a scale of new physics of $\Lambda = 2$ TeV. A simultaneous fit to all channels is performed in order to extract the triple gauge coupling parameters. The advantage of this analysis is that the effects of possible anomalous $WW\gamma$ coupling can be directly disentangled from the effects of anomalous WWZ parameters. In order to compare the results to the limits derived from the LEP experiments, the results on the three coupling parameters $\Delta\kappa_\gamma$, Δg_1^Z and λ_γ have been chosen and are quoted in table 4.22. For the LEP results no corrections due to the inclusion of the form factors have been included since for LEP2 energies of around 200 GeV they are of the order of a few percent and therefore negligible.

4.9 Future Prospects

By the end of the LEP2 program each of the four LEP experiments is expected to have collected an integrated luminosity of around 500pb^{-1} . The centre-of-mass energy is planned to reach about 200 GeV in the last year of LEP running.

As discussed in section 4.2.3, the sensitivity of the W -pair production to anomalous couplings becomes larger for higher centre-of-mass energies. The behaviour of the cross-section as a function of energy can be derived from the explicit form of the helicity amplitudes for the gauge coupling relevant transfer of angular momentum $J_0 = 1$, c.f. table 4.1. Most of the triple gauge coupling parameters enter with a linear or quadratic gamma-factor in the subamplitudes ($\gamma = \sqrt{s}/(2m_W)$), except for the subamplitudes C (c.f. equation 4.17), which originate from the ν -exchange diagrams and thus do not contribute in the TGC vertex. Therefore the high energy behaviour of the cross-sections or the spin density matrices is either proportional to γ^2 or γ^4 . In this way the gain in sensitivity for higher centre-of-mass energies can be estimated. The raise in energy from 183 to 200 GeV results in an enhanced sensitivity of 20-40%. Here

it becomes clear why the longitudinally polarised W-bosons are more important for a TGC analysis than the transversely polarised ones: it is this γ -factor which enhances, via its extra power of energy, possible deviations of the gauge coupling parameters from the Standard Model expectation. For dimension-four interactions, for example, the high-energy behaviour for the tree level amplitudes is given by γ^n , where n denotes the number of longitudinally polarised W bosons in the final state. For dimension-six interaction, there are two extra factors of γ . All in all, until the end of the LEP2 program the errors of the triple gauge coupling analysis could be significantly reduced: LEP2 is expected to deliver around ten times more statistics than was collected in the year 1997 and together with the enhanced sensitivity because of the higher energy a reduction by a factor of about four to five can be expected.

The experiments at TEVATRON should be able to improve their limits on anomalous couplings significantly with the data of run II, which is planned to start 1999 and is expected to reach an integrated luminosity of 2fb^{-1} , i.e. 20 times the luminosity employed in their present results. A future high energy e^+e^- linear collider would be the ideal instrument to investigate the trilinear gauge couplings. With its clean environment, an energy of around 500 GeV or more and a very high integrated luminosity of 300fb^{-1} per year aimed for such a collider, the couplings could be measured with very high precision.

In figure 4.31 the helicity amplitudes and the differential cross-section as a function of the W production angle $\cos\theta$ are shown for a centre-of-mass energy of 183 and 500 GeV, respectively. It can be seen that the forward peaking structure is clearly enhanced for the higher energy. This is due to the stronger dominance of the t -channel ν -exchange, because the cancellations discussed in section 4.2.3 are nearly in full operation. For energies around the W-pair production threshold the helicity amplitude $(+-)$ drops for very forward peaking W bosons for kinematic reasons. This is no longer the case for higher energies. This behaviour is illustrated in figure 4.32, where the longitudinally and transversely polarised cross-section $e^+e^- \rightarrow W_{L,T}W$ is shown as a function of the W production angle. The relative contribution of the longitudinally polarised W bosons is 3% at 500 GeV, whereas at 183 GeV it is 27% in the Standard Model. The second W can have any helicity in either case. However, it is this contribution of longitudinally polarised W bosons which exhibits a much higher sensitivity at higher energies. From the analysis of the W-pair production alone, i.e. taking into account the CC03 diagrams only, an enhancement in the sensitivity to anomalous couplings of a factor of ten or even more can be expected for a 500 GeV e^+e^- collider compared to LEP2.

In [78] a study of the trilinear gauge coupling parameters at a e^+e^- linear collider taking into account the complete set of 4-fermion processes has been performed. The total cross-section and, with the optimal observable method, the angular distributions are considered in the final states $q\bar{q}e^+\bar{\nu}_e$ and $q\bar{q}\mu^+\bar{\nu}_\mu$. At future linear collider energies especially for the $q\bar{q}e^+\bar{\nu}_e$ channel the contribution of the single resonant W production is important, because this process is sensitive to possible anomalous couplings and is dominant in certain phase space regions. A fit of the five coupling parameters $\alpha_{W\Phi}$, $\alpha_{B\Phi}$, α_W , $\tilde{\alpha}_{BW}$ and $\tilde{\alpha}_W$ has been performed, taking into account the correlation between the parameters. Assuming an centre-of-mass energy of $\sqrt{s} = 500$ GeV, a luminosity of 20fb^{-1} and unpolarised e^+e^- -beams the following sensitivity can be expected:

$$\alpha_{W\Phi} : \pm 0.00098, \quad \alpha_{B\Phi} (= \Delta\kappa_\gamma) : \pm 0.0028, \quad \alpha_W (= \lambda_\gamma) : \pm 0.00081$$

and for the CP-violating couplings

$$\tilde{\alpha}_{BW} : \pm 0.0084, \quad \tilde{\alpha}_W : \pm 0.00079,$$

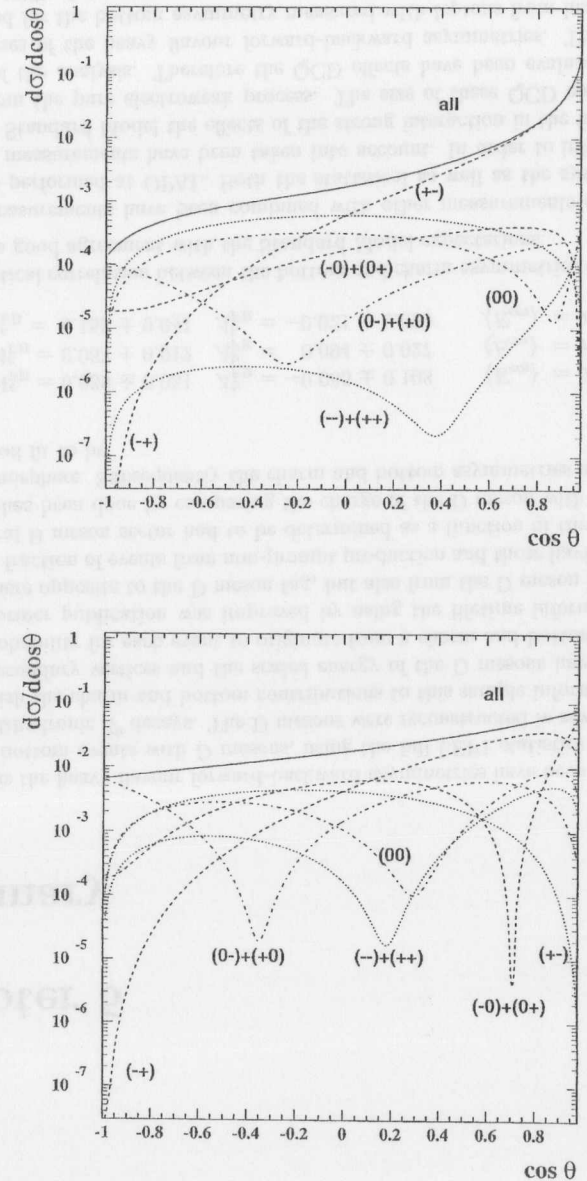


Figure 4.31: The helicity amplitudes as a function of the W production angle for a centre-of-mass energy of 500 GeV (upper figure) and 183 GeV (lower figure).

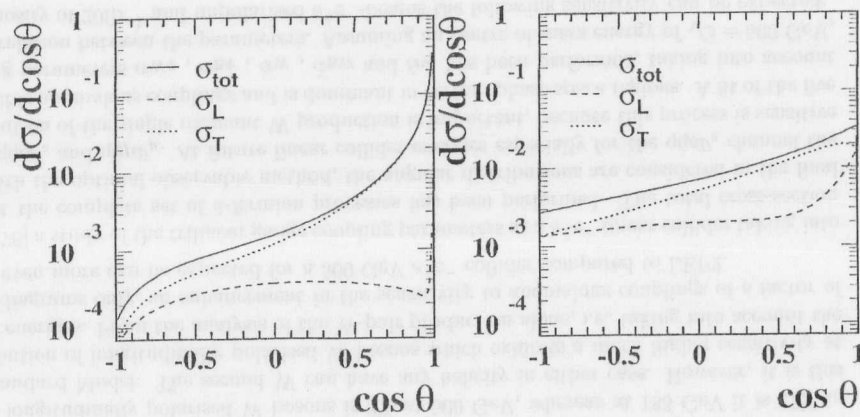


Figure 4.32: The contribution of the longitudinally and transversely polarised cross-section $e^+e^- \rightarrow W_{L,T}W$, where the second W can have any helicity for a centre-of-mass energy of 500 GeV (left hand side) and 183 GeV (right hand side).

where the one standard deviation errors are given. This study is restricted to generator level Monte Carlo, neither detector effects nor the problem of incorporating initial state radiation into the analysis is taken into account.

The results of this estimate are very encouraging. With a sensitivity as determined in [78] and in view of the high luminosity versions of the future linear collider, where about a factor of 25 more data are aimed for than assumed in [78], the sensitivity of the couplings parameters reaches the interesting region, where effects in various models of new physics are expected. In the minimal version of the supersymmetric Standard Model (MSSM), for example, the anomalous coupling parameters $\Delta\kappa_\gamma$ and $\Delta\kappa_Z$ for a centre-of-mass energy of 500 GeV are expected to be in the order of 10^{-3} [79]. In general the expectation in the Standard Model and in MSSM models are not too different, so that a very high precision is needed to distinguish both scenarios. The predicted anomalous couplings in models involving new physics via heavy neutrinos [80] or Two-Higgs-Doublet models [81] is similar to the MSSM case. For the CP-violating coupling parameters the situation is different. Here in the Standard Model only two-loop contributions are expected. In the supersymmetric scenarios, however, CP-violating is predicted from one-loop contributions involving charginos and neutralinos, and are thus in the order of 10^{-3} to 10^{-4} for couplings of the γ and 10^{-4} to 10^{-6} for the Z boson [64, 82]. Thus any detectable CP-violating contribution to the triple gauge coupling vertex can be interpreted as new physics.

Chapter 5

Summary

In this thesis the heavy flavour forward-backward asymmetries have been measured by tagging charm and bottom events with D mesons, using the full LEP1 statistics of approximately 4.5 million multihadronic Z^0 decays. The D mesons were reconstructed in seven different channels. To distinguish the charm and bottom contributions to this sample information from jet-shape variables, secondary vertices and the scaled energy of the D mesons have been utilised to estimate a probability for each event to originate from a charm and bottom event. The method used in a former publication was improved by using the lifetime information not only from the hemisphere opposite to the D meson tag, but also from the D meson hemisphere. For that purpose the fraction of events from non-prompt production and those having undergone mixing in the neutral B meson sector had to be determined as a function of the decay length probability. This has been done by comparing the charge of the D meson with the jet-charge in the opposite hemisphere. Subsequently the charm and bottom asymmetries have been determined in a likelihood fit to be

$$\begin{aligned} A_{FB}^c &= 0.039 \pm 0.051 & A_{FB}^b &= -0.086 \pm 0.108 & \langle E_{cm} \rangle &= 89.45 \text{ GeV} \\ A_{FB}^c &= 0.063 \pm 0.012 & A_{FB}^b &= 0.094 \pm 0.027 & \langle E_{cm} \rangle &= 91.22 \text{ GeV} \\ A_{FB}^c &= 0.158 \pm 0.041 & A_{FB}^b &= -0.021 \pm 0.090 & \langle E_{cm} \rangle &= 93.00 \text{ GeV}, \end{aligned}$$

with a statistical correlation between the bottom and charm asymmetries of around -28%. The results are in good agreement with the Standard Model expectations.

These measurements have been combined with other measurements of the heavy flavour asymmetries performed at OPAL. Both the statistical as well as the systematic correlations between the measurements have been taken into account. In order to interpret the results in terms of the Standard Model the effects of the strong interaction in the final state have to be separated from the pure electroweak process. The size of these QCD corrections depend on the details of the analysis. Therefore the QCD effects have been evaluated for the different OPAL analyses of the heavy flavour forward-backward asymmetries. The largest correction was estimated for the bottom asymmetry measured with leptons from heavy quark decays to be $(1.97 \pm 0.45)\%$ of the asymmetry value.

The OPAL combined results for the bottom and charm forward-backward asymmetries, after correcting for QCD and higher order electroweak effects, yield

$$A_{FB}^{b,0} = 0.0968 \pm 0.0037 \quad \text{and} \quad A_{FB}^{c,0} = 0.0673 \pm 0.0064,$$

where the systematic and statistical errors have been combined in quadrature. The values of the bottom and charm asymmetries are correlated to 1.5%. From these results a value for the weak mixing angle has been determined to be

$$\sin^2 \theta_W^{\text{lept,eff}} = 0.23270 \pm 0.00060.$$

In a second analysis the trilinear gauge couplings have been investigated with the spin density matrix method, using the 57pb^{-1} OPAL data collected in 1997 with a centre-of-mass energy of 183 GeV. For the first time the polarisation properties of the W bosons have been directly observed via the measurement of the spin density matrix elements. For this analysis 362 W-pair events are reconstructed in the decay channel $W^+W^- \rightarrow q\bar{q}l\bar{l}$. From the diagonal elements of the single W spin density matrix the fraction of W bosons with longitudinal polarisation has been derived to be

$$0.242 \pm 0.091(\text{stat.}) \pm 0.023(\text{syst.}).$$

The spin density matrix elements and the angular distribution of the W production angle are compared to the theoretical predictions and a fit has been performed to determine parameters for anomalous trilinear gauge couplings in various models. For the three parameters $\Delta\kappa_\gamma$, Δg_1^Z and λ_γ the fits for a single parameter yields

$$\Delta\kappa_\gamma = -0.67^{+0.38}_{-0.33} \pm 0.19$$

$$\Delta g_1^Z = +0.15^{+0.20}_{-0.20} \pm 0.08$$

$$\lambda_\gamma = -0.16^{+0.19}_{-0.17} \pm 0.07.$$

A simple and model-independent test of CP invariance of the WWZ/WW γ vertex has been performed by comparing the imaginary parts of the density matrices of the W^- and W^+ bosons. These investigations have been quantified by fit for the CP-violating triple gauge coupling parameters $\tilde{\alpha}_{BW}$ and $\tilde{\alpha}_W$. The results of these fits are

$$\tilde{\alpha}_W = +0.09^{+0.18}_{-0.14} \pm 0.03$$

$$\tilde{\alpha}_{BW} = +0.33^{+0.77}_{-0.56} \pm 0.12.$$

The measurements of the CP-conserving coupling parameters have been combined with other OPAL measurements, where the W-pairs are reconstructed in the decay channels $W^+W^- \rightarrow q\bar{q}q\bar{q}$ and $W^+W^- \rightarrow l^+\nu_l l^-\bar{\nu}_l$ and the measurement of the total W-pair production cross-section. The resulting values and the one sigma errors are

$$\Delta\kappa_\gamma = -0.32^{+0.38}_{-0.30}$$

$$\Delta g_1^Z = +0.15^{+0.13}_{-0.14}$$

$$\lambda_\gamma = -0.16^{+0.12}_{-0.14}.$$

Finally the future prospects for triple gauge coupling measurements at LEP2 and a high energy e^+e^- linear collider have been discussed.

Bibliography

- [1] See for example: E. Leader, E. Predazzi, *An introduction to gauge theories and modern particle physics*, Cambridge University Press, 1996.
- [2] The LEP collaborations ALEPH, DELPHI, L3, OPAL, the LEP Electroweak Working Group, and the SLD Heavy Flavour Group, *A combination of preliminary LEP electroweak Measurements and constraints on the Standard Model* 2 December 1997, CERN-PPE/97-154 and M.W. Grünewald *Combined Analysis of Electroweak Precision Results*, talk presented at the 29th International conference on High Energy Physics, Vancouver, 1998.
- [3] The program ZFITTER, described in: D. Bardin et al., CERN-TH 6443/92 (May 1992); Phys. Lett. BB255 (1991) 290; Nucl. Phys B351 (1991) 1; Z. Phys. CC441989493.
- [4] Physics at LEP2, Edited by G. Altarelli, T. Sjöstrand and F. Zwirner, Report on the LEP2 workshop 1995, CERN 96-01 (1996) Vol. 1, 525.
- [5] The OPAL Collaboration, K. Ahmet et al., Nucl. Instr. Meth. A305 (1991) 275, P.P. Allport et al., Nucl. Instr. Meth. A324 (1993) 34, P.P. Allport et al., Nucl. Instr. Meth. A346 (1994) 476.
- [6] S. Anderson et al., Nucl. Instr. Meth. A403 (1998) 326.
- [7] See for example: D.H. Perkins, *Introduction to High Energy Physics*, 3rd Edition, Addison - Wesley Publishing Comp., 1987.
- [8] G. Aguillion et al., *Thin Scintillating Tiles with High Light Yield for the OPAL Endcaps*, CERN-EP/98-069, accepted by Nucl. Instr. Meth.
- [9] OPAL Collaboration, G. Alexander et al., Z. Phys. C 52 (1991) 175.
- [10] T. Sjöstrand, Comp. Phys. Comm. 82 (1994) 74.
- [11] OPAL Collaboration, G. Alexander et al., Z. Phys. C 69 (1996) 543.
- [12] C. Peterson et al., Phys. Rev. D 27 (1983) 105.
- [13] J. Allison et al., Nucl. Instr. Meth. A 317 (1991) 47.
- [14] OPAL Collaboration, K.Ackerstaff et al., Z. Phys. C 75 (1997) 385.
- [15] OPAL Collaboration, R. Akers et al., Z. Phys. C66 (1995) 19.

- [16] OPAL Collaboration, G. Alexander *et al.*, *Z. Phys. C* **70** (1996) 357.
- [17] OPAL Collaboration, *Updated Measurement of Heavy Quark Forward-Backward Asymmetries and Average B Mixing Using Leptons in Multihadronic Events*, OPAL Physics Note PN226, 2nd July 1996.
- [18] G. Altarelli *et al.* *Nucl. Phys. B* **208** (1982) 365.
- [19] CLEO Collaboration, S. Henderson *et al.*, *Phys. Rev. D* **45** (1992) 2212.
- [20] DELCO Collaboration, W. Bacino *et al.*, *Phys. Rev. Lett.* **43** (1979) 1073.
- [21] MARK III Collaboration, R.M. Baltrusaitis *et al.*, *Phys. Rev. Lett.* **54** (1985) 1976.
- [22] N. Isgur, D. Scora, B. Grinstein and M. Wise, *Phys. Rev. D* **39** (1989) 799.
- [23] The LEP collaborations ALEPH, DELPHI, L3, OPAL and the LEP Electroweak Working Group, *A combination of preliminary LEP electroweak measurements and constraints on the Standard Model* 24 November 1995, CERN-PPE/95-172.
- [24] ARGUS Collaboration, H. Albrecht *et al.*, *Phys. Lett. B* **278** (1992) 202.
- [25] OPAL Collaboration, R. Akers *et al.*, *Z. Phys. C* **60** (1993) 601.
- [26] OPAL Collaboration, R. Akers *et al.*, *Z. Phys. C* **67** (1995) 27.
- [27] OPAL Collaboration, G. Alexander *et al.*, *A study of Charm Hadron Production in $Z^0 \rightarrow c\bar{c}$ and $Z^0 \rightarrow b\bar{b}$ decays at LEP*, CERN-PPE/96-51, to be published in *Z. Phys. C*.
- [28] OPAL Collaboration, G. Alexander *et al.*, *Z. Phys. C* **70** (1996) 357.
- [29] OPAL Collaboration, P.D. Acton *et al.*, *Z. Phys. C* **58** (1993) 523.
- [30] Particle Data Group, *Review of Particle Properties*, *Phys. Rev. D* **54** (1996) 1., *Eur. Phys. J. C* **3** (1998) 1.
- [31] C. Burgard, *Electroweak Charm Physics on and near the Z^0 Peak and a Search for $D^0\bar{D}^0$ Mixing*, PhD thesis, Hamburg 1995, unpublished.
- [32] S. Petzold, *Messung der Charm-Asymmetrie auf der Z-Resonanz mit dem OPAL-Detektor*, Diplomarbeit, Hamburg 1995, unpublished.
- [33] C. Schwick, *Investigation of the Charm Fragmentation with the OPAL Detector at LEP*, PhD thesis, Hamburg 1994, unpublished.
- [34] See for example: P.J. Franzini, *Physics Reports* **173** (1989) 1.
- [35] R. D. Field and R. P. Feynman, *Nucl. Phys. B* **136** (1978) 1.
- [36] OPAL Collaboration, R. Akers *et al.*, *Phys. Lett. B* **327** (1994) 411.
- [37] OPAL Collaboration, *A Measurement of the Charm and Bottom Forward-Backward Asymmetry Using D Mesons with the OPAL Detector at LEP* OPAL Physics Note PN183, 17th July 1995.

- [38] The Particle Data Group, R.M. Barnett *et al.*, *Phys. Rev. D* **54** (1996) 1.
- [39] The working group on LEP energy: *LEP energy calibration in 1993, 1994 and 1995*, LEP energy group/96-05, 22 July 1996.
- [40] OPAL Collaboration, R. Akers *et al.*, *Phys. Lett. B* **353** (1995) 595.
- [41] The LEP Collaborations, ALEPH, DELPHI, L3 and OPAL, and the LEP Electroweak working group, CERN-PPE/96-017, to be published in *Nuclear Instruments and Methods*.
- [42] ALEPH Collaboration, D. Buskulic *et al.*, *Z. Phys. C* **62** (1994) 1; ALEPH Collaboration, *The Forward-Backward Asymmetry for Charm Quarks at the Z Pole*, ALEPH 98-018 CONF 98-088; DELPHI Collaboration, P. Abreu *et al.*, *Z. Phys. C* **65** (1995) 569; DELPHI Collaboration, P. Abreu *et al.*, *Z. Phys. C* **66** (1995) 341; DELPHI Collaboration, *Measurement of the Forward-Backward Asymmetries of $e^+e^- \rightarrow Z \rightarrow b\bar{b}$ and $e^+e^- \rightarrow Z \rightarrow c\bar{c}$* , DELPHI 95-87 PHYS 522, contributed paper to EPS-HEP-95 Brussels eps0571. " 365.
- [43] A. Djouadi, B. Lampe, P. Zerwas, *Z. Phys. C* **67** (1995) 123.
- [44] G. Altarelli, B. Lampe, *Nucl. Phys. B* **391** (1993) 3.
- [45] D. Abbaneo *et al.*, *Eur. Phys. J. C* **4** (1998) 185.
- [46] ALEPH Collaboration, D. Buskulic *et al.*, *Z. Phys. C* **55** (1992) 209.
- [47] DELPHI Collaboration, P. Abreu *et al.*, *Z. Phys. C* **73** (1996) 11.
- [48] L3 Collaboration, B. Adeva *et al.*, *Z. Phys. C* **55** (1992) 39.
- [49] G. Marchesini *et al.*, *Nucl. Phys. B, Comp. Phys. Comm.* **67** (1992) 465.
- [50] OPAL Collaboration, G. Alexander *et al.*, *Z. Phys. C* **73** (1996) 379.
- [51] See for example: L. Lyons, D. Gibaut and P. Clifford, *Nucl. Instr. Meth. A* **270** (1988) 110.
- [52] The LEP Experiments: ALEPH, DELPHI, L3 and OPAL, *Nucl. Instr. Meth. A* **387** (1996) 101.
- [53] The LEP collaborations ALEPH, DELPHI, L3, OPAL, the LEP Electroweak Working Group and the SLD Heavy Flavour Group, *A combination of preliminary LEP electroweak measurements and constraints on the Standard Model* 6 December 1996, CERN-PPE/96-183.
- [54] J. Erler *et al.*, *A wide scalar neutrino resonance and $b\bar{b}$ production at LEP*, hep-ph/9612397.
- [55] K. Hagiwara, S. Ishihara, R. Szalapski and D. Zeppenfeld, *Phys. Lett. B* **283** (1992) 353, *Phys. Rev. D* **48** (1993) 2182.
- [56] K. Gaemers and G. Gounaris, *Z. Phys. C* **1** (1979) 259.

- [57] K. Hagiwara, R.D. Peccei, D. Zeppenfeld and K. Hikasa, Nucl. Phys. **B282** (1987) 253.
- [58] M. Bilenky, J.L. Kneur, F.M. Renard and D. Schildknecht, Nucl. Phys. **B409** (1993) 22.
M. Bilenky, J.L. Kneur, F.M. Renard and D. Schildknecht, Nucl. Phys. **B419** (1994) 240.
- [59] A. De Rujula, M.B. Gavela, P. Hernandez and E. Masso, Nucl. Phys. **B384** (1992) 3.
- [60] G. Gounaris and C.G. Papadopoulos, hep-ph/9612378.
- [61] G. Gounaris, J. Layssac, G. Moulhaka and F.M. Renard, Int. Journal of Modern Physics **A19** (1993) 3285.
- [62] G. Gounaris, D. Schildknecht and F.M. Renard, Phys. Lett. **B263** (1991) 291.
- [63] K.F. Smith *et al.*, Phys. Lett. **B234** (1990) 191.
- [64] Ochanomizu CP Study Group, A. Sugamoto *et al.*, *A study of CP violation: Electroweak baryogenesis and anomalous W boson couplings*. To be published in the proceedings of 5th KEK Meeting on CP Violation and Its Origin, Tsukuba, Japan, 6-7 Mar 1997.
- [65] On the Kinematic Reconstruction of $e^+e^- \rightarrow W^+W^- \rightarrow q\bar{q}\tau\bar{\nu}_\tau$ Events, OPAL Technical Note, TN332, 17th Nov 1995.
- [66] F.A. Berends, R. Pittau and R. Kleiss, Comp. Phys. Comm. **85** (1995) 437,
F.A. Berends and A.I. van Sighem, Nucl. Phys. **B454** (1995) 467.
- [67] M. Skrzypek *et al.*, Comp. Phys. Comm. **94** (1996) 216,
M. Skrzypek *et al.*, Phys. Lett. **B372** (1996) 289.
- [68] Minami-Tateya group, T. Ishikawa *et al.*, *GRACE Manual: Automatic generation of tree amplitudes in Standard Models: version 1.0*, KEK-92-19, Feb. 1993.
- [69] T. Sjöstrand, Comp. Phys. Comm. **82** (1994) 74.
- [70] J. Fujimoto *et al.*, KEK-CP-046, Comp. Phys. Comm. **100** (1997) 128.
- [71] S. Jadach, Z. Was, R. Decker, J.H. Kühn, Comp. Phys. Comm. **76** (1993) 361.
- [72] OPAL Collaboration, K. Ackerstaff *et al.*, CERN-PPE/97-116, submitted to Z. Phys. C.
- [73] OPAL Collaboration, G. Abbiendi *et al.*, *W⁺W⁻ production and triple gauge boson couplings at energies up to 183 GeV*, CERN-EP/98-167, Accepted by Eur. Phys. J.
- [74] D0 Collaboration, B. Abbott *et al.*, Phys. Rev. Lett. **80** (1998) 3008,
CDF Collaboration, F. Abe *et al.*, Phys. Rev. Lett. **75** (1995) 11.
- [75] OPAL Collaboration, K. Ackerstaff *et al.*, CERN-PPE/97-125, accepted by Zeit. f. Physik.
- [76] OPAL Collaboration, K. Ackerstaff *et al.*, Phys. Lett. **B397** (1997) 147.
- [77] D. Bardin *et al.*, Nucl. Phys. B, Proc. Suppl. **37B** (1994) 148-157.
- [78] G. Gounaris and C.G. Papadopoulos, Eur. Phys. J. **C 2** (1998) 365.
- [79] E.N. Argyres, A.B. Lahanas, C.G. Papadopoulos and V.C. Spanos, Phys. Lett. **B383** (1996) 63.
- [80] Y. Katsuki, M. Marui, R. Najima, J. Saito and A. Sugamoto, Phys. Lett. **B354** (1995) 363.
- [81] T.G. Rizzo, Phys. Rev. **D46** (1992) 3894.
- [82] M. Kitahara, M. Marui, N. Oshimo, T. Saito and A. Sugamoto, Eur. Phys. J. **C 4** (1998) 661.

Acknowledgements

An dieser Stelle möchte ich allen danken, die zum Gelingen dieser Arbeit beigetragen haben.

Ganz besonders möchte ich Prof. Albrecht Wagner für seine Unterstützung danken, die auch den Besuch von Sommerschulen, Konferenzen und den längeren Aufenthalt am CERN ermöglichte. Besonderen Dank auch an Dr. Ties Behnke und Dr. Christoph Burgard, die beide durch viele Diskussionen und konstruktive Kommentare zu dieser Arbeit beigetragen haben. Auch vielen Dank der TGC-Gruppe, und hier ganz besonders Dr. Gideon Bella, Dr. Peter Clarke und Helge Voss für die vielen Anregungen und die ausgezeichnete Zusammenarbeit, die auch über viele tausend Kilometer gut geklappt hat. Auch bei der gesamten Hamburger OPAL-Gruppe, also bei Dr. Johannes Steuerer, Jens, Petra, Alexander, Andreas, Frank, Götz, Kristian und Christian, möchte ich mich für Hilfe bei verschiedenen Fragen und viel Kurzweil bedanken. Dank auch der TE-Gruppe, und hier ganz besonders Dr. Austin Ball, für die Einführungen in die Welt der Hardware und die Unterweisungen in seltsamen Cockney-Reimen. Vielen Dank auch an DESY für die Finanzierung der Schulen, Konferenzen, des CERN-Aufenthaltes und die guten Arbeitsbedingungen. Und ganz besonderen Dank meinen Eltern für die Unterstützung und ihr Zutrauen während meiner ganze Ausbildung und Kira für ihre viele gute Laune.